



Ho Chi Minh City
University of Technology



Mien Tay
Construction University



South Vietnam
Geological Mapping Division

(USGEG) Union of Science Geology Environmental and Geophysics



法政大学
HOSEI University



川崎地質株式会社
Kawasaki Geological Engineering Co.,Ltd.

PROCEEDING FOR SYMPOSIUM

VIETNAM - JAPAN

SYMPOSIUM ON NATURAL DISASTERS



November 27-30, 2018

TABLE OF CONTENTS

Page	Paper title
iv	INFORMATION ABOUT SYMPOSIUM
vi	SYMPOSIUM PROGRAM
	SESSION 1
1	STUDY ON TOPPLED VEHICLES IN THE 2016 KUMAMOTO EARTHQUAKE, JAPAN Junji Kiyono, Rishi Ram Parajuli
6	SEISMIC RISK ASSESSMENT AND LOSS ESTIMATION FOR HO CHI MINH CITY Nguyen Hong Phuong, Nguyen Viet Ky, Pham The Truyen, Nguyen Ngoc Thu
20	EVALUATION OF GROUND STRAIN IN A SEDIMENT-FILLED VALLEY WITH PGV GRADIENT Yasuko Kuwata, Atsuki Okamoto
26	APPLICATION OF SAR IMAGES FOR EVALUATING THE GROUND SUBSIDENCE IN NAM SON USING THE DINSAR TECHNIQUE Nguyen The Duoc, Tran Anh Tu
32	SIMULATION OF STRONG GROUND MOTIONS FOR THE 2016 KUMAMOTO EARTHQUAKE SEQUENCE AROUND THE PORT OF KUMAMOTO Atsushi Nozu
	SESSION 2
39	A NEW APPROACH FOR ESTIMATING SEISMIC DAMAGE OF BURIED WATER SUPPLY PIPELINES H. Sakai, N. Pulido, K. Hasegawa and Y. Kuwata
57	CHARACTERISTIC OF STRUCTURE AND MODERN ACTIVITY OF NAM SON RIVER FAULT AND IMPLICATION FOR: THE GROUND SUBSIDENCE AND FLOODING IN HO CHI MINH CITY AREA Do Van Linh, Thai Quang, Ha Thuy Hang, Lai Van Thuy, Duong Chi Cong, Le Anh Dung, Dong Bich Phuong, Pham The Tai, Vu Van Thanh.
60	EVACUATION SIMULATION METHOD FOCUSING ON EVACUATION START Yoshihiro Okumura and Yuji Dohi
66	SEISMIC RISK ASSESSMENT OF HANOI USING THE JAPANESE METHOD Takanobu Suzuki, Ha Thai Son
	SESSION 3
70	STUDY ON NUMERICAL ANALYSIS OF IMPACT RESPONSE OF CONCRETE PLATE SUBJECTED TO MEDIUM SPEED COLLISION OF STEEL PROJECTILE Aiko Furukawa, Masato Goto, Junji Kiyono and Hitoshi Nakase
75	GEOSYNTHETIC ENCASED COLUMN – AN ALTERNATIVE OF TECHNICAL SOLUTIONS IN SOFT SOIL IMPROVEMENT FOR CONSTRUCTION WORKS IN VIET NAM Pham Tien Bach, Vo Dai Nhat, Le Quan
81	ISOLATION RISK ANALYSIS OF RESIDENTIAL SETTLEMENTS IN MOUNTAINOUS REGION: CASE STUDIES FOR 2004 NIIGATA-KEN CHUETSU AND 2016 KUMAMOTO EARTHQUAKES Yusuke Ono and Keishin Hibi
86	EFFECT OF DRILLING MUDS AND CUTTINGS DISCHARGED TO THE ENVIRONMENT Do Quang Khanh, Hoang Trong Quang, Tran Thi Mai Huong, Kieu Phuc
91	FORCE-DISPLACEMENT ANALYSIS OF BURIED STEEL PIPELINES FOR STRIKE-SLIP FAULTING Farzad Talebi, Junji Kiyono

SESSION 4

- 96 DAMAGE ANALYSIS OF WATER SUPPLY SYSTEM IN HEAVY RAIN DISASTERS
N. Iwamoto and M. Miyajima
- 104 DEVELOPING AN ANALYTICAL METHOD FOR DETERMINING THE RADIUS OF FAILURE ZONE OF SINGLE PILE IN SAND
Tran Van Tuan, Bui Huu Trong, Vo Van Dau, Le Tuan An
- 109 STRONG GROUND MOTION SIMULATION OF THE MAINSHOCK OF THE 2016 KUMAMOTO EARTHQUAKES WITH MULTIPLE POINT SOURCES AND NEAR SURFACE RUPTURES
Yosuke Nagasaka and Atsushi Nozu
- 114 EFFECTS OF MAJOR NATURAL DISASTERS IN VIETNAM, GOVERNMENTAL SOLUTIONS AND PEOPLE'S ATTITUDES DEAL WITH THE NATURAL DISASTERS
Nguyen Van Tho
- 119 VERIFICATION OF DYNAMIC RESPONSE OF A LONG-PERIOD BRIDGE SUBJECTED TO AN EXTREME GROUND EXCITATION
Gaku Shoji, Ryota Harigaya, Sumika Miura

SESSION 5

- 123 NATURAL DISASTERS AND THEIR EFFECTS ON LIVELIHOODS OF THE PEOPLE IN VINH LONG PROVINCE
Ha Chi Tam and Nguyen Van Tho
- 128 EFFECTS OF OVERBURDEN LOADS ON LIQUEFACTION-INDUCED SETTLEMENTS WITH SAND BOILING
Tetsuo Tobita and Yuya Yoshimura
- 132 EVALUATION OF THE JOINT CHARACTERISTICS DISTRIBUTION IN THE EXPLORATORY ADIT
Nguyen Thi Kieu Mi, Nguyen Huynh Thong, Naotoshi Yasuda
- 140 VERIFICATION OF THE CORRECTED EMPIRICAL GREEN'S FUNCTION METHOD – EFFECTS OF FREE SURFACE ON FLING STEPS –
Shuanglan Wu, Atsushi Nozu, Yosuke Nagasaka

FURTHER

- 145 STUDY, ANALYSIS AND ASSESS EFFECTIVENESS OF SOFT SOIL IMPROVEMENT USING PVD COMBINE VACUUM PRELOADING AT HYOSUNG VINA CHEMICALS PROJECT AT BA RIA VUNG TAU PROVINCE, VIET NAM BASED ON MONITORED RESULTS AND SOIL INVESTIGATION BEFORE AND AFTER GROUND IMPROVEMENT
Phan Thanh Tien and Nguyen Tan Son, Dang Hoang Thai, Dao Ba Linh, Tran Van Dung, Hoang Minh Phuong, Tran Thanh Vu, Luu Ba Giap, Truong Thanh Can, Nguyen Van Tinh, Nguyen Phu Tay
- 157 LANDSLIDE RISK ASSESSMENT BY SITE INVESTIGATION AND NUMERICAL ANALYSIS IN AN KHE PASS, VIETNAM
Nguyen Huynh Thong, Le Thanh Phong, Bui Trong Vinh, Toshihiro Asakura, Naotoshi Yasuda
- 170 THE SLOPE STABILITY ASSESSMENT FOR OPEN PIT MINING EXTRACTION
Tran Le Hoang Tu, Nguyen Huynh Thong
- 170 LANDSLIDE DISASTER AND APPLICATION POSSIBILITY OF LANDSLIDE EARLY WARNING SYSTEM (LEWS) IN LAM DONG PROVINCE, SOUTHERN VIETNAM
Bui Trong Vinh, Pham Thanh Phuc, Le Thanh Phong, Nguyen Huynh Thong, Tran Anh Tu, Nguyen Viet Ky, Kanno Takami, Kiyono Junji
- 171 RIP CURRENT AND BEACH CIRCULATION HAZARDS IN VUNG TAU BEACH – VIETNAM
Bui Trong Vinh, Huynh Trung Tin, Jung Lyul Lee
- 172 APPLICATION OF S-SHAPE CURVE EQUATION TO DESCRIBE CONSOLIDATION TEST RESULTS USING CURVE FITTING TOOL
Vo Dai Nhat, Tran Van Thanh

- 173 EVALUATION OF EFFECTS OF UNDRAINED AND DRAINED CONDITIONS ON RAFT FOUNDATION WITH DIFFERENT FACTORS OF SAFETY USING THREE DIMENSIONS FINITE ELEMENT ANALYSIS
Tran Van Tuan, Nguyen Qui Ninh, Truong Quynh Nhu, Luu Duc Cuong
- 174 DETERMINE GROUND WATER IN CENTRAL HIGHLAND IN VIETNAM
Truong Quoc Thanh, Nguyen Xuân Kha, Nguyen Thi Nhu Dung, Do Quang Khanh, Tran Van Xuan
- 175 PREDICTION OF OILFIELD SCALE DEPOSITION ALONG THE WELLBORE: FUNDAMENTALS AND APPLICATIONS
Lan Mai-Cao, Bao-Tram Bui-Nguyen
- 176 SAND PRODUCTION POTENTIALS IN PETROLEUM WELLS AT VIETNAM
Do Quang Khanh, Nguyen Tuan, Kieu Phuc
- 177 APPLICATION OF CAPACITACE – RESISTANCE MODELS TO SECONDARY OIL RECOVERY BY WATERFLOODING
Ta Quoc Dung, Pham Son Tung, Huynh Van Thuan
- 177 THE GROUNDWATER RESOURCES SUSTAINABILITY OF THE UPPER – MIDDLE PLEISTOCENE AQUIFER IN CA MAU PENINSULA UNDER IMPACT OF CLIMATE CHANGE AND SOME OF ADAPTIVE SOLUTIONS
Dao Hong Hai, Nguyen Viet Ky, Bui Tran Vuong
- 178 DETERMINE THE COMPONENTS OF LITHOLOGY - RATIO OF MINERALS AND CHARACTERISTICS OF POROSITY AND PERMEABILITY IN FRACTURED BASEMENT
Nguyen Xuan Kha, Pham Xuan Son, Nguyen Lam Anh, Hoang Van Quy, Truong Quoc Thanh, Nguyen Thi Y Nhi1, Tran Van Xuan

INFORMATION ABOUT SYMPOSIUM

ORGANIZED BY

- Ho Chi Minh City University of Technology (HCMUT)-VNU-HCMC;
- Mien Tay Construction University (MTU);
- South Vietnam Geological Mapping Division (SVGMD);
- Union of Science Geology, Environmental and Geophysics (USGEG).
- Kyoto University, Japan
- Hosei University, Japan
- Kanazawa University, Japan
- Kansai University, Japan
- Kobe University, Japan
- Tottori University, Japan
- Toyo University, Japan
- University of Tsukuba, Japan
- Port and Airport Research Institute, JP
- Kawasaki Geological Engineering Co., Ltd. (KGE), Japan

INTRODUCTION

Natural disasters have been occurring all over the world, causing serious damages to human lives and properties. For instance, until December 2017, natural disasters have caused over 60,000 billion VND in economic losses exclusive of damages on people in Vietnam. In 2018, many natural disasters such as earthquakes, typhoons, landslides, heavy rain caused so much damage in Japan. In order to understand more about natural disasters and to look for prevention solutions aiming to reduce human and material losses, the Ho Chi Minh City University of Technology (HCMUT), Mien Tay Construction University (MTU), the South Vietnam Geological Mapping Division (SVGMD) and Union of Science Geology, Environmental and Geophysics (USGEG) collaborated with Kyoto Univ., Hosei Univ., Kanazawa Univ., Kansai Univ., Kobe Univ., Tottori Univ., Toyo Univ., University of Tsukuba, Port and Airport Research Institute and Kawasaki Geological Engineering Co., Ltd (KGE) organize Vietnam - Japan symposium on natural disasters with following topics: Earthquakes, Tsunami, Landslides, Land Subsidence, Riverbank Erosion, Typhoon, Geotechnical Solutions ect...

ORGANIZING COMMITTEE

Chairman: Dr. Nguyen Van Chieu, Vice Rector, MTU.

Co-chairman: Dr. Ta Quoc Dung, Dean of GEOPET, HCMUT.

MEMBERS

1. Dr. Bui Trong Vinh - HCMUT
2. Prof. Junji Kiyono - KYOTO Univ.
3. Dr. Nguyen Ngoc Thu - USGEG
4. Mr. Thai Quang - SVGMD
5. Dr. Do Van Linh - SVGMD
6. A/Prof. Nguyen Viet Ky - HCMUT
7. A/Prof. Tran Van Xuan - HCMUT

8. Dr. Mai Cao Lan - HCMUT
9. Dr. Vo Dai Nhat - HCMUT
10. Dr. Tran Anh Tu - HCMUT
11. A/Prof. Le Trung Chon - HCMUT
12. Prof. Masakatsu Miyajima - KANAZAWA Univ.
13. Prof. Takanobu Suzuki - TOYO Univ.
14. Prof. Kazuhisa Sakai - HOSEI Univ.
15. Dr. Takami Kanno - KGE
16. Dr. Le Bao Quoc - MTU
17. Dr. Vu Duy Thang - MTU
18. Dr. Nguyen Van Tho - MTU
19. M.S. Nguyen Ngoc Long Giang - MTU
20. M.S. Dang Huu Loi - MTU

SECRETARIAT

1. Dr. Nguyen Huynh Thong – HCMUT
Email: nhthong@hcmut.edu.vn
2. M.S. Trinh Cong Luan – MTU
Email: trinhcongluan@mtu.edu.vn

SYMPOSIUM PROGRAM

November 27-30, 2018

Day 1: Nov. 28, 2018		
Start	End	Ho Chi Minh City University of Technology – VNU-HCMC
08:30	09:00	Registration
09:00	09:30	Opening Remarks <ul style="list-style-type: none"> - Prof. Le Minh PHUONG, Vice-Rector of HCMUT - Dr. Nguyen Van CHIEU, Vice-Rector of Mien Tay Construction Univ., - Prof. KIYONO Junji, Kyoto Univ. - Dr. Nguyen Ngoc THU, General Director, USGEG - Dr. Do Van Linh, Deputy Director, SVGMD
10:00	10:15	Photo Session
PLENARY SESSION 1 (10:30 – 12:10): Chair: Prof. KIYONO Junji		
10:30	10:50	KIYONO Junji , Professor, Kyoto University, JAPAN <i>Study on Toppled Vehicles in the 2016 Kumamoto Earthquake, Japan</i>
10:50	11:10	Nguyen Hong PHUONG , Professor, Institute of Geophysics, Vietnam Academy of Science and Technology, VIETNAM <i>Seismic Risk Assessment and Loss Estimation for Ho Chi Minh City, Vietnam</i>
11:10	11:30	KUWATA Yasuko , A/Professor, Kobe Univ., JAPAN <i>Evaluation of Ground Strain in a Sediment-Filled Valley with PGV Gradient</i>
11:30	11:50	Tran Anh TU , Dr.Eng, Vice-Dean, GEOPET, HCMUT, VIETNAM <i>Application of SAR images for evaluating the ground subsidence in Nam Sai Gon using the DInSAR technique</i>
11:50	12:10	NOZU Atsushi , Dr.Eng, Port and Airport Research Institute, JAPAN <i>Simulation of Strong Ground Motions for the 2016 Kumamoto Earthquake Sequence around the Port of Kumamoto</i>
PLENARY SESSION 2 (14:00 – 15:10): Chair: Prof. Nguyen Hong PHUONG		
14:00	14:20	SAKAI Hisakazu , Professor, Hosei University, JAPAN <i>A new approach for estimating seismic damage of buried water supply pipelines</i>
14:20	14:40	Do Van LINH , Dr.Eng., Deputy Director, South Viet Nam Geological Mapping Division <i>Characteristic of Structure and Modern Activity of Sai Gon River Fault and Implication for the Ground Subsidence and Flooding in Ho Chi Minh City Area</i>
14:40	15:10	OKUMURA Yoshihiro , A/Professor, Kansai Univ., JAPAN <i>Evacuation Simulation Method Focusing on Evacuation Start</i>
15:10	15:30	SUZUKI Takanobu , Professor, Toyo University, JAPAN <i>Seismic Risk Assessment of Hanoi Using the Japanese Method</i>
PLENARY SESSION 3 (15:30 – 16:30) Chairman: Prof. SAKAI Hisakazu		
15:50	16:10	FURUKAWA Aiko , A/Professor, Kyoto University, JAPAN <i>Study on Numerical Analysis of Impact Response of Concrete Plate Subjected to Medium Speed Collision of Flying Object</i>
16:10	16:30	Pham Tien BACH , Doctor Candidate, GEOPET, HCMUT, VIETNAM <i>Geosynthetic Encased Column – An Alternative of Technical Solutions in Soft Soil Improvement for Construction Works in Viet Nam</i>
16:30	16:50	ONO Yusuke , A/Professor, Tottori Univ., JAPAN <i>Isolation Risk Analysis of Residential Settlements in Mountainous Region: Case studies for 2004 Niigata-ken Chuetsu and 2016 Kumamoto Earthquakes</i>

16:50	17:10	Do Quang KHANH , Dr.Eng., Head, Simulation Lab., GEOPET, HCMUT <i>Effect of Drilling Muds And Cuttings Discharged to the Environment</i>
17:10	17:30	Farzad TALEB , Doctor Candidate, Kyoto University <i>Force-displacement analysis of buried steel pipelines for strike-slip faulting</i>
DAY 2: NOV. 29, 2018		
Start	End	Mien Tay Construction University, Vinh Long Province
13:30	14:00	Registration
PLENARY SESSION 4 (14:00 – 15:35), Chairman: Prof. MIYAJIMA Masakatsu		
14:00	14:15	Opening Remarks <ul style="list-style-type: none"> - Dr. Nguyen Van XUAN, Rector of Mien Tay Construction Univ., - Dr. Ta Quoc DUNG, Dean, GEOPET, HCMUT - Prof. MIYAJIMA Masakatsu, Kanazawa Univ., Japan
14:15	14:35	MIYAJIMA Masakatsu , Professor, Kanazawa Univ., JAPAN <i>Impact of Heavy Rain on Drinking Water Supply System</i>
14:35	15:55	Tran Van TUAN , Dr.Eng., Can Tho Univ., VIETNAM <i>Developing An Analytical Method For Determining The Radius Of Failure Zone Of Single Pile In Sand</i>
15:55	15:15	NAGASAKA Yosuke , Dr.Eng, Port and Airport Research Institute, JAPAN <i>Strong ground motion simulation of the main shock of the 2016 Kumamoto earthquakes with multiple point sources and near surface ruptures</i>
15:15	15:35	Nguyen Van THO , Dr. Eng., Mien Tay Construction Univ., VIETNAM <i>Effects Of Major Natural Disasters In Vietnam, Governmental Solutions And People's Attitudes Deal With The Natural Disasters</i>
Photo session and Coffee break (15:35 – 15: 50)		
PLENARY SESSION 5 (15:50 – 17:10)		
15:50	16:10	SHOJI Gaku , A/Professor, Tsukuba Univ., JAPAN <i>Verification of Dynamic Response of a Long-Period Bridge Subjected to an Extreme Ground Excitation</i>
16:10	16:30	Ha Chi TAM , Dr.Eng, Deputy head of Committee Division of Environment and Natural Resources, the People Committee of Vinh Long City, VIETNAM <i>Natural Disasters and Their Effects on Livelihoods of the People in Vinh Long Province</i>
16:30	16:50	TOBITA Tetsuo A/Professor, Kansai Univ., JAPAN <i>Experimental study on liquefaction-induced settlements with sand boiling</i>
16:50	17:10	Nguyen Huynh THONG , Dr. Eng, GEOPET, HCMUT, VIETNAM <i>Evaluation of the joint characteristics distribution in the exploratory adit</i>
17:10	17:30	Shuanglan WU , Port and Airport Research Institute, JAPAN <i>Verification of the corrected empirical Green's function method – Effects of free surface on fling steps –</i>
DAY 3: NOV. 30, 2018		
Start	End	
8:00	11:00	Field Trip on Boat along Mekong River

STUDY ON TOPPLED VEHICLES IN THE 2016 KUMAMOTO EARTHQUAKE, JAPAN

Junji Kiyono, Rishi Ram Parajuli

ABSTRACT

Kumamoto earthquake M7.3 hit southern Japan on April 16, 2016. Extensive damages on structures were concentrated in the areas where the rupture exposed to the surface. We found many vehicles toppled on the site during damage survey in Tateno and Kurokawa area. Seismic response analyses of car are executed to find out the scenario of toppling condition. Relationship of lateral peak ground acceleration (PGA) associated with toppling under several conditions are presented. Relationship of amplitude of vertical component, dominant frequency of the input wave and phase difference of lateral to the vertical wave are presented and formulated as ground motion characteristics of the earthquake. Cars toppled during Kumamoto earthquake were analyzed using the seed ground motion recorded in KMMH16, NIED K-Net station in Mashiki town, data available nearby of the epicenter, having the highest PGA. Suzuki Every Wagon was selected for analysis. The car got toppled when the PGA is 14.17 m/sec^2 in 10.86 seconds as scaling factor is 2.654 for lateral component, keeping the vertical components unchanged.

KEYWORDS: 2016 Kumamoto earthquake, Strong ground motion, Toppled vehicle

DR. JUNJI KIYONO

Professor, Department of Urban Management, Graduate School of Engineering, Kyoto University, Japan

Email: kiyono.junji.5x@kyoto-u.ac.jp, **corresponding author**

Tel: +81-75-383-3249

DR. RISHI RAM PARAJULI

Lecturer, Institute of Engineering, Tribhuvan University, Nepal

Email: rishiramparajuli@gmail.com

1. Introduction

Earthquake might not be noticed when the level of shaking is in lower range while the running vehicle itself has certain accelerations in it. However, excessive shaking in forward, lateral and vertical directions result the unusual behavior of vehicle as response of the shaking. Drivers' responses during the earthquakes in Japan (M7.7 Nihon-kai-chubu earthquake, 1983 and M6.7 Chiba-ken-oki earthquake, 1987) were studied based on questionnaire survey (Kawashima et al. 1989). That survey conducted in Akita prefecture and Chiba prefecture respectively where the seismic intensity level was of V in JMA scale (JMA 1996). Most of the drivers (65% and 43.3%) stopped their vehicle where 50% of the drivers noticed the earthquake upon the vehicle behaved unusual. Following the M7.0 Miyagiken-oki earthquake in 2003, a study on drivers' response in relation with JMA intensity was conducted (Maruyama and Yamazaki 2006). It found that only 40% of the drivers recognized the earthquakes of JMA intensity less than 4.0 in contrary 80% recognized and reacted during higher intensity of shaking.

Studies related to vehicle responses are not intensive as compared with other safety aspects. Seismic response analysis on the stability of running vehicles was studied in 2002 using the six degree of freedom system vehicle model (Maruyama & Yamazaki, 2002). Vehicle with constant speeds of 100 kmph and 120 kmph were analysed under five different earthquakes (Kobe, El Centro, Tottori, Mexico and Chiba-ken-oki). This study revealed vehicle responses are depend on the ground motion characteristics as the long period dominant ground motion result the higher responses of the vehicle. This method could not well define the condition of stationary or parked vehicles. We previously proposed CPLM method for seismic response analysis of vehicles (Parajuli & Kiyono, 2016). The method can be used in the cases of stationary and running condition of vehicle where the model was validated with response of the stopped vehicle during Gorkha earthquake 2015 having long period ground motion in Kathmandu (Parajuli & Kiyono, 2015). The method well explained about the response in longitudinal and lateral directions but rotational motions were left as previous studies. Vehicle response and risks associated with location and speed during the earthquake, running on the elevated structures were also studied (Parajuli, Kiyono, & Yatsumoto, 2017). This study is now focusing on the analysis of toppling condition and mechanism of the vehicle with a car model.

2. Earthquake and toppled vehicles

2.1 The 2016 Kumamoto Earthquake

April 16, 2016, M7.3 earthquake struck in Kumamoto of Kyushu region in Japan at depth of about 12 km. The main shock followed the two major foreshocks of M6.4 and M6.5 in 15th and 14th. At least 49 people lost their life with tens of thousands moved to the evacuation centers where thousands of structures got collapsed. JMA seismic intensity due to the main shock was recorded up to 6.5 in Mashiki area at station KMMH16 (NIED, 2016b), about 7 km far from the epicenter. Tateno area in Kumamoto, about 26 km NE from the epicenter was hit by the large landslide, triggered due to the earthquake shaking. Structures in Kurokawa, adjacent to Tateno area were also severely damaged where rupture line exposed to the surface. A1 in the Figure 1 shows the Tateno and Kurokawa area where the fault slip is in range of 4-5 meters and the corresponding values on the surface is in range of 3-3.5 m (NIED, 2016a).

During the survey in Kurokawa area we found some cars (C1 – C5) toppled on the site due to the earthquake ground motion. The high speed train (TR1) and normal JR train (TR2) shown in Figure 1 were also derailed at nearby Kumamoto station and Akamizu station respectively. We used the google earth map that updated post-earthquake to find the more cases where we found a truck (TRK) and a car (C6) in Tateno area got toppled on April 16. Locations of all the toppled vehicles and their direction of toppling are also shown by red arrows in Figure 2 along with the rupture line. All of the vehicles toppled toward main rupture line (fault normal direction) except one car that toppled in fault parallel direction. Such phenomenon is localized in the distance of about 100 meters from the line of rupture that

exposed to the surface in Kurokawa area. An example of the toppled vehicles is shown in Figure 3. All of the cars toppled are registered with yellow plate that denotes the light vehicles.

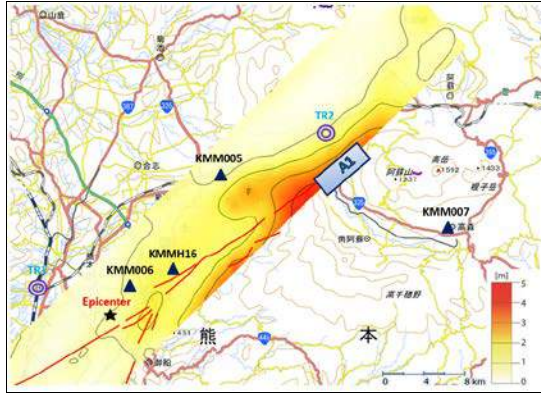


Figure 1: Fault slip distribution (NIED, 2016a)

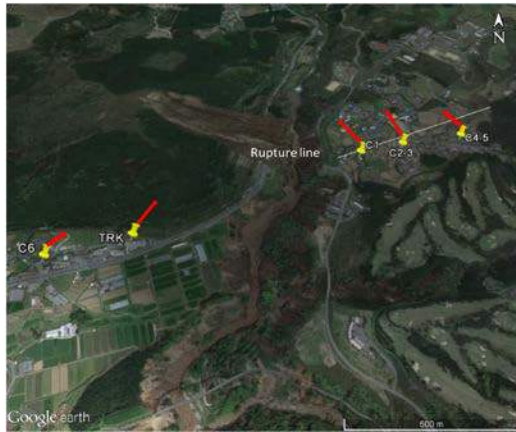


Figure 1: Locations of vehicles toppled and toppling direction with surface rupture lines



Figure 3: Toppled vehicle in Kurokawa area

2.2 Vehicle model

Car model is same as the model used by (Maruyama & Yamazaki, 2002) in their analysis. Total weight of the vehicle is 1200 kg where the wheel base and trades are of 2.635m and 1.505m. Vehicle parameters and notations used in the

analysis are shown in Table 1. Figure 4 shows the simple vehicle model with six degree of freedom, three translational motions with rotational motions rolling, pitching and yawing along X, Y and Z axes. Mass of the car body is taken as m_2 where each tyre has mass m_1 . Horizontal ground motions are transferred from ground to the vehicle using the spring and dashpot system of single degree of freedom model. Vertical motion is defined by the double degree of freedom system. Quarter vehicle model with tyre and body of car is used for the up down response of the vehicle using the equation of motion.

Table 1: Parameters of the vehicle models

Parameters		Value	Unit
Tyre mass	m_1	25.00	kg
Vehicle mass	m_2	1100.00	kg
Length: front wheel - CG	l_f	1000.00	mm
Length: rear wheel - CG	l_r	1635.00	mm
Height of CG	h	350.00	mm
Length: right - left axel	d	1505.00	mm
Stiffness for rolling motion	K_ϕ	117.60	kN m
Elastic constant of steering	K_{st}	48.50	kN m/r
Spring const.: tyre-ground	k_1	800.00	kN/m
Suspension spring constant	k_2	70.00	kN/m
Tyre damping	c_1	0.098	kN s/m
Suspension damping	c_2	4.90	kN s/m

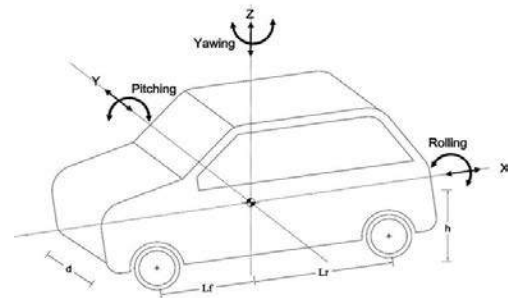


Figure 2: Vehicle model showing all translational and rotational motions

3. Analysis

Translational and rotational motions except the rolling motion in the analysis followed as specified in CPLM method. Previously proposed CPLM method is not sufficient to define the toppling condition. Here we introduce the angular momentum method in calculation of rolling angle when the vehicle tilted enough to take load by right or left tires only. Rolling motion of the vehicle that does not start toppling is similar as specified in the previous study. A simple model for rolling analysis is shown in figure 5 where

d is the trade, h is the height of the CG, θ_g is the angle from lower corner to CG, θ is roll angle. When we analyze the parked vehicle, we supposed it with locked brake that the rolling of tyre effect is null. Coefficient of friction, maximum steering angle and maximum radius of turn are taken as specified in previous study. We do not consider the super elevation, camber and the gradient of the road.

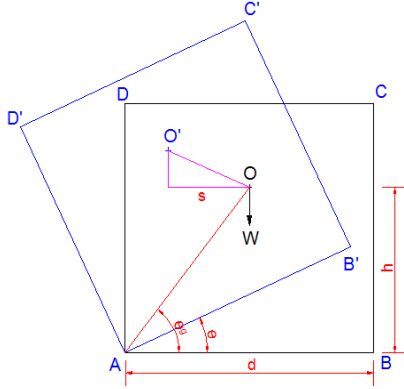


Figure 3: Vehicle model to analyze the rolling motion in toppling condition

Vehicle toppling mechanism starts when the vehicle load initiates to transfer to ground through the tires in one side. Considering the up-down component of the ground motion, threshold value of the lateral acceleration a_t to start the toppling mechanism of vehicle is given by Eq.(1).

$$a_t = \frac{d(g - \ddot{z})}{2h} \quad (1)$$

Where g is the gravitational acceleration and d^2z/dt^2 is the vertical acceleration. Total angle θ_a including the rolling angle and θ_g is calculated for location of CG in each step as shown in Eq.(2). Changes in angular momentum due to the vertical and lateral accelerations are calculated by using the Eq.(3).

$$\theta_a = (\theta_g + \theta_i) \quad (2)$$

$$\Delta L = MR[\ddot{y} \sin(\theta_a) \mp \{(g - \ddot{z}) \cos(\theta_a)\}] \quad (3)$$

Where ΔL change in angular momentum, M is total mass of the vehicle, R is the distance from bottom corner to the locus of CG (AO in Figure 5). Lateral acceleration and velocity of the vehicle are denoted by d^2y/dt^2 and dy/dt . Sign of vertical component of momentum in Eq.(3) is depends on support condition of vehicle. When we consider the left bottom corner as the support and the lateral acceleration is anticlockwise, negative is used and vice versa. Summation of angular momentum in each step of calculation is now used to find out the linear velocity of body in lateral direction centered on lower corner by Eq.(4). Eq.(5) shows the calculation of change in rolling angle.

$$V_i = \frac{L_i}{RM} \quad (4)$$

$$\Delta\theta = \frac{V_i \cdot dt}{R} \quad (5)$$

$$\theta_{i+1} = \theta_i + \Delta\theta \quad (6)$$

When the rolling angle reaches $\pi/2$, the vehicle toppled on the side.

3. Vehicle toppling in Kurokawa area during Kumamoto earthquake

Target areas where the vehicles got toppled are Kurokawa and Tateno, about 26 km far from the epicenter. Toppled vehicles are registered with yellow plates those licensed as light cars (under 660 CC). We select a model SUZUKI Every Wagon as the sample car in this study (Car sensor Lab, 2016). The total weight of the vehicle is 950 Kg, wheel base is 2.35 m, rear and front treads both are equal of 1.28 meters. Total length, breadth and height of the car is 3.395 m, 1.475 m and 1.87 m respectively. Ground clearance of the car is 0.145 m but we could not found the exact CG location of this car. CG of the vehicle is variable with rotational motion, it has higher variation when subjected to the pitching than in rolling motion (Hejtmanek, Blatak, & Vancura, 2015). Height of CG of Skoda Yeti car is 0.5642 m and 0.714 m in rolling and pitching where total height of car is 1.671 m with ground clearance of 0.18 m (Hejtmanek et al., 2015). Ratio of height of CG to body height is 0.3784 excluding the ground clearance when subjected to rolling motion. In case of SUZUKI Every Wagon, configuration of the car is different than the Skoda hence we suppose the height of CG is 20% of height of car body excluding the ground clearance. Now the total height of CG of the car is 0.490 m and b/h ratio is 2.612. We estimate the lateral PGA to topple the car using the regression coefficients stated previously in section 4 and from the analysis using our method.

Recorded ground motions are not available in Kurokawa area hence we use the most likely ground motion in the analysis as seed ground motion. NIED has dense network of ground motion recording stations in Japan. KMM005 is the nearest station from the epicenter located in about 5 km. The highest PGA recorded was in station KMMH16, about 7.6 km far from the epicenter, near the fault in the Mashiki town. PGA recorded in KMMH16 are 11.57, 6.53 and 8.73 m/sec^2 in EW, NS and UD components (NIED, 2016b). This station is about 18.7 km far from the site (Kurokawa). Locations of the NIED stations, epicenter and Kurokawa area are shown in Figure 1.

We found from the geological map that the Mashiki area has the similar geological condition with Kurokawa area. Fault slip distribution of Kumamoto earthquake is shown in figure 1. Fault slip in Kurokawa area is about 4–5 meters when the value in Mashiki area is about 1 meter (NIED, 2016b). Hence we used the ground motion record of KMMH16 in the analysis with amplifying factors to get the condition of vehicles to be toppled. We transferred recorded ground motion to the axis of fault parallel and normal supposing the strike angle of fault is N40°E, PGA values now changed to 12.2, 5.34 and 8.73 m/sec^2 . Ground motion in fault parallel, fault normal and vertical directions in left, with the corresponding Fourier spectrum in right are shown in Figure 6.

Vehicle toppling mechanism initiates in the section of ground motion with peak records, we select the time window of 10.3–10.94 sec and find the phase difference and dominant frequency. Figure 7 shows the lateral and vertical components of acceleration and corresponding Fourier

spectrum. Dominant frequency of lateral component is about 1 Hz where vertical has around 10 Hz, phase difference of the lateral and vertical component is 5.146 radian.

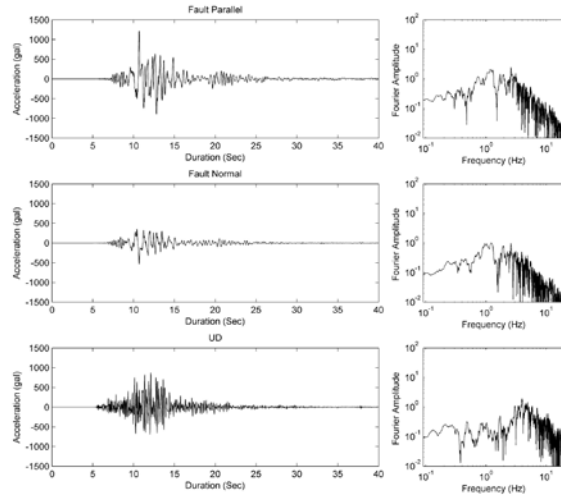


Figure 6: Ground motions recorded in KMMH16 and corresponding Fourier spectrum after transferred to the fault parallel and fault normal axes

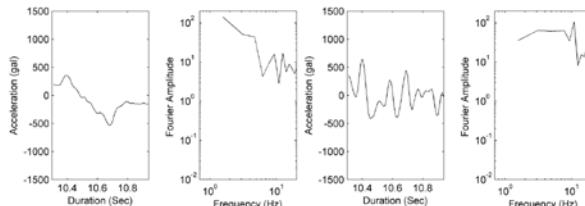


Figure 7: Acceleration and Fourier spectrum of the lateral and vertical components in peak time window of 10.3-10.94 seconds of recorded ground motion in KMMH16 from left to right

When the vertical amplitude is 8.73 m/sec^2 , phase difference 5.146 radian and dominant frequency of 1 Hz, PGA to topple the car is just 4.64 m/sec^2 and 31.13 m/sec^2 for dominant frequency of 10 Hz. Here in Kurokawa, cars were in parking area so ρ_v is taken as unit but we have to find ρ_d as dimensional scaling factor. Dimensional parameters d/h ratio is 2.612 and weight is 9.5 KN. ρ_d for dominant frequency of 1Hz is 0.61 and 0.69 for 10 Hz.

PGA required to topple the car is 2.83 m/sec^2 when considering dominant frequency of 1 Hz and 21.48 m/sec^2 for 10 Hz. PGA value to topple the car in smaller frequency with higher vertical amplitude is very small as it consider the same frequency of vertical component. Resonance of the lateral and vertical component is not likely to happen hence we take the average of these two values to introduce the threshold PGA to topple the car is 12.155 m/sec^2 .

Now, we use the seed ground motions in the analysis, keeping the vertical component constant. The car got toppled when the PGA is 14.172 m/sec^2 in 10.86 seconds as scaling factor is 2.654 for lateral component. Fault normal ground motion used in lateral and fault parallel in longitudinal direction of vehicle. When we use the smaller scaling factors then the vehicle starts to tilt in one direction after it crosses the threshold to start toppling but later it comes back to the stable position. Roll and pitch angles

under the different PGA of seed ground motion are shown in Figure 8. When the PGA value of seed ground motion reaches 13.35 m/sec^2 , it has maximum tilt in 10.48 seconds and it comes back to stable position. Figure 9 shows the conditions of the vehicle in different time corresponding to PGA 13.35 m/sec^2 . Figure 10 shows the conditions of the toppled vehicle in different time.

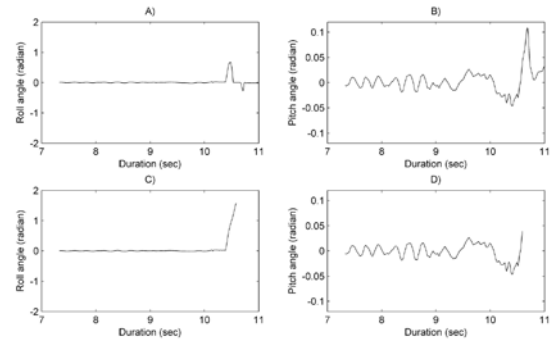


Figure 8: Rolling and pitching angles of the vehicle in the time window of 7.34 to 11.00 seconds duration A) roll angle and B) pitch angle in response for PGA of 13.35 m/sec^2 and C) roll angle and D) pitch angle in response for PGA of 14.172 m/sec^2 of seed ground motion



Figure 9: Toppling of vehicle in response to PGA value of 13.35 m/sec^2 of seed ground motion with timestamp

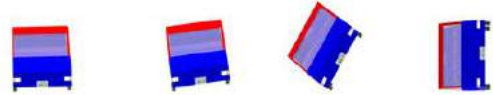


Figure 10: Toppling of vehicle in response with PGA of 14.172 m/sec^2 of seed ground motion with timestamp

4. Conclusions

Vehicle analysis has done by solving equations of motion of the vehicle to make clear the toppling condition. PGA required to topple the vehicle depends on the dominating frequency together with the amplitude of vertical acceleration and phase delay. Analysis of toppled vehicle during Kumamoto earthquake in Kurokawa area near the Minami Aso bridge suggested the PGA value of fault normal is about 14.172 m/sec^2 , 2.654 times in reference with the Mashiki area. From the calculation using the ground motion and vehicle parameters with regression coefficients provided in this study threshold PGA to topple the car in Kurokawa area is 12.155 m/sec^2 , around 10% sort of result from analysis. Evidences of large slip and surface rupture along with the damages to the buildings in that area could agree with this level of ground shaking in that area.

References

1. Car sensor Lab. (2016). Suzuki Every Wagon catalog. Retrieved August 1, 2016, from http://catalog.carsensorlab.net/suzuki/every_wagon/f001/m006/g003/
2. Hejtmanek, P., Blatak, O., & Vancura, J. (2015). New approach to measure the vehicle center of gravity

- height. Perner's Contacts, X(4), 18–27. Retrieved from http://pernerscontacts.upce.cz/41_2015/Hejtmanek.pdf
3. JMA. (1996). The Japan Meteorological Agency (JMA) seismic intensity scale. Retrieved March 20, 2016, from <http://www.jma.go.jp/jma/kishou/known/shindo/index.html> (in Japanese)
 4. Kawashima, K., Sugita, H., & Kanoh, T. (1989). Effect of earthquake on driving of vehicle based on questionnaire survey. *Structural Eng./Earthquake Eng.*, 6(2), 405–412.
 5. Maruyama, Y., & Yamazaki, F. (2002). Seismic response analysis on the stability of running vehicles. *Earthquake Engineering & Structural Dynamics*, 31(11), 1915–1932. <http://doi.org/10.1002/eqe.195>
 6. Maruyama, Y., & Yamazaki, F. (2006). Relationship Between Seismic Intensity and Drivers' Reaction in the 2003 Miyagiken-Oki Earthquake. *Structural Engineering / Earthquake Engineering*, 23(1), 69s–74s. <http://doi.org/10.2208/jscesee.23.69s>
 7. NIED. (2016a). Fault slip distribution map of Kumamoto earthquake 2016.04.16. Retrieved August 8, 2016, from <http://map03.ecom-plat.jp/map/map/?cid=20&gid=587&mid=2963>
 8. NIED. (2016b). Strong-motion Seismograph Networks (K-NET, KiK-net). Retrieved August 1, 2016, from <http://www.kyoshin.bosai.go.jp/>
 9. Parajuli, R. R., & Kiyono, J. (2015). Ground motion characteristics of the 2015 gorkha earthquake, survey of damage to stone masonry structures and structural field tests. *Frontiers in Built Environment*, 1(23). <http://doi.org/10.3389/fbuil.2015.00023>
 10. Parajuli, R. R., & Kiyono, J. (2016). Circular Path and Linear Momentum Method for Seismic Response Analysis of Vehicles. *Frontiers in Built Environment*, 2(16). <http://doi.org/10.3389/fbuil.2016.00016>
 11. Parajuli, R. R., Kiyono, J., & Yatsumoto, H. (2017). Safety analysis of vehicles running on bridge during an earthquake. In 16th World Conference on Earthquake. Santiago, Chile.

Seismic Risk Assessment and Loss Estimation for Ho Chi Minh City

^{1, 2, 3}Nguyen Hong Phuong*, ⁴Nguyen Viet Ky, ^{1, 2}Pham The Truyen, ⁵Nguyen Ngoc Thu

¹*Institute of Geophysics, Vietnam Academy of Science and Technology, 18 Hoang Quoc Viet street, Cau Giay District, Hanoi, Vietnam*

²*Graduate University of Science and Technology, Vietnam Academy of Science and Technology*

³*IRD, Sorbonne Universités, UPMC Univ Paris 06, Unité Mixte Internationale de Modélisation Mathématique et Informatiques des Systèmes Complexes (UMMISCO) 32 avenue Henri Varagnat, 93143 Bondy Cedex, France.*

⁴*Faculty of Geology and Petroleum, Ho Chi Minh city University of Technology, 268, Ly Thuong Kiet street, District 10, Ho Chi Minh city.*

⁵*The Union of Science Geology, Environment and Geophysics.*

*Corresponding author, Email: phuong.dongdat@gmail.com

Abstract

Located in the territory of the Southern Vietnam, the Ho Chi Minh City has been recognized as a low seismicity area for a long time. However, the seismic threat has really become a concern of the city community since 2005, when two off-shore earthquakes of magnitudes $M=5.1$ and $M=5.5$ occurred at the distance of 150 km southeastward the city had shaken many high-rise buildings in the city, causing panic from the public. In the consecutive years, earthquakes of medium magnitude were continuously occurring in the southeastern continental shelf of Vietnam until the end of 2012. In addition to this fact, the World's experiences on damage and loss during recent earthquakes have demonstrated the need for conducting seismic risk assessment for Ho Chi Minh City for disaster management purpose.

Starting from the year 2000, a methodology of urban seismic risk assessment and loss estimation suitable for Vietnam was developed and applied to several megacities of Vietnam. Together with the methodology, a GIS-based software called ArcRisk was also developed to help implementing different stages of the seismic risk assessment and loss estimation procedure.

This paper presents the results of applying the methodology to assess the seismic risk and estimate losses for the downtown districts, covering the 1st, 3rd, 4th, 7th and Nha Be districts of Ho Chi Minh City. The scenario earthquakes have been created using the knowledge on seismotectonic characteristics of the Ho Chi Minh City and surrounding region and the damage and disruption caused by them are estimated. In addition to the information on engineering geology and hydrogeology, the building inventory and demographic data of the study area have been collected for use. The resulting "loss estimate" is presented in terms of maps showing building damage and casualties at different levels and at different times of a day.

The results of urban risk assessment show a realistic picture of damage and loss in Ho Chi Minh City that may result from future earthquakes. The estimates of damage and human impacts due to earthquakes can help the decision-makers at local, regional and national levels in:

1. Mitigating the possible consequences of earthquakes;

2. Anticipating the possible nature and scope of the emergency response needed to cope with an earthquake-related disaster, and
3. Developing plans for recovery and reconstruction following earthquakes.

Key words: Urban Seismic Risk, Geographic Information System, Decision Support System.

1. Introduction

Ho Chi Minh City is the largest city in Vietnam by population. As for the 2016 statistics, the city covers an area of 2,095 km² with 8,441,902 inhabitants. The city is also an industrial, cultural, science-technological center of the key economical regions of the Southern Vietnam. From the risk aspect, Ho Chi Minh City is therefore vulnerable to any type of natural disaster.

Located in the Southern Vietnam, Ho Chi Minh City has long been recognized as an aseismic area. Observation data shows a low level of seismicity in the whole territory of South Vietnam, where all earthquakes recorded with magnitudes not exceeding 5.5. Within the city's boundary, since 2006, a newly established seismograph station network has only recorded small events with magnitudes not exceeding 3.0. However, the low level of seismicity is not the only decisive factor of seismic safety for a region. For Ho Chi Minh City community, the transmission of shaking from distant earthquakes of medium or higher magnitudes, or the site effects caused by local ground condition under seismic load might be a reason for significance threat. In fact, the weak ground beneath the city could be a reason for the amplification of ground motions caused by local and regional earthquakes. The shaking that shook high-rise buildings in Ho Chi Minh City in 2005 are vivid evidence of the transmission effects, as they were caused by two off-shore earthquakes of medium magnitude ($M=5.1$ and $M=5.5$), with epicenters located 150 km southeastwards the city. After 2015, a swarm of small and medium earthquakes were continuously occurring in the continental shelf of Vietnam. The shakings of these earthquakes were trembling the high-rise buildings in Ho Chi Minh City, causing panic in public and emphasizing the warning on an existing

earthquake threat. Seismic hazard and urban risk assessment for Ho Chi Minh City has therefore become not only a social issue, but really an urgent need in the new situation.

This paper presents some preliminary results of seismic risk assessment and loss estimation for a downtown area of Ho Chi Minh City, covering the 1, 3, 4, 7 and Nha Be districts. The work has been implemented during the period from 2008 to 2012 within framework of the scientific research projects [9, 12]. Coupling with existing knowledge on engineering geology and seismicity of the study region (including the new observation data), the application of GIS technology allows developing a powerful tool for quantitatively risk evaluation and loss estimation if a strong earthquake occurs. The results show a realistic portrayal of the level and spatial distribution of damage and loss in Ho Chi Minh City caused by future earthquakes.

2. Methodology and technique used

The first research idea on urban seismic risk assessment was started in Vietnam since the year 2000. In order to develop a methodology suitable for Vietnam, many Worldwide existing methodologies have been considered [2,

3, 4]. In 2003, the first methodology on urban seismic risk assessment and loss estimation (from here referred to as the Methodology) was developed for Vietnam based on the modification of the HAZUS's methodology and applied for the Hoan Kiem district, downtown of Hanoi [6, 7]. In the following years, with the implementation of a number of the scientific research projects on this direction, the Vietnamese methodology has been continuously improved, standardized and applied for different urban areas, including the biggest cities of Vietnam as Hanoi, Ho Chi Minh City and Nha Trang [7, 8, 9, 10, 11].

Fig. 1 illustrates the framework of the Methodology as applied for urban seismic risk and loss estimation in Vietnam. Only two elements at risk are targeted by Methodology, which are buildings and people. The Methodology is implemented through two stages, namely: 1) Seismic hazard assessment and 2) seismic risk assessment. The seismic hazard assessment stage includes two modules, namely a) Ground motion assessment and b) Ground failure assessment. The seismic risk assessment stage includes two modules, namely a) Direct Physical Damage to buildings and b) Casualties.

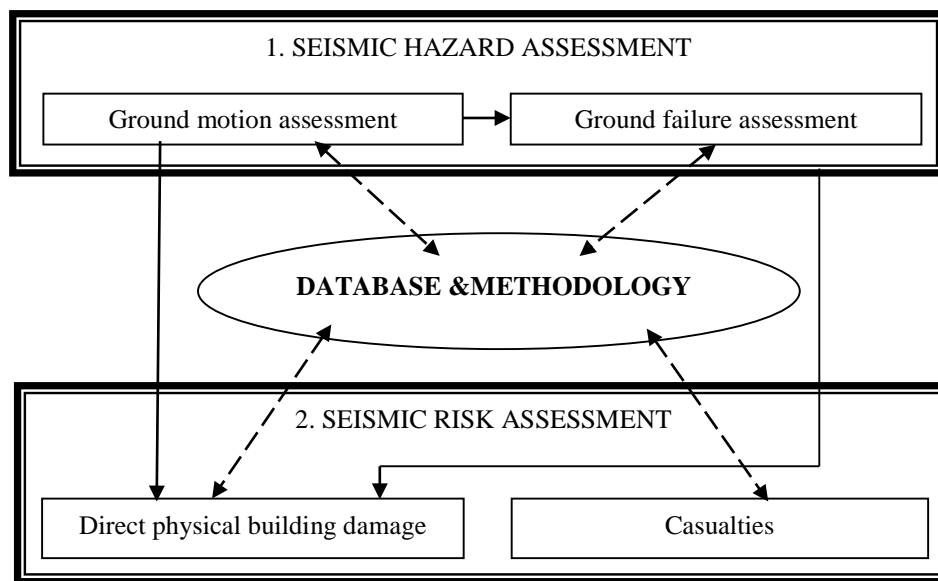


Figure 1. Framework of the Urban seismic risk assessment and loss estimation methodology in Vietnam.

The Methodology has been coded into a user-friendly software (called ArcRisk), that can be run in the ArcView GIS environment. Figure 2 shows the steps that are typically performed in a procedure of urban seismic risk assessment in Vietnam. Each step shown in the Figure 2 corresponds to an analysis module of ArcRisk, where the numbered boxes correspond to 5 analysis modules of the system. As indicated by the arrows, the steps are interdependent, i.e. outputs of some modules are used as input to others. The procedure starts with definition of a study area, which follows administrative boundaries such as city, district(s) or ward(s) limits. Then, a scenario earthquake, which is an earthquake

with predefined magnitude and location, is defined for the study region. On the basis of existing data on seismicity, seismotectonics, engineering geology and local site conditions, the ground shaking is assessed for the study area. The ground motion characteristics obtained then are used as input data for assessment of ground failure due to liquefaction and landslides during earthquake. Finally, information on vulnerability of elements at risk such as demographic and infrastructure data can be used in combination with the ground failure outputs to evaluate risk and to estimate losses for the study area.

ArcRisk has been verified and validated through many research studies on seismic hazard assessment in Vietnam. Not only a powerful risk calculator, the software can be used as a decision support system in seismic risk management strategy of megacities in Vietnam [7, 11]

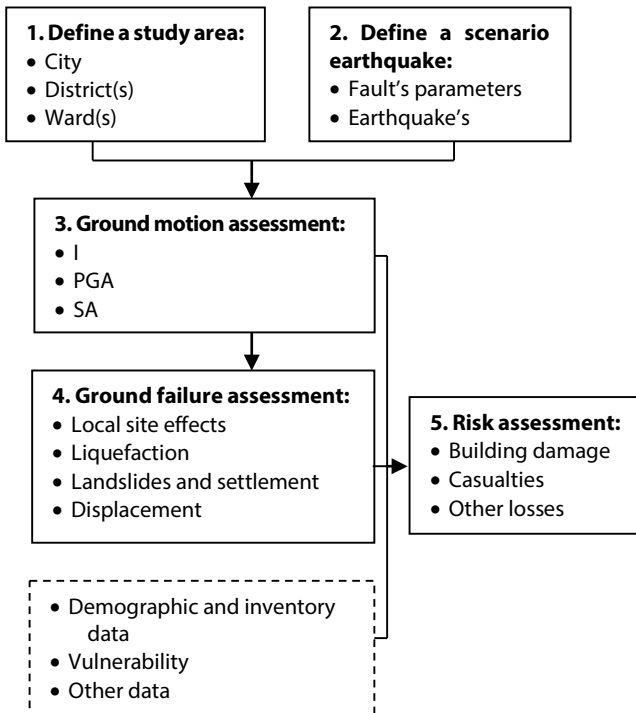


Figure 2. A procedure for urban risk assessment and loss estimation

3. Data used

3.1. Existing data

Data used for seismic risk assessment and loss estimation for Ho Chi Minh City has been collected from many sources, part of which comes from the previously published scientific research projects, covering such related fields as seismology, geophysics, tectonic and engineering geology, civil engineering. The extents and details of datasets are different depending on the study purpose. The collected data can be grouped into the following datasets:

- 1) Tectonic and active faults data.
- 2) Earthquake data.
- 3) Engineering and hydro-geologic data.
- 4) Building inventory and demographic data.
- 5) Administrative and social-economical data.

3.2. Survey data

During implementation of projects, field trips have been conducted with two different purposes. To assess the ground failure, detail seismic survey has been carried out to obtain the V_{S30} values in the study areas. Fig. 3 shows the distribution seismic survey points and boreholes in the study

area [9, 12]. On another hand, taking into account the fast change of the urban infrastructure of the cities in Vietnam, field trips have been organized to investigate the current construction situation and to update the building inventory data within the study areas. In results, the attributes of building data were added into the GIS database and linked with spatial data to be used in the building damage calculation. The survey data shows five most typical structures of building in Ho Chi Minh City (Fig. 4). Specific symbols were assigned to each building type according to the classification given in the Methodology [5, 14].

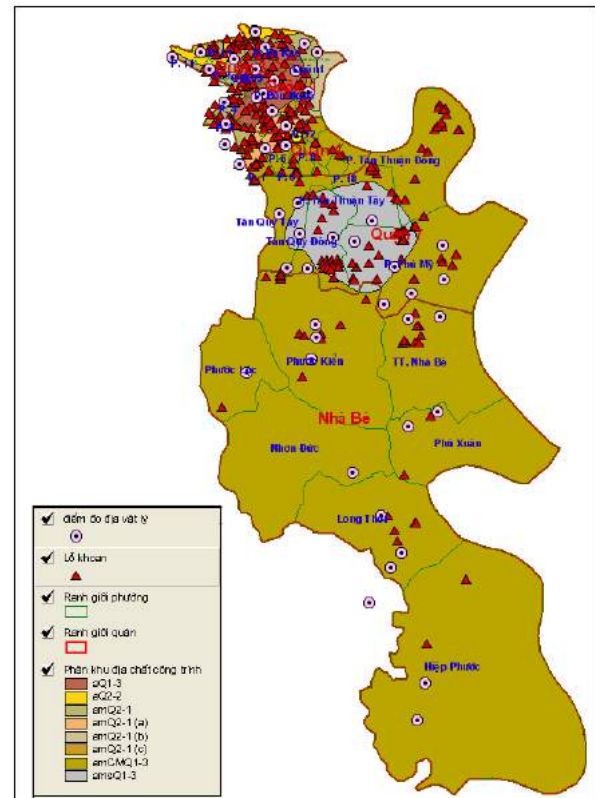


Figure 3. Distribution of seismic survey points and boreholes in the study area.



a)



b)



c)



d)



e)



Figure 4. Typical building types in the urban areas of Ho Chi Minh City: a) Few-Floor (C3M); b) Many-Floor (C3H); c) High-rise (PC2H); d) Industrial (S1L, S2L); e) Residential (C1L, URML) and f) Low-rise (RM1L).

4. Assessment of ground motion for Ho Chi Minh City using scenario earthquakes

4.1. Seismic source model

A quantitative assessment of seismic hazard usually bases on a seismic source model, which is predefined for the study area and can be used to simulate the process of energy release and seismic wave propagation during an earthquake. Although the seismic source model is applied in both probabilistic and deterministic seismic hazard assessment, in this paper only the latter case is discussed.

In order to assess the ground shaking for Ho Chi Minh City region, a seismic source model was constructed, using a database of the seismically active faults defined Southern Vietnam [9, 12, 15]. The faults are grouped in two ranks, depending on their depth of active layers and magnitude thresholds. The faults systems are simplified and digitized as single polylines in a GIS environment, and linked with their attribute data. There are two types of faults attribute data stored in the database. The first type is the descriptive information, including fault name, fault rank, type of faulting, main direction, total length, etc... More important attribute type is the fault parameters, which can be used directly to the hazard calculation as maximum moment magnitude, surface and subsurface rupture sizes, dip angle, etc...

A fault source model was developed for Ho Chi Minh City using active faults database and the relationship between earthquake magnitude M and rupture length L proposed by Wells and Coppersmith [17]:

$$\log_{10}(L) = a + b \cdot M \quad (1)$$

where L is the rupture length (km) and M is the moment magnitude of the earthquake; a and b are regression coefficient, determined for different types of faults.

Fig. 5 illustrates a seismotectonic map of Ho Chi Minh City and surrounding region, used for construction of the fault source and the areal source models for seismic hazard assessment of Ho Chi Minh City.

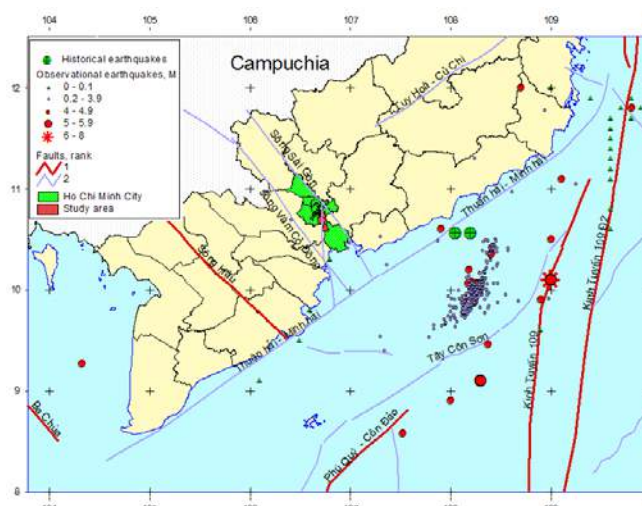


Figure 5. Seismotectonic map of Ho Chi Minh City used for construction of fault and areal seismic source models.

4.2. Scenario earthquakes

The seismic source models were used for creation of scenario earthquakes to be used for urban seismic risk assessment and loss estimation [13]. A scenario earthquake is the event, most likely to have to occur in the future, and with predefined parameters. In another words, scenario earthquake is a simulation of an event in the past for predicting the effects of a future event. The scenario earthquakes were created for Ho Chi Minh City on the following assumptions:

- 1) Earthquake originated on one of the active tectonic faults which crosses through or nearby the urban area.
- 2) For fault ruptures, the closest point on the fault to the site is taken as the distance.
- 3) For areal source zones, commonly the shortest distance to the source boundary is selected as the distance.
- 4) For the zone that contains the site or for the background source, the worst case would be to have the earthquake occur right under the site.

Determination of parameters of seismic source is based on the knowledge of the local seismicity and geologic setting of the study area, which are controlled by the existing seismotectonic regime of the whole country. This important fact decides the accuracy of the source model used and therefore allows creating so called a close-to-reality scenario earthquake that likely to occur. In this study, two scenario earthquakes were assumed to occur on the Saigon River and Vam Co Dong River active faults (Fig. 6). Both events have magnitude of 5.5 and focal depth of 12 km. The parameters of these scenario earthquakes are presented in Table 1.

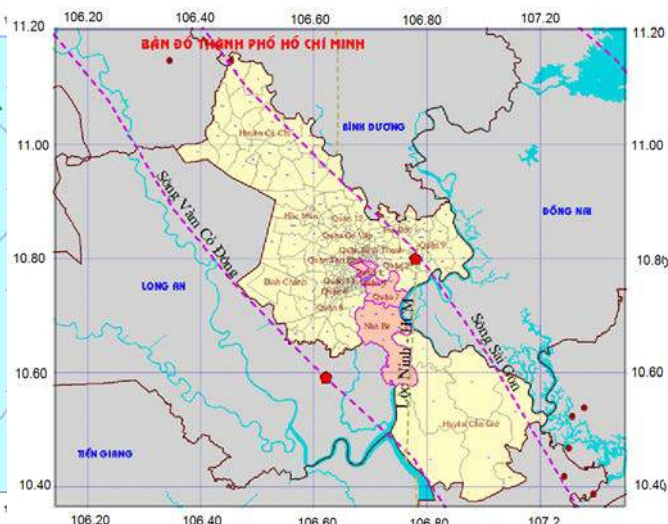


Figure 6. Epicenters of scenario earthquakes with magnitude $M=5.5$ assumed to occur in the Vam Co Dong River fault and Saigon River fault (the pentagons).

Table 1. Parameters of the scenario earthquakes used in seismic risk assessment for Ho Chi Minh City

Nº	Scenario	Fault name	M_w	Epicenter coordinates		Focal depth, km
				Long	Lat	
1	Q47NB_VC	Vam Co Dong River	5.5	106.62	10.59	12
2	Q47NB_SG	Saigon River	5.5	106.78	10.80	12

4.3. Scenario-based assessment of ground shaking

Ground shaking caused by an earthquake at a given site can be calculated using empirical relationship between ground shaking parameters, earthquake magnitude and source to site distance. Such empirical relationship, also called the attenuation law can be expressed in the following general form:

$$Y = a e^{bM} R^c \quad (2)$$

where Y is one of the ground shaking parameters, M is the earthquake magnitude, R is the source to site distance, a , b and c are spatial dependent constants.

Figs. 7a and 7b show the PGA maps caused by two scenario earthquakes in the 4th, 7th and Nha Be districts. Shaking attenuation is clearly reflected on both maps, with highest values of PGA observed near the epicenters areas. The shaking caused by the Saigon River scenario earthquake is in the range of 0.05 to 0.15 g, while the Vam Co Dong River scenario causes the PGA values in the range of 0.05 to 0.14 g.

Based on the shake maps, one can conclude that the local shakings with maximum intensity of VII-VIII on the MSK-64 scale can be expected in the study area. Even the far most from epicenters areas could be impacted by the VI grade of the MSK-64 intensity scale.

The PGA maps were calculated for the rock site, which corresponds to the site of class B according to the NEHRP

Provisions [2, 3]. To obtain the reliable shaking values for the study area, the site effect assessment was conducted, considering the local impact caused by geological setting, ground water level and some other site conditions. According to the Methodology, amplification of ground shaking to account for local site conditions is based on the site classes and soil amplification factors were used following the 1997 NEHRP Provisions.

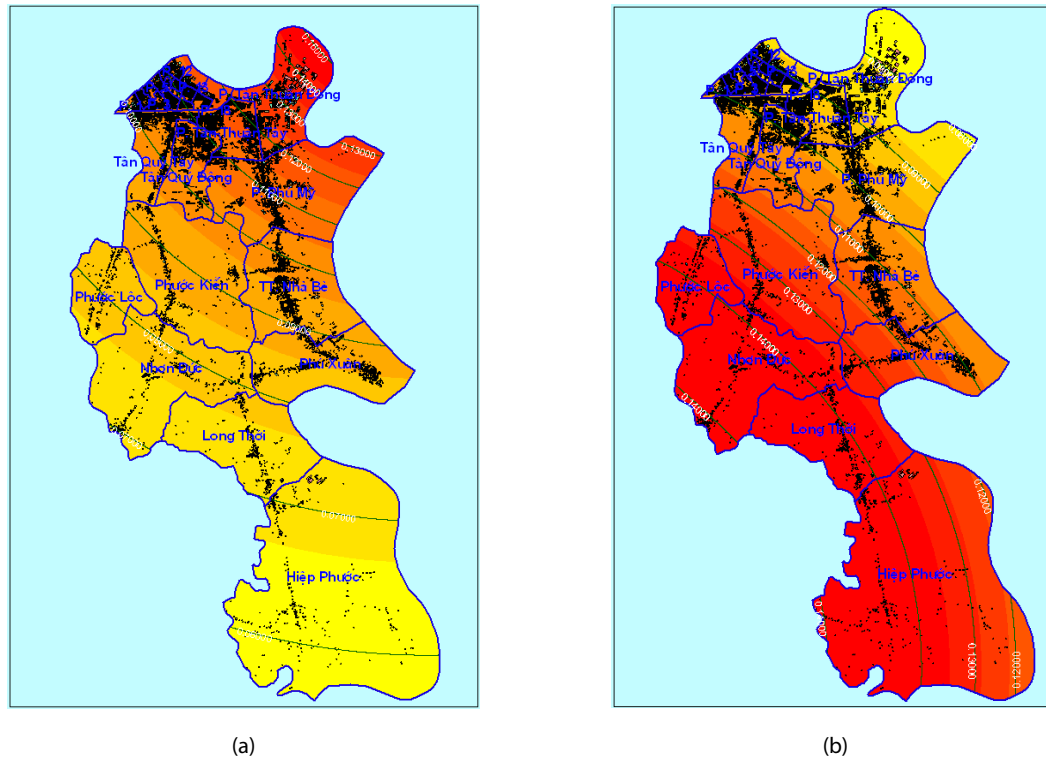


Figure 7. Distribution of PGA in the 4th, 7th and Nha Be districts caused by the Saigon River scenario earthquake (a) and the Vam Co Dong River scenario earthquake (b).

The Methodology amplifies rock (Site Class B) PGA by the same factor as that factor for short-period (0.3-second) spectral acceleration, as expressed in the following equation:

$$PGA_i = PGA \cdot F_{Ai} \quad (3)$$

where PGA_i is peak ground acceleration for Site Class i (in units of g); PGA is peak ground acceleration for Site Class B (in units of g); and F_{Ai} is the short-period amplification factor for Site Class i for spectral acceleration.

5. Estimation of building damage in Ho Chi Minh City

In this study, only structural building damage due to ground shaking is considered. To estimate the building damage for in Ho Chi Minh City, the Methodology uses the model building types developed by FEMMA with some modification [2, 3, 12]. Table 2 lists the most popular building types which can be found in downtown area of Ho Chi Minh City, as illustrated in Fig. 8.

Table 2. Classification of the most popular model building types in Ho Chi Minh City [14]

N ^o	Building usual name	Common functionality	Description of structure	Structure code
1	Few-floor	Hospitals, apartment buildings.	Concrete frame with unreinforced masonry infill walls, Mid-Rise	C3M
2	Many-floor	Hotels, offices, apartment, hospitals.	Concrete frame with unreinforced masonry infill walls, High-Rise	C3H
3	High-floor	Offices, apartments, hotels.	Precast concrete frames with concrete shear walls, High-Rise	PC2H

Nº	Building usual name	Common functionality	Description of structure	Structure code
4	Industrial	workshops, exhibitions, fairs.	Steel Moment Frame	S1L, S2L
5	Residential	One or more family houses, small shops and services.	Concrete moment frame/ Unreinforced masonry bearing walls	C1L/UR ML
6	Low-floor	Hospitals, schools, banks, super markets.	Reinforced masonry bearing walls with deck diaphragms	RM1L, RM1M

The process of scenario-based estimation of building damage using the ArcRisk software is described below in detail. Results of application of the Methodology for the 4th, 7th and Nha Be Districts, Ho Chi Minh City using the Saigon River and Vam Co Dong River scenario earthquakes are illustrated.

5.1. Construction of building capacity curves

The Methodology uses elastic response spectra (5% damping) to characterize ground shaking demand. Response of a building to seismic impact is characterized by building capacity curves. These curves demonstrate the pushover displacement of each building type and seismic design level as a function of laterally-applied earthquake load. Following the Methodology, capacity curves of 36 building types were constructed with four anti-seismic design levels and resided in ArcRisk.

5.2. Estimation of peak response of the building types to ground shaking

The Methodology uses the capacity spectrum method to estimate peak building response as the intersection of the building capacity curve and the response spectrum of ground shaking demand at the building's location (demand spectrum) [1, 2, 3, 16]. Figure 8 shows an example of the capacity curve constructed for the low-rise unreinforced masonry bearing walls buildings (URML) and the response spectrums constructed for different site classes used in ArcRisk [12].

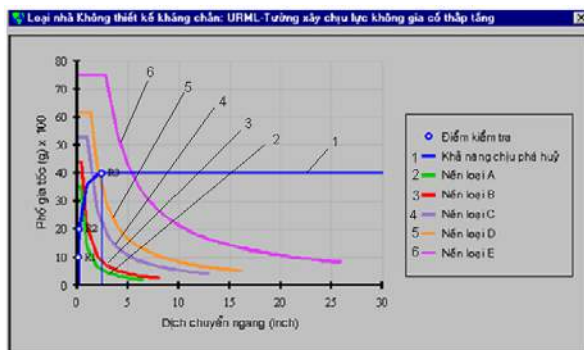


Figure 8. Estimation of peak response of the low-rise unreinforced masonry bearing walls buildings (URML) building

using ArcRisk.

5.3. Estimation of buildings structural damage states

Structural damage of a building under seismic load can be expressed in the form of lognormal fragility curves that relate the probability of being in, or exceeding, a building damage state to a given demand parameter (the response spectrum displacement in our case). Four damage states considered in the Methodology are Slight, Moderate, Extensive and Complete.

Each fragility curve is defined by a median value of the seismic demand parameter (i.e., either spectral displacement, spectral acceleration, PGA or PGD) that corresponds to the threshold of the damage state and by the variability associated with that damage state. The spectral displacement, S_d , that defines the threshold of a particular damage state (ds) is assumed to be distributed by:

$$S_d = \bar{S}_{d,ds} \cdot \epsilon_{ds} \quad (4)$$

where $\bar{S}_{d,ds}$ is the median value of spectral displacement of damage state, ds , and ϵ_{ds} is a lognormal random variable with unit median value and logarithmic standard deviation, β_{ds} . The conditional probability of being in, or exceeding, a particular damage state, ds , given the spectral displacement, S_d , is defined by the function:

$$P[(ds|S_d)] = \Phi \left[\frac{1}{\beta_{ds}} \ln \left(\frac{S_d}{\bar{S}_{d,ds}} \right) \right] \quad (5)$$

where $\bar{S}_{d,ds}$ is the median value of spectral displacement at which the building reaches the threshold of damage state, ds , β_{ds} is the standard deviation of the natural logarithm of spectral displacement for damage state, ds , and Φ is the standard normal cumulative distribution function.

ArcRisk includes the $\bar{S}_{d,ds}$ and β_{ds} values pre-defined for each building type used in the Methodology and for all damage states. Figure 9 shows the plot of capacity curve and damage-state medians for mid-rise concrete frame with unreinforced masonry infill walls buildings (3CM) produced by the ArcRisk software.

Results of calculation at any point in the study area can be viewed in the form of a graph showing discrete probabilities of being in each of the five following damage states: None (KO), Slight (NH), Moderate (TB), Extensive (NG) and Complete (HT). Figure 10 shows a graph of damage states calculated for the low-rise reinforced masonry bearing walls with deck diaphragms buildings (RM1L) using ArcRisk.

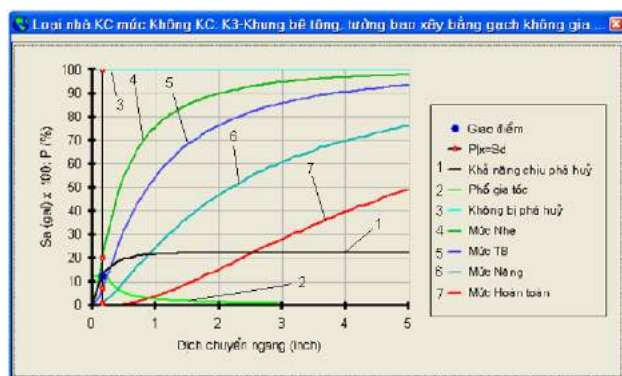


Figure 9. Estimation of damage states for mid-rise concrete frame with unreinforced masonry infill walls buildings (3CM) using ArcRisk.

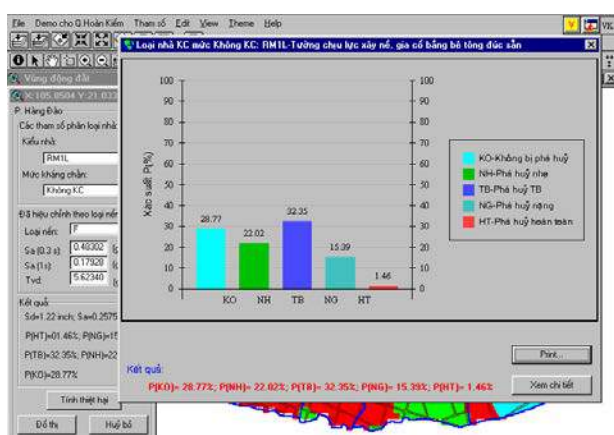


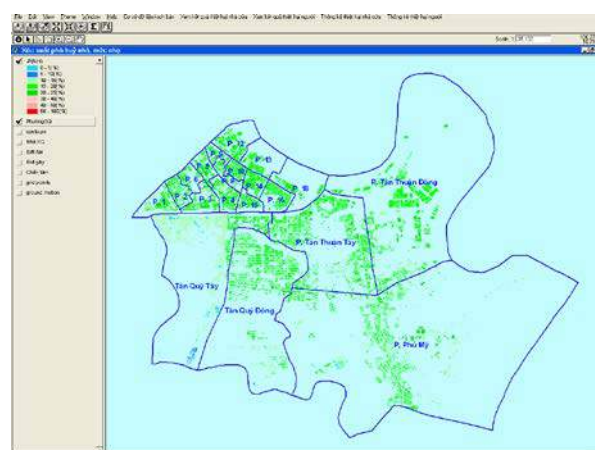
Figure 10. Damage states due to scenario earthquake calculated for the low-rise reinforced masonry bearing walls with deck diaphragms buildings (RM1L) using ArcRisk.

5.4. Mapping the building damage

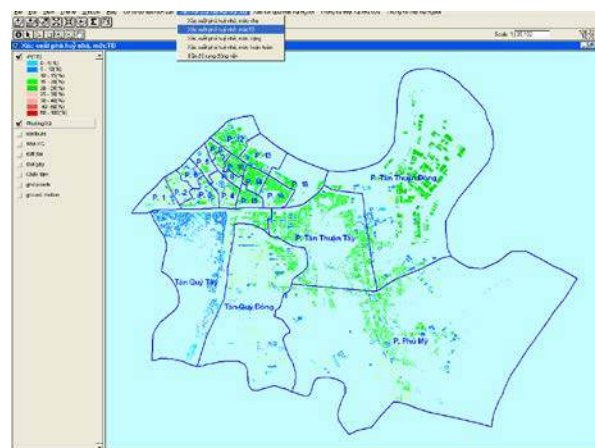
The results of building damage estimation show information about the level of damage to the study area's general building stock. ArcRisk calculates damage for groups of buildings with the same structural class in terms of the probability that a specific model building type will reach or exceed a specific level of damage when subjected to a certain level of ground shaking. ArcRisk automatically assigns the building damage results to centroid point of each building stock to used for the mapping. In results, a set of building damage maps is created with layers displaying probability of being in each of the five damage states: None, Slight, Moderate, Extensive and Complete. The damage probabilities can also be interpreted as the fraction of all buildings of the same types that would be in the particular damage state of interest. Figures 11a and 11b illustrate the maps of building damage probability in Slight and Moderate states due to Saigon River scenario earthquake in the 4th and 7th districts, Ho Chi Minh City.

ArcRisk also produces the building damage results in the form of Reports. Tables 3 and 4 list the building damage probability by ward, calculated for above

mentioned four damage levels in the 4th, 7th and Nha Be districts due to Saigon River and Vam Co Dong River scenarios, respectively. As can be seen from the tables, the heaviest building damage caused by the Saigon River scenario can be expected in Tân Thuận Tây ward of 7th district, while for the Vam Co Dong River scenario, the heaviest building damage can be expected in the Phuoc Kien and Phuoc Loc of Mha Be district. Overall, majority of building damage is expected in the 4th and the 7th districts, where the the density of buildings is higher than in the Nha Be district. However, the highest level of building damage is observed in Nha Be district.



(a)



(b)

Figure 11. Building damage in Slight (a) and Moderate (b) damage states in the 4th and 7th districts due to Saigon River scenario.

Table 3. Building damage by ward in the 4th, 7th and Nha Be districts due to Saigon River scenario earthquake ($M=5.5$; $h=12$ km)

District	Ward	Slight	Moderate	Extensive	Complete
4 th	1	15.99	11.64	1.51	0.24
	2	16.96	13.50	1.89	0.31
	3	17.10	12.83	2.16	0.35
	4	16.52	13.45	1.71	0.30

District	Ward	Slight	Moderate	Extensive	Complete
	5	17.03	14.11	1.93	0.33
	6	16.19	12.19	1.58	0.24
	8	17.92	15.90	2.36	0.34
	9	16.57	14.60	1.61	0.28
	10	17.74	15.38	2.16	0.38
	12	16.70	14.27	1.65	0.28
	13	17.56	15.39	2.01	0.33
	14	17.34	15.31	1.87	0.30
	15	16.99	14.47	1.73	0.29
	16	17.34	16.51	1.82	0.33
	18	18.46	16.96	2.50	0.45
7 th	Tan Quy Tay	11.76	6.74	0.73	0.08
	Tan Quy Dong	15.85	12.65	1.55	0.27
	Phu My	17.21	14.63	2.02	0.37
	Tan Thuan Tay	17.02	16.64	3.02	0.51
	Tan Thuan Dong	17.45	15.84	2.32	0.43
Nha Be	Nha Be	14.45	10.36	1.13	0.18
	Phu Xuan	12.35	7.81	0.74	0.11
	Phuoc Kien	17.62	11.10	2.54	0.37
	Phuoc Loc	13.53	7.97	1.21	0.16
	Nhan Duc	13.14	7.27	1.20	0.15
	Long Thoi	13.22	7.10	1.23	0.15
	Hiep Phuoc	9.54	4.36	0.52	0.05

Table 4. Building damage by ward in the 4th, 7th and Nha Be districts due to Vam Co Dong River scenario earthquake (M=5.5; h=12 km)

District	Ward	Slight	Moderate	Extensive	Complete
4 th	1	15.73	11.25	1.45	0.23
	2	15.72	11.57	1.51	0.23
	3	15.35	10.48	1.62	0.24
	4	13.77	9.48	1.00	0.16
	5	14.14	9.79	1.13	0.17
	6	14.05	9.42	1.06	0.15
	8	14.80	10.52	1.23	0.15

District	Ward	Slight	Moderate	Extensive	Complete
	9	12.78	8.88	0.69	0.11
	10	13.99	9.52	1.04	0.15
	12	11.89	7.59	0.56	0.08
	13	12.44	8.19	0.72	0.10
	14	13.28	8.96	0.75	0.10
	15	13.85	9.54	0.86	0.13
	16	13.13	9.24	0.63	0.10
	18	13.39	8.81	0.89	0.13
7 th	Tan Quy Tay	11.89	6.59	0.64	0.06
	Tan Quy Dong	15.51	11.97	1.40	0.23
	Phu My	14.88	10.98	1.29	0.22
	Tan Thuan Tay	11.04	6.67	0.62	0.08
	Tan Thuan Dong	13.41	9.26	1.00	0.16
Nha Be	Nha Be	17.60	15.60	2.19	0.40
	Phu Xuan	19.29	17.28	2.53	0.47
	Phuoc Kien	23.48	20.70	6.25	1.33
	Phuoc Loc	22.16	24.31	6.03	1.31
	Nhan Duc	23.65	23.66	6.60	1.48
	Long Thoi	23.13	23.98	7.05	1.58
	Hiep Phuoc	22.51	23.89	5.78	1.24

6. Estimation of casualties in Ho Chi Minh City

As a matter of fact, earthquakes have never caused serious casualties in Vietnam up to now. Therefore, the HAZUS methodology was adopted for use in deterministic estimation of casualties for urban areas in Vietnam. This section demonstrates a casualty estimation procedure applied for Ho Chi Minh City using ArcRisk software. It is assumed that casualties are caused by direct physical damage of buildings due to earthquakes. ArcRisk uses all results obtained from the building damage module as input to the casualty calculation module.

6.1. Form of casualty estimate

The output from ArcRisk consists of a casualty breakdown by injury severity level, defined by a four level injury severity scale. Table 5 defines the injury classification scale used in this study [2, 3, 12].

Table 5. Injury classification scale

Injury severity level	Injury description
Severity 1	Injuries requiring basic medical aid without requiring hospitalization
Severity 2	Injuries requiring a greater degree of medical care and hospitalization, but not expected to progress to a life threatening status
Severity 3	Injuries that pose an immediate life threatening condition if not treated adequately and expeditiously. The majority of these injuries are the result of structural collapse and subsequent entrapment or impairment of the occupants.
Severity 4	Instantaneously killed or mortally injured

6.2. Earthquake casualty model

Casualties caused by a future earthquake can be modeled by an event tree as illustrated in Fig. 12. Each branch of the tree is assigned a probability of occurrence. Evaluation of the branching probabilities constitutes the main effort in the earthquake casualty modeling. Assuming that all the branching probabilities are known or inferred, the probability of an occupant being killed (P_{killed}) is given as follows [2, 3]:

$$P_{killed} = P_A * P_E + P_B * P_F + P_C * P_G + P_D * (P_H * P_J + P_I * P_K) \quad (6)$$

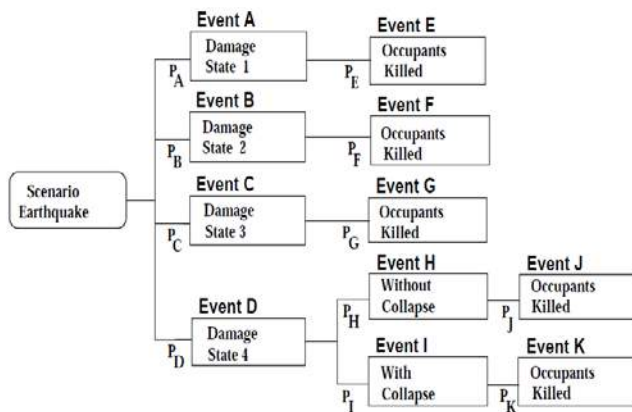


Figure 12. Casualty Event Tree Modeling.

The expected number of occupants killed ($EN_{occupants\ killed}$) is a product of the number of occupants of the building at the time of earthquake ($N_{occupants}$) and the probability of an occupant being killed (P_{killed}).

$$EN_{occupants\ killed} = N_{occupants} * P_{killed} \quad (7)$$

6.3. Population data

For estimation of casualties, the census data of study area detailed to the ward level was used. Population in each ward consists of the following main group:

- Residential population
- Commercial population
- Industrial population
- Commuting population

The default population distribution provided by HAZUS methodology was used to calculate casualties for the three times of day for each ward [2, 3]. The following time options are used:

- Earthquake striking at 2:00 a.m. (night time)
- Earthquake striking at 2:00 p.m. (day time)
- Earthquake striking at 5:00 p.m. (commute time)

These scenarios are expected to generate the highest casualties for the population at home, the population at work/school and the population during rush hour, respectively.

6.4. Scenario-based estimation of casualties

For illustration, the casualties in the 4th, 7th and Nha Be districts caused by Saigon River and Vam Co Dong River scenario earthquakes will be presented. ArcRisk calculates casualties at the ward level, and the output is aggregated into casualty maps of study region. The reports on casualties are produced as well.

Tables 6 and 7 list the casualty estimates by ward for three times of day in the 4th, 7th and Nha Be districts, Ho Chi Minh City due to the Saigon River and Vam Co Dong River scenario earthquakes, respectively. Note that only casualties at severity levels 1 and 2 are presented. Casualty maps due to Saigon River scenario are illustrated in Figures 13 a, b, c, d, e and f.

The following remarks can be made from the casualty estimation results:

- Severity level of casualty due to earthquake in the study area depends on the parameters of scenario earthquake, such as magnitude M , distance from source to element at risk (for example the distance from epicenter to study area). In addition, building structure, anti-seismic design level, construction age and population density can also directly impact to the casualty estimation results.

- Both scenario earthquakes, having magnitude of 5.5, can only cause casualties of 1 and 2 severity levels.

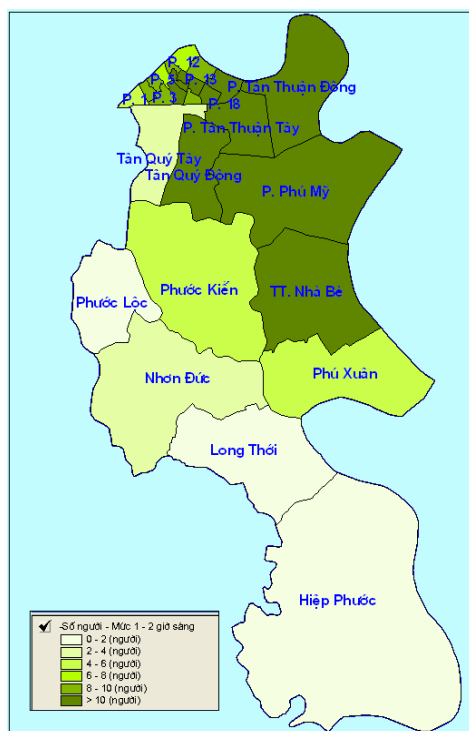
- The most severe casualties caused by Saigon River scenario earthquake are expected in Tan Thuan Tay and Tan Thuan Dong wards, 7th district and in 8th Ward, 4th district (See Table 6). The Vam Co Dong River scenario causes the most severe casualties in Nha Be town and Phuoc Kien, Nhan Duc and Hiep Phuoc wards, Nha Be district (See Table 7).

Table 6. Casualties by Ward in the 4th, 7th and Nha Be, Ho Chi Minh City due to Saigon River scenario earthquake ($M=5.5$; $H=12$ km).

District	Ward	2 h		14 h		17 h	
		Level 1	Level 2	Level 1	Level 2	Level 1	Level 2
4 th	1	5	1	9	1	7	1
	2	9	1	15	2	11	2
	3	9	1	16	2	11	2
	4	11	1	18	2	13	2
	5	8	1	14	2	10	1
	6	10	1	17	2	12	2
	8	14	2	25	3	17	2
	9	9	1	16	2	12	1
	10	11	1	19	2	14	2
	12	7	1	13	1	9	1
	13	10	2	17	3	12	2
	14	11	1	19	2	13	2
	15	9	1	16	2	11	1
	16	13	2	23	4	17	3
	18	13	2	23	4	16	3
7 th	Tan Quy Tay	4	0	8	1	5	0
	Tan Quy Dong	13	2	23	3	16	2
	Phu My	11	2	19	3	13	2
	Tan Thuan Tay	15	2	26	4	18	3
	Tan Thuan Dong	20	3	34	5	24	4
Nha Be	Nha Be	11	2	18	3	13	2
	Phu Xuan	5	0	8	1	6	1
	Phuoc Kien	6	1	11	2	8	1
	Phuoc Loc	2	0	3	0	2	0
	Nha Duc	3	0	5	1	4	0
	Long Thoi	2	0	4	0	3	0
	Hiep Phuoc	2	0	3	0	2	0

District	Ward	2 h		14 h		17 h	
		Level 1	Level 2	Level 1	Level 2	Level 1	Level 2
4 th	1	5	1	9	1	6	1
	2	7	1	12	2	9	1
	3	7	1	12	2	9	1
	4	6	1	11	2	8	1
	5	5	1	9	2	6	1
	6	7	1	11	2	8	1
	8	8	1	14	3	10	2
	9	4	1	8	2	5	1
	10	6	1	10	2	7	1
	12	3	1	5	1	4	1
	13	4	1	7	1	5	1
	14	5	1	9	2	6	1
	15	5	1	9	2	6	1
	16	6	1	10	2	7	2
	18	5	1	9	2	6	1
7 th	Tan Quy Tay	4	0	7	1	5	0
	Tan Quy Dong	12	2	21	3	15	2
	Phu My	7	1	13	2	9	1
	Tan Thuan Tay	4	0	6	1	4	1
	Tan Thuan Dong	9	2	16	3	11	2
Nha Be	Nha Be	19	3	33	5	23	4
	Phu Xuan	14	2	23	3	17	2
	Phuoc Kien	18	3	30	5	22	4
	Phuoc Loc	9	1	15	2	11	2
	Nhan Duc	19	3	33	6	24	4
	Long Thoi	14	2	23	4	17	3
	Hiep Phuoc	19	3	34	5	24	4

Table 7. Casualties by Ward in the 4th, 7th and Nha Be, Ho Chi Minh City due to Vam Co Dong River scenario earthquake ($M=5.5$; $H=12$ km).

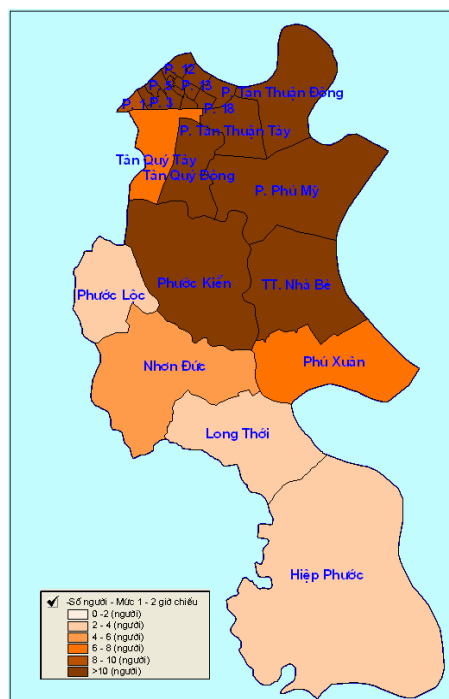


a)

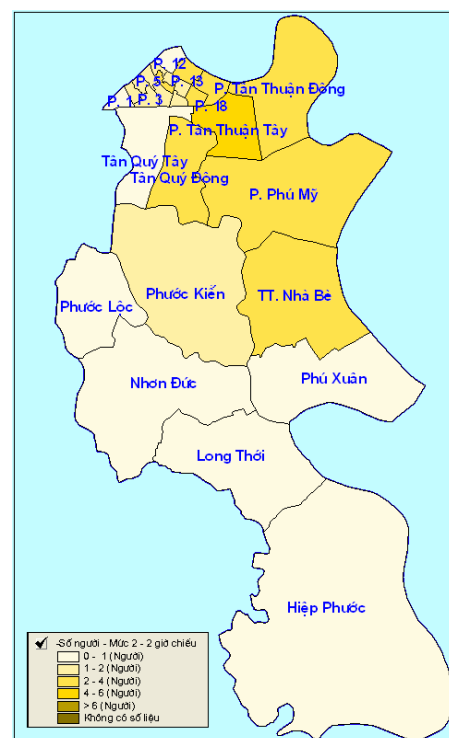


b)

Figure 13. Casualties in the 4th, 7th and Nha Be at severity level 1 (a) and 2 (b) at 2:00 due to the Saigon River scenario.

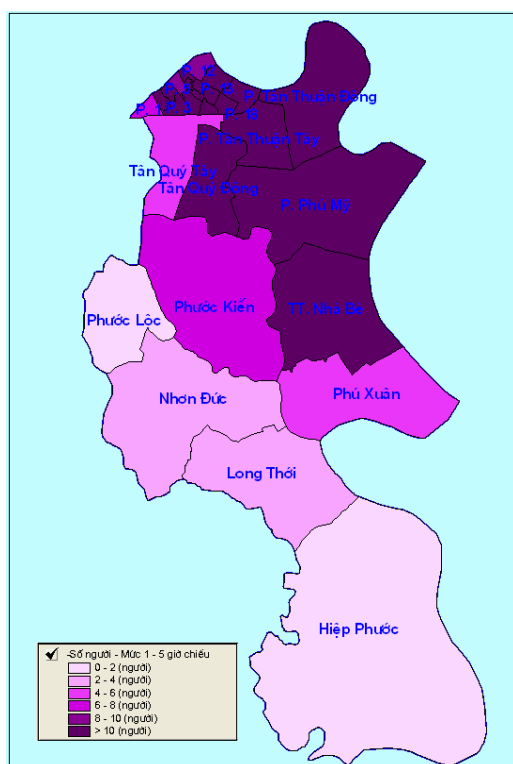


c)

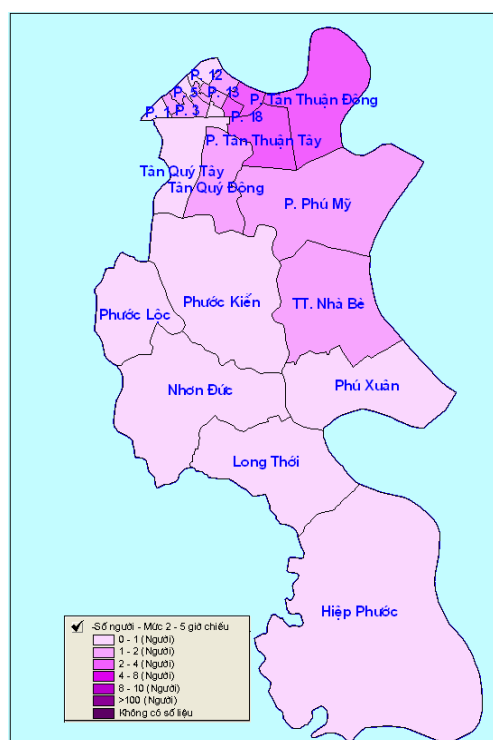


d)

Figure 13. Casualties in the 4th, 7th and Nha Be at severity level 1 (c) and 2 (d) at 14:00 due to the Saigon River scenario.



e)



f)

Figure 13. Casualties in the 4th, 7th and Nha Be at severity level 1 (e) and 2 (f) at 17:00 due to the Saigon River scenario.

7. Conclusion

Since the year 2000, a Methodology of urban seismic risk assessment and loss estimation was developed and applied to several big cities in Vietnam. A GIS-based tool called ArcRisk, having function of a Decision Support System was developed to fulfill the tasks of Methodology.

This paper describes some main results of application of the Methodology for downtown districts of Ho Chi Minh City. Based on updated information on earthquakes, tectonic setting, engineering geology and hydro-geology of the Ho Chi Minh City region, postulated scenario earthquakes were created. Results of estimation of building damage and casualties caused by the scenario earthquakes in the 1st, 3rd, 4th, 7th and Nha Be districts are illustrated.

The Methodology and Decision Support System will have important contribution to earthquake risk management and loss mitigation for the cities located in earthquake prone areas of Vietnam. The estimates of damage and human impacts due to earthquakes can help the decision-makers at local, regional and national levels in:

1. Mitigating the possible consequences of earthquakes;
2. Anticipating the possible nature and scope of the emergency response needed to cope with an earthquake/tsunami-related disaster, and
3. Developing plans for recovery and reconstruction following such a disaster.

8. Acknowledgements

This research has been supported by a grant for the basic research project (No.105.05-2017.10) from National Foundation for Science and Technology Development (Nafosted) of Vietnam to Nguyen Hong Phuong.

9. References

1. Federal Emergency Management Agency (1996). NEHRP Guidelines for the Seismic Rehabilitation of Buildings. FEMA 273. Washington, D.C.
2. Federal Emergency Management Agency and National Institute of Building Sciences, 2003: "Hazus - Earthquake loss estimation methodology User Manual", FEMA, Washington D.C.
3. Federal Emergency Management Agency and National Institute of Building Sciences, 2017. Multi-hazard Loss Estimation Methodology. Earthquake model. Hazus-MH 2.1 Technical manual. 718 pp.
4. Ken Granger, Trevor Jones, Marion Leiba And Greg Scot, 1999: "Cities Project. Community Risk in Cairns, A Multi-Hazard Assessment", Australian Geological Survey Organisation.
5. Nguyen Viet Ky, Nguyen Hong Phuong, Nguyen Hong Bang, Tran Anh Tu. Status of buildings in the 1st and 3rd wards, Ho Chi Minh City and the anticipated risk from geohazard. Journal of Science and Technology Development, Vol.11, N^o11, 2008 (in Vietnamese).
6. Nguyen Hong Phuong (Project Manager), 2002. Study of seismic risk of Hanoi city. Project code 01C-04/09-2001-2. Institute for Marine Geology and Geophysics, VAST (in Vietnamese).
7. Nguyen Hong Phuong, 2005: "Development of a Decision Support System for Earthquake Risk

- Assessment and Loss Estimation: the Hanoi Case Study", *International Journal of GeoInformatics*, 1(1), 191-196.
8. Nguyen Hong Phuong (Project Manager), 2007. Application of GIS technology to Development of a model for seismic risk analysis for Hanoi city. Final Report of Research Project, Institute for Marine Geology and Geophysics, VAST (in Vietnamese).
 9. Nguyen Hong Phuong, 2008. Assessment of earthquake risk for Ho Chi Minh city using GIS and mathematical models. Final Report of Research Project, Institute of Geophysics, VAST (in Vietnamese).
 10. Nguyen Hong Phuong, 2009. Integrated Spatial decision support Systems for Urban Emergencies (ISSUE), Final Report of Vietnam-French Research Project, Hanoi.
 11. Nguyen Hong Phuong. Seismic Risk Assessment for Mega-cities in Vietnam. *Vietnam Journal of Earth Sciences*, 33(3), 337-346, 2011 (in Vietnamese).
 12. Nguyen Hong Phuong (Project Manager), 2012. Assessment of Earthquake Risk and Loss Estimation for the 4th, 7th and Nha Be Districts, Ho Chi Minh city using GIS. Final Report of Research Project, Institute of Geophysics, VAST (in Vietnamese).
 13. Nguyen Hong Phuong, Pham The Truyen. Development of a fault-source model for earthquake hazard assessment in Vietnam. *Vietnam Journal of Earth Sciences*, 29 (3), 228-238, 2007 (in Vietnamese).
 14. Nguyen Hong Phuong, Hoang Don Dzung. Assessment of building damage due to earthquakes in urban area of Ho Chi Minh city. *Vietnam Journal of Earth Sciences*, 32(3), 231-252, 2010 (in Vietnamese).
 15. South Vietnam Geological Mapping Division (2009). "Seismic microzoning for Ho Chi Minh City". Report on implementation of the 2nd stage of the Project, from January to December 2008 (in Vietnamese).
 16. State of California, Seismic Safety Commission (1996). Seismic Evaluation and Retrofit of Concrete Buildings. Report No. SSC 96-01, Sacramento, California.
 17. Wells D.L. and Coppersmith K.J., (1994) "New Empirical Relationships Among Magnitude, Rupture Length, Rupture Width, and Surface Displacement", *Bulletin of the Seismological Society of America*, v 84, pp. 974-1002.

EVALUATION OF GROUND STRAIN IN A SEDIMENT-FILLED VALLEY WITH PGV GRADIENT

Yasuko Kuwata, Atsuoki Okamoto

ABSTRACT

Since seismic ground strain near the boundary of sediment-filled valley is predominant during an earthquake resulting in the damage to buried pipeline, its seismic response had been studied based on analytical solutions and numerical calculations. Sakai et al. showed that a new index called PGV (peak ground velocity) gradient could explain the damage to a water-supply pipeline well in a case study of the 2004 Niigata Chuetsu earthquake in Japan. They also confirmed its validity for the 1995 Kobe earthquake. By the way, the ground strain and PGV gradient are different physical quantities, and the theoretical relationship between them is not yet clear. This study aimed to clarify the relationship between ground strain and PGV gradient using theoretical and numerical approaches for a sediment-filled valley where the basement inclines under sediment. This study adopted a theoretical approach for a simple sediment-filled valley, making a relation with the ground amplification function. In addition, this study analyzed the ground responses of several sediment-filled valleys using FEM analysis as a numerical approach.

DR. YASUKO KUWATA

Associate Professor, Department of Civil Engineering,
Faculty of Engineering, Graduate School of Kobe
University, Japan
Email: kuwata@kobe-u.ac.jp, **corresponding author**
Tel: +81-78-803-6047

MR. ATSUOKI OKAMOTO

Ex-master course student, Department of Civil
Engineering, Faculty of Engineering, Graduate School
of Kobe University, Japan

1. Introduction

Lifelines are important infrastructures used in daily utilities, communication tools, and transportation measures. They are composed of line-shaped structures and are generally constructed under the ground. Therefore, lifelines are affected by seismic-related ground displacements as well as by transient seismic wave propagation during an earthquake. This study focuses on the latter. The differential ground displacement between two structures/parts caused by seismic waves results in ground strain; and then, for example the buried segmented pipeline have damage by pulling out at a joint. Therefore, evaluating seismic ground strain well is important.

To date, the seismic responses of surface waves in sediment-filled valleys have been studied based on analytical solutions and numerical calculations. Haskell proposed an analytical solution for multilayer media using a transfer matrix; this method for the SH wave enhanced the method for the P and SV waves (1), (2), (3). Aki and Larner proposed a wave number integration-based method for determining the seismic response of a layered medium with an irregular interface

(4). Trifunac and Wong introduced a solution for the surface wave of a semi-cylindrical alluvial valley for incident-plane SH waves (5), (6). These studies focused on the seismic wave itself and did not evaluate the ground strain to estimate damage to a buried pipeline.

In a case study of the 2004 Niigata Chuetsu earthquake in Japan, Sakai et al. (7) demonstrated that a new index called PGV gradient could explain the damage to a water-supply pipeline. They also confirmed the validity of the PGV gradient for the 1995 Kobe earthquake (8). PGV gradient is defined as the spatial gradient of PGV at approximately 250 m intervals. Their studies found that the PGV gradient describing transient ground movement shows a good correlation with the seismic damage to pipelines, which may be damaged by axial and shear ground strains. Because PGV can be calculated from the record of ground motion immediately after an earthquake, in future it may be a useful index for quickly estimating damage. It should be noted that the relationship between ground strain and PGV gradient was not clarified analytically in any of the above studies. Ground strain describes the maximum ground strain at a certain time during an earthquake, whereas PGV gradient is the spatial difference in PGV between two points, which might not be observed at the same time as the maximum ground strain. Thus, ground strain and PGV gradient are different physical quantities, and the theoretical relationship between them is not yet clear.

This study aims to clarify the relationship between ground strain and PGV gradient using theoretical and numerical approaches developed for a sediment-filled valley with inclined basement. As mentioned above, ground strain and PGV gradient are different physical quantities and have different meanings in terms of seismic ground response; thus, it is difficult to compare them directly. Therefore, this study adopts a theoretical approach for a simple sediment-filled valley, making a relation between two indexes with the ground amplification function. In addition, this study analyzes the ground responses of several sediment-filled valleys using FEM analysis as a numerical approach.

2. Theoretical formulation

2.1 Outline

In this section, the relation between ground strain and PGV gradient on the ground surface is attempted to make using a theoretical approach. Using a simple sediment model, the expressions for ground strain and PGV gradient are compared based on the two following steps.

(1) Let the ground strain and PGV gradient to make a relation theoretically with amplification function H under limited assumptions: the ground strain is denoted as $|\partial H/\partial x|$, and the PGV gradient is denoted as $\partial|H|/\partial x$, where x is a horizontal coordinate.

(2) Clarify that $|\partial H/\partial x|$ and $\partial|H|/\partial x$ are mathematically equivalent by developing an analytical solution. Note that the case where an incident wave has

a frequency near the natural frequency of the simple sediment is considered.

2.2 Associating with ground amplification function

When a SH incident wave propagates from the bottom of one-dimensional simple sediment (uniform material, horizontal layering, etc.), the analytical solution can be expressed in the frequency domain by the Haskell matrix method. When the displacement of the SH incident wave, $u_0(\omega)$, and the response displacement at the free surface, $u(\omega)$, are given, the ground amplification function $H(\omega)$ can be expressed as their ratio as follows:

$$H(\omega) = \frac{u(\omega)}{u_0(\omega)} \quad [1]$$

where: ω - circular frequency.

Consider the case where the amplification function in the frequency domain can be given for a simple sediment model, as in a one-dimensional ground response. The ground amplification function can be denoted as $H(x, \omega)$; thus, it may not be constant horizontally in the x-direction. The displacement on the surface, $u(x, t)$, can be written in the form of a reverse-Fourier transform as:

$$u(x, t) = \int_{-\infty}^{\infty} H(x, \omega) u_0(\omega) e^{i\omega t} d\omega \quad [2]$$

The ground strain ε_x and the PGV gradient $dPGV$ can be respectively defined as:

$$|\varepsilon_x| = \left| \int_{-\infty}^{\infty} \frac{\partial H(x, \omega)}{\partial x} u_0(\omega) e^{i\omega t} d\omega \right| \quad [3]$$

$$dPGV = \frac{\partial}{\partial x} \left[\max_t \left| \int_{-\infty}^{\infty} i\omega H(x, \omega) u_0(\omega) e^{i\omega t} d\omega \right| \right] \quad [4]$$

Thus, the ground strain is the spatial differentiation of the amplification function, whereas the PGV gradient is obtained by spatially differentiating the maximum value of the integral of the amplification function with respect to time. Therefore, the ground strain and PGV gradient cannot be easily compared. The PGV gradient can be related to the amplification function using the following assumptions.

(1) Assumption 1: Consider the amplification function as a kind of frequency filter. Assume that the ground response filtered by the amplification function has a high amplitude near the natural frequency of the sediment. The maximum ground response in the time domain is determined from the amplitude near the natural frequency of the sediment.

(2) Assumption 2: Assume that $i\omega$, which is set to express velocity, makes relevant shifts in natural frequency toward the higher-order side. In particular, consider not only the first mode but also the second and third modes.

Based on the above assumptions, the PGV gradient in Eq. [4] can be expressed as

$$dPGV = \frac{\partial}{\partial x} |H(x, \omega) u_0(\omega)| \quad [5]$$

When the input wave has a high amplitude near the natural frequency of the sediment, the ground strain can be expressed as follows:

$$|\varepsilon_x| = \left| \frac{\partial H(x, \omega)}{\partial x} u_0(\omega) \right| \quad [6]$$

The right-hand term in Eq. [5] also describes the peak ground displacement (PGD) gradient. If $i\omega$ in Assumption 2 is not considered, the PGD gradient resembles an alternative index for ground strain. In this study, the PGD gradient and the PGV gradient are examined in the following analysis, and the assumptions is validated by numerical analysis. Here, we continue to examine the characteristics of ground strain and PGD gradient based on the two assumptions.

3. Analysis for theoretical formulation

3.1 Analytical model

The ground response analysis in the SH wave field is demonstrated by the linear FEM. The sediment model and its element geometry are shown in Figure 1. The topography of the sediment and basement is the same as in the model used in the theoretical approach, allowing us to compare the solutions. The vertical boundary is located at $x = 20$ m. The incident wave in velocity inputs from 20 m depth from the surface. The sediment element is an isoperimetric element with four nodes. The element size is 0.5 m in width and height, ensuring accuracy for body waves with frequencies greater than 10 Hz. The analytical model has a width of 1,020 m, of which 450 m is attached on each side of the 120-m-wide target model to avoid reflection waves. The wave velocities are 100 m/s for the sediment and 300 m/s for the basement, and the respective densities are 1,600 and 2,000 kg/m³. Rayleigh damping is adopted to have almost 3 % of damping constant from 1.5 to 5.0 Hz. S-wave velocity and density of the basement and Rayleigh damping of the sediment are different from the conditions used in the theoretical approach.

The incident wave is a sine wave with a frequency equal to the natural frequency of the sediment; cases range from the first to the third natural frequency. The duration of the input wave is 5 s with constant amplitude.

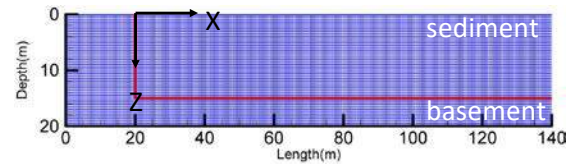


Figure 1: FEM model of a simple sediment-filled valley.

3.2 Analytical result

Figure 2 shows the ground strain, PGV gradient, and PGD gradient on the ground surface of the sediment. The PGV and PGD gradients shown in Figure 2 are normalized by the maximum values in the range of the target sediment width from the vertical boundary to 120 m. For ground strain, the axis is adjusted so that the maximum ground strain has the same height as the maximum normalized gradient (1.0). Figure 2 shows that FEM analysis provides solutions for the gradients when the frequency of the input wave is the same as the natural frequency of the sediment (when the asymptotic solution cannot be obtained). Both the PGV and PGD gradients have similar distributions. The distribution of ground strain envelopes those of both PGV and PGD gradients for all input frequencies.

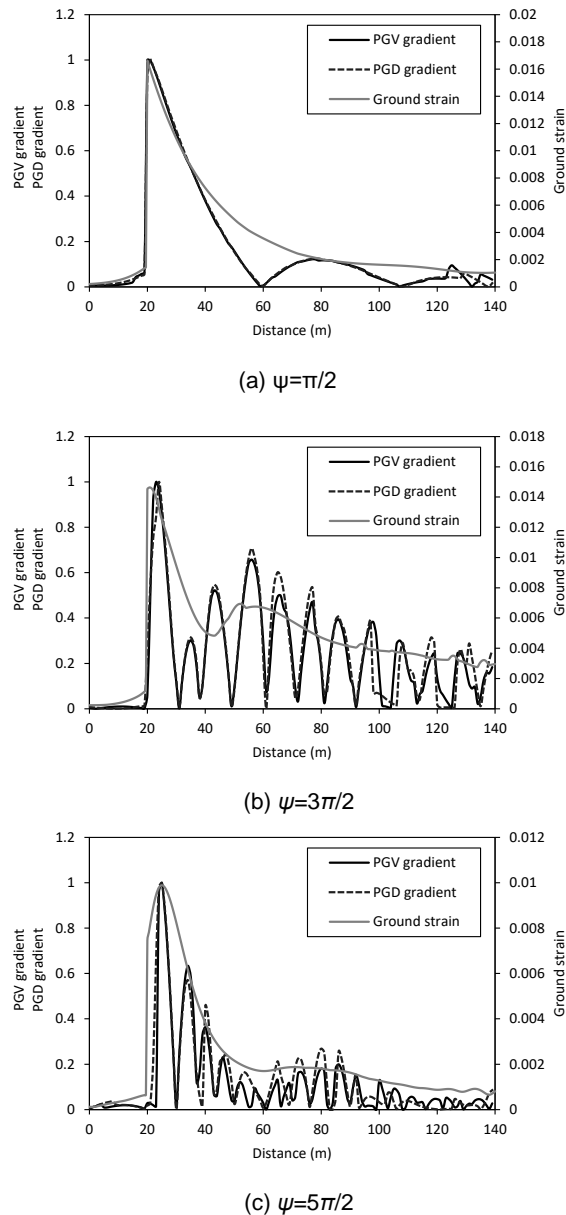


Figure 2: Distributions of ground strain, PGV gradient, and PGD gradient obtained by FEM analysis at different input frequencies . Normalized PGV and PGD gradient values are shown.

Based on the FEM results, we compare the PGV gradient and the partial differentiation of the amplification function H . $|\partial H/\partial x|$ and $\partial|H|/\partial x$ are calculated as follows. The amplification function H is obtained by identifying the amplification rate for each frequency ψ at surface points with intervals of 1 m. The amplification rate at each surface point is derived as the velocity response spectrum at the surface point divided by the input velocity spectrum. The natural frequencies of the sediment are taken into account from the first mode to the third mode. Next, $|\partial H/\partial x|$ and $\partial|H|/\partial x$ are calculated by spatially differentiating the amplification function H . Table 1 summarizes the $|\partial H/\partial x|$, and $\partial|H|/\partial x$ for each incident wave. The distribution of $\partial|H|/\partial x$ is similar to those of the PGV and PGD gradients

in the FEM analysis. The distribution of $|\partial H/\partial x|$ is enveloped by the ground strain distribution. Therefore, when the input frequency is equal to the natural frequency of the sediment, the ground strain and both gradients can be regarded as spatial differentiations of amplification function H according to the FEM analytical results.

Finally, the distribution shapes of the amplification function H and its spatial differentiation are compared between the FEM analytical result and the theoretical solution. Their different point is that the wave shape expressed in the PGV and PGD gradients of FEM analysis cannot be obtained in the theoretical solution in the case of $\psi = \pi/2$ and the amplitude of wave excited from the vertical boundary attenuates toward the distance in the FEM analytical result in the cases of $\psi = 3\pi/2$ and $\psi = 5\pi/2$. These differences can be attributed to the basement having S-wave velocity and density along with Rayleigh damping of the sediment.

Table 1: Comparison of $|\partial H/\partial x|$ and $\partial|H|/\partial x$ obtained by FEM analysis for the case where the incident wave frequency is equal to the natural frequency of the sediment

	$ \partial H/\partial x , \partial H /\partial x$
$\psi=\pi/2$	
$\psi=3\pi/2$	
$\psi=5\pi/2$	

4. Parametric study on the relation between ground strain and PGV gradient

The previous sections dealt with the case where the sediment model has a vertical boundary and a flat basement and the frequency of incident wave is equal to or near the natural frequency of the sediment. Several conditions will be dealt with in this section through parametric study, and the generality of the spatial

distributions of ground strain and PGV gradient will be found on the basis of FEM analysis.

In the previous section considered only the case where a frequency of incident wave is equal to the natural frequency of the sediment is given, such an input is not actually given in the ground motion. When the input wave in a wide frequency band is given, the relationship among ground strain, PGV gradient, and PGD gradient is examined. Then, the waves of the three cases shown in Figure 3 were used as the input wave. Each wave is composed in the frequency band of 0.1–10 Hz and has a different frequency composition. The phase is random. In Case 1, the velocity wave has constant amplitude in the range of 0.1–10 Hz. In the same frequency band, the acceleration wave of Case 2 and the displacement wave of Case 3 have constant amplitudes. In terms of the Fourier amplitude of velocity, the wave in Case 2 contains a greater long-period component, and the wave in Case 3 contains a greater short-period component. The wave in Case 1 has constant amplitude. The amplitudes of velocities in these waves are adjusted to 0.1 m/s at maximum.

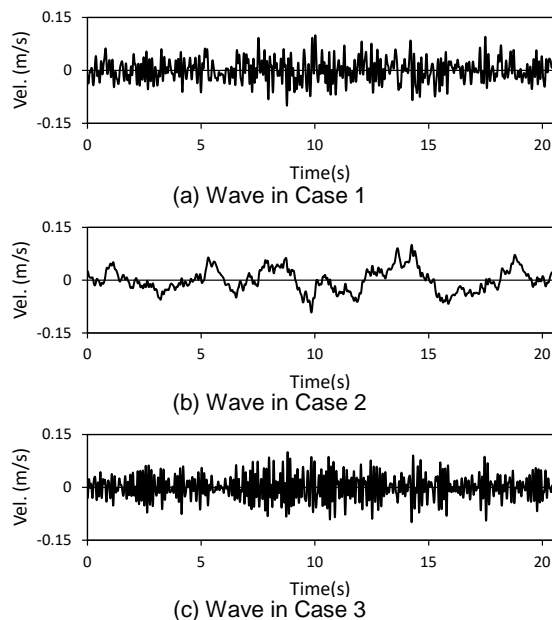


Figure 3: Input waves in the three cases.

Actual earthquake damage to a buried pipeline concentrates on the sediment, beneath which the basement inclines irregularly. In such cases, the ground response changes locally. It is necessary to confirm the analysis results for the sediment facing with irregular-shaped boundary. Several sediment models with irregular-shaped boundaries with the basement were constructed, as shown in Figure 4. The relationships among ground strain, PGV gradient, and PGD gradient are clarified by FEM analysis. The sediment model used in the above analysis is Model 1. The ground surface is completely covered with the sediment, and the irregular boundary with the basement changes the angles in Model 2 and Model 3. The boundary between the sediment and the basement inclines by 1:1 for Model 2, 1:5 for Model 3. The S-wave velocities in all models are 100 m/s for the sediment and 300 m/s for the basement. The densities are 1,600 kg/m³ for the sediment and

2,000 kg/m³ for the basement. The top of the slope boundary of the basement is adjusted to 20 m from the left of the sediment model. The sediment depth is 5 m on the left side of the top of the slope and 15 m on the right side. The natural frequency of the sediment is 5 Hz on the left side and 1.66 Hz on the right side; these frequencies correspond to the second and first natural frequencies of the sediment for Model 1, respectively. In this section, the influence of sediment irregularity is examined by comparing the analytical results of ground strain, PGV gradient, and PGD gradient, not by comparing both gradients and the reference mode of the amplification function.

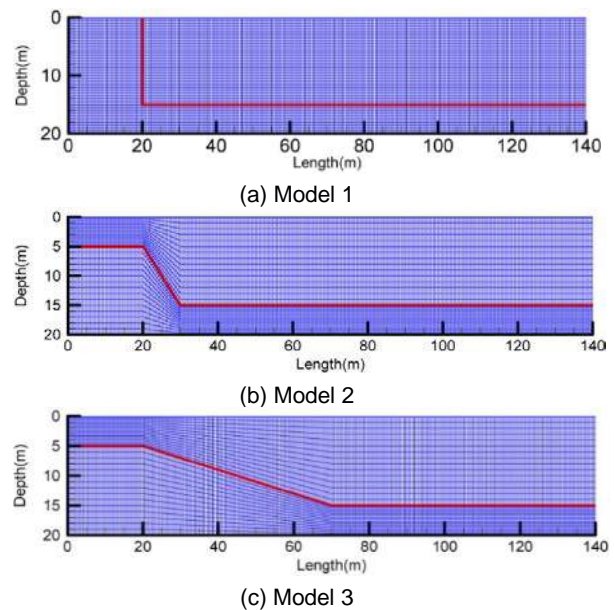


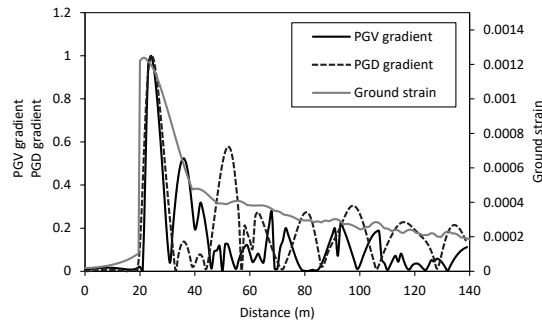
Figure 4: Models of sediment with an irregular basement.

The relationships among ground strain, PGV gradient, and PGD gradient for Case 1 are shown for the different models in Figure 5. The distribution of the PGV gradient is similar to that of the ground strain near the vertical boundary because it refers to the third mode of the amplification function. The distribution of the PGD gradient is similar to that of the ground strain far from the vertical boundary because it refers to the second mode. As shown in Figure 5, the ground strain distribution envelopes the PGV and PGD gradients. The peak of the ground strain distribution moves in the direction of the bottom of the basement inclination as it becomes redundant. A clear peak cannot be seen with a basement inclination of 1:5. As the basement inclination becomes loose, the peak locations of the PGV and PGD gradients do not match with that of the ground strain. However, even in Model 3, which has a clear peak in the strain distribution, the PGV and PGD gradients show similar distributions to the ground strain.

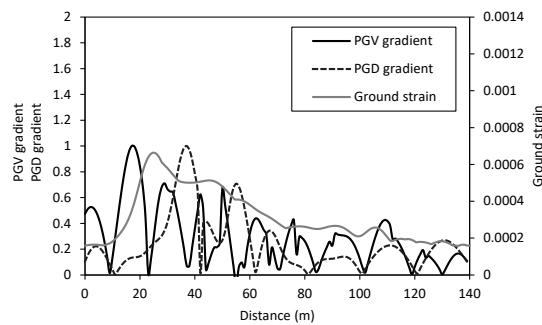
Figure 6 shows the relationships among ground strain, PGV gradient, and PGD gradient for the input wave in Case 2. Because the input wave in this case has a predominant long-period component (lower-order mode), the PGV gradient refers to the second mode of the amplification function, whereas the PGD gradient refers to the first mode. The PGV gradient always has a

strong relationship with the ground strain in the target area.

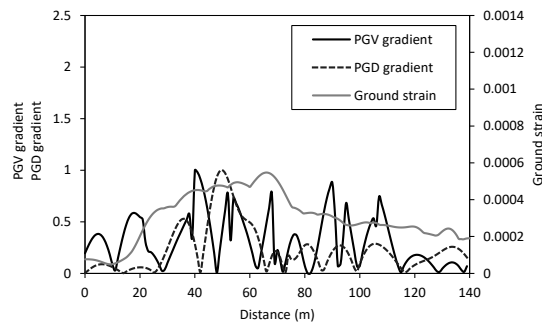
The ground strain distribution in Case 2 is quite similar to that in Case 1. Thus, the input frequency does



(a) Model 1 (L basement outcropped)



(b) Model 2 (inclination 1:1)



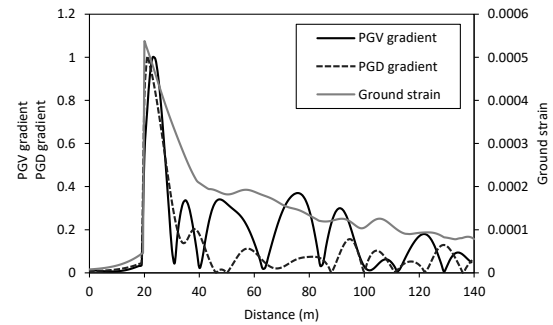
(f) Model 6 (inclination 1:5)

Figure 5: Relationships among PGV gradient, PGD gradient, and ground strain for the input wave of Case 1. Normalized values of PGV gradient and PGD gradient are shown.

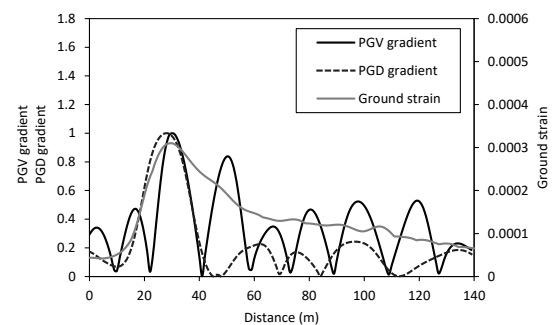
not affect the ground strain distribution. The peak location of the ground strain distribution moves in the direction of the bottom of the basement inclination according to the looser inclination. As the basement inclination becomes loose, the peak locations of the PGV and PGD gradients do not match well with that of the ground strain. However, even in Model 3, which has a clear peak in the ground strain distribution, the PGV and PGD gradients show similar distributions to the ground strain.

Figure 7 shows the relationships among ground strain, PGV gradient, and PGD gradient for the input wave in Case 3, which has a predominant short-period component (higher-order mode). Both the PGV and PGD gradients refer to the third mode of the amplification function. The distribution shapes of the

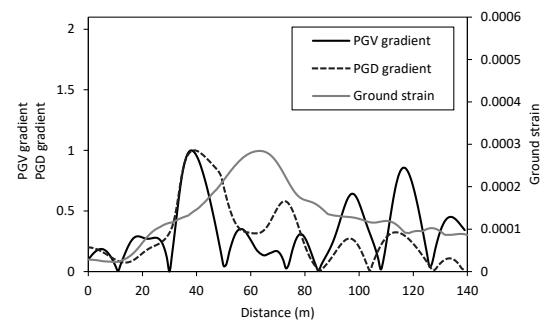
PGV and PGD gradients are similar to each other as well as to the ground strain distribution. Furthermore, the ground strain distribution in this case is similar to that in Case 1. The peak location of the ground strain



(a) Model 1 (L basement outcropped)



(b) Model 2 (inclination 1:1)



(f) Model 3 (inclination 1:5)

Figure 6: Relationships among PGV gradient, PGD gradient, and ground strain for the input wave of Case 2. Normalized values of PGV gradient and PGD gradient are shown.

distribution moves in the direction of the bottom of the basement inclination according to the more gentle inclination. The peak of the ground strain distribution cannot be seen in Models 3. On the other hand, the PGV and PGD gradients have similar distributions in all the models and show good correlation with ground strain distribution.

The effect of sediment irregularity can be summarized as follows from the above results. First, the peak location of the ground strain distribution appears near the bottom of the basement inclination. When the basement inclination becomes gentle, no distinct peak can be identified in the ground strain distribution. This tendency is observed in all three cases. Thus, the distribution of ground strain will become similar one to the other, and is not affected by input frequency. On the

other hand, the peak locations of the PGV and PGD gradients tend not to match that of ground strain as the basement inclination becomes loose.

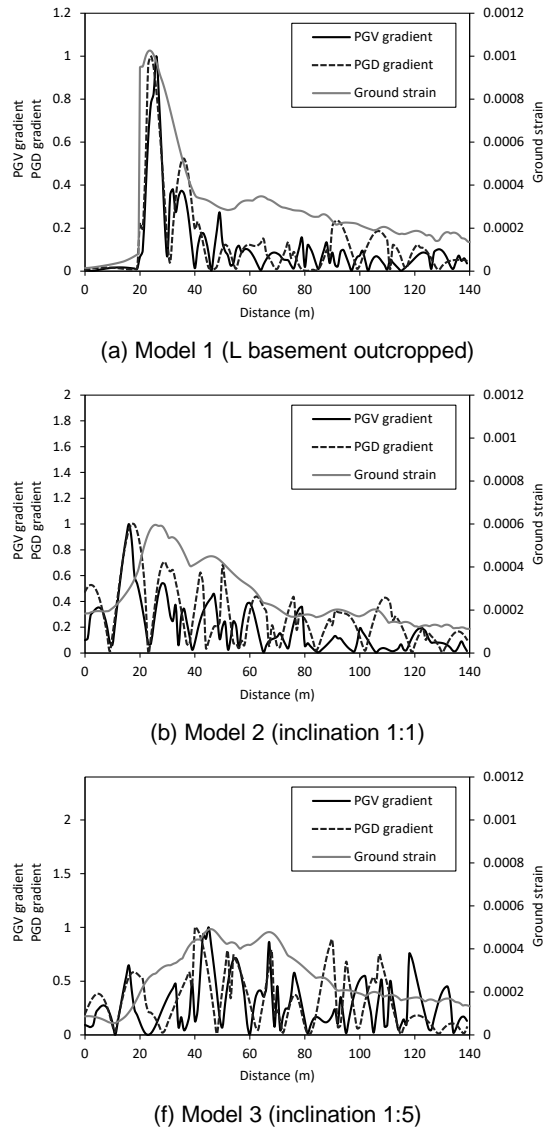


Figure 7: Relationships among PGV gradient, PGD gradient, and ground strain for the input wave of Case 3. Normalized values of PGV gradient and PGD gradient are shown.

5. Conclusions

This study tried to clarify the relationship between ground strain and PGV gradient using theoretical and numerical approaches for a sediment-filled valley where the basement inclines under sediment. This study analyzed the ground responses of several sediment-filled valleys using FEM analysis as a numerical approach.

Even when an input wave not localized to the natural frequency of the ground is given, it was found that the distributions of ground strain, PGV gradient, and PGD gradient can be regarded as an index obtained by

spatially differentiating the ground amplification function. However, the modes referenced by both gradients are different, it is necessary to refer to all natural frequency modes included in the input wave.

The closer the slope of the basement, the worse the correlation between the distribution shapes of the two gradients and the ground strain becomes worse. However, if the ground model has a slope of about 1: 5, the correlation of the distribution tends to be maintained. In addition, it was also confirmed that the influence of the wave excited from the inclined base appears in both gradient distribution near the boundary of inclination.

References

1. Haskell, N.A., The dispersion of surface waves on multilayered media, *Bull. Seism. Soc. Am.*, Vol.43(1), 17–34, 1953.
2. Haskell, N.A., Crustal reflection of plane SH waves, *J. Geophys. Res.*, Vol.65(12), 4147–4159, 1960.
3. Haskell, N.A., Crustal reflection of plane P and SV waves, *J. Geophys. Res.*, Vol.67(12), 4751–4767, 1962.
4. Aki, K. and Larner, L., Surface motion of a layered medium having an irregular interface due to incident plane SH waves, *J. Geophys. Res.*, Vol.75(5), 933–954, 1970.
5. Trifunac, M.D., Surface motion of a semi-cylindrical alluvial valley for incident plane SH waves, *Bull. Seism. Soc. Am.*, 61(6), 1755–1770, 1971.
6. Sakai, H., Hasegawa, K. and Pulide, N., A new seismic damage prediction methodology of water supply pipelines for wide regions; application to the 2004 Niigata-ken Chuetsu earthquake, Japan, *Journal of Japan Society for Civil Engineers*, A, 66 (3), 561-567, 2010 (in Japanese).
7. Sakai, H., Pulide, N., Hasegawa, K. and Kuwata, Y., A new approach for estimating seismic damage of buried water supply pipelines, *Earthquake Engineering and Structural Dynamics*, 2017.

APPLICATION OF SAR IMAGES FOR EVALUATING THE GROUND SUBSIDENCE IN NAM SAI GON USING THE DINSAR TECHNIQUE

ỨNG DỤNG ẢNH SAR ĐÁNH GIÁ LÚN MẶT ĐẤT KHU VỰC NAM SÀI GÒN BẰNG KỸ THUẬT DINSAR

Nguyen The Duoc, Tran Anh Tu

ABSTRACT

Synthetic Aperture Radar (SAR) images have widely utilized in environmental monitoring as well as geological hazards (subsidence, landslide,...), however, this is still a quite new technology in Vietnam. Therefore, the main purpose of this study is to introduce the DInSAR technique and effects to SAR images analysis processing.

Nam Sai Gon has been selected as the study area, which has been strong subsidence process due to geological characteristic and urbanization. In this work, the SAR images are collected from Sentinel-1 satellite and analyzed in open source SNAP software through the Differential Interferometric SAR (DInSAR) technique.

The results show the subsidence values in the 3, 6 and 12 months with the value from 0-10cm in 6 months and 2.5-15cm in 12 months. Through the analysis of noise areas, the results can be affected by the tide factor. For detailed assessment, 28 sites of subsidence survey in the study area were collected. This results indicate that the anomalous areas (bridge, main road) have large subsidence.

KEYWORDS: SAR, Radar, DInSAR, SNAP, Interferometry, Sentinel-1, Subsidence.

TÓM TẮT

Ảnh Radar khẩu độ mở tổng hợp (SAR) được sử dụng rộng rãi trong giám sát môi trường cũng như tai biến địa chất trên thế giới (lún mặt đất, trượt lở,...). Tuy nhiên, đây vẫn còn là công nghệ khá mới ở Việt Nam. Vì vậy, mục đích chính của nghiên cứu này là giới thiệu cách tiếp cận kỹ thuật DInSAR và phân tích các yếu tố ảnh hưởng đến quá trình xử lý hình ảnh SAR.

Nam Sài Gòn được chọn là khu vực nghiên cứu, vì đây là khu vực này có quá trình lún mạnh do đặc điểm địa chất và quá trình đô thị hóa. Trong nghiên cứu này, các cặp ảnh SAR được thu thập từ vệ tinh Sentinel-1 và được phân tích trong phần mềm mã nguồn mở SNAP thông qua kỹ thuật giao thoa khẩu độ mở tổng hợp vi phân (DInSAR).

Kết quả cho ra giá trị lún trong 3, 6 và 12 tháng là từ 0-10cm trong 6 tháng và từ 2.5-15cm trong 12 tháng. Thông qua phân tích các khu vực nhiễu, kết quả có thể bị ảnh hưởng bởi yếu tố thủy triều. Để đánh giá chi tiết, 28 điểm khảo sát lún trong khu vực nghiên cứu được thu thập. Kết quả chỉ ra các vùng dị thường (cầu, các tuyến đường lớn) có giá trị lún lớn.

TỪ KHÓA: SAR, Radar, DInSAR, SNAP, giao thoa, Sentinel-1, lún mặt đất.

NGUYEN THE DUOC

Master's student, Department of Earth Resources and Environmental, Faculty of Geology and Petroleum Engineering, HCMC University of Technology (HCMUT)
Email: ntduoc@hcmut.edu.vn, **corresponding author**
Tel: 0902 114 839

Dr. TRAN ANH TU

Lecturer, Department of Earth Resources and Environmental, Faculty of Geology and Petroleum Engineering, HCMC University of Technology (HCMUT)
Email: trantu@hcmut.edu.vn
Tel: 0918 410 939

1. Introduction

Differential Interferometric Synthetic Aperture Radar (DInSAR) using spaceborne sensors has become an established tool for analysis of very small surface deformations. This technique uses multi-temporal SAR images taken at different times to analyze the surface deformation (Tempfli et al., 2009).

It opens many applications in geology such as monitoring subsidence, earthquake monitoring, landslide, etc. Many scientists in the world have applied the above technology to monitor subsidence, landslide such as Przyłucka et al. (2015) analyzed TerraSAR-X satellite images by combining between the DInSAR conventional and advanced methods to calculate subsidence in urban areas in the Upper Silesian Basin with a difference of 7mm/yr. Gao et al. (2015) used TerraSAR-X images to analyze subsidence through the InSAR technique in the Beijing for the period of 2013-2014 with an average subsidence of -97.5mm/yr. Fiaschi et al. (2017) used two stacks of Sentinel-1A scenes acquired in both ascending and descending orbits to assess the landslide vulnerability using the Permanent Scatterer Interferometry (PSI) technique in Veneto, Italy with an average speed of 7mm/yr. In addition, this technique has been successfully applied to ground deformation in many places such as Bangkok (Thailand), Tokyo (Japan), Shanghai (China), Paris (France). (Trung, 2015).

Especially, in Ho Chi Minh City, Trung et al. (2008) used the DInSAR technique to monitoring subsidence with an average subsidence of -20cm in District 7 and Binh Thanh District from 12/2003 to 5/2004, Dinh et al. (2015) estimate the average subsidence of -8.0mm/yr and the maximum of -70mm/yr in center city with the PSInSAR technique in the 2006-2010 period.

Nam Sai Gon has been selected as a research area, in which the area for analysis is 7x10 km. This area (Figure 1) is mainly located in modern sedimentary areas with two types of topographic features: irregular alluvial ground and low alluvial ground regularly flooded in Districts 7 and Nha Be District. Therefore, it is still in the natural cohesion process. (Nam, 2016).

In this area, the dense river systems divide the area into small areas. The results of the analysis of the highest tide data in the period from 1990 to 2016 at Nha Be station (SRHC, 2017) indicate that the water level fluctuations have increased over the years with an average increase of 1.42cm/yr.

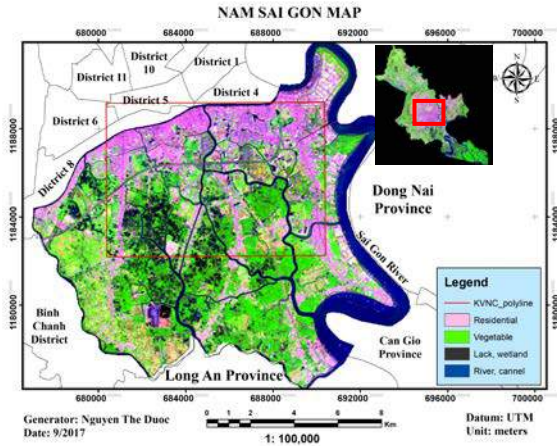


Figure 1. Location map of Nam Sai

Nam (2016) has shown that the weak soil layer thickness is very large and there is area up to 35m, and the subsidence velocity is correlated with the thickness of weak soil layer with the correlation coefficients $r_2 = 0.7$. According to the surveyed status on National Highway 50 and Pham Hung Street in the study area, some constructions in this area have showed signs of strong subsidence around citizen areas such as 1 Gia Hoa Residential on National Highway 50 (Figure 2a) with a subsidence of -19cm, Easter City Building (Figure 2b) on Pham Hung Street has a subsidence of -9.5cm.



a. 1 Gia Hoa Residential on National Highway 50
b. Easter City Building on Pham Hung Street

Figure 2. Current status of subsidence in Nam Sai Gon.

In conclusion, the paper aims to introduce this methodological approach and also shows the effects on data analysis.

2. Methodology

2.1 Materials

In this paper, the radar images from the Sentinel-1 satellite were used to evaluate the ground subsidence in Nam Sai Gon. The whole image area is approximately 20 km × 30 km, see Figure 3, and Table 1 show information of four Sentinel-1 SAR SLC images (SLC - Single Look Complex).

Table 1: Information of radar images (radar images, 2017).

Image information	Master	Slave	Slave	Slave
Date	25/12/2015	17/03/2016	09/06/2016	24/12/2016
Polarisation	VV (Vertical transmission and Vertical reception)			

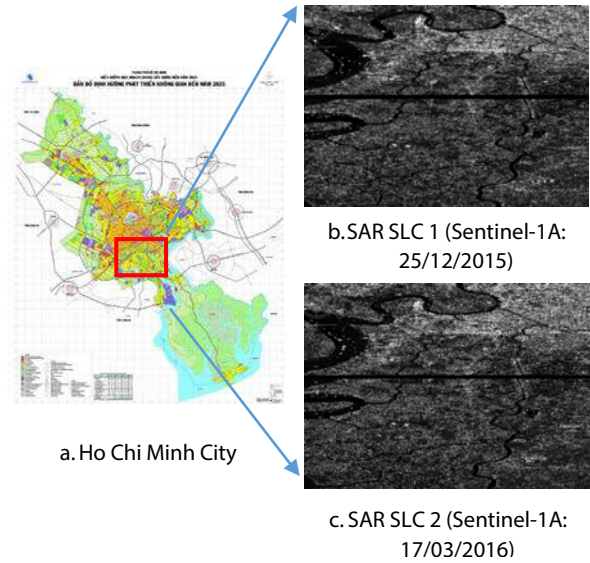


Figure 3. Sentinel-1 SAR SLC images. (HCMC map & radar images, 2017)

2.2 InSAR and DInSAR theory

SAR Interferometry (InSAR) is a technique for handling digital signals from at least two SAR images (or more) in the same area at different times. The operation of InSAR is based on the principle of extracting the phase variation between two SAR images in the same area at two slight different positions to determine the difference in the path length of the radar waves (Duy, 2015). This relate to important parameters such as terrain elevation, surface deformation and atmospheric disturbance (Goldstein et al., 1988).

If the surface deformation does not occur among the two radar image acquisition systems, the phase values from φ_1 and φ_2 of the two radar images can be illustrated as formula (Ferretti et al., 2007) follows:

$$\Delta \varphi = \varphi_1 - \varphi_2 = \frac{2r_1}{\lambda} 2\pi - \frac{2r_2}{\lambda} 2\pi = \frac{4\pi}{\lambda} \Delta r \quad (1)$$

where: $\frac{2r_1}{\lambda} 2\pi$ and $\frac{2r_2}{\lambda} 2\pi$ is the quantity causing the delay.

The phase difference can have contributions from five different sources:

- (1) $\Delta \varphi_{\text{flat}}$ is called flat Earth phase which is the phase contribution due to the earth curvature.
- (2) $\Delta \varphi_{\text{elevation}}$ is the topographic contribution to the interferometric phase.
- (3) $\Delta \varphi_{\text{displacement}}$ is the surface deformation contribution to the interferometric phase.
- (4) $\Delta \varphi_{\text{atmosphere}}$ is the atmospheric contribution to the interferometric phase. It is introduced due to the atmospheric humidity, temperature and pressure change between the two acquisitions.
- (5) $\Delta \varphi_{\text{noise}}$ is the phase noise introduced by temporal change of the scatterers, different look angle, and volume scattering.

From the five sources above, formula 1 will be expanded to the following formula 2:

$$\Delta \varphi = \Delta \varphi_{\text{flat}} + \Delta \varphi_{\text{elevation}} + \Delta \varphi_{\text{displacement}} + \Delta \varphi_{\text{atmosphere}} + \Delta \varphi_{\text{noise}} \quad (2)$$

Assume two images in the same condition, the $\Delta \varphi_{\text{atmosphere}}$ and $\Delta \varphi_{\text{noise}}$ are eliminated and only three

elements of the interfering phase in formula 3 (Ferretti et al., 2007):

$$\Delta\varphi = -\frac{s}{\tan\theta} \frac{B_n}{R} \frac{4\pi}{\lambda} - \frac{\Delta q}{\sin\theta} \frac{B_n}{R} \frac{4\pi}{\lambda} + \frac{4\pi}{\lambda} d \quad (3)$$

where:

B_n : perpendicular baseline (B_\perp in Figure 4).

R : the distance from the SAR sensor to the object (r_1).

q : the difference between vertical objects in the vertical direction.

s : the tension between adjacent objects is oblique.

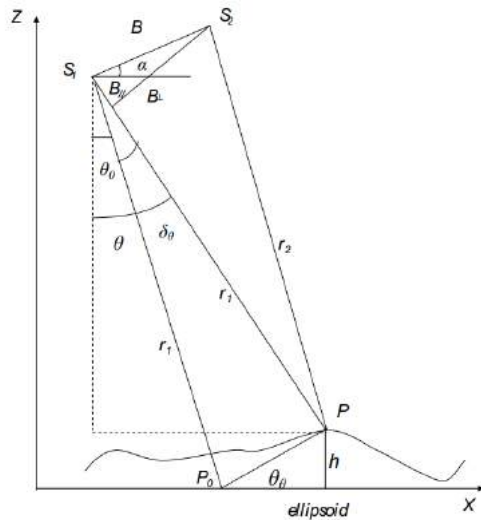


Figure 4. The geometry of the InSAR technique.
(Joughin et al., 1996)

Figure 4 shows the geometry of InSAR technique, where:

S_1 : Master, S_2 : Slave, B : Baseline, θ : angle of incidence, r_1 and r_2 : the slant ranges from the antenna to the P point on the ground, α : the angle formed by the baseline and the nadir.

To determine the deformation component (subsidence or outcrop), the altitude in the phase value was separated. The technique is based on the elimination of the altitude component in the phase value to determine the final interference value called the InSAR Differential technique (DInSAR) (Massonnet et al., 1993).

Displacement elements can be separated in two ways (Trung et al., 2008):

- (1) Using the digital elevation model (DEM), called DInSAR using DEM.
- (2) Use more pairs of SAR images, called multi-temporal DInSAR. In the study, DInSAR technique was applied to analyze subsidence in Nam Sai Gon.

2.3 DInSAR Processing

In the DInSAR technique, there are three important factors in selecting SAR images: (1) two SAR SLC images need to have a good coherence, (2) baseline (distance between two antennas when photographing), and (3) weather. The seven main steps of the processing can be synthesized as follows in SNAP program:

(1) The images are complex images consisting of two bands: a band containing amplitude information and a band containing phase information (Dinh, 2006). It is necessary to calibrate some pixels and select the study area as well as the polarization (choose polarization VV for subsidence).

(2) The images are coregistered with TOPSAR Interferometry, in order to find the same image pixels on the two SAR images and select the Master and Slave images (SNAP guide, 2017).

(3) After the coregistration of the images, the image will be deburst to create one single image since SAR images from Sentinel-1 include many image swaths. Then, the result will be cut to fit the study area.

(4) The combined SAR images are interfered by multiplying the conjugate of each complex pixel of the second image (Slave) together with the corresponding complex pixel of the first image (Master). Displacement elements are excluded by performing conjugate multiplication (Zebker et al., 1986).

(5) Unwrapping phase is the key step to find displacement phase by determining the number of cycles lost during the interference phase. To run this processing, the topographic phase is removed and filtered to decrease error due to noise, and atmosphere through Goldstein Phase Filtering tool. Then, the process to open the phase to recover the displacement phase value by the MCF problem (Dinh, 2006) is running on the Linux operating system.

(6) The unwrapping phase value is converted to displacement value.

(7) Finally, coordinates are geocoded and the subsidence model is generated. The subsidence results obtained from the Ellipsoid surface with datum is in WGS84 and the projection is UTM, Zone 48.

2.4 Field Survey Method

To assess the results of the subsidence model, 28 points in real data near residential area are collected on the field by survey method (Figure 5).



Figure 5: Map of sampling locations in the study area.

The survey was conducted as follows: (1) Identifying sites of surveyed on major roads (Nguyen Huu Tho, Pham Hung, Nguyen Van Linh). (2) Investigating the current state of the construction such as tilted, cracks, expansion of cracks in the walls of the house, construction and other information collection such as construction time, structural foundation, time of occurrence of subsidence, cracks and their evolution over time. (3) Evaluating the results of the survey with previous survey results to select appropriate results for the analysis.

3. Results and discussion

The results of the study focused on the residential areas. Therefore, vacant land and flooded areas were removed. After analyzing, the subsidence results in 3, 6 and 12 months are shown in Figure 6.

The overall assessment results in Figure 6 show the subsidence value from 0 to 0.1m (positive value) in 6 months and from -0.15m to -0.025m in 12 months (negative value). With two different legends, the evaluation of subsidence is difficult for comparing the subsidence in three stages. Hence, it is necessary to calibrate two legends to the same scale to evaluate. The quantization is based on stable areas (subsidence $0 \div 0.025$ m over a 3-month) as well as analysis on Google Earth. Then the values of 6 and 12 months are quantized.

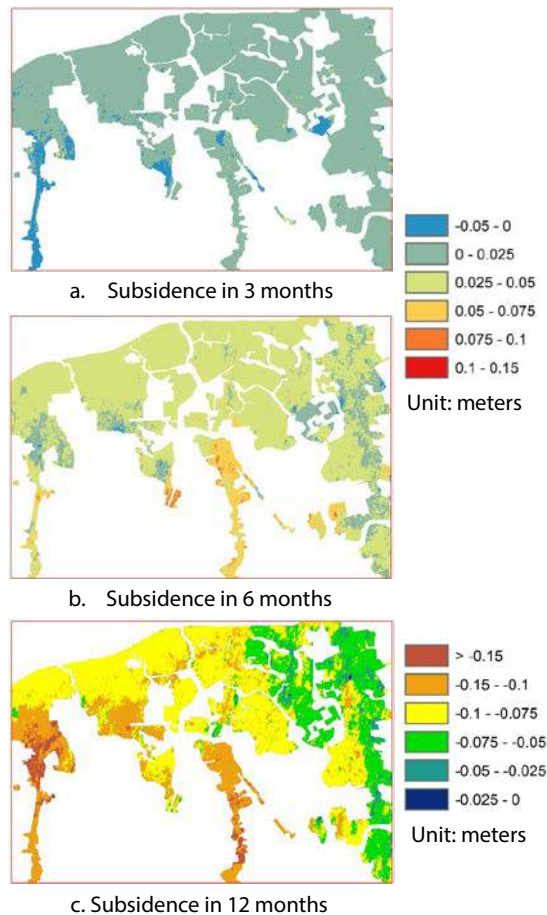


Figure 6. The subsidence results in 3, 6 and 12 months.

The quantification results with gray areas are shown in Figure 7 below, where residential areas are considered stable in subsidence value. After bringing the same legend, the values in blue circle areas were unevenly varied with subsidence decreasing from $-0.05 \div -0.025$ m to $-0.025 \div 0$ m after 3 months and increased to $-0.05 \div -0.025$ m after 6 months. Similar to the red, yellow and green circle areas, these areas have high and low subsidence variations. To explain this, tidal observation data was collected to evaluate this change and it was shown in Table 2.

Table 2: Tide information during radar image collection (SRHC, 2017).

Date	Time to take pictures	Water level (cm)			
		22h	23h	22h 45	Differen -ce
24/12/2015	22:45:05	34	76	65.5	0

17/03/2016	22:44:59	62	54	56	9.5
09/06/2016	22:44:54	-94	-150	-136	201.5
24/12/2016	22:44:15	96	116	111	-45.5

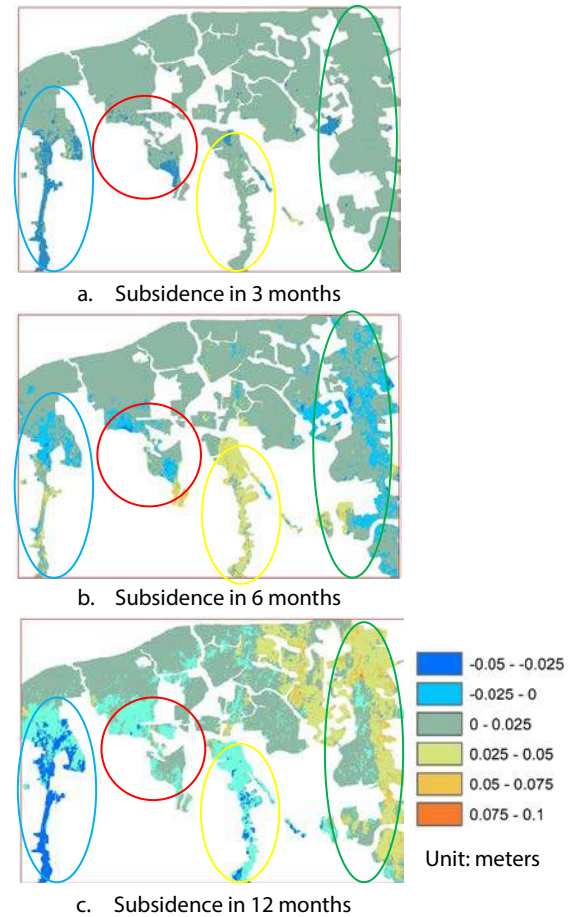


Figure 7. The quantized subsidence results in 3, 6 and 12 months.

With the pair of images 24/12/2015 (1) and 17/03/2016 (2), the difference of water level is low (9.5cm) so the difference in terrain of time (2) compared to time (1) will be less volatile. Therefore, the results in Figure 7a give the value mainly positive (lift) and some negative value (blue). The cause is the influence of wetlands and surrounding canals.

With the pair of images (1) and 09/06/2016 (3), the difference of water level is very high (201.5cm) so the difference of terrain of time (3) compared to time points (1) large fluctuations. This leads to more expanses of terrain, which helps the energy to reflect well and to correlate better. So that, the results of Figure 7b give all value positive (lift).

With the pair of images (1) and 24/12/2016 (4), the water level difference here is also very high (-45.5cm). This leads to the terrain becoming narrower due to rising water levels. Therefore, the reflected energy of the satellite will be low, giving a negative value (less than 0) in Figure 7c.

To evaluate the detailed analysis results, the field results are collected to give a more general overview of the results and shown in Table 3. The comparison chart between the survey subsidence value analysis will be shown in Figure 8 based on data from Table 3.

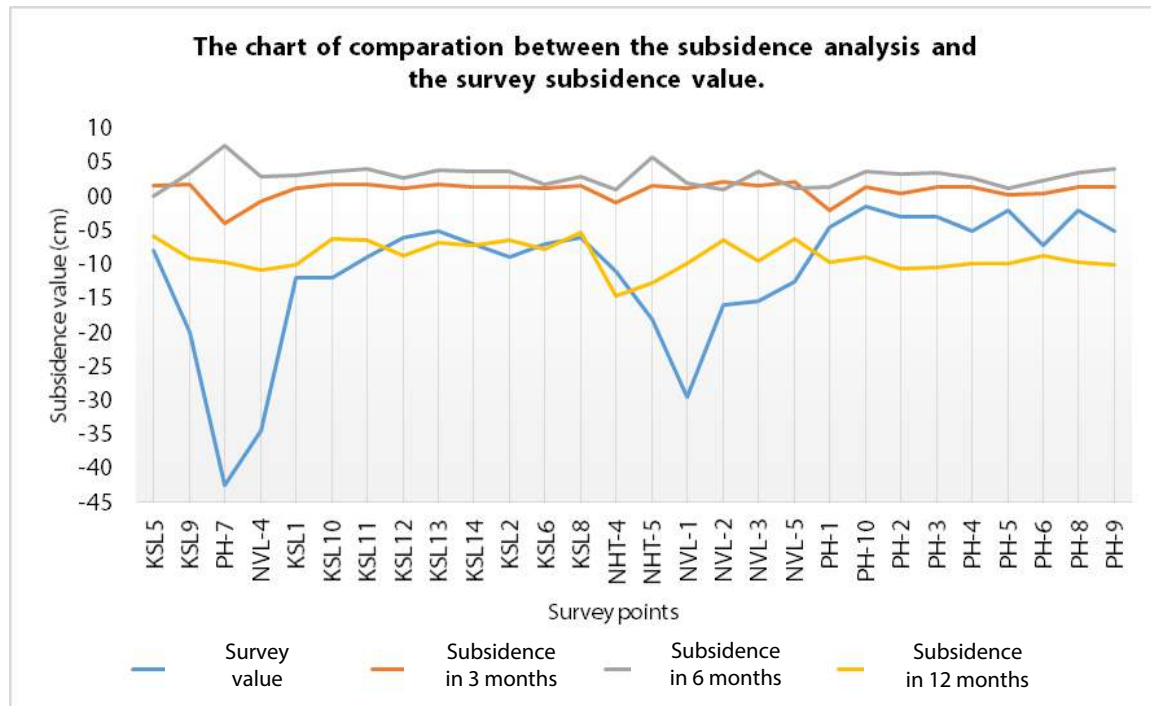


Figure 8. The chart compares the subsidence value with the survey subsidence.

Table 3. Results of subsidence value of 28 points of field survey and analysis (unit: cm)

No.	Point	Y	X	Year	Subsidence value survey	Subsidence value for 3 months	Subsidence value for 6 months	Subsidence value for 12 months
1	KSL5	689007	1186593	5.0	-8.0	1.49	0.14	-5.82
2	KSL9	690334	1188098	7.0	-20.0	1.70	3.56	-9.09
3	PH-7	684410	1184477	11.0	-42.5	-3.99	7.45	-9.71
4	NVL-4	688713	1185869	11.0	-34.5	-0.77	2.91	-10.75
5	KSL1	686822	1186442	7.0	-12.0	1.18	3.13	-9.99
6	KSL10	690037	1186809	3.0	-12.0	1.71	3.75	-6.21
7	KSL11	689835	1187045	3.0	-9.0	1.79	3.96	-6.38
8	KSL12	687961	1187585	6.0	-6.0	1.24	2.63	-8.73
9	KSL13	687907	1187264	6.0	-5.0	1.73	3.82	-6.83
10	KSL14	687288	1187714	6.0	-7.0	1.43	3.66	-7.19
11	KSL2	687055	1186101	3.0	-9.0	1.43	3.68	-6.51
12	KSL6	689279	1187263	3.0	-7.0	1.12	1.81	-7.72
13	KSL8	689153	1187912	3.0	-6.0	1.55	2.92	-5.35
14	NHT-4	686911	1184452	10.0	-11.0	-0.85	1.00	-14.70
15	NHT-5	686383	1185124	5.0	-18.0	1.65	5.68	-12.65
16	NVL-1	689250	1187467	9.0	-29.5	1.22	1.87	-9.93
17	NVL-2	688361	1186320	8.0	-16.0	2.07	0.97	-6.39
18	NVL-3	688760	1185365	7.0	-15.3	1.66	3.68	-9.44
19	NVL-5	688483	1186691	5.0	-12.5	2.07	1.19	-6.27
20	PH-1	684246	1184968	3.0	-4.5	-1.95	1.43	-9.59
21	PH-10	684017	1185318	2.0	-1.5	1.34	3.60	-8.88
22	PH-2	683893	1185025	1.0	-3.0	0.41	3.23	-10.72
23	PH-3	683928	1185039	2.0	-3.0	1.42	3.55	-10.37
24	PH-4	683990	1185285	3.0	-5.0	1.32	2.70	-9.95
25	PH-5	684318	1185122	2.0	-2.0	0.25	1.14	-9.93
26	PH-6	683593	1186204	6.0	-7.2	0.49	2.32	-8.80
27	PH-8	684136	1185262	1.0	-2.0	1.41	3.55	-9.66
28	PH-9	683891	1185195	3.5	-5.0	1.42	4.13	-10.02

From Figure 8, the study indicates the areas of abnormalities (high subsidence) and the areas of low subsidence. Firstly, the points at the foot of the bridge: KSL5 (-8cm), KSL9 (-20cm), PH7 (-45.5cm) and NVL4 (-34.5cm) are four points with high subsidence value because many vehicles move through here and make the bridge shake continuously. Secondly, the points located near major roads: NVL1 (-29.5cm), NVL2(-16cm), NVL3 (-15.3cm), NHT4 (-11cm), NVL5 (-12.5cm) and PH1 (-4.5cm). These are also

areas affected by vehicles, which also affects the value of subsidence. Finally, the remaining points did not change much: PH5 (-2cm), PH8 (-2cm), PH3 (-3cm), etc. This shows that this area has a stable subsidence.

4. Conclusions

The analysis can be resulted as follows:

- (1) The main purpose of this study is to introduce how to approach the DInSAR technique and indicates the effect in SAR images analysis processing in Nam Sai Gon. In which, SAR image pairs are collected from Sentinel-1 satellite and processed on open source SNAP software using the DInSAR technique.
- (2) The analysis shows that the value in 3 (from 0 to 2.5cm) and 6 months (from 0 to 10cm) were positive and negative in 12 months (-2.5 to -15cm). After calibrating subsidence value in same scale and comparing value in 3, 6 and 12 months, this leads to the tide factor can be suspected to affect the interference as well as the unwrapping phase.
- (3) The results of the 28 surveyed sites with the analysis showed that the bridges and high-building near the roads gave anomalous results (high value). Hence, we need to consider and do more survey in here.

In order to improve the results of the study, a number of recommendations were made as follows:

- (1) Increase the analysis time to two years or more to evaluate the subsidence over time.
- (2) Evaluate the impact of tides on the wetlands and vacant land to assess the potential impact on subsidence values of the population in the area.
- (3) To evaluate the accuracy and also trend of research, the PSInSAR (Permanent Scatterer InSAR) technique will be used to analyze and identify PS deformation points over time. This result will evaluate the accuracy of the topic using InSAR/DInSAR technology for monitoring subsidence as well as other applications in the field of Geological Environment.

References

1. H.T.M. Dinh and L.V. Trung, (2006). *Application of the InSAR technology for generating DEM*, Journal of Science and Technology Development (2006), Vol 9, No.11, pp. 35-42.
2. H.T.M. Dinh, L.V. Trung and L.T. Thuy, (2015). *Mapping Ground Subsidence Phenomena in Ho Chi Minh City through the Radar Interferometry Technique Using ALOS PALSAR Data*, Remote Sens (2015), 7, 8543-8562.
3. N.T. Duoc (2018), *Application DInSAR technique to evaluate the ground subsidence in Nam Sai Gon by Radar band-C*, Senior thesis (2018), Ho Chi Minh University of Technology, Viet Nam.
4. N.B. Duy, (2015). *Studying on the Interferometry SAR (InSAR) technique for Digital Elevation Model (DEM) generation using Open source of Software NEST and SNAPHU*. Can Tho University Journal of Science (2015), Part A: Natural Sciences, Technology and Environment: 36: pp. 77-87.
5. A. Ferretti, A. Monti-Guarnieri, C. Prati, F. Rocca and D. Massonet, (2007). *InSAR Principles: Guidelines for SAR Interferometry Processing and Interpretation*, ESA Publications.
6. S. Fiaschi, M. Mantovani, S. Frigerio, A. Pasuto and M. Floris, (2017). *Testing the potential of Sentinel-1A TOPS interferometry for the detection and monitoring of landslides at local scale (Veneto Region, Italy)*. Environ Earth Sci (2017) 76:492. DOI 10.1007/s12665-017-6827-Y.
7. M. L. Gao, H. L. Gong, B. B. Chen, C. F. Zhou, K. S. Liu, and M. Shi, (2015). *Mapping and characterization of land subsidence in Beijing Plain caused by groundwater pumping using the Small Baseline Subset (SBAS) InSAR technique*. The International Association of Hydrological Sciences (2015), 372, 347-349.
8. R. Goldstein, H. Zebker and C. Werner, (1988). *Satellite radar interferometry Two dimension-al phase unwrapping*, Radio Sci. (1988), 23, 713–720.
9. "Ho Chi Minh City Map", Available: <http://www.planic.org.vn/ban-do.aspx>, [Accessed: Jul 2018].
10. I. Joughin, R. Kwok and Fahnestock, (1996). *Estimation of ice-sheet motion using satellite radar interferometry: method and error analysis with application to the Humboldt Glacier, Greenland*, Journal of Glaciology (1996), No.42, pp. 564-575.
11. D. Massonnet, M. Rossi, C. Carmona, F. Adragna, G. Peltzer, K. Feigl and T. Rabaute (1993). *The displacement field of the Landers earthquake mapped by radar interferometry*. Nature, 364, 138–142.
12. N.G. Nam, (2016). *Application of GIS to generating weak soil layer map in District 7, Ho Chi Minh City and assess the subsidence possibility*. Senior thesis (2016), Ho Chi Minh University of Technology, Viet Nam.
13. M. Przyłuck, G. Herrera, M. Graniczny, D. Colombo and M. Béjar-Pizarr, (2015). *Combination of Conventional and Advanced DInSAR to Monitor Very Fast Mining Subsidence with TerraSAR-X Data: Bytom City (Poland)*, Remote Sens. 2015, 7, 5300-5328; doi:10.3390/rs70505300.
14. "Radar images", Available: <https://scihub.copernicus.eu/dhus/#/home>, [Accessed: Jul 2017].
15. K. Tempfli, N. Kerle, G.C. Huureman and L. L. F. Janssen (eds.), (2009). *Principles of Remote Sensing*, ITC, 7500 AA Enschede, The Netherlands, pp. 345-388.
16. "Tidal observation data from 1996-2016". *Southern Regional Hydrometeorological Center (SRHC)*. 2017.
17. L.V. Trung, (2015). *Remote Sensing*. Vietnam National University, Ho Chi Minh City Publishing, pages 9-17 and 120-152.
18. L.V. Trung and H.T.M. Dinh (2008). *Measuring ground subsidence in Ho Chi Minh City using differential InSAR techniques*, Journal of Science and Technology Development, Vol 11, 12-2008, pp. 121-130.
19. Sentinel-1 Team, *Sentinel-1 User Handbook*, 2013.
20. "SNAP guide", Available: <https://sentinel.esa.int/web/sentinel/toolboxes/sentinel-1/tutorials>, [Accessed: Jul 2017].
21. H.A. Zebker, and Goldstein (1986). *Topographic mapping from interferometric SAR observation*, J. Geophys. Res. (1986) 91, 4993-4999.

SIMULATION OF STRONG GROUND MOTIONS FOR THE 2016 KUMAMOTO EARTHQUAKE SEQUENCE AROUND THE PORT OF KUMAMOTO

Atsushi Nozu

ABSTRACT

The 2016 Kumamoto earthquake sequence caused slight by not-negligible damage to facilities at the Port of Kumamoto. To estimate strong ground motions at the port, the applicability of the fault models for the foreshock and main shock (Nozu and Nagasaka, 2018a) was studied. To validate the models, they were applied to strong-motion stations surrounding the port. It was found that the source models can well explain strong ground motions recorded at those stations provided that the multiple nonlinear effects are appropriately considered.

KEYWORDS: the 2016 Kumamoto earthquake sequence, the Port of Kumamoto, strong ground motion, fault model, the corrected empirical Green's function method, multiple nonlinear effects

DR. ATSUSHI NOZU

Director of Earthquake Disaster Prevention Engineering Division, Port and Airport Research Institute (PARI)

Email: nozu@pari.go.jp, **corresponding author**

Tel: +81-46-844-5058

1. Introduction

In 2016, a series of damaging earthquakes hit the Kumamoto and Oita prefectures, Kyushu, Japan, including the M_w 6.1 foreshock (April 14, 21:26 JST) and the M_w 7.1 main shock (April 16, 1:25 JST). The entire sequence was named “the 2016 Kumamoto earthquake” by the Japan Meteorological Agency (JMA). The earthquakes resulted in significant damage in the near-source region including Mashiki Town (represented by KMMH16 in Figure 1).

In contrast to serious damage in the near-source region, the damage to facilities at the Port of Kumamoto (Figure 1) was found to be generally minor. However, slight damage did occur. For example, a gravity-type quay wall, constructed on SCP improved ground, suffered residual horizontal displacement of 12 cm (Photo 1). In addition, movable bridges for the ferries became out of order, which could be attributed to the deformation of ground.

To reveal the damage mechanism and to evaluate the appropriateness of the current design method, it was important to evaluate strong ground motions at the port. Unfortunately, the Port of Kumamoto was not covered by the Strong Motion Earthquake Observation in Japanese Ports (e.g., Nozu and Nagasaka, 2018b). Therefore, strong ground motions at the port remained unknown.

To estimate strong ground motions at the port, we employed the corrected empirical Green's function method (Kowada et al. 1998; Nozu and Sugano 2008; Nozu et al. 2009). As explained later, the method is advantageous in incorporating site effects, i.e., the effect of sediments on both the Fourier amplitude and phase of strong ground motions (Figure 2). To simulate strong ground motions with this method, we decided to use the simplified source models for the foreshock and the main shock, which were developed in our group

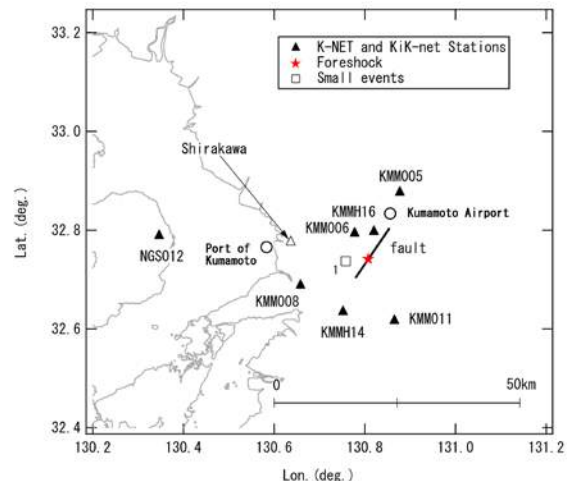


Figure 1: Locations of the foreshock fault plane, the small event used for the analysis (numbered open rectangle), the strong motion stations (triangles) and the Port of Kumamoto. The star indicates the epicenter of the foreshock.



Photo 1: Slight damage to a quay wall at the Port of Kumamoto

(Nozu and Nagasaka, 2018a).

In this study, to investigate the applicability of the source models to the target region, those models were applied to simulate strong ground motions at strong motion observation stations surrounding the port, namely, KMM008, NGS012 and Shirakawa (Figure 1). In the simulation, multiple nonlinear effects (Nozu and Morikawa, 2003) were also considered. The applicability of the fault models was discussed based on comparison between the observed and simulated ground motions.

2. Simulation method

A brief overview of the corrected empirical Green's function method (the corrected EGF method) (Kowada et al. 1998; Nozu and Sugano 2008; Nozu et al. 2009) is

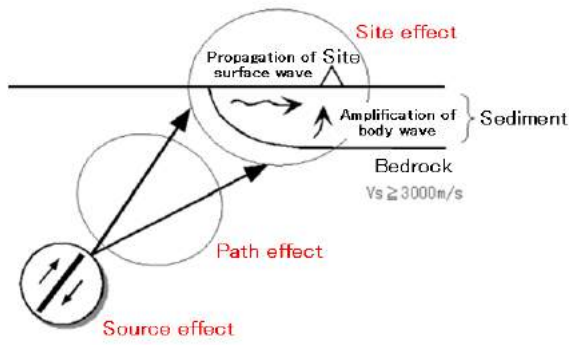


Figure 2: Source, path and site effects

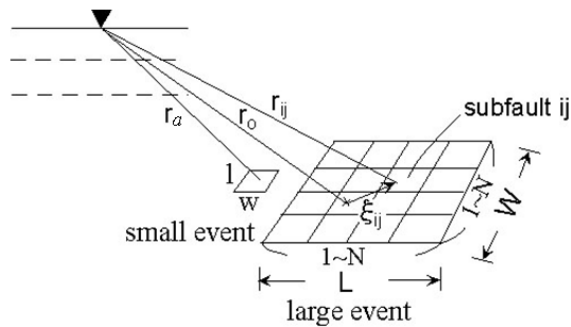


Figure 3: Superposition of Green's functions

given in the following:

The first step is to evaluate ground motions from a small event (Figure 3). The ground motion generated by a small event is referred to as the "Green's function." The Fourier amplitude of the Green's function is evaluated as a product of the source spectrum $|S(f)|$, the path effect $|P(f)|$ and the site amplification factor $|G(f)|$. The source spectrum is assumed to follow the ω^{-2} model (Aki, 1967). Geometrical spreading and non-elastic attenuation are considered for the path effect (Boore, 1983) as follows:

$$|P(f)| = (1/r) \exp(-\pi f r / Q \beta), \quad (1)$$

where r is the distance from the source to the site, β is the shear wave velocity, and Q stands for the Q value along the propagation path that is proportional to some power of frequency. Empirical site amplification factors are generally used in this method. Then, Fourier phase of an actual record of a small earthquake at the site of interest is used as the Fourier phase of the Green's function. Thus, we can obtain a frequency-domain Green's function which incorporates the effects of sediments both on the Fourier amplitude and Fourier phase as follows:

$$|S(f)| |P(f)| |G(f)| O_s(f) / |O_s(f)|_p, \quad (2)$$

where $O_s(f)$ is the Fourier transform of an actual record at the site of interest and $|O_s(f)|_p$ is its Parzen-windowed amplitude (a band width of 0.05 Hz was used in this application). If several records are available for the site, it is preferable to choose an event that has a similar incident angle and a similar back-azimuth to the target event. The Green's function in the time domain can be obtained by the inverse Fourier transform.

The second step is to superpose the Green's function to obtain strong ground motions from a large event (or a subevent of a large event) in the same way as the conventional EGF method (Irikura et al., 1997). When soil nonlinearity is considered, the time-domain Green's

function is corrected with the method proposed by Nozu and Morikawa (2003), as will be explained later.

In this particular application to the Kumamoto earthquake, the Q value estimated for the region ($Q=104 f^{0.63}$) (Kato 2001) was used. At K-NET and KiK-net stations (Figure 1), the empirical site amplification factors evaluated by Nozu and Nagao (2005) were used. The site amplification factor at Shirakawa (Figure 1) was newly evaluated in this study, which will be explained later. To evaluate the Fourier phase characteristics of the Green's functions, weak motion records were used. For each site, a small event that occurred close to the nearest asperity was selected whenever possible, and it was made sure that the Fourier phase characteristics resemble those of the main shock.

In this study, nonlinear soil response was considered using the simple method proposed by Nozu and Morikawa (2003). The method uses two parameters to consider soil nonlinearity; one representing the reduction of averaged shear wave velocity within the sediment (v_1) and the other representing the increase of averaged damping factor within the sediment (v_2). In the simulation, the nonlinear parameters were manually determined with the aim of reproducing the observed ground motions as accurately as possible. Among the nonlinear parameters, v_1 was basically determined by referring to the ratio of the peak frequencies of strong and weak motions at the same site, because the parameter v_1 represents the ratio of the shear wave velocities within the sediments between the linear and nonlinear cases, and thus v_1 represents the ratio of the resonant frequencies of the sediments between the linear and nonlinear cases. The parameter v_2 was determined so that the observed ground motions could be simulated as accurately as possible, with special reference to the duration of the later phases.

Other parameters used for the simulation were as follows: For the radiation coefficient, the averaged value of 0.63 was used. The parameter $PRTITN$ (Boore, 1983), which represents the partition of S-wave energy into two horizontal components, was determined so that the observed ground motions can be reproduced as accurately as possible. For the S-wave velocity and density in the source region, 3.5 km/s and 2.7×10^3 kg/m³ were used.

3. Foreshock

Figure 1 shows the location of the foreshock fault plane. Figure 4 shows the simplified source model for the foreshock (Nozu and Nagasaka, 2018a). The color contour in the background shows the peak slip velocity distribution for the foreshock estimated from the waveform inversion analysis (Nozu and Nagasaka, 2018a). The solid star indicates the JMA hypocenter, which was used as the rupture starting point in the inversion analysis. The rectangles numbered as 1 and 2 are the asperities that constitute the simplified source model. Asperity 1 is located near the hypocenter and Asperity 2 is located 3 km northeast of the hypocenter on the shallower part of the fault. These asperities were aligned on the fault plane used for the inversion analysis with the strike angle of 212 degrees and the dip angle of 89 degrees. The open star indicates the rupture starting point for Asperity 2, from which rupture propagates radially. The parameters of the source model are listed in Table 1.

At K-NET stations (KMM008 and NGS012), the empirical site amplification factors evaluated by Nozu

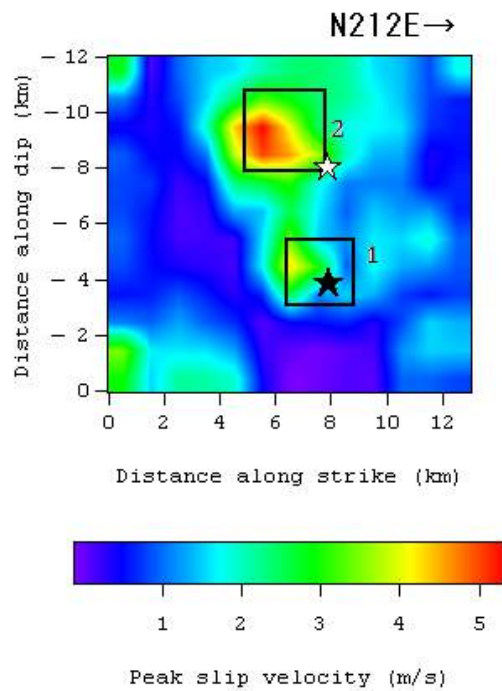


Figure 4: Simplified source model for the foreshock (Nozu and Nagasaka, 2018a)

Table 1: Parameters of the simplified source model for the foreshock (Nozu and Nagasaka, 2018a)

	Asperity 1	Asperity 2
Local rupture starting point longitude (deg.)	130.808	130.809
Local rupture starting point latitude (deg.)	32.742	32.742
Local rupture starting point depth (km)	11.0	7.0
Length(km)×Width(km)	2.5×2.5	3.0×3.0
M_0 (Nm)	0.15E+18	0.13E+18
Relative rupture starting time (s)	0.0	2.7
Rupture velocity (km/s)	2.8	2.8
Rise time (s)	0.33	0.40
Number of discretization	5×5×5	5×5×5

Table 2: Nonlinear parameters and $PRTITN$ values used for the foreshock

	v_1	v_2	$PRTITN$ for EW	$PRTITN$ for NS
KMM008	0.90	0.010	0.63	0.77
NGS012	–	–	0.69	0.72
Shirakawa	0.90	0.010	0.85	0.53

and Nagao (2005) were used. The site amplification factor at Shirakawa (Figure 1) was newly evaluated as follows. At Shirakawa, ground motions were observed at several different depths. In this study, ground motions observed at GL-8m was used, which were the shallowest records except for the records at the top of the river dike. We could find two earthquakes that were recorded at Shirakawa and KMM008 simultaneously, namely, the April 16, 13:15, M3.9 aftershock and the April 18, 20:41, M5.8 aftershock. For these events,

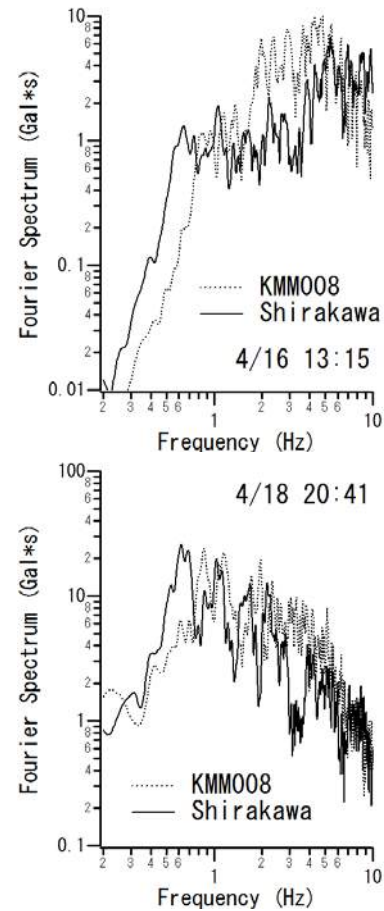


Figure 5: Fourier spectra for observed weak motion records at Shirakawa and KMM008 for the April 16, 13:15, M3.9 aftershock (top) and the April 18, 20:41, M5.8 aftershock (bottom). The spectra are the composition of two horizontal components, processed through a Parzen window with a band width of 0.05 Hz.

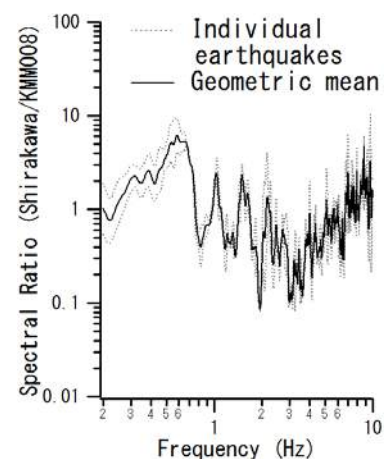


Figure 6: Fourier spectral ratios between Shirakawa and KMM008 for the April 16, 13:15, M3.9 and the April 18, 20:41, M5.8 aftershocks (dotted lines) and their geometrical mean.

Fourier spectral ratios between two stations were calculated as shown in Figure 5 and Figure 6. Then the site amplification factor at KMM008 (Nozu and Nagao,

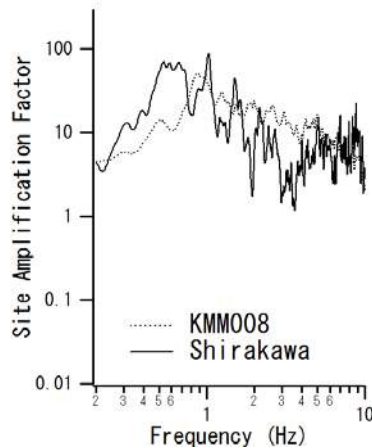


Figure 7: Site amplification factors at KMM008 and Shirakawa

2005) was multiplied by the geometric mean of the spectral ratios to obtain the site amplification factor at Shirakawa as shown in Figure 7.

To evaluate the Fourier phase characteristics of the Green's functions, weak motion records for the April 15, 0:50, M4.2 aftershock were used. The epicenter of the aftershock is plotted in Figure 1.

The parameters to consider soil nonlinearity (v_1 and v_2) and the parameter $PRTTN$ were determined so that the observed ground motions could be simulated as accurately as possible, as shown in Table 2.

Observed and synthetic velocity waveforms (0.2-2 Hz) for the foreshock at strong motions stations surrounding the port are compared in Figure 8. Main features of the observed ground motions including the direct S phase and the later phases were successfully reproduced in the simulation, although at Shirakawa the amplitude of the later phases were overestimated for the EW component and underestimated for the NS component.

Examples of parametric studies to determine the nonlinear parameters for KMM008 are shown in Figure 9 and Figure 10. In Figure 9, v_2 (increase of damping

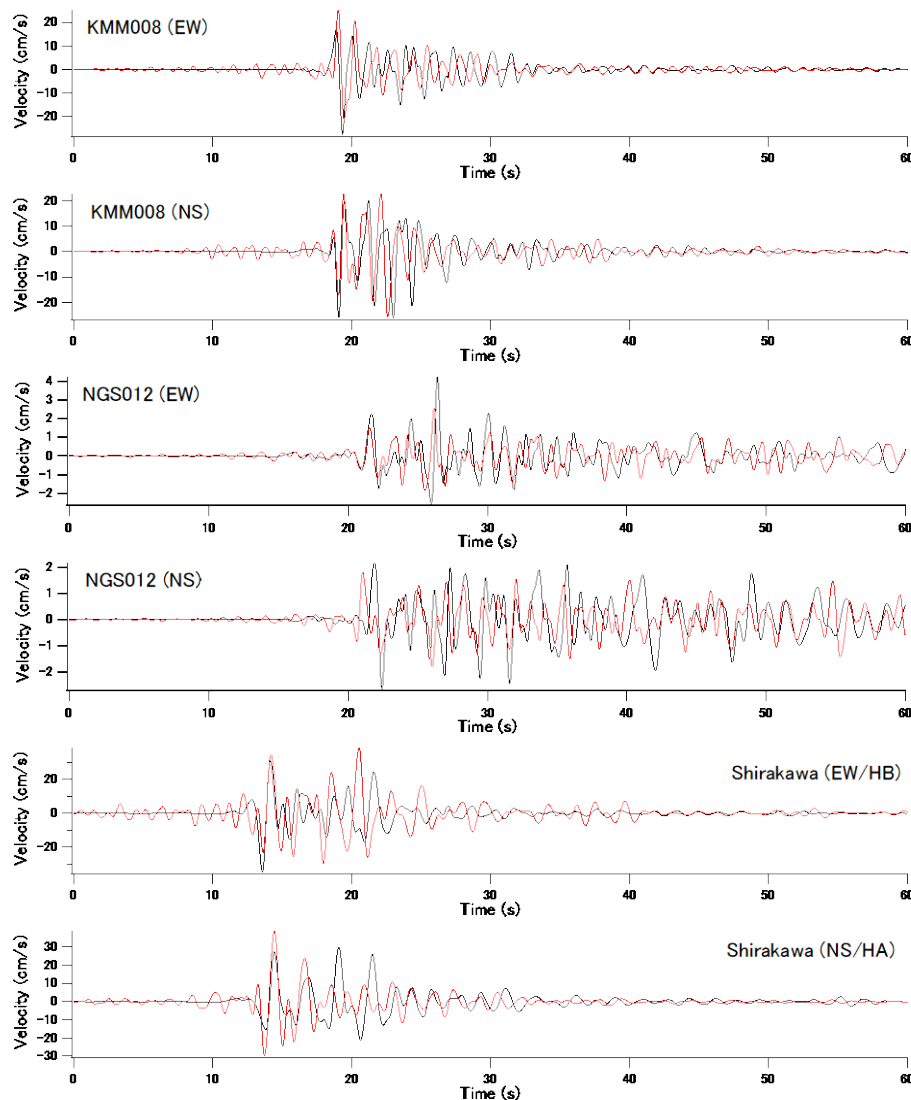


Figure 8: Observed (black) and synthetic (red) velocity waveforms (0.2-2 Hz) for the foreshock at strong motions stations surrounding the Port of Kumamoto

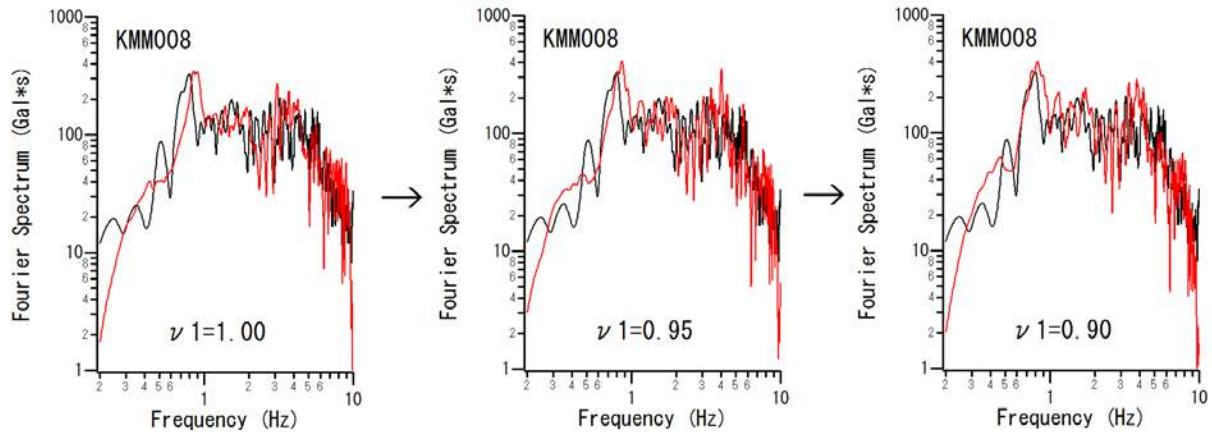


Figure 9: Parametric study to determine the nonlinear parameter ν_1 . With the decrease of ν_1 , the peak frequency of the synthetic spectrum (red) decreases and approaches to the peak frequency of the observed spectrum (black).

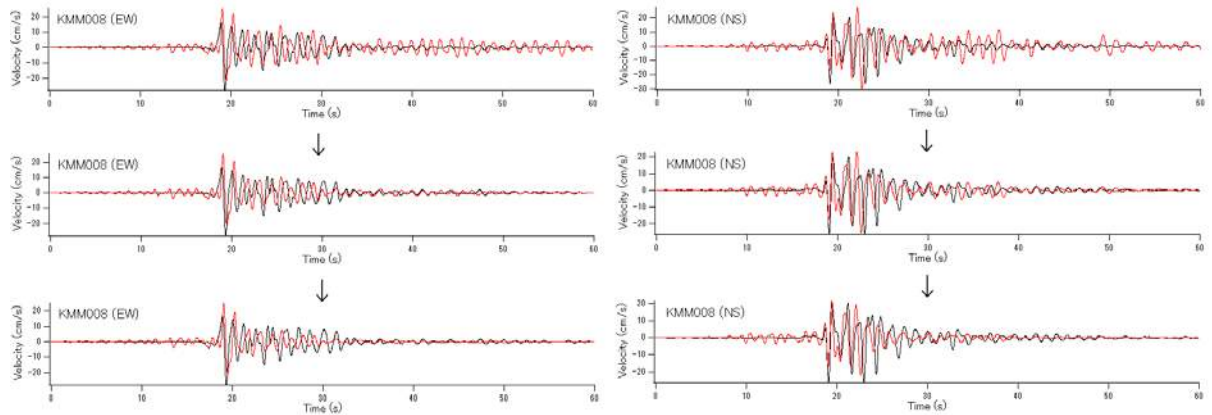


Figure 10: Parametric study to determine the nonlinear parameter ν_2 . In the simulation, ν_1 was fixed to 0.90 and ν_2 was varied from 0.00 (top) to 0.02 (bottom). With the increase of ν_2 , the duration of the velocity waveforms (0.2-2 Hz) (red) decreases. With $\nu_2=0.01$ (middle), the duration is close to that of the observed velocity waveforms (black).

factor) was fixed to zero and ν_1 (reduction of shear wave velocity) was varied from 1.00 to 0.90 in the calculation of Fourier spectra at KMM008. With the decrease of ν_1 , the peak frequency of the synthetic spectrum decreases and approaches to the peak frequency of the observed spectrum. Based on the results, $\nu_1=0.90$ was selected for KMM008. Then, in Figure 10, ν_1 was fixed and ν_2 was varied from 0.00 to 0.02 in the calculation of velocity waveforms at KMM008. With the increase of ν_2 , the duration of the later phases decreases. By comparing the duration of the synthetic and observed signals, $\nu_2=0.01$ was selected for KMM008.

As a whole, the preceding analyses reveals that the simplified source model for the foreshock is applicable to the target region; the source model can well explain strong ground motions recorded at the target region provided that the multiple nonlinear effects are appropriately considered.

4. Main shock

Figure 11 shows the location of the main shock fault plane. Figure 12 shows the simplified source model for the main shock (Nozu and Nagasaka, 2018a). The color contour in the background shows the peak slip velocity distribution for the main shock estimated from the waveform inversion analysis (Nozu and Nagasaka, 2017). The solid star indicates the JMA hypocenter, which was used as the rupture starting point in the inversion

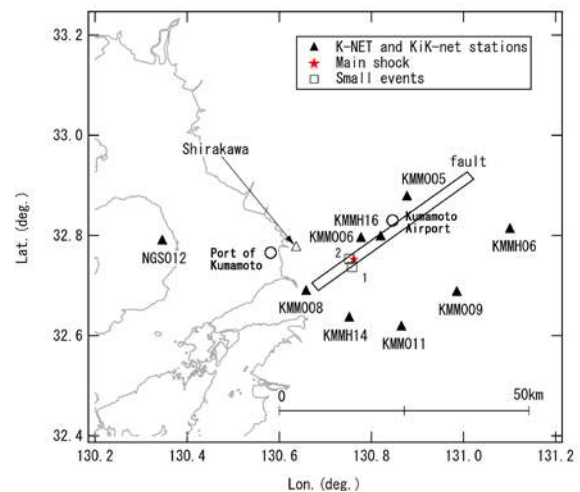


Figure 11: Locations of the main shock fault plane, the small events used for the analysis (numbered open rectangles), the strong motion stations (triangles) and the Port of Kumamoto. The star indicates the epicenter of the main shock.

analysis. The rectangles numbered as 1, 2 and 3 are the asperities that constitute the simplified source model. Asperity 1 and 2 are located at approximately 5 km

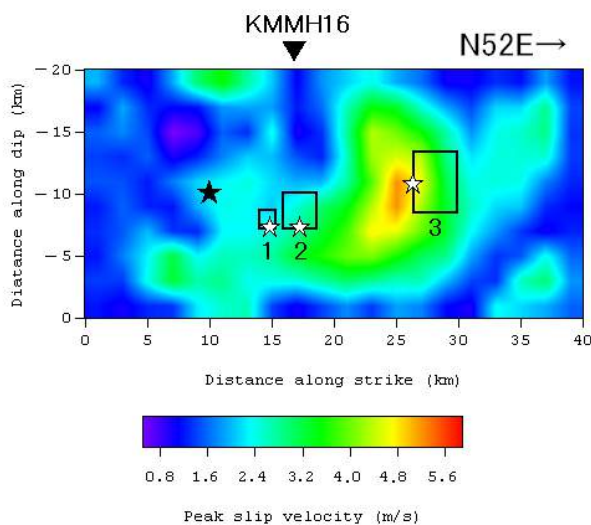


Figure 12: Symplified source model for the main shock (Nozu and Nagasaka, 2018a)

Table 3: Parameters of the simplified source model for the main shock (Nozu and Nagasaka, 2018a)

	Asperity 1	Asperity 2	Asperity 3
Local rupture starting point longitude (deg.)	130.802	130.823	130.898
Local rupture starting point latitude (deg.)	32.783	32.797	32.841
Local rupture starting point depth (km)	15.0	15.0	11.0
Length(km)×Width(km)	1.5×1.5	3.0×3.0	4.0×5.0
M_0 (Nm)	$0.10E+18$	$0.25E+18$	$2.5E+18$
Relative rupture starting time (s)	0.0	0.9	4.1
Rupture velocity (km/s)	2.8	2.8	2.8
Rise time (s)	0.13	0.27	1.00
Number of discretization	5×5×5	5×5×5	10×10×10

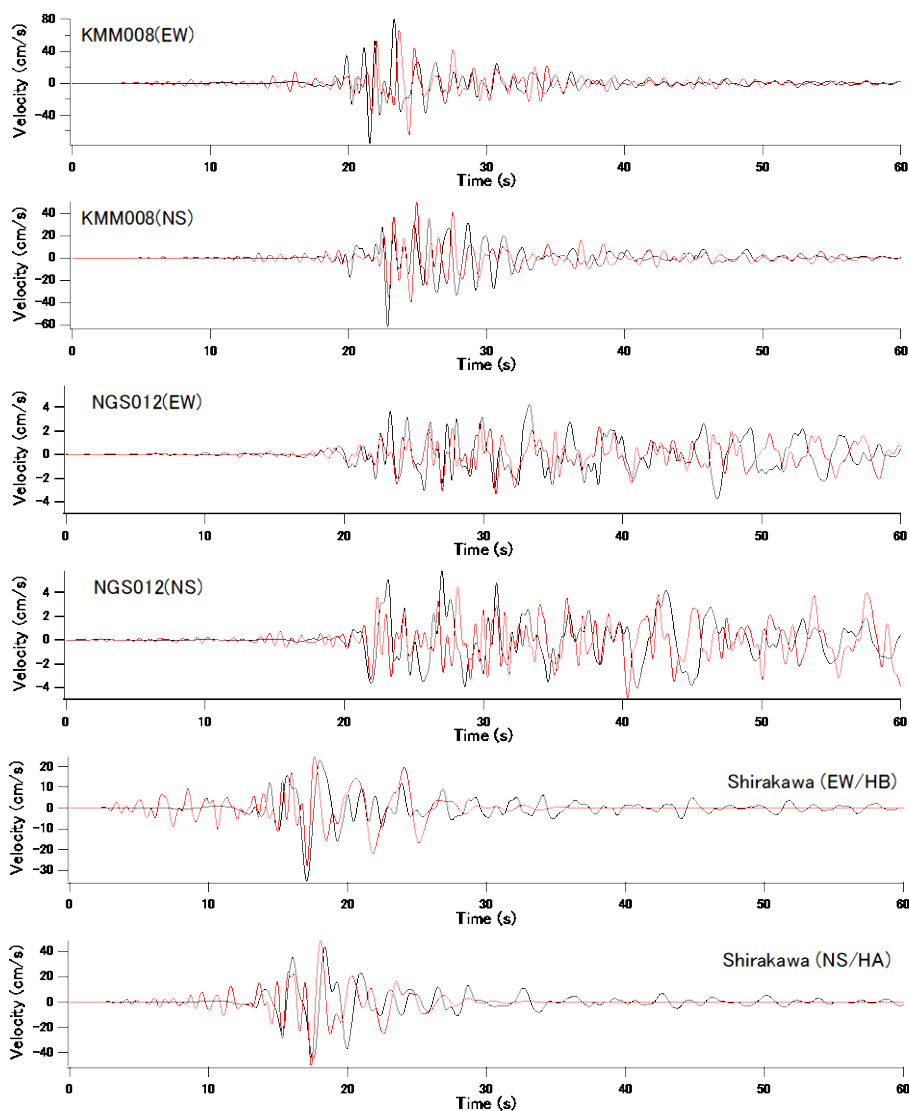


Figure 13: Observed (black) and synthetic (red) velocity waveforms (0.2-2 Hz) for the main shock at strong motions stations surrounding the Port of Kumamoto

northeast of the hypocenter. Asperity 3 is located at approximately 15 km northeast of the hypocenter. These asperities are located on the fault plane for the inversion analysis with the strike angle of 232 degrees and the dip angle of 84 degrees (Nozu and Nagasaka, 2017). The open stars indicate the rupture starting point for each asperity, from which rupture propagates radially. Asperity 3 corresponds to the primary asperity in the inversion result. The parameters of the source model are listed in Table 3.

The same site amplification factors as the main shock were used for KMM008, NGS012 and Shirakawa. To evaluate the Fourier phase characteristics of the Green's functions, weak motion records for the April 15, 0:50, M4.2 aftershock were used at KMM008 and Shirakawa. At NGS012, weak motion records for the April 16, 4:51, M4.3 aftershock were used. The epicenters of the aftershocks are plotted in Figure 11.

The parameters to consider soil nonlinearity (v_1 and v_2) and the parameter $PRTITN$ were determined so that the observed ground motions could be simulated as accurately as possible, as shown in Table 4, as were done for the foreshock.

Observed and synthetic velocity waveforms (0.2-2 Hz) for the main shock at strong motions stations surrounding the port are compared in Figure 13. Main features of the observed ground motions including the direct S phase and the later phases were successfully reproduced in the simulation, although at Shirakawa the amplitude of the later phases were slightly overestimated for the EW component and slightly underestimated for the NS component.

Table 4: Nonlinear parameters and $PRTITN$ values used for the main shock

	v_1	v_2	$PRTITN$ for EW	$PRTITN$ for NS
KMM008	0.92	0.005	0.81	0.59
NGS012	–	–	0.53	0.85
Shirakawa	0.86	0.010	0.85	0.53

5. Conclusions

The 2016 Kumamoto earthquake sequence caused slight by not-negligible damage to facilities at the Port of Kumamoto. To estimate strong ground motions at the port, the applicability of the fault models for the foreshock and main shock (Nozu and Nagasaka, 2018a) was studied. To validate the models, they were applied to strong-motion stations surrounding the port. It was found that the source models can well explain strong ground motions recorded at those stations provided that the multiple nonlinear effects are appropriately considered. The source models were subsequently used to estimate strong ground motions at the Port of Kumamoto by Yamada et al. (2018).

Acknowledgement

I would like to thank National Research Institute for Earth Science and Disaster Resilience, Kyushu Regional Development Bureau, and National Institute for Land and Infrastructure Management for providing strong motion data.

References

1. A. Nozu and Y. Nagasaka, (2018a). Rupture process of the foreshock and the main shock of the 2016 Kumamoto earthquake and simplified source models to explain damaging ground motions. Report of the Port

- and Airport Research Institute, Vol.57, No.1, 3-35 (in Japanese with English abstract).
2. A. Nozu and Y. Nagasaka, (2018b). Borehole vertical arrays in Japanese ports. The 16th European Conference on Earthquake Engineering, 18-21 June 2018, Thessaloniki.
3. A. Kowada, M. Tai, Y. Iwasaki and K. Irikura, (1998). Evaluation of horizontal and vertical strong ground motions using empirical site-specific amplification and phase characteristics. J. Struct. Constr. Eng., AIJ, No.514: 97-104 (in Japanese with English abstract).
4. A. Nozu and T. Sugano, (2008). Simulation of strong ground motions based on site-specific amplification and phase characteristics – accounting for causality and multiple nonlinear effects –. Technical Note of the Port and Airport Research Institute, No.1173 (in Japanese with English abstract).
5. A. Nozu, T. Nagao and M. Yamada, (2009). Simulation of strong ground motions using empirical site amplification and phase characteristics – modification to incorporate causality –. Journal of JSCE, Ser. A, 65: 808-813 (in Japanese with English abstract).
6. A. Nozu and H. Morikawa, (2003). An empirical Green's function method considering multiple nonlinear effects, Zisin 55: 361–374 (in Japanese with English abstract).
7. K. Aki, (1967). Scaling law of seismic spectrum. J. Geophys. Res. 72: 1217-1231.
8. D.M., Boore, (1983). Stochastic simulation of high-frequency ground motions based on seismological models of the radiated spectra. Bull. Seism. Soc. Am. 73: 1865-1894.
9. K. Irikura, T. Kagawa and H. Sekiguchi, (1997). Revision of the empirical Green's function method by Irikura (1986). SSJ Fall Meeting, B25 (in Japanese).
10. K. Kato, (2001). Evaluation of source, path and site amplification factors from the K-NET strong motion records of the 1997 Kagoshima-ken-Hokuseibu earthquakes. J. Struct. Constr. Eng., AIJ, No.543: 61-68 (in Japanese with English abstract).
11. A. Nozu and T. Nagao, (2005). Site amplification factors for strong-motion sites in Japan based on spectral inversion technique. Technical Note of the Port and Airport Research Institute, No.1102 (in Japanese with English abstract).
12. A. Nozu and Y. Nagasaka, (2017). Rupture process of the main shock of the 2016 Kumamoto earthquake with special reference to damaging ground motions: waveform inversion with empirical Green's functions. Earth Planets and Space 69: 22, DOI 10.1186/s40623-017-0609-3.
13. M. Yamada, A. Sone, N. Kuwabara, K. Ebisu, S. Yamamoto, M. Sato and T. Kidou, (2018). Accurate estimation of strong ground motions and simulation of structural damage at Kumamoto Port during the 2016 Kumamoto earthquake. The 16th European Conference on Earthquake Engineering, 18-21 June 2018, Thessaloniki.

A new approach for estimating seismic damage of buried water supply pipelines

H. Sakai^{1,*†} , N. Pulido², K. Hasegawa³ and Y. Kuwata⁴

¹*Hosei University, 2-33, Ichigayatamachi, Shinjuku-ku, Tokyo 162-0843, Japan*

²*National Research Institute for Earth Science and Disaster Resilience, 3-1, Tennodai, Tsukuba, Ibaraki 305-0006, Japan*

³*OYO International Corporation, 1-1-17, Koishikawa, Bunkyo-ku, Tokyo 112-0002, Japan*

⁴*Kobe University, 1, Rokkodai-cho, Nada-ku, Kobe 657-8501, Japan*

SUMMARY

Conventional damage prediction methods for lifeline structures are primarily based on peak ground motion measurements. However, line structures such as lifelines suffer damage that is mainly induced by the strain of the ground and therefore are likely to be vulnerable to sharp spatial changes in the ground motion. In this study, we propose a measure for evaluating the damage incurred by underground water supply pipelines based on the spatial gradient of the peak ground velocity (PGV), in an attempt to quantify the effects of the geospatial variabilities in the ground motion on pipeline damage. We investigated the spatial distribution of the damage caused to water pipelines during the Niigata-ken Chuetsu earthquake on October 10, 2004 (Japan Meteorological Agency magnitude (M_{JMA}) of 6.8) and the Kobe earthquake on January 17, 1995 (M_{JMA} 7.3) and compared the surveyed damage with the PGV distribution as well as with the gradients of the PGV calculated around the damage areas. For the Kobe earthquake, we used the PGV distribution obtained by the strong-motion simulation performed by Matsushima and Kawase [1]. In case of the Chuetsu earthquake, we estimated the ground motion using a broadband-frequency-based strong-ground-motion simulation method based on a multiasperity source model. In both cases, we calculated the gradients of the PGV along the geographical coordinates, with the amplitude of the PGV gradient vector being employed as the damage estimator. Our results show that the distribution of damage to underground water supply pipelines exhibits a greater correlation with the gradients of the PGV than with the PGV itself. Thus, the gradient of the PGV is a useful index for preparing initial-screening hazard maps of underground facilities. Copyright © 2017 John Wiley & Sons, Ltd.

Received 20 February 2016; Revised 10 December 2016; Accepted 11 December 2016

KEY WORDS: underground lifeline; seismic assessment; spatial gradient of peak ground velocity

1. INTRODUCTION

Lifeline facilities such as roads and gas and water pipelines invariably suffer severe damage during large earthquakes. The damage to roads isolates the affected regions, while the failure of gas and water supply pipelines (WSPs) further distresses the earthquake victims. The Niigata-ken Chuetsu earthquake on October 23, 2004 (Japan Meteorological Agency magnitude (M_{JMA}) of 6.8; hereafter referred to as the Chuetsu earthquake) was the most damaging earthquake in Japan since the 1995 Kobe earthquake. The earthquake resulted in ground accelerations higher than 1.7 g and velocities of up to 130 cm/s. This extreme ground motion caused extensive damage to lifeline facilities such as roads as well as the WSP system in the Niigata prefecture. During the Kobe earthquake, similar ground motion (peak ground velocity (PGV) \approx 130 cm/s) inflicted severe damage to roads and various lifeline

*Correspondence to: Hisakazu Sakai, Department of Civil and Environmental Engineering, Hosei University, Japan.

†E-mail: hisakai@hosei.ac.jp

facilities ([2–6]). Thus, these earthquakes highlighted the importance of developing appropriate seismic assessment and damage prediction methods for lifeline facilities.

Conventional damage prediction methods for lifeline facilities are typically based on some type of a ground motion index. Jeon and O'Rourke [7] studied the relationship between pipeline damage and the peak ground acceleration (PGA), the PGV, and the spectral intensity corresponding to the Northridge earthquake that occurred on January 17, 1994, and found a strong correlation between the pipeline repair rate (for earthquake-induced pipeline damage), the pipe material used, and the PGV. Further, the American Lifelines Alliance [8] has reported two simple methods for assessing transient ground movement: one is a chart method for water pipelines based on parameters such as the PGA, the PGV, and the permanent ground displacement and does not involve any mathematical calculations, while the another is an equivalent static method based on the ground strain, which is calculated using the PGV and the propagation speed of the seismic wave. Most self-governing bodies, lifeline facility companies, and government agencies in Japan use the PGA, PGV, seismic intensity, and degree of liquefaction or intensity as measured by instruments to predict the damage to lifeline facilities. For instance, G&E Engineering Systems Inc. [9] has summarized the various damage assessment methods used for water pipelines according to their intended function and the pipe material used, based on the transient ground movement (i.e., the PGA and PGV) and the permanent ground displacement induced by landslides and liquefaction. The Tokyo Prefecture Office and the Japan Water Works Association have adopted methods based on the PGV for designing seismically sound WSPs. A large number of Japanese self-governing bodies use modified methods based on a technique that uses the PGA values [10] obtained from damage assessment studies performed during the 1995 Kobe earthquake for predicting the seismic damage caused to water supply and sewer pipelines. Gas supply companies evaluate the damage that could be caused to gas pipeline networks by future earthquakes based on the PGV and spectral intensity values. A study from India has reported a seismic design method for buried pipelines based on the axial ground strain calculated using the PGV for transient ground movements [11]. Kuwata et al. [12] determined the trend in the pipe repair rate for high-level ground motion through a numerical analysis while using the PGV. Using the PGV and the other above-mentioned measures has a number of advantages, in that they allow for real-time observations during earthquakes and can be used for quick damage predictions. However, a pipeline that is underground is more likely to be affected by strong local variations in the ground motion instead of the absolute values of the peak ground motion. To address this problem, O'Rourke et al. [13] showed that the ground strain can be calculated using the PGV, the apparent wave velocity, and the predominant period of the seismic wave. The Eurocode [14] also has a simple method for calculating the ground strain caused by the transient ground motion based on the Newmark method while using a sinusoidal wave and the apparent wave velocity [15]. However, it is difficult to estimate the apparent wave velocities or the predominant period of the seismic waves for future earthquakes. Paolucci and Smerzini [16] introduced a method for calculating the in-plane strain tensor at the ground surface based on previous observations made using dense seismic arrays. This method might be useful for evaluating the strain distribution for well-recorded previous earthquakes but might not be appropriate for producing hazard maps for lifeline facilities in the case of future earthquakes. As mentioned above, the ground strain is considered a useful index for predicting the damage that will be incurred by underground pipelines. In fact, the major failure mode during the Kobe and Chuetsu earthquakes was reported to be cast-iron pipes falling off at the joints [17, 18]. This type of failure is mainly caused by axial-ground-strain-induced tensile forces. (A bending failure is induced by a shear strain.) From this viewpoint, the change in the peak ground displacement (PGD), namely, the PGD gradient, would be a more suitable index for predicting damage to WSPs, because this index has the same unit as that of strain. However, it is difficult to calculate the PGD due to transient ground movements. This is because the amplification factor of the displacement is usually not known with as much accuracy as those of the PGA and PGV. In this paper, we propose a method based on the PGV gradient for evaluating the seismic damage of WSPs. In the rest of the document, we will present an outline of the method and its application in estimating the damage caused to WSPs by the 2004 Chuetsu and 1995 Kobe earthquakes. We will show that the PGV gradient is a better predictor of damage to WSP systems than is the PGV, which is the index used currently.

2. STRONG-MOTION SIMULATION AND PGV GRADIENT

2.1. Strong-motion simulation in Chuetsu region

In order to be able to compare the damage caused to lifeline facilities by the Chuetsu earthquake and the various corresponding ground motion indices, it is necessary to measure the ground motions for a spacing finer than those used for the strong ground motions observed by K-NET and KiK-net (nationwide strong-motion measuring networks operated by the National Research Institute for Earth Science and Disaster Prevention (NIED), Japan, and consisting of 1800 stations). This is also true those for the intensities recorded using JMA instruments (interstation spacing of ~10 km). For this purpose, we calculated the seismic-bedrock broadband strong ground motions for every 250 m within the near-fault region and incorporated the site amplifications in the simulated PGV values using a 7.5-arcsec (250 m) Vs30 (time-averaged S-wave velocity for the shallower 30 m of soil) map of the Chuetsu region (Wakamatsu et al. 2005 [19]). The seismic-bedrock ground motions were determined using a hybrid method that combined wave propagation within a one-dimensional crustal model at low frequencies and a semistochastic modeling approach at high frequencies by using a multiasperity source model. The source model parameters such as the stress drop of the asperities were obtained by optimizing the fit between the simulated and observed near-fault strong ground motions. Details of the strong-motion simulation method as well as the simulation results for the Chuetsu earthquake are described by Pulido and Kubo [20] and Pulido and Matsuoka [21]. To incorporate the site amplifications into the bedrock ground motions, we used the following expression relating the Vs30 (in m/s) to the PGV amplification factors with respect to a seismic bedrock site ($V_s = 2600$ m/s) (Pulido and Matsuoka [21]):

$$\log PGV_{amp} = 1.83 - 0.53 \log V_{s30}. \quad (1)$$

This equation was obtained by combining the frequency-dependent site amplifications observed at 31 strong-motion sites within the Chuetsu region (Pulido and Matsuoka 2006 [21]) as well as a 250-m-grid-cell Vs30 map of the Chuetsu region (Wakamatsu et. al. 2005 [19]). A Vs30 map at this fine a scale is based on a detailed geomorphological map of the region in question as well as data from dense Vs30 measurements (Wakamatsu et. al. 2006 [22]).

The simulated PGV values exhibited a complex pattern around the hypocenter (Figure 1, color scale). It can be seen that the ground motion was relatively small just above the hypocenter as compared to that in the areas adjacent to the hypocenter. This is because the radiation pattern distribution of a reverse-type earthquake such as the Chuetsu earthquake was used. The values of the PGV in the western and southern regions of Ojiya city were large and so were those for the entire towns of Kawaguchi and Yamakoshimura, where the simulated PGV was higher than 80 cm/s for large areas. Figure 1 also shows the observed instrumental intensity distribution (black contour lines), obtained from a dense network of intensity meters in the Chuetsu region, which is a part of a nationwide network managed by the JMA (~3600 instruments nationwide). It can be seen that there is good agreement between the simulated PGV values and the observed instrumental intensity distributions. The inset of Figure 1 shows a comparison of the simulated PGV values and those observed at the 31 K-NET and KiK-net strong-motion stations within the Chuetsu region. It can be seen that these values are also in good agreement.

2.2. Estimating strong motion in Kobe city

We also selected the 1995 Kobe earthquake as a case study to investigate the relationship between the extent of pipeline damage and the PGV gradients within Kobe city, which is in the Chuetsu region and has a significantly higher population than that of Nagaoka city. The residential area in Kobe extends along a narrow region between the slopes of the Rokko mountains to the north and the coast to the south. During the Kobe earthquake, the damage done to residential buildings was concentrated along a narrow region subparallel to the coast (known as the ‘damage belt’), where the seismic intensity was 7 as per the JMA scale (see Figure 2 [23]).

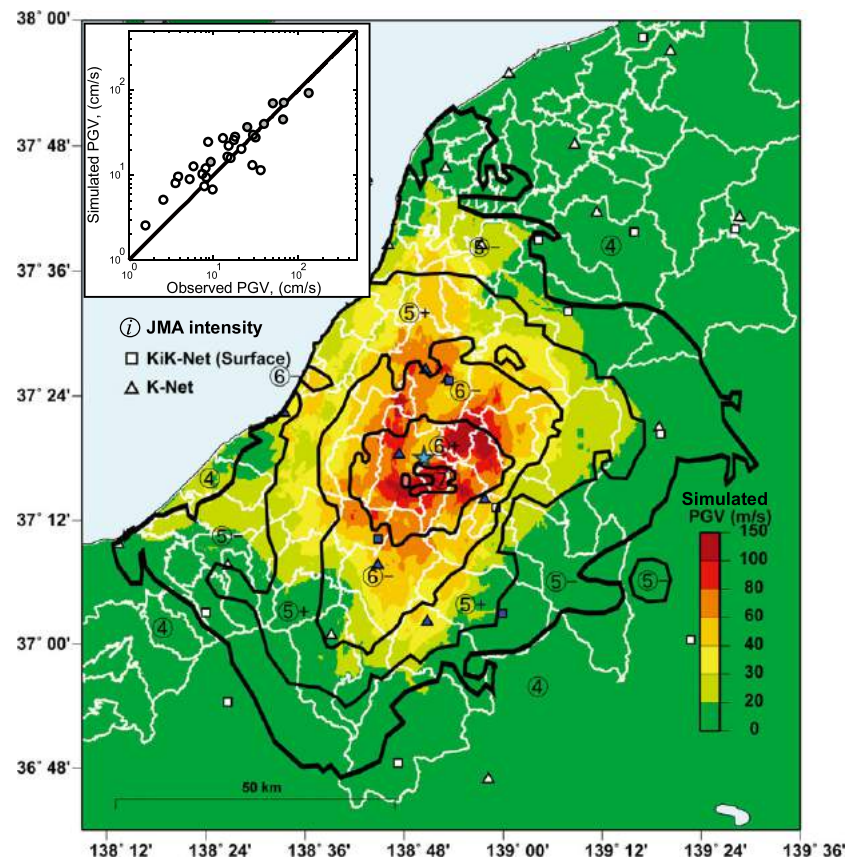


Figure 1. Simulated PGV values for the 2004 Chuetsu earthquake (color scale). The black contour lines as well as the numbered open circles represent the intensities observed using JMA instruments during the earthquake. Inset shows a comparison of the simulated PGV values and those observed at the KiK-net and K-Net sites within the Chuetsu region. The triangles and squares depict the K-NET and KiK-net strong-motion stations within the Chuetsu region, while the filled symbols represent the stations used for estimating the asperity parameters. [Colour figure can be viewed at wileyonlinelibrary.com]

We used the PGV distribution obtained from the strong-motion simulation by Matsushima and Kawase [1]. They developed a source model of the Kobe earthquake using a grid search method while employing a three-dimensional velocity structure of the basin and used it to predict strong motion near the hypocenter as well as the strong-motion belt in Kobe City. The source model was obtained by optimizing the fit of the simulated data to the strong-motion data recorded at the JMA Kobe, Kobe University, Motoyama-Daiichi elementary school, and JR Takatori stations. The JMA Kobe station was located on a hill and is not significantly affected by subsurface ground amplifications. The data recorded at the JR Takatori station were characterized by a significant pulse. The strong motion was calculated using a three-dimensional finite difference method while using a grid interval of 0.04 km. The source-time functions were assumed to be a simple triangular pulse with a duration of 0.06 s. The three-dimensional structure of the velocity of the S-wave above the bedrock was calibrated using the records of the aftershocks at the target observation stations. The rupture model consisted of five rectangular strong-motion-generation areas. The ground motion simulated by Matsushima and Kawase [1] was estimated for a velocity model in the upper layer and corresponded to an S-wave velocity of 350 km/s, which, given the grid size used, implied that the ground motion would be numerically accurate only up to a frequency of ~2 Hz. Further, the significant damage experienced in Kobe was attributed to ground motion with periods of approximately 1 s, as determined using a deeper underground velocity model [1]. We calculated the PGV at the ground surface for a mesh with a size of 250 m by multiplying the simulated PGV values reported by Matsushima and Kawase [1] by an amplification factor corresponding to an

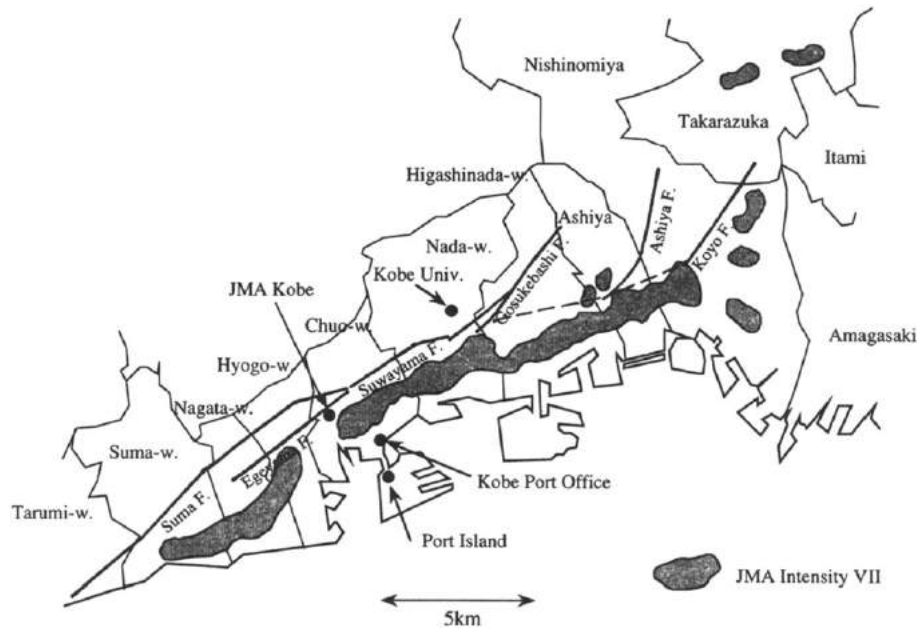


Figure 2. Map of Kobe-Osaka region annotated with major faults and geographic reference points, including the inferred rupture during the 1995 earthquake as well as the damage belt. [23]

engineering bedrock, with V_s being 400 m/s (the calculation is described in Appendix 1). The amplification factor used, PGV_{amp} , is a function of the average S-wave velocity from the surface to a depth of 30 m, V_{S30} (Fujimoto and Midorikawa [24]):

$$\log PGV_{amp} = 2.367 - 0.852 \log V_{S30}. \quad (2)$$

In this study, we used the V_{S30} data obtained from the Earthquake Hazard Information Station (J-SHIS [25]), which is available for a grid space of 250 m for all regions in Japan. We must note that Eq. (2) is used for calculating the PGV amplification factor of all regions in Japan with respect to the engineering bedrock ($V_s=400$ m/s); in contrast, Eq. (1) was proposed for the Chuetsu region and is with respect to the seismic bedrock ($V_s=2600$ m/s). Figure 3 shows the calculated PGV at the ground surface. We can observe the damage belt caused by the so-called ‘basin edge effect’.

2.3. PGV gradient

In order to estimate the differential ground motions that could be a potential source of damage to lifeline facilities during an earthquake, we calculated the gradients of the PGV along the

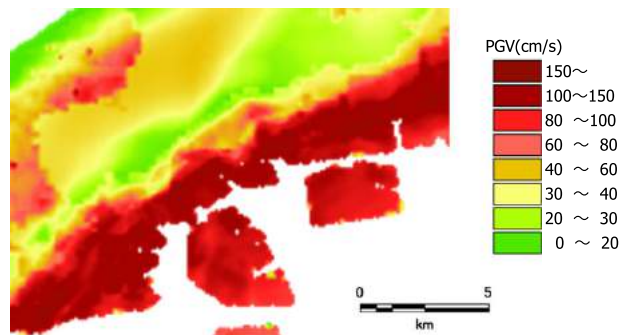


Figure 3. PGV distribution on ground surface. [Colour figure can be viewed at wileyonlinelibrary.com]

geographical coordinates (\vec{G}) based on the simulated PGV values for a dense and uniform grid mesh as follows:

$$\vec{G} = \frac{\partial PGV_{xy}}{\partial x} \vec{i} + \frac{\partial PGV_{xy}}{\partial y} \vec{j} \quad (3)$$

where PGV_{xy} is the peak ground velocity in the x, y grid, and \vec{i} and \vec{j} are the unit vectors along the east and north directions. The amplitude of vector \vec{G} was used as an indicator of pipeline damage. Intuitively, PGV gradients would be better predictors of pipeline damage than PGV, because such structures are buried underground and are thus more likely to be affected by out-of-phase motions and the associated axial or shear strain of the ground along the line.

A brief description of the numerical method used to calculate the gradients as well as the effect of the grid size is given in the appendix 2.

3. RELATIONSHIP BETWEEN STRONG MOTION AND DAMAGE TO WATER SUPPLY PIPELINES IN CHUETSU REGION

3.1. Damage to water supply pipelines

A survey of the damage sustained by WSPs during the Chuetsu earthquake revealed that the Nagaoka city water system suffered damage at 329 locations, while that of Ojiya city suffered damage at 95 locations. Figure 4 shows the WSP damage points as well as the liquefaction and landslide areas corresponding to the Chuetsu earthquake on a geomorphologic map of Nagaoka and Ojiya cities [26]. It can be seen from the figure that the WSP damage points can be separated into five distinct groups. The first group, labeled as A in Figure 4, is located in a geomorphologically complex region

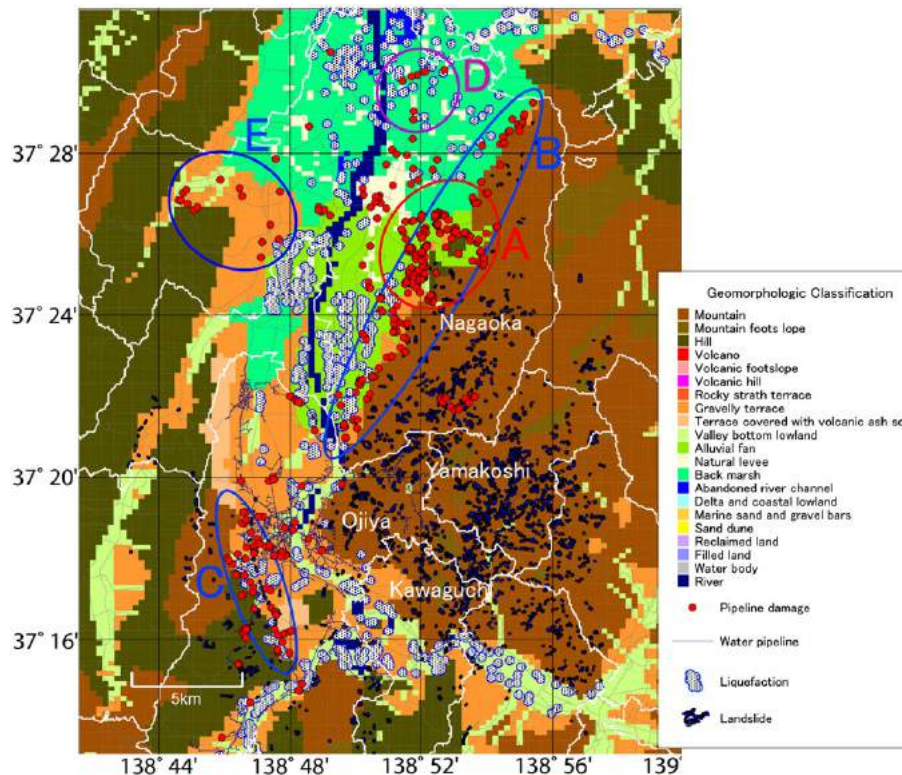


Figure 4. Distribution of WSP damage points in Ojiya and Nagaoka cities. [Colour figure can be viewed at wileyonlinelibrary.com]

that consists of a mountainous area to the east of Nagaoka as well as a region consisting of gravelly terraces, hills, alluvial fans, valley bottom lowlands, and back marshes in the Yamadori and Suyoshi regions. The second group, labeled B in Figure 4, is located along the boundary between two dissimilar geomorphological units, namely the mountainous area east of Nagaoka city and a region of alluvial fans and gravelly terraces to the west of the city. This boundary lies in a zone west of the surface projection of the causative fault of the Chuetsu earthquake. The third area, labeled C in Figure 4, lies in a gravelly terrace region in Ojiya city, where widespread liquefaction was observed. Some degree of WSP damage also occurred at the boundary between the mountainous region and the gravelly terrace west of Ojiya, where numerous landslides were observed. The fourth zone, labeled D in Figure 4, is located to the east of the Nagaoka city basin, where widespread liquefaction was observed as well. The last zone, labeled E in Figure 4, is located to the west of Nagaoka city. The WSP damage incurred in this zone occurred at the boundaries between the different geomorphologic regions such as zone B. In addition, several areas in the gravelly terrace also experienced damage. These areas are narrow strips of land sandwiched between paddy fields and forests. Therefore, it can be assumed that the groundwater level in this gravelly terrace is high.

3.2. Relationship between PGV and damage to water supply pipelines

Figure 5 shows the points where the WSPs were damaged during the Chuetsu earthquake overlapping with the simulated PGV values. It can be seen from the figure that the WSP damage points are located along a narrow region with a width of 5 km and oriented along the NNE–SSW direction. It can also be seen that most of the points are not concentrated around the highest simulated PGV values in the

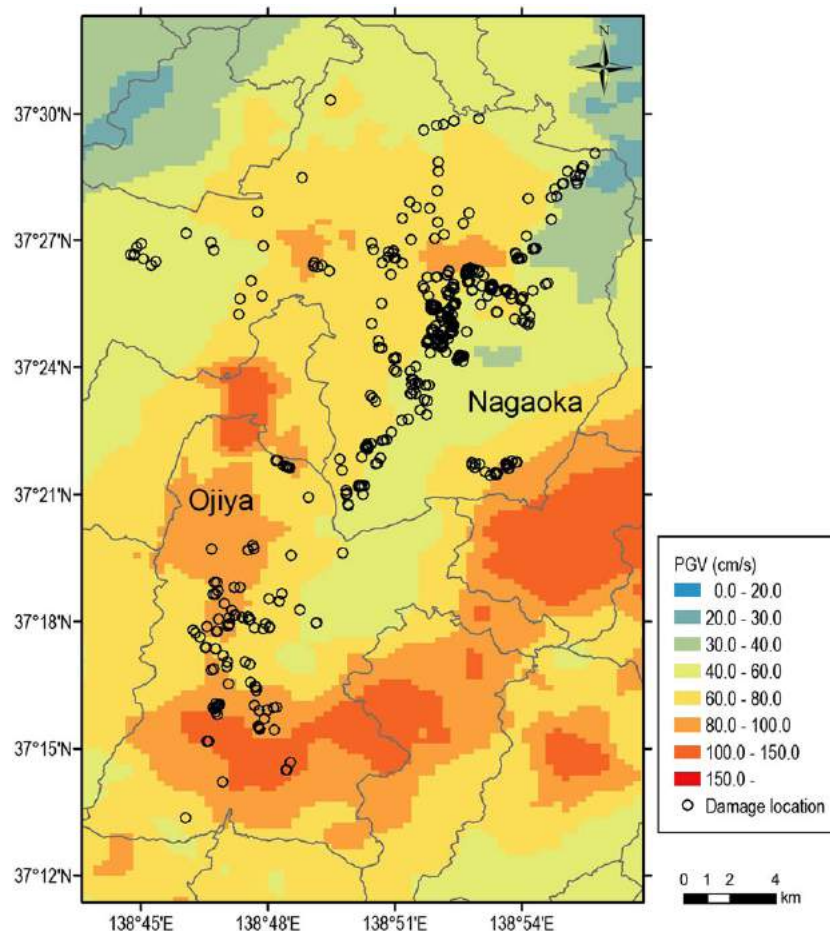


Figure 5. Simulated PGV values for the 2004 Chuetsu earthquake (color scale). Open circles represent points of damage to WSPs during the earthquake. [Colour figure can be viewed at wileyonlinelibrary.com]

region, which are mostly higher than 80 cm/s. The WSP damage points are mainly concentrated in the areas with PGV values lower than 60 and 80 cm/s in the cases of Nagaoka and Ojiya cities, respectively. The previous results suggested that the damage to the WSPs was not highly correlated to the PGV values. On the other hand, we noticed that the WSP damage points align perfectly along a region in which the PGV values change rapidly from 40 to 80 cm/s. This change in the PGV begins at the boundary between two dissimilar geomorphological units, namely, the mountainous region to the east of Nagaoka city and the alluvial fans to the west of the city (Figure 5). The previous observations strongly suggested that the damage to the WSPs might have originated from the large spatial variations in the ground motion and were not related to the actual magnitude of the motion. These variations can be explained on the basis of pronounced spatial changes in the site amplifications arising from dissimilarities in the geomorphologies, which were incorporated in the ground motion simulations.

In order to estimate the extent of WSP damage, we determined the WSP repair rate within Ojiya and Nagaoka cities. We defined the WSP damage rate (WDR, %), as follows:

$$WDR = \frac{N_w}{L_w} \quad (4)$$

where N_w is the number of damaged WSPs (count) and L_w is the WSP length (in km).

We calculated the PGV values at the center of every grid cell where WSP damage had been observed previously. Figure 6 shows the relationship between the WDR and the simulated PGV values. For all the analyses involving the PGV, the WDR was calculated for PGV values averaged for a WSP length of 50 km. Specifically, we prepared a dataset of the number of WSPs damaged, the pipeline length, and the PGV per mesh. This dataset was sorted by the PGV and WDR values, and the PGV was calculated as an average for every 50 km. It can be seen from Figure 6 that the correlation between the simulated PGV and WDR values is very poor (correlation coefficient $R=0.22$). These results together with the observations shown in Figure 5 strongly suggest that the WSP damage is not highly correlated to the PGV. An inspection of the above-mentioned database also indicated that most of the WSP systems in Nagaoka and Ojiya cities experienced PGV values between 50 and 90 cm/s. For reference, we also show the regression line for the dataset containing values averaged for a WSP length of approximately 34 km ($R=0.28$). A length of 34 km was the shortest with a nonzero WDR. The plotted dataset for this study was calculated using the weighted means method. Therefore, the regression lines corresponding to the different WSP lengths should

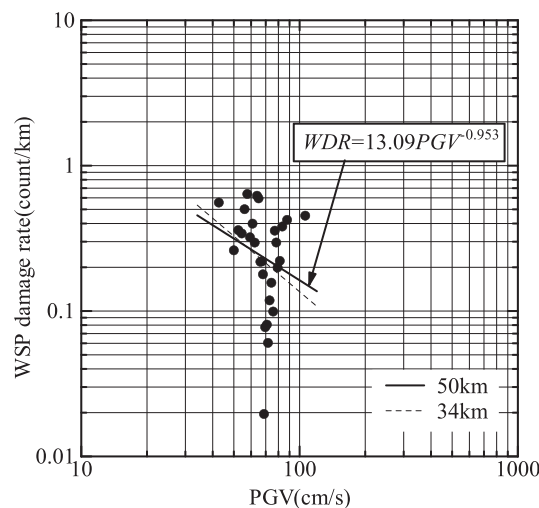


Figure 6. Relationship between the WDR and PGV values. The WDR was calculated as the number of damaged WSPs divided by the total length of the WSP in the grid cells. The dataset was determined by averaging the PGV values for a WSP length of 50 km. The dashed line represents the equation relating the PGV and WDR values in the dataset as calculated by averaging the values for a WSP length of 34 km.

have been approximately coincident. However, it can be seen from Figure 6 that the regression line for the dataset corresponding to a WSP length of 34 km was slightly different from the one for the dataset corresponding to a length 50 km. This difference must be explained because almost all the data points were distributed within the PGV range of 50–90 cm/s.

3.3. Relationship between PGV gradient and damage to water supply pipelines

Figure 7 shows the points of damage to the WSPs on a map of the simulated PGV gradients within the Chuetsu region. This figure suggests that there is a higher correlation between WSP damage and the PGV gradients. It can be seen that most of the points of damage to the WSPs align perfectly along stripes with high PGV gradients; the exception is a cluster of damage points enclosed by a blue ellipse in Figure 7. This cluster actually corresponds to an area damaged by landslides (the lower part of region A in Figure 4). The observed good agreement between the extent of WSP damage and the PGV gradients may be explained by the fact that lifeline structures such as water and gas pipelines suffer damage because of the axial or shear strain of the ground along the length; this strain is likely generated by out-of-phase ground vibrations along the structure.

Figure 8 shows the relationship between the WDR and the PGV gradients. For the all analyses involving the PGV gradients, the WDR was calculated for PGV gradients averaged for a WSP length of approximately 50 km.

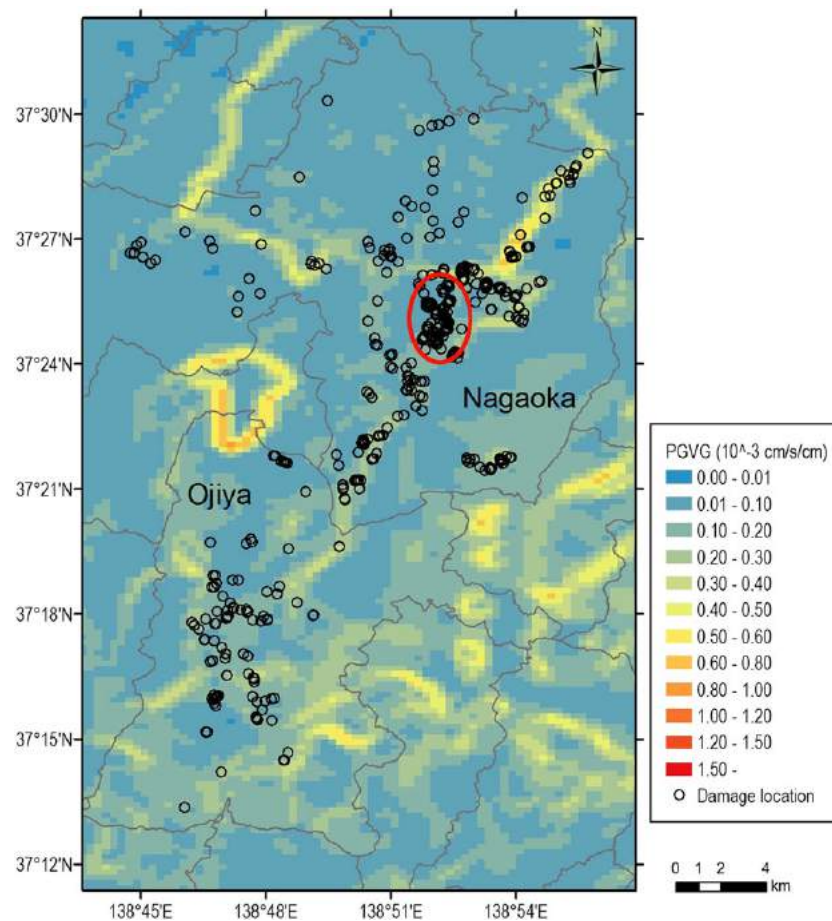


Figure 7. Simulated PGV gradient values for the 2004 Chuetsu earthquake (color scale). Crosses show the points of damage to the WSPs during the Chuetsu earthquake. It can be seen that there is a high correlation between the PGV gradients and the points of damage to the WSPs; the exception is the region enclosed by a red ellipse, which is a landslide-affected area. [Colour figure can be viewed at wileyonlinelibrary.com]

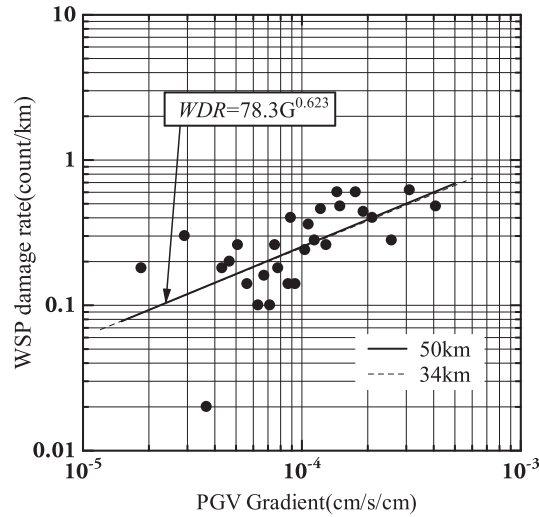


Figure 8. Relationship between the WDR and the simulated PGV gradients. The WDR was calculated for PGV gradients averaged over a WSP length of 50 km. The dashed line represents the equation relating the PGV gradient and the WDR values in the dataset determined by averaging for a WSP length of approximately 34 km.

It can be seen from Figure 8 that there is good agreement between the PGV gradients and the WSP damage rate (correlation coefficient $R=0.62$). A comparison of Figures 6 and 8 shows clearly that the WDR exhibits a significantly higher correlation with the PGV gradients than with the PGV values.

We determined the equation relating the PGV gradient (G , in cm/s/cm) and the WDR (in count/km) using the least squares method:

$$WDR = 78.3G^{0.623}. \quad (5)$$

This equation can be used as a WSP damage rate estimator for past earthquakes as well as for scenario earthquakes, provided that the PGV values have been obtained using a uniform and dense grid cell that allows the G values to be calculated. Our results indicate clearly that the simulated PGV gradients for a scenario earthquake can be a very useful index for the first screening of seismic hazards as well as for preparing seismic damage prediction maps for underground structures such as WSPs. Similar to Figure 6, Figure 8 also shows the regression line for the dataset of the values averaged for a WSP length of 34 km. It can be seen from the figure that the regression line corresponding to a WSP length of 50 km almost coincides with the one for a length of 34 km. As mentioned above, this is because the datasets of the WDR and PGV gradient values were generated using the weighted mean method based on the WSP length.

4. RELATIONSHIP BETWEEN STRONG MOTION AND DAMAGE TO WATER SUPPLY PIPELINES IN KOBE CITY

In this section, we examine the relationship between WSP damage and strong ground motion during the 1995 Kobe earthquake. The damage to WSPs was digitized in the vector format using paper-based maps. Figures 9, 10, and 11 show the WSP distribution, the PGV and PGV gradient distributions, and the locations of WSP repair, respectively. The WSP damage points are defined as the point-wise repair locations.

It can be seen from Figure 10 that approximately half of the WSP damage points coincide with an area with a PGV value greater than 100 cm/s. However, the other half of the WSP damage points are located on a mountain side and in areas with comparatively smaller PGV values. On the other hand, the distribution of the PGV gradient exhibits a high correlation with the damage points, especially on the

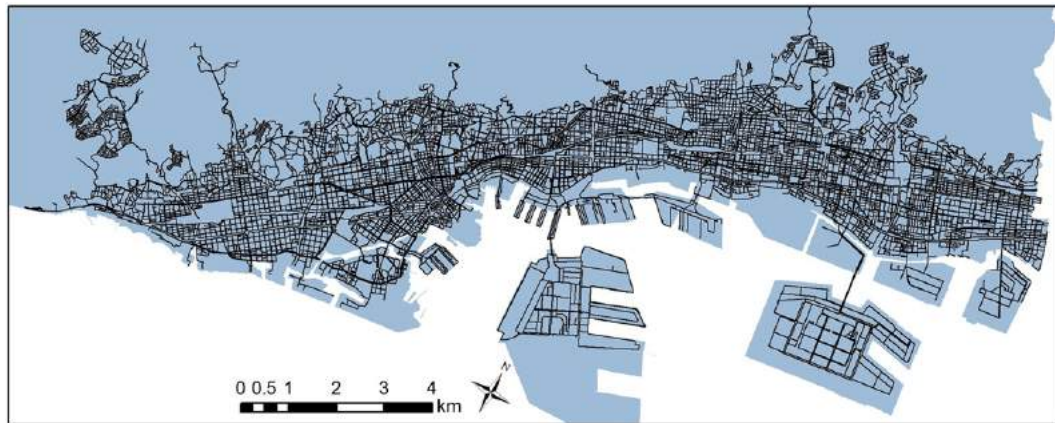


Figure 9. Distribution of WSPs in Kobe city. [Colour figure can be viewed at wileyonlinelibrary.com]

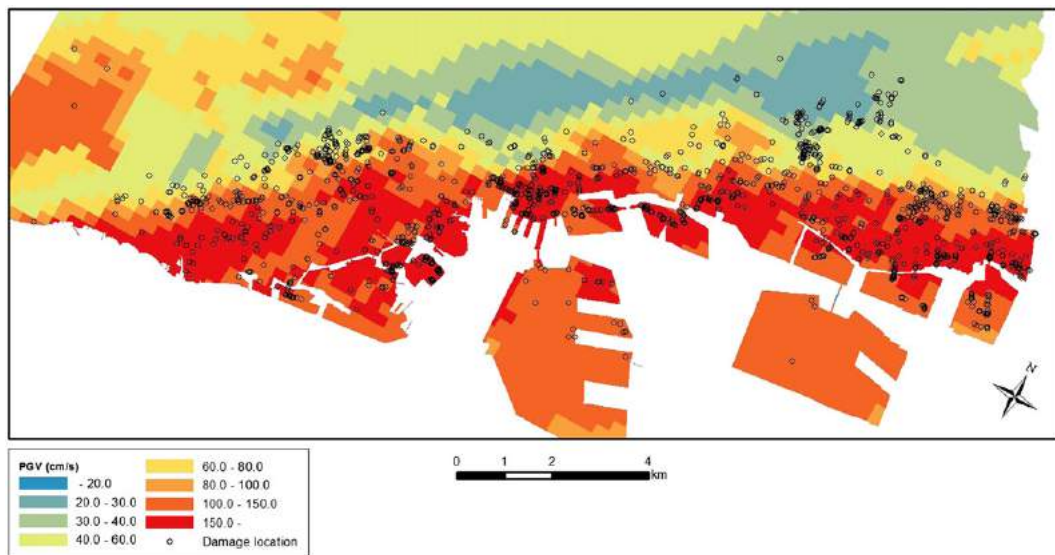


Figure 10. PGV distribution and locations of WSP damage points in Kobe city. Dots represent points of damage to WSPs during the 1995 Kobe earthquake. [Colour figure can be viewed at wileyonlinelibrary.com]

eastern side of the map, with the WSP damage points being concentrated in the area with a PGV gradient greater than $0.40 \times 10^{-3} \text{ cm/s/cm}$ (see Figure 11). However, there are a few regions where the WSP damage points do not overlap with the PGV gradient distribution. For example, in the Uzugamori-dai and Sumiyoshiyamate areas, which are located within the red ellipse in Figure 11, a large number of landslides or tensile cracks were observed around places of residence, while in the middle of Port Island severe damage due to liquefaction had occurred. The landslides and liquefaction at these spots were caused by strong ground motion; however, the damage was not related to a change in the motion. In order to evaluate the relationship between the WSP damage and the PGV or the PGV gradient values quantitatively, the damage rate was defined Port Island in the same manner as in Eq. (4).

Figure 12 shows the relationship between the WDR and the simulated PGV values for the Kobe and Chuetsu earthquakes. For all the analyses involving the PGV, the WDR was calculated for the PGV values averaged for a WSP length of approximately 50 km. It can be seen from the Figure 12 that the correlation between the simulated PGV values and the WDR is better (correlation coefficient $R=0.47$) than that for only the 2004 Chuetsu earthquake. Further, the correlation coefficient

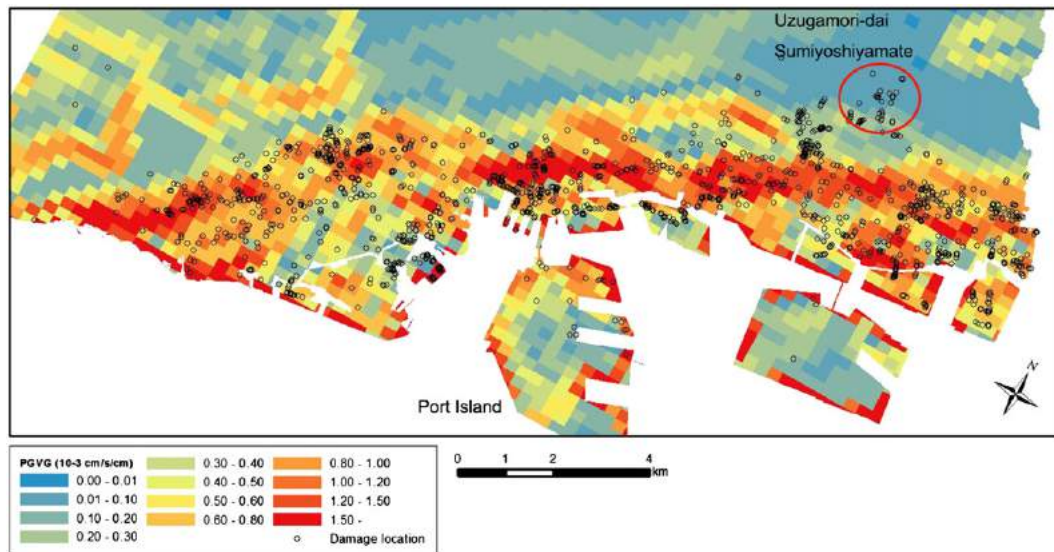


Figure 11. PGV gradient distribution and locations of WSP damage points in Kobe city. Dots represent the points of damage to WSPs during the 1995 Kobe earthquake. [Colour figure can be viewed at wileyonlinelibrary.com]

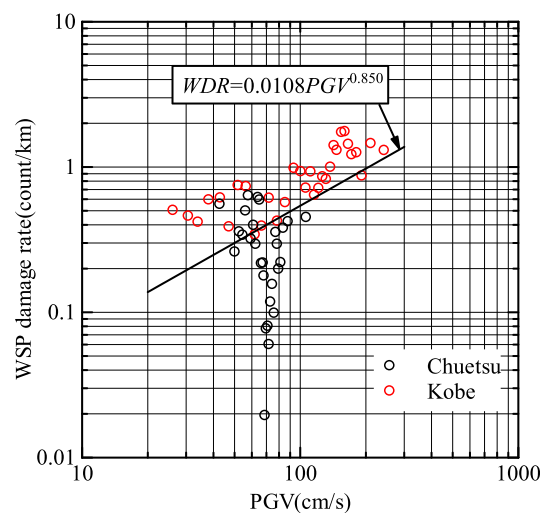


Figure 12. Relationship between the WDR and PGV values. The WDR was calculated as the number of places of damage to the WSP divided by the total length of the WSP in the grid cells. The dataset was calculated by averaging the PGV values for a length of approximately 50 km of the WSP. The regression line was calculated for data corresponding to both the Kobe and the Chuetsu earthquakes. [Colour figure can be viewed at wileyonlinelibrary.com]

between the simulated PGV values and the WDR for only the Kobe earthquake was 0.79. The WDR values for the Kobe earthquake were higher than the ones corresponding to the equivalent PGV range for the Chuetsu earthquake. This difference between the Kobe and Chuetsu earthquakes can be explained by the fact that the degree of liquefaction-induced damage to WSPs during the Kobe earthquake was much larger than that during the Chuetsu earthquake. This was because liquefaction at a site is strongly correlated to the seismic characteristics at the site, such as the PGV value and the seismic intensity. We describe the investigation in more detail in the latter half of this section.

Figure 13 shows the relationship between the WDR and the simulated PGV gradients. It can be seen from the figure that the correlation between the WDR and the PGV gradients (correlation coefficient $R=0.83$) is even better than that between the WDR and the PGV values for the Kobe earthquake.

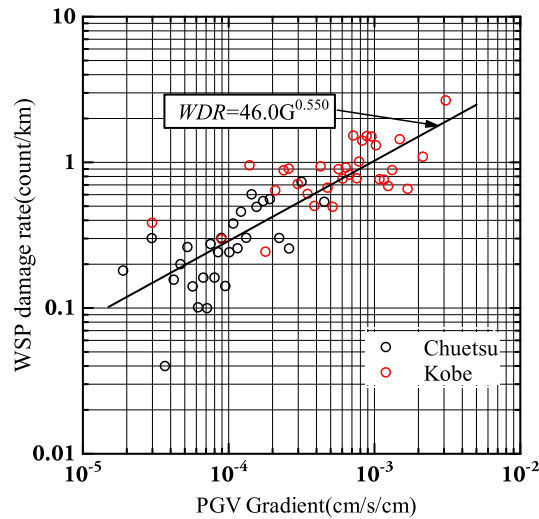


Figure 13. Relationship between the WDR and the simulated PGV gradients. The WDR was calculated for the PGV gradients averaged for a WSP length of approximately 50 km. [Colour figure can be viewed at wileyonlinelibrary.com]

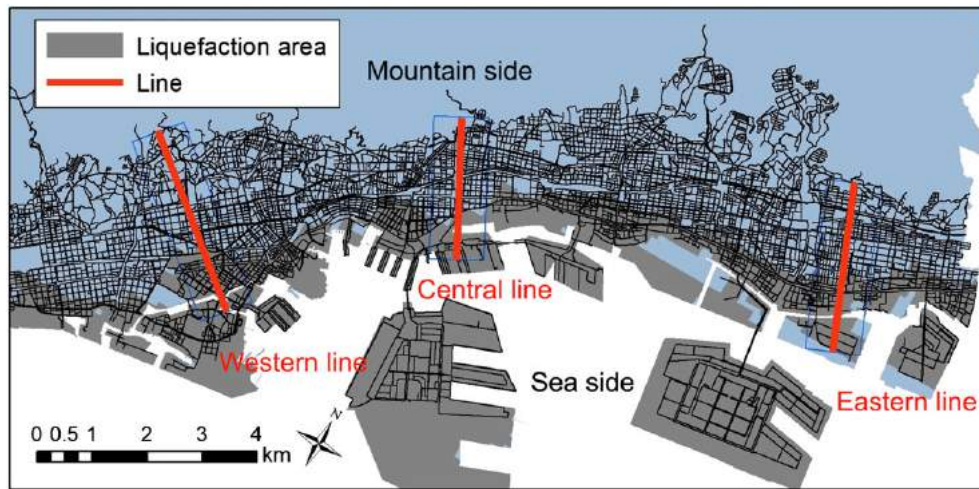


Figure 14. Traverse lines targeted in the case study on Kobe. [Colour figure can be viewed at wileyonlinelibrary.com]

Further, this trend is similar to the one observed in case of the 2004 Chuetsu earthquake. The data corresponding to the Kobe earthquake confirm the relationship between the WDR and the PGV gradient for a large range of gradient values, with the trend being the same as that in the case of the Chuetsu earthquake. Although the data obtained using the PGV amplification factor [24] exhibited a large variance and the accuracy of the factor was not high, it was observed that the correlation between the WDR and the PGV gradients was high ($R=0.91$). This result indicated that the ground strain increases around the boundary between two dissimilar geomorphological regions with a marked difference in their V_{s30} values, owing to which the damage to WSPs is concentrated around the boundary. Therefore, we proposed the equation relating the PGV gradient (G , in cm/s/cm) and the WDR (in count/km) for as a WSP damage rate estimator for future scenario earthquakes:

$$WDR = 46.0G^{0.550}. \quad (6)$$

Herein, the lowest threshold of PGV gradient can be 1.5×10^{-5} cm/s/cm for Eq. (6) on the safe side. Because, from the original data of damage to the WSPs and the PGV gradient without averaging for

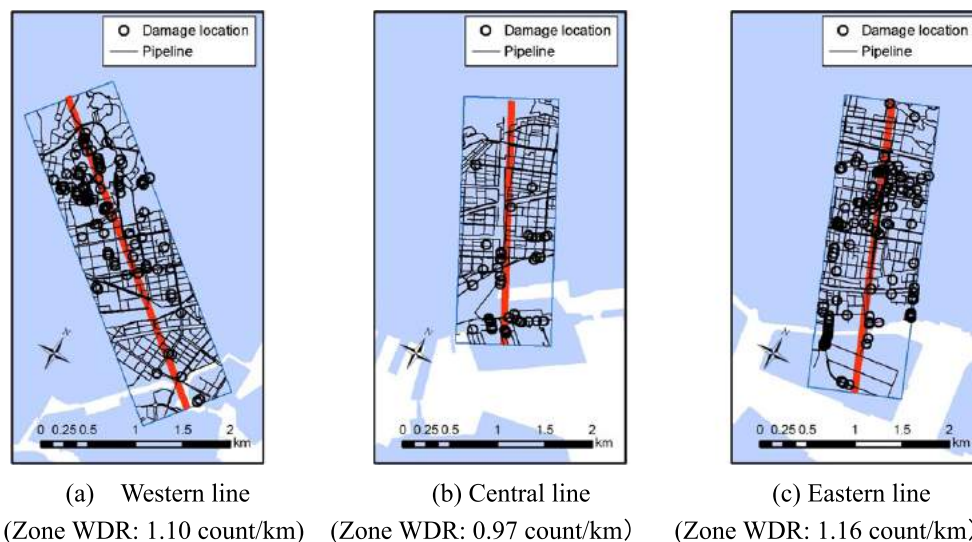


Figure 15. WSP and its repair locations near the traverse lines. [Colour figure can be viewed at wileyonlinelibrary.com]

WSP length of about 50 km, no damage to the WSPs occurred under PGV gradient of 1.2×10^{-5} cm/s/cm in the Chuetsu and Kobe cases. From Figures 7 and 11, we can observe that no damage points are located in meshes under the PGV gradient of 1.0×10^{-5} cm/s/cm.

Next, we focused on several subregions. These regions, which included three traverse lines that are set along the gradient direction of the ground elevation and their surrounding areas, are shown in Figure 14. The traverse lines roughly cross over the damage belt corresponding to a seismic intensity of 7. Figure 15 shows the WSP damage locations. The pipeline and damage spots are trimmed in the zone, which is buffered at 500 m from the traverse lines.

For these three traverse regions, we calculated the averages of the PGV and the PGV gradient within a buffer zone 500 m from the traverse lines. The WDR was calculated for every 100 m within the 500-m buffer zone along the traverse lines. Figure 16 shows the WDR, PGV, and PGV gradient values along the traverse lines. The horizontal axis indicates the length of the traverse line from the coast to the mountain. The region that experienced seismic activity with an intensity of 7 (denoted by SI 7) and the liquefaction region are also shown in the upper part in Figure 16. The damage to the WSP was concentrated on the mountain side on the western traverse line as well as in the liquefied area next to the sea on the central and eastern traverse lines. The pipeline damage in the liquefied area was probably due to permanent deformation resulting from the liquefaction and not necessarily owing to the intense shaking of the ground.

The damage to the WSP on the mountain side of the western traverse line (Figures 16a and 16b) appeared to be severe, because fragile cast-iron pipes are used widely in this area (JWWA, 1996 [27]).

Regarding the PGV values simulated by Matsushima and Kawase [1], the largest values of the PGV along the lines corresponded well with the region that experienced a JMA seismic intensity of 7. The PGV was high along the seaside but decreased as one moved towards the mountain. It can also be seen that the PGV values were relatively small in the areas that experienced liquefaction (Figures 16c, 16d, 16e, and 16f). The peaks corresponding to WSP damage neither correspond to the highest PGV values and nor to the region with a seismic intensity of 7 (Figures 16a, 16c, and 16e). On the other hand, the results indicated that there is a high degree of agreement between pipeline damage and the PGV gradients and not the PGV values in the regions along the western traverse line (Figure 16b). Figures 16e and 16f also show that the distribution of WSP damage is correlated more with the PGV gradient values than with the PGV values.

In case of the central line, the peak values of the PGV and the PGV gradients did not correspond to the peak values of WSP damage (Figures 16c and 16d). This might be due to the occurrence of widespread liquefaction in this region, which may have been the primary cause of WSP damage. In

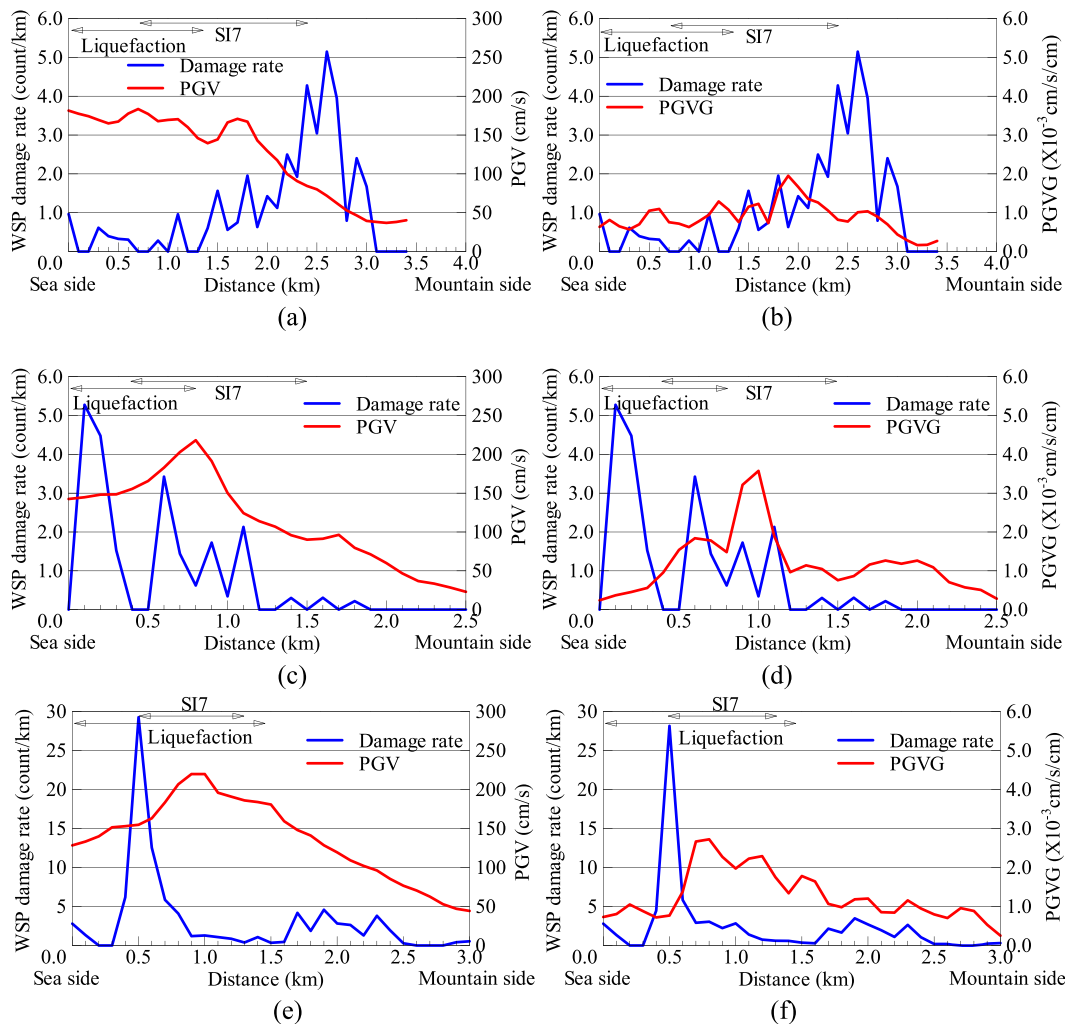


Figure 16. (a), (c), and (e) Relationships between the WDR and PGV along the western, central, and eastern transverse lines, respectively. (b), (d), and (f) Relationships between the WDR and PGV gradient (PGVG) along the western, central, and eastern transverse lines, respectively. The PGV and PGV gradient values were calculated as the averages within a buffer zone 500 m from the traverse lines. [Colour figure can be viewed at wileyonlinelibrary.com]

the case of liquefaction, pipeline damage is expected to result primarily from the permanent deformation of the ground rather than from the shaking motion of the ground. This may explain why measures of the ground motion such as the PGV and the PGV gradient do not show a good correlation with the pipeline damage in this case.

Our results indicate that the PGV gradient is a better indicator of pipeline damage than is the PGV or seismic intensity. However, it can only be used with soils that have not experienced liquefaction.

5. DISCUSSION AND CONCLUSIONS

We developed a new method to estimate the damage incurred by WSPs owing to earthquakes, based on the ground velocity gradients, which were obtained from simulated PGV values that incorporated the site amplifications (every 250 m). We surveyed the damage to WSPs in Ojiya and Nagaoka cities in the Niigata prefecture during the 2004 Chuetsu earthquake and analyzed the distribution of the damage points based on the simulated PGV and PGV gradient values as well as a geomorphologic

classification map of the Chuetsu region. Our results indicate that the majority of the points of damage to WSPs are located along stripes of lands with high PGV gradient values. These gradients are associated with rapid changes in the PGV at the boundary between two dissimilar geomorphologic units, namely, the mountainous region to the east of Nagaoka city and the alluvial fans to the west of the city. Further, the results show that there is a statistically significant correlation between the WSP damage and the PGV gradients. A possible explanation for this strong correlation is that the damage incurred by underground structures such as water and gas pipelines is due to a severe axial or shear strain of the ground surrounding the structures, which is generated by the differential motions of the ground. We also examined the applicability of the proposed method in understanding the characteristics of damage to WSPs in Kobe city during the 1995 earthquake in the city. For this earthquake, the location of the WSP damage points do not always correspond to the areas with large PGV values, in contrast to the case for Nagaoka and Ojiya cities during the Chuetsu earthquake. On the other hand, the areas with PGV gradients values higher than $0.4 \times 10^{-3} \text{ cm/s/cm}$ showed a high degree of correlation with the WSP damage; the exception were the areas that experienced widespread landslides or tensile cracks in the soil. The results of the statistical analyses of the Chuetsu and Kobe earthquakes demonstrate that the PGV gradient is correlated to a greater degree to the WSP damage rate than is the PGV. Further, the results show that the wide range of the WSP damage data corresponding to the two earthquakes can be explained based on a common linear empirical relationship with the PGV gradients.

Based on the above-mentioned analyses of the Chuetsu and the Kobe earthquakes, we derived an empirical relationship to predict the WSP damage rate from earthquakes based on the PGV gradients. The proposed method is not applicable in the case of regions that experience widespread liquefaction or landslides during earthquakes. We are aware that highly detailed estimates of WSP damage from earthquakes may require information regarding the material used for the pipelines as well as their intended function, in addition to the effects of the permanent ground displacement induced by the landslides and liquefaction. However, we consider that the proposed method is suitable for obtaining an initial estimate of WSP damage because of scenario earthquakes for large regions.

APPENDIX

1. To calculate the peak velocity at the engineering bedrock with $V_s=400 \text{ m/s}$, we used the following equation, which was proposed by Midorikawa et al. [28]:

$$\log ARV = 1.83 - 0.66 \log V_{S30} \quad (A1)$$

where ARV is the amplification factor of the PGV with respect to the engineering bedrock for $V_s=600 \text{ m/s}$, and V_{S30} is the average S-wave velocity from the surface to a depth of 30 m.

Using Eq. (A1), the values of ARV obtained by substituting $V_{S30}=400$ and 350 m/s were 1.30 and 1.42, respectively. Next, we calculated the amplification factor for the engineering bedrock for 400 m/s while taking that for 350 m/s to be 0.92 ($=1.30/1.42$). In this study, we obtained the peak velocities in the engineering bedrock for 400 m/s by multiplying the amplification factor (0.92) and the peak velocities. The peak velocity for every 250 m mesh was calculated by the spatial linear interpolation of the one simulated by Matsushima and Kawase for a 40 m mesh [1].

2. To calculate the gradient of the simulated PGV values, we used the central finite differencing approach (CDF):

$$G_i = \frac{A(x_i + h_i) - A(x_i - h_i)}{2h_i} \quad (A2)$$

where G_i is the numerical approximation of the derivative of PGV at x_i across the i direction (each of the components in Eq. (3)), h_i is the grid size along the i direction, and A is the PGV amplitude evaluated one grid before and after the coordinate x_i . For points located at the borders of the simulated PGV arrays, we used the forward or backward finite differencing approach.

The numerical calculation of the gradient involved two types of error: the deterministic error and the stochastic one. By using the Taylor's series approximation of function A , one could determine that the deterministic error of A_2 is proportional to the grid size (h). On the other hand, Brekelmans et al. [29] showed that the stochastic error of A_2 is inversely proportional to h . In the present case, we assumed that the stochastic component in the calculation of PGV was zero. Therefore, the error in the calculation of the gradient would only be proportional to the grid size. This meant that this error would be bounded by the smallest possible grid, for which information regarding site amplification is available. However, in a future work, we might consider including information on the stochastic nature of the error by evaluating different scenarios when simulating the ground motion. This would allow us to estimate the optimal grid spacing for the simulation in terms of the accuracy of the gradient, as suggested by Brekelmans et al. [29].

ACKNOWLEDGEMENTS

The K-NET and KiK-net strong-motion data and site amplification factor data used in this study were provided by NIED. We would like to express our gratitude to the Nagaoka, Ojiya, and Kobe city offices for providing the WSP network data and WSP damage data. We thank Matsushima and Kawase for providing the strong-motion simulation results for Kobe city corresponding to the 1995 Kobe earthquake. We also thank the reviewers for their useful comments, as well as the associated editor for handling our manuscript.

REFERENCES

1. Matsushima S, Kawase H. Re-evaluation of strong motion and damage of wooden houses in Kobe City during the 1995 Kobe earthquake. *Journal of Structural Engineering, Architectural Institute of Japan* 2009; **55B**(3):537–543(in Japanese).
2. Editorial Committee for the Report on the Hanshin-Awaji Earthquake Disaster: Report on the Hanshin-Awaji earthquake disaster, Earthquake and strong motions, 1997 (in Japanese).
3. Okimura T, Takada S, Koid TH. Outline of the Great Hanshin earthquake, Japan 1995. *Natural Hazards* 1996; **14**(1):39–71.
4. Takada S, Hassani N, Abdel-Azi M. Quick report of main damage caused by 1995 Hyogo-ken Nambu earthquake. *Journal of Natural Disaster Science* 1995; **16**(3):59–70.
5. Editorial Committee for the Report on the Hanshin-Awaji Earthquake Disaster: Report on the Hanshin-Awaji earthquake disaster, Damage and restoration of lifeline systems, 1997 (in Japanese).
6. Toki K, Irikura K, Kagawa T. Strong motion records in the source area of the Hyogo-ken-Nambu earthquake, January 17, 1995. *Japan, Journal Natural Disaster Science* 1995; **16**(2):31–37.
7. Jeon S, O'Rourke TD. Northridge earthquake effects on pipelines and residential buildings. *Bulletin of the Seismological Society of America* 2005; **95**(1):294–318.
8. American Lifelines Alliance: seismic guidelines for water pipelines, 2005.3.
9. G&E Engineering Systems Inc.: seismic guidelines for water pipelines, G&E Report 80.01.01, Revision 0, March, 2005.
10. Kubo, K., Katayama, T. and Sato, N.: Quantitative analysis of seismic damage to buried pipelines, Proceedings, 4th Japan Earthquake Engineering Symposium, Tokyo, 1975; 655–662 (in Japanese).
11. Indian Institute of Technology Kanpur and Gujarat State Disaster Management Authority: IITK-GSDMA Guidelines for Seismic Design of Buried Pipelines, 2007.
12. Kuwata Y, Takada S, Tanaaka Y, Miyazaki H, Komatsu Y. Fragility of underground pipeline under high levels of ground motion, *Journal of Water Supply: Research and Technology. AQUA* 2009; **59**(6–7):400–407.
13. O'Rourke, T. D., Wang, Y. and Shi, P.: Advances in lifeline earthquake engineering, 13th World Conference on Earthquake Engineering, No.5003, 2004.
14. European Committee for Standardization: Eurocode 8—Design of Structures for Earthquake Resistance—Part 4: Silos, Tanks and Pipelines, 2006.
15. Newmark NM. *Problems in Wave Propagation in Soil and Rock*. University of New Mexico, Albuquerque, New Mexico: Proc. International Symposium on Wave Propagation and Properties of Earth Materials, 1967. p 7–26.
16. Paolucci R, Smerzini C. Earthquake-induced transient ground strains from dense seismic networks. *Earthquake Spectra* 2008; **24**(2):453–470.
17. Ballantyne, D.: Seismic vulnerability assessment and design of pipelines, *Journal—American Water Works Association*, May 2010 **102**, 5 88-97.
18. Survey team on water supply utilities damages due to the Niigata-ken Chuetsu earthquake: a survey report on water supply utilities damages due to the Niigata-ken Chuetsu earthquake, 2005 (in Japanese).
19. Wakamatsu, K., Matsuoka, M. and Sakakura, H.: Development of an engineering geomorphologic classification map of 250 meters grid cell for the Niigata Region and its applications, Abstract Volume of the 28th JSCE Earthquake Engineering Symposium, 2005, 4 (in Japanese).

20. Pulido N, Kubo T. Near-fault strong motion complexity of the 2000 Tottori earthquake (Japan) from a broadband source asperity model. *Tectonophysics* 2004; **390**:177–192.
21. Pulido, N. and Matsuoka, M.: Broadband strong motion simulation of the 2004 Niigata-ken Chuetsu earthquake: source and site effects, Third International Symposium on the Effects of Surface Geology on Seismic Motion, Grenoble, France, 2006; 1, 657–666.
22. Wakamatsu, K. and Matsuoka, M.: Development of the 7.5-arc-second engineering geomorphologic classification database and its application to seismic microzoning, Bulletin of Earthquake Research Institute, The University of Tokyo, 81, 317–324, 2006.
23. Kawase H. The cause of the damage belt in Kobe, “The basin-edge effect,” constructive interference of the direct s-wave with the basin-induced diffracted/Rayleigh waves. *Seismological Research Letters* 1996; **67**:25–34.
24. Fujimoto, K. and Midorikawa, S.: Relationship between average shear-wave velocity and site amplification inferred from strong motion records at nearby station pairs, Journal of JEEA, Japan Association for Earthquake Engineering, 6, 1, 11–22, 2006 (in Japanese).
25. National Research Institute of Earth Science and Disaster Prevention: Japan Seismic Hazard Information Station (<http://www.j-shis.bosai.go.jp/>).
26. Wakamatsu, K., Matsuoka, M. and Sakakura, H.: 7.5-arc-second Japan engineering geomorphologic classification map in Niigata prefecture, http://www.kedm.bosai.go.jp/japanese/daidaitoku/Niigata_GISdata/deta.Niigata_GISdata.html (in Japanese) [8 December 2008].
27. Japan Water Works Association, Damage to water supply pipeline during the 1995 Kobe earthquake and its analysis, 1996 (in Japanese).
28. Midorikawa, S., Matsuoka, M. and Sakugawa, K.: Site effects on strong-motion records observed during the 1987 Chhiba-ken-toho-oki, Japan earthquake, Proc. 9th Japan Earthquake Engineering Symposium, pp.E-085–E-090, 1994 (in Japanese).
29. Brekelmans RCM, Driessen LT, Hamers HJM, den Hertog D. Gradient estimation schemes for noisy functions. *Journal of Optimization Theory and Applications* 2005; **126**(3):529–551. DOI:10.1007/s10957-005-5496-2.

EXTENDED ABSTRACT:

CHARACTERISTIC OF STRUCTURE AND MODERN ACTIVITY OF SAI GON RIVER FAULT AND IMPLICATION FOR: THE GROUND SUBSIDENCE AND FLOODING IN HO CHI MINH CITY AREA

Do Van Linh¹, Thai Quang¹, Ha Thuy Hang², Lai Van Thuy³, Duong Chi Cong³, Le Anh Dung³, Dong Bich Phuong³, Pham The Tai¹, Vu Van Thanh¹.

¹South Viet Nam Geological Mapping Division (SVGMD)

²The University of Science HCM city (HCMUS)

³Viet Nam Institute of Geodesy and Cartography (VIGAC)

Corresponding email: dovalinh@gmail.com

1. INTRODUCTION

The Sai Gon River fault (SGRF) is a part of the Maeping (Song Hau) fault from Cambodia to Viet Nam crossing Ho Chi Minh city (HCM) - the largest socialist politic economic center of the nation (Figure.1a). The fault have been studied by many geologists and there were many remarkable achievements (Hai&Co.,1988; Duyen., 2002; Chinh&Linh., 2008; Cat et al, 2010; Linh., 2010; Linh et al., 2016). Climate Change Scenario to 2100 (MONRE., 2012), flooding is about 39% HCM's area to 2100 years. The flood phenomenon in HCM is a big challenge for the socialist economic development. Therefore, searching the causes of flooding and it's mitigation is an imperative request. There are many geologist to study the cause of flooding in HCM and ground subsidence such as: because overlimit exploitation of underground water (Dinh et al., 2010; Nam et al., 2015; Laura et al., 2013), or tectonic moving, increasing building load, magneto-change characteristics of ground (Linh et al., 2016; Ky et al., 2015). As result from, the scientists still have many different ideas about the causes of ground subsidence in HCM area. However, the cause of ground subsidence due to characteristic of structure and modern activity of SGRF still no anybody to mention. This paper provides the results about structural characteristic and modern activity of the SGRF that has a part to determine the cause of ground subsidence. This problem imply for forecasting flooding in HCM area.

2.MATERIAL AND METHOD

New data used to include: aerial photographs and Landsat TM 5 satellite; DEM-SRTM with resolution 90 metres of Nasa (USA); about 100 outcrops/240km itinerary; 47 deep structure boreholes; 200 boreholes of Holocen thickness analysis; 8 seismic reflection; 7 sub-bottom profile lines, 5 geodynamic benchmarks (A13-Vung Tau; A14-An Thoi, Can Gio, A15-Duc Hoa, Long An; A16-Tan Uyen, Binh Duong; A17-Long Thanh, Dong Nai) monitoring over 3 cycles from 2013 to 2015; 600 stations of measured

Radon gas ($^{222}\text{Rn}_{86}$), catalogue of 27 earthquakes epicenter of 4 monitoring station during 2006-2008 (Hung et al., 2010). Nine main methods used to: 1- Review to available data; 2- Analysis image of remote sensing; 3- The itinerary of geological survey; 4-Tectonophysics (Linh., 2010); 5- Iso-top of basement, isopach of sediment (Linh et al., 2016); 6- Coulomb stress change (Okada Y., 1992; King et al., 1994; Linh., 2010; Hung et al., 2010); 7- The modern movement observation by GPS technology and 8-Measure intensity of Radon gas exhalation (Hung et al., 2010; Linh et al., 2016); 9- Analysis of autocompaction sediment (Meckel et al., 2007; Linh et al., 2015). The detail about these methods is mentioned (Linh, 2010., Linh et al., 2016).

3. THE RESULTS AND DISCUSION

3.1. Structural Characterictis of The Sai Gon River fault

HCM area's geological structure include: 1-Jura sedimentary rock and Late Mesozoic pluton-volcanic complex; 2- Late Miocene-Quaternary sediment has thickness to be about 300m consist of Pleistocen and Holocen sediment. Holocen sediment has thicknes from several metres to 40m, to occupy about 60% HCM area. The SGRF could have been formed from Early Kainozoic time (Hai &Ma., 1988; Hung et al., 2010; Linh et al., 2016).

This paper result show that the SGRF is mainly with the dip - direction foward to west-south with dip of 60° - 86° , average of 75° , has been divided into 3 fault segments (FS) (Figure.1b). The Tay Ninh - Dau Tieng FS has dip of 80° ; The Buu Long - Chau Thoi FS has dip of 78° with two active phases: 1-left-lateral strike-slip and 2-right- lateral strike-slip. The Long Son-Vung Tau FS with dip of 77° , recorded 3 main slip phases: 1-left-lateral strike-slip; 2-right-lateral strike-slip and 3-normal-right strike-slip (latest) with pitch of 40° . The SGRF has the influent depth is about 30km as well forward to west-south with dip of 80° (Hung et al., 2010). Thickness of Holocen sediment varried from several metres to 40m at Can Gio and develops along strike of the fault (Figure.1b).

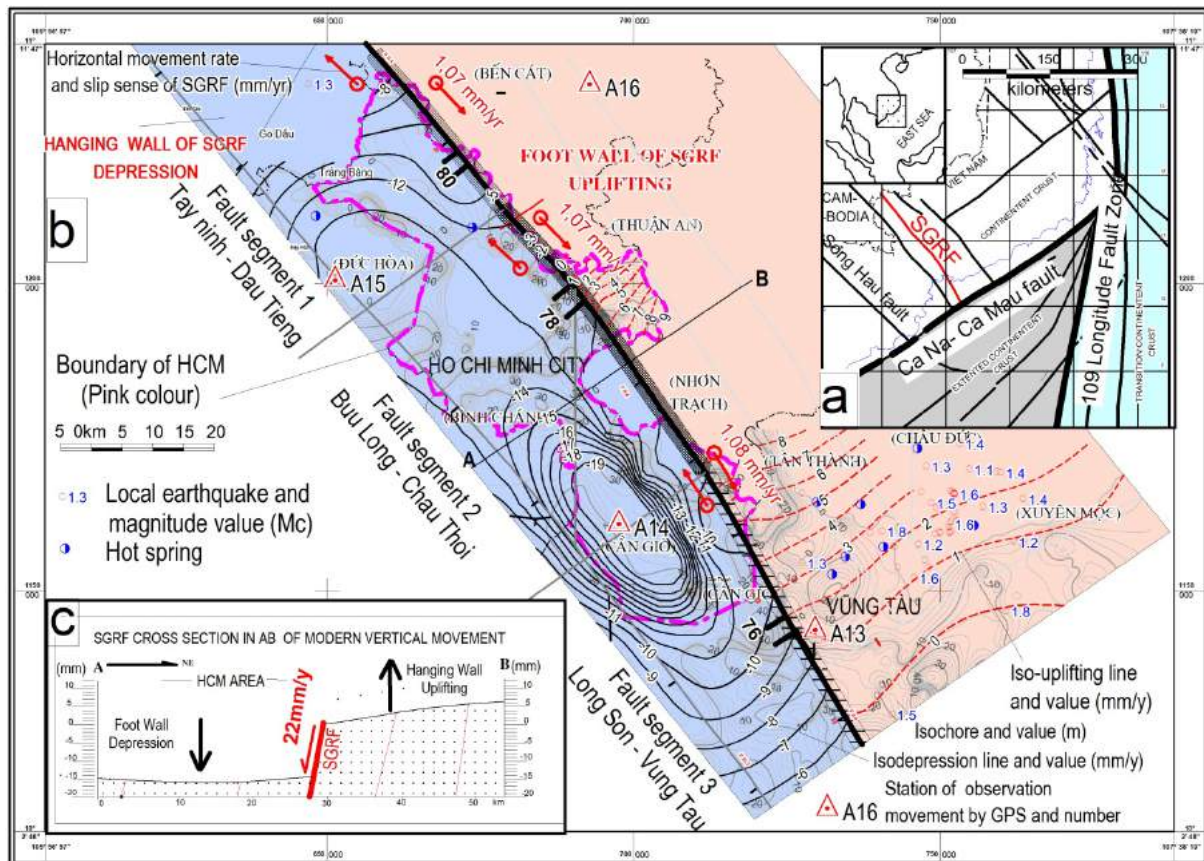


Figure 1. Characteristics of structure and activity of RGRF (a-SGRF in The fault tectonic map of the South Part of Central Part of Viet Nam; b-Modern movement of SGRF; c-AB section of vertical throw)

3.2. Modern activity of the SGRF

The result of the modern movement observation by GPS technology show that SGRF has normal-right strike-slip type with horizontal rate is about 1- 1.8mm/year, in current time. The modern relative vertical moving rate between two sides of SGRF each other is about 22mm/year (Figure.1c), absolute ground subsidence from 1mm/year to 19.9mm/year (in Can Gio), average depression rate is about 6 ± 3 mm/year in the foot wall of the SGRF. Uplifting to the hard rock basement (at Vung Tau site) is of 0.8mm/year in the hanging wall of SGRF. The active fault during Holocen to has made the differentiated subsided structures, which of are filled with Holocene sediment (the maximum thickness is about 40 meters in Can Gio) along the SGRF development strike. It cut and vertical displaced suddenly the Holocen sedimentary bottom-basement with throws of 4m and 6m at Can Gio. The sediment autocompaction with rate of 0-4.2mm/year, the medium about 2mm/year, maximum 4.2mm/year at Can Gio. The ground medium subsided element total is calculated about 9 ± 3 mm/year. This result and normal-right strike-slip SGRF will help finding one among the causes of the subsidence and the flood phenomenon in HCM (Figure.1b, Figure.1c).

Along with strike of the SGRF, there is the occurrence in the borehole for hot and mineral water at Binh Loi with temperature of 31°C , exhalation radon gas with maximum intensity of 11.000Bq/m^3 at Quang Trung bridge, for My Phuoc area is nearly 2700Bq/m^3 , Nha Be is from 1200Bq/m^3 to 2800Bq/m^3 . Observation of 4 monitoring stations found 56 earthquake foci during 2007-

2008 years with magnitude from $M_s = 1.3$ (in Ba Ria) to 2,7 richter (in Dau Tieng) to distribute along with development strike of SGRF (Figure.1b).

3.3. Discussion

If you think that "Exploitation groundwater overlimit to causes the ground subsidence", so why Can Gio area where there is seldom for exploitation groundwater but the ground average subsided rate is about 2-3cm/year. Therefore, the groundwater exploitation isn't the main reason for subsidence. Subsidence at the HCM downtown is still only 1mm/year (Dinh et al., 2010) or under 5mm/year (MONRE carried out from 2005 to 2015 year by Geodesy technology). Excluding factors to cause subsidence of HCM ground show that the appearance with three main reasons cause the subsidence such as autocompaction sediments, tectonic movement and other,... example as the urbanization?

This paper result show that SGRF being active with normal-right strike-slip type and total of the ground subsided factors in HCM area is about 9 ± 3 mm/year, relatively suitable with the result of Dinh et al., 2010. So that, what do the reason cause to subside at Can Gio to 19.9mm/year or 2-3cm/year (Ky et al., 2015). This problem need to continue study.

That why, the modern activity of SGRF is one of the main reasons to cause flooding in HCM nowadays. The forecast and evaluations about the flooding must be consider the structure factor and activity of the SGRF as parameters input into that and need synchronous for planning and developing economic socialist of HCM.

4. CONCLUSION

1-The SGRF has 3 segment of faults and the modern active expression to be normal-right strike-slip with pitch is about 40° and absolute movement rate: horizontal is about 1.8mm/year and vertical is about 0.8 to 19.9 mm/year. The maximum relative depression rate of footwall of SGRF to be 22mm/year, average of 6 ± 3 mm/year. Dip-direction of the SGRF forward to west-south, dip of $77-80^{\circ}$; prolong the northwest-east-south strike crossing through HCM area; its modern activity must be consider as one of the main reasons to cause ground subsidence and flooding in HCM area.

2-The total of ground subsided factors of HCM area estimates to be about 9 ± 3 mm/year.

3-The forecast and flooding evaluation need be considered and invest knowledge for autocompaction sediment factor, structure and activity of the SGRF as the parameters input that and need synchronous for planning and developing economic socialist of HCM city.

5. ACKNOWLEDGMENT

The paper used to some results of the project: "Investigation and assessment of the modern geodynamics to improve climate change scenarior and adaptation solution proposals in Song Cuu Long (Me Kong) Plain" carried out for 2012-2015 years by South Viet Nam Geological Mapping Division-General Department of Geology and Mineral of Viet Nam belong to National Target Program Cope with Climate Change, it's final report accepted in 2016 year by Ministry of Natural Resource and Environment

Authos are grateful to your help and MONRE's financial support!

REFERENCES

- Chinh, V.D., Linh, D.V., 2008. *Primarily analysing DEM model to indentify the Saigon River active fault during Late Pleistocen-Holocen*, 2008. Journal of development of Scientific and Technology, No 11, Volume 11-2008, 12-22. Ho Chi Minh City National University, (in Vietnames).
- Dinh H.T.M et al, 2010. Mapping Ground Subsidence Phenomena in Ho Chi Minh City through the Radar Interferometry Technique Using ALOS PALSAR Data. Remote Sens. 2015,7,8543-8562; doi:10.3390/rs70708543.
- Duyen, T.P., 2002. Modern active manifestation of Sai Gon River Fault. Journal of Geology, Series A, No.142, 12/2002, 60-70 (in Vietnames).
- Hai, H.Q.,Co, M.C., 1988. Final report result of geological mapping and looking for minerals of Ho Chi Minh Sheets, scale of 1/50.000. Store at South Viet Nam Geological Mapping Division, 342, Ho Chi Minh city, (in Vietnames).
- Hung, C.N et al., 2010. Earthquake microzoning for Ho Chi Minh city. Store at Department of Science and Technology of Ho Chi Minh city, 500 papers (in Vietnames).
- King, G.C.P., Stein, R.S and J. Lin., 1994. Static stress changes and the triggering of earthquakes, Bull. Seismol. Soc. Amer., 84 (3), 935-953.
- Ky, N.V., Hai, D.H., Thuyen, L.X., Linh, D.V., 2015. Land surface subsidence in Mekong Delta - due to the groudwater extraction?. Journal of Geology, Series A, No.352-354, 7-12/2015, 95-104, (in Vietnames).
- Laura E. Erban, et al, 2013. Release of arsenic to deep groundwater in the Mekong Delta, Vietnam, linked to pumping-induced land subsidence. PNAS | August 20, 2013 | vol. 110 | no. 34 | 13751-13756.

Linh, D.V., 2010. Cenozoic tectonic evolution of South Part of Central Part of Viet Nam and relationship with earthquake. Thesis of Doctor Level in Engineering, 286. Library of General Sceince of Ho Chi Minh city (in Vietnames).

Linh, D.V et al., 2015. The primary results of monitoring for present aggradation and degradation in Song Cuu Long (Me Kong) plain during 2013 - 2014 stage, 2015. Journal of Geology, Series A, No.352-354, 7-12/2015, 70-82, (in Vietnames).

Linh, D.V., Hung, C.N., Thu, N.N., Trieu, C.D., Xuyen, N.D., Nga, P.T., Hang, N.T., 2015. Seismic Hazard Assessment for Ho Chi Minh City, 2015. Journal of Geology, Series A, No.352-354, 7-12/2015, 111-121 (in Vietnames).

Linh, D.V et al., 2016. Final result report of investigation and assessment of modern geodynamics to improve climate change scenarior and adaptation solution proposals in Me Kong Plain. Geological Information Centre, 500, Ha Noi, (in Vietnames).

Meckel T.A., Ten Brink U.S and Williams S. J., 2007. Sediment compaction rates and subsidence in deltaic plains: numerical constraints and stratigraphic influences. Basin Research (2007) 19, P19–31. Blackwell Publishing Ltd., USA.

Ministry of Natural Resource and Environment (MONRE), 2012. Climate Change Scenario, Sea rise level for Việt Nam. Natural Resource-Environment & Cartography of VietNam Press, Ha Noi (in Vietnames).

Nam, P.C., Long, P.N., Vuong, B.T., 2015. Preliminary assessment of land surface subsidence due to groundwater exploitation in Ho Chi Minh City. Geology and Natural Resource of Viet Nam. Proceeding of National Conference of 70 years development Anniversary. Natural Science and Society Press, 365-369. Ha Noi, (in Vietnames).

Okada, Y., 1992. Internal deformation due to shear and tensile faults in half-space. Bull. of the Seism. Soc. of America, 82/ 2 : 1018-1040.

Trieu, C.D&Long, P.H., 2002. Tectonics of faulting in Viet Nam Territory. Science and Technology Press, 250, Ha Noi, (in Vietnames).

Evacuation Simulation Method Focusing on Evacuation Start

Yoshihiro Okumura and Yuji Dohi

ABSTRACT

It has been clarified the number of those who did not evacuate during the 2011 Tohoku Tsunami. In Iwate, Miyagi and Fukushima Prefectures, the ratio of non-evacuation people to survived people was estimated to be 11 % (Cabinet office of Japan et. al, 2011). In the city of Ishinomaki in Miyagi Prefecture, the ratio of non-evacuation people to dead people was estimated to be 56.8 % (Mikami et. al, 2012). It is important to promote evacuation measures to reduce the number of non-evacuation people.

In the present paper, we develop the evacuation simulation focusing on the process of evacuation start. This simulation consists of the distinct element method (DEM) based evacuee behavior model and the evacuee generation model, which refer to the theoretical concept “Cooperative creation of social reality”. People can start evacuation by feeling a growing sense of urgency in a community, which is cooperatively created by various stakeholders including residents, local officials and so on. The simulation is applied to reproduce the evacuation behaviors of the staff members and users of the elderly care facility in Miyagi Prefecture during the 2011 Tohoku Tsunami.

The following conclusions have been obtained. (1) The governing equation we proposed describes the evacuation start as follows; (1-1) various sources raises a sense of urgency, which raise people’s awareness level of danger (ALoD); (1-2) a person start evacuation when ALoD reaches their own upper limit; (1-3) they raise a sense of urgency in a community as a new source. (2) The weight is defined to describe differences of effectiveness among sources, and the upper limit is defined to describe a personal difference of evacuation start. (3) The good agreement to the results from interviews on people’s behavior is shown in the numerical results.

KEYWORDS: evacuation simulation, evacuation start, the sense of urgency

DR. YOSHIHIRO OKUMURA

Associate professor, Faculty of Societal Safty Sciences at Kansai University, Japan
E-mail: okumura@kansai-u.ac.jp, **corresponding author**
Tel: +81-72-684-4162

DR. YUJI DOHI

Associated research fellow, the National Research Institute for Earth Science and Disaster Resilience (NIED), Japan
Email: dohi@bosai.go.jp

1. Introduction

Past tsunamis have killed many people, especially those who were incapable and did not evacuate in time from the calamity area. For example, 15,894 people were killed and 2,546 are still missing after the 2011 Tohoku earthquake and tsunami (National Police Agency, 2017). In addition, more than 90% of the people were killed due to the tsunami. Some reports say that more than half of the tsunami victims could not or did not start evacuation, despite having sufficient evacuation time (more than half an hour) and receiving warning information about the tsunami in Ishinomaki city,

which suffered heavy damage (e.g., Mikami, 2014). Therefore, we think that solving the problem of starting the evacuation is most important to mitigate human loss of life due to tsunami disasters.

In Japan, the tsunami evacuation system (tsunami warning information) has been used since 1952. Regarding the start of tsunami evacuation, the following scheme has been discussed so far (Figure 1, lower left): First, the Japan Meteorological Agency (JMA) issues a tsunami warning and informs people of impending danger. Second, local governments encourage local people to begin tsunami evacuation. Third, each person logically judges whether to begin evacuation or not, based on his or her experience, knowledge, etc. During the 2011 Tohoku tsunami, many people received the information (e.g., tsunami warning, evacuation instruction) that public agencies issued.

On the other hand, there is the viewpoint that various agents in our society (including not only public agencies but also local people) play important roles in starting the tsunami evacuation. This viewpoint can be explained by the concept of “cooperative creation of social reality” (Yamori, 2009). Yamori pointed out that people start evacuation after feeling a growing sense of urgency in a community, which is cooperatively created by various stakeholders including residents, local officials, etc. (Figure 1, lower right). That is to say, all stakeholders in our society construct the reality of urgency, which prompts the need for evacuation in communities. The research survey about the start of evacuation during the 2011 Tohoku tsunami (Cabinet Office, Government of Japan, 2012) revealed the main triggers: strong shaking sensation for 45.6 % of the respondents, tsunami warnings for 27.9 %, someone’s encouragement or voice for 17.5–27.0 %, neighbors’ evacuation behaviors for 16.8 %, expected high height of the tsunami for 15.1 %, and witnessing the tsunami for 14.7 %. Therefore, we believe that

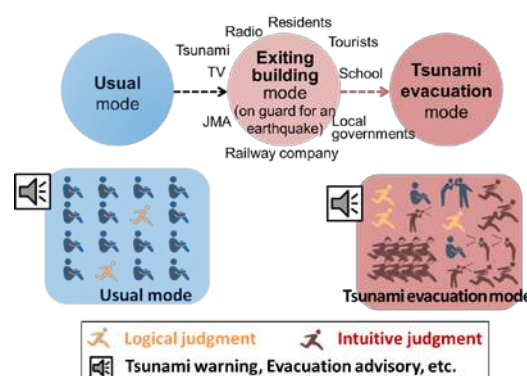


Figure 1: Concept of the start of evacuation (above: schematic diagram of the start of evacuation, lower left: usual mode based on logical judgment, lower right: usual mode based on intuitive judgment)

the concept of “cooperative creation of social reality” is the key to understanding the start of tsunami evacuation at a deeper level.

As described above, we believe that the start of evacuation is one of the most important matters for mitigating human loss of life due to tsunami disasters. We especially focus on the concept of “cooperative creation of social reality” and seek an effective method of beginning tsunami evacuations, which is different from the approach so far. In our concept, each person intuitively judges whether to begin evacuation or not, affected by the reality. Figure 1 (above) shows the schematic diagram of the start of evacuation used in our concept. First, people change from their usual mode to an exiting building mode (being on guard for an earthquake). Next, people change to the tsunami evacuation mode. We developed a simulation model for evacuee generation and have been improving it. Here, we simulate and analyze the start of tsunami evacuation by using the model for an elderly facility heavily damaged by the 2011 Tohoku tsunami.

2. Method

In this study, the tsunami evacuation simulation consists of two models: evacuee generation and evacuee behavior (Figure 2). We developed an evacuee generation model and combined it with an evacuee behavior model based on the distinct element method (DEM) (Kiyono et al, 1994).

2.1 Evacuee generation model

2.1.1 Basic concept

We developed the numerical simulation model for evacuee generation, which refers to the theoretical concept of “cooperative creation of social reality.” This model is explained as following three steps (Figure 3).

First, the reality of evacuation start (RES) is created by various sources (Figure 3, left). RES is expressed as

$$RES(x, y, t) = F_{con}(n(x, y, t)) \sum_{i_s=1}^{n_s} (R_{i_s}(x, y, t) X_{i_s}(t) W_{i_s}(x, y, t)) \quad (1)$$

where $RES(x, y, t)$ is RES at coordinates (x, y) at the time t , $F_{con}(n(x, y, t))$ is the function related to the conformity bias, n_s is the total number of sources that create $R_{i_s}(x, y, t)$ is the function related to the spatial relationship between RES $RES(x, y, t)$ and the source i_s at coordinates (x, y) at the time t , $X_{i_s}(t)$ is the output of the source i_s that has a value of zero or one at the time t , and $W_{i_s}(x, y, t)$ is the effectiveness level of the source i_s (weight). In this simulation, $F_{con}(n(x, y, t))$ is defined in Eq. (2) and $R_{i_s}(x, y, t)$ is defined in Eq. (3).

$$F_{con}(n(x, y, t)) = 1 + \frac{45.09}{45.68} \ln(n(x, y, t)) \quad (2)$$

$$R_{i_s}(x, y, t) = \begin{cases} 0, & \text{if RES } RES(x, y, t) \text{ is located outside} \\ & \text{the effective area of the source } i_s \\ 1, & \text{if RES } RES(x, y, t) \text{ is located inside} \\ & \text{the effective area of the source } i_s \end{cases} \quad (3)$$

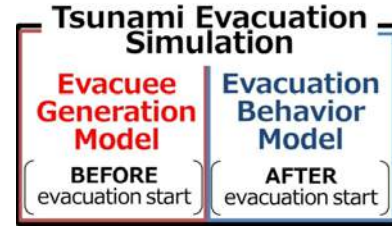


Figure 2: Composition of the tsunami evacuation simulation

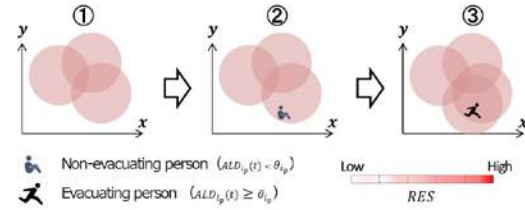


Figure 3: Basic concept of the evacuee generation model

In Eq. (2), we applied the observation results conducted by Milgram (1969). They focused on the relationship between the size of a stimulus crowd, standing on a busy street looking up at a building, and the responses of passersby. Considering the plateau of the function shape, we used a logarithmic approximation and formulated the observation results.

Second, awareness level of danger (ALD) of a person is increased gradually by feeling RES (Figure 3, center). ALD is expressed as

$$ALD_{i_p}(t) = \min\{\theta_{i_p}, \int_{c_{i_p}} RES(x, y, t) ds\} \quad (4)$$

where $ALD_{i_p}(t)$ is ALD of the person i_p at coordinates (x, y) at the time t and θ_{i_p} is the upper limit of ALD of the person i_p .

Third, when ALD reaches the upper limit θ , the person starts evacuation and becomes a new source (Figure 3, right). The function related to the activeness of i_p as a source is expressed as

$$X_{i_p}(t) = \begin{cases} 0, & ALD_{i_p}(t) < \theta_{i_p} \\ 1, & ALD_{i_p}(t) \geq \theta_{i_p} \end{cases} \quad (5)$$

2.1.2 Sources that creates RES

We categorized sources that create RES depending on the effective area of each source. Table 1 shows the four fundamental types of sources that create RES in this model. Every source can be categorized into (a) the whole area, (b) the whole area with a partial non-effective area, (c) a round shape, or (d) a round shape with a partial non-effective area.

The weights of sources imply their effectiveness level and indicate which source is more important in our society or in local communities. It can be set by using the research survey regarding the triggers of the start of tsunami evacuation.

With regard to the case of the elderly care facility during the 2011 Tohoku tsunami, we focus on the tsunami, shouting evacuees, and evacuating people as sources. Each weight of

the sources that create RES is set by using Okumura et al (2016). Table 2 summarizes the above. In this case, no source is applied to the category (a). However, a strong shaking sensation due to the earthquake could be applied to the category (a), as an example.

A sound source (e.g., shouting evacuees) is often categorized into (c) a round shape. In this model, an effective range (audible distance) of the sound source is expressed as

$$d_{i_s}(t) = 10^{\frac{1}{20}(SI_{i_s}(t) - SI_0)} \quad (6)$$

where $d_{i_s}(t)$ is an effective range (m) of the sound source i_s at the time t , $SI_{i_s}(t)$ is the sound intensity (dB) that the sound source i_s makes, and SI_0 is the sound intensity (dB) that people can hear. In the case of the elderly care facility, we set the effective range of shouting as 30 m when $SI_{i_s}(t) = 90$ dB (constant) and $SI_0 = 60$ dB.

A visual source (e.g., evacuating people) is often categorized into (d) a round shape with a partial non-effective area. This category considers a non-effective area as a place where there is a wall inside an effective area. In this model, an effective range (visual distance) of the visual source is expressed as

$$d_{i_s}(t) = k_V h_{i_s} \quad (7)$$

where $d_{i_s}(t)$ is an effective range of the visual source i_s at the time t (m), k_V is a vision factor, and h_{i_s} is the size of the visual source i_s . In the case of the elderly care facility, we set the effective range of evacuating people at 110 m when $h_{i_s} = 1.65$ m (mean height of the Japanese) and $k_V = 66.7$, according to a visual acuity test with the use of the Landolt C. Those who could see it (7.5 cm wide) from 5 m away were judged to have 20/20 vision.

2.1.3 Upper limit of ALD

The upper limit of ALD should differ among people because of their individual characteristics, as determined by their experiences, education, personality, etc. In our model, this variety is defined as the difference of θ . We set an upper

limit for the start of evacuation for each person. This is expressed using a uniformly distributed random number r_{i_p} ($0 < r_{i_p} \leq 1$) as follows:

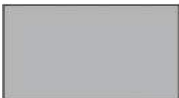
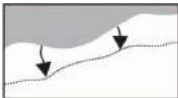

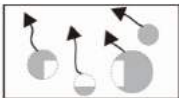
$$\theta_{i_p} = \frac{R}{r_{i_p}} \quad (8)$$

Here, θ_{i_p} is the upper limit of ALD for person i_p and R is a regional coefficient. The upper limit of ALD should depend on areas because of their cultures, characteristics, etc. The regional coefficient R expresses an areal difference regarding the start of evacuation. This equation is defined considering the situation wherein most people whose upper limit of ALD θ_{i_p} is not so large can start evacuation comparatively easily. On the other hand, only a few people will not start evacuation because their upper limit of ALD θ_{i_p} is quite large.

2.2 Evacuee behavior model

We used the evacuee behavior model based on the DEM developed by Kiyono et al (1994). A human body is modeled as a double circle element with a physical and psychological radius, and the interaction between people is modeled by a spring and damping, as shown in Figure 4. The movement of each person is determined by solving the equation of motion. In the case of the elderly care facility, we set the parameters as Table 3 summarizes. In this model, each reference velocity of the evacuee is automatically determined using the mean, maximum, and minimum velocity. Without external forces, an evacuee can move at the reference velocity. When an evacuee is subjected to external forces, solving the equation of motion, acceleration occurs and the velocity changes. Each reference velocity on increasing slopes is half of the normal one.

Table 1: Four fundamental types of sources that create RES

	(a) Whole area	(b) Whole area (partial non-effective area)	(c) Round shape	(d) Round shape (partial non-effective area)
Image*				
Example	Strong shaking sensation	Tsunami	Tsunami siren Shouting evacuees TV/radio	Evacuating people


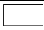
*  : effective area,  : non-effective area

Table 2: Four fundamental types of sources that create RES

Source Category (effective area)	Tsunami (b) Whole area with partial non-effective area	Shouting evacuees (c) Round shape	Evacuating people (d) Round shape with partial non-effective area
Spatial characteristics	-	30 m from a staff member	100 m from a staff member
Weight	3.00×10^{-3}	5.25×10^{-3}	3.01×10^{-3}
Remarks	Non-effective for people inside a building.	-	Non-effective if there is a wall inside an effective area.

3. Tsunami evacuation simulation in the elderly care facility during the 2011 Tohoku tsunami

3.1 The facility during the 2011 tsunami

Here, we simulate tsunami evacuation in the elderly care facility, located in Minami-sanriku town, heavily damaged by the 2011 Tohoku tsunami. Figure 5 (upper) shows the location of the facility. It is located 12–13 m above sea level and approximately 1 km from the coastline. The spatial model is shown in Figure 5 (lower). People in the facility were unexpectedly attacked by the devastating tsunami because the facility had not been identified as an expected inundation area before the 2011 Tohoku tsunami. A total of 41 out of 69 users and one staff member out of 30 were killed by the unexpected tsunami. According to interviews with four staff members conducted one and a half years after the 2011 Tohoku tsunami (Okumura, et al., 2013), the tsunami evacuation steps were as follows: First, four staff members at the parking lot (Figure 5, lower) realized the tsunami was flooding the town and started evacuation. Second, they shouted to others to start evacuation. The result of the tsunami propagation simulation indicated that it only took 160 s from the start of the evacuation of four staff members to the tsunami reaching the facility.

3.2 Setting the initial conditions

We set the initial conditions based on the interviews (Okumura, et al., 2013). Table 4 summarizes the initial conditions common to the evacuee generation and evacuee behavior models. Table 5 summarizes the initial locations of 30 staff members and 69 users. They were at the parking lot, area B, area C, area D, or area E (Figure 5, lower).

Regarding the evacuee generation model, we set the following sources to create RES: tsunami, shouting evacuees, and evacuating people. Each weight of the source that creates RES is summarized in Table 2. The tsunami as the source was not effective for people in the elderly care facility because they could not see the tsunami until it reached the facility. Regarding shouting evacuees as the source, we set the condition where every staff member shouted to others to start evacuation. Evacuating people as the source was also not effective if there was a wall inside an effective area.

Regarding the evacuee behavior model, we focused on the evacuation behaviors of 30 staff members. Each staff member took users by the hand and proceeded with the evacuation, heading toward the goal (Figure 5, lower). Users could not evacuate by themselves. In this simulation, we set a rule wherein a staff member takes one user by the hand and evacuation velocity is taken to be half of the normal velocity. The evacuation routes of four staff members at the parking lot are given. The routes of the others are randomly determined in the simulation.

3.3 Validation

According to the validation of the simulation results, we set two evaluation indices based on the interview (Okumura et al., 2013). One is that about 10 staff members had finished the evacuation before the tsunami struck. The other is that the staff members outside the area B (Figure 5, lower) started evacuation as soon as they heard other staff members shouting.

In the simulation, 12 staff members out of 30 finished the evacuation. In addition, the simulation shows that the staff

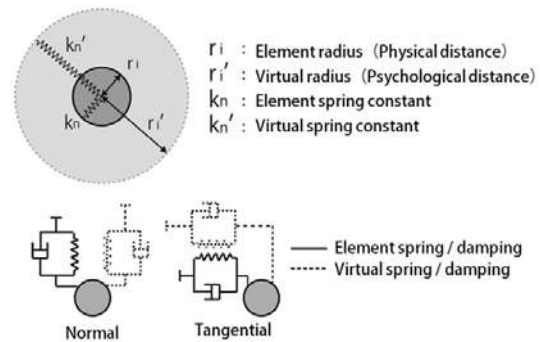


Figure 4: Concept of the evacuee behavior model based on the DEM (Kiyono et al, 1994)

Table 3: Parameters of the evacuee behavior model

Mean velocity (m/s)	1.21
Standard deviation of the velocity	0.30
Minimum velocity (m/s)	0.67
Maximum velocity (m/s)	2.40

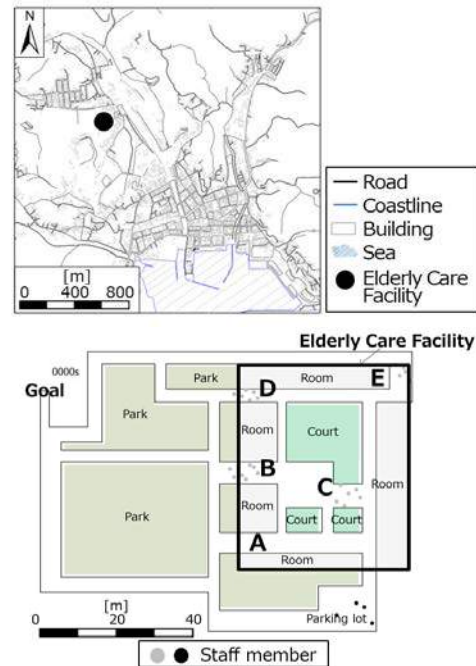


Figure 5: Spatial condition the elderly care facility (upper: location in Minami-sanriku town, lower: spatial model of the simulation)

Table 4: Initial conditions

The number of people (Staff members)	30
Total time for analysis (s)	160

Table 5: Initial locations

Position	Staff members	Users
Parking lot	4	0
Area A	0	0
Area B	7	15
Area C	6	15
Area D	7	17
Area E	6	22
Total	30	69

members outside the area B started evacuation as soon as they heard other staff members shouting. Considering the above, the simulation is validated.

3.4 Results and discussion

Figure 6 shows the snapshots of this simulation. They reveal the different RES characteristics among the left side (areas B and D), lower right side (near the parking lot), and upper right side (area E) in the elderly care facility. RES in the left side has been created for a long time. However, RES in the lower right side is lower than in the left side and is not created toward the end. In addition, RES in the upper right side is not created at all. Considering the abovementioned points, the area on the route toward the goal and close to the goal is advantageous for the start of evacuation from the viewpoint of RES. Similar results are mentioned in the tsunami evacuation simulation of Ishinomaki city during the 2011 Tohoku tsunami (Dohi et al., 2016).

Figure 7 shows the change in the mean ALD in each area. Focusing on the change in the whole area, it reveals three trends: before 40 s, 40–50 s, after 50 s. The sharp increase (40–50 s) starts as soon as the mean ALD in area C reaches the upper limit. It means that the start of the evacuation of the staff members at the area C played an important role in effecting the start of the evacuation of others in the elderly care facility.

Figure 7 also shows that the mean ALD in area E does not increase at all. No staff

member at the area E began evacuation in the simulation. This reason can be seen in the snapshots. Focusing on the area E in Figure 6, RES is not created at all there. Therefore, the staff member there cannot start evacuation. These results and discussion correspond to the interview result of the staff member who was at area E. She said that she did not hear any shouting or see any evacuating

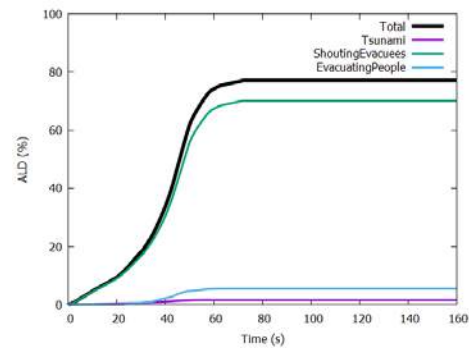


Figure 7: Change in the mean ALD in each area (initial positions of staff members)

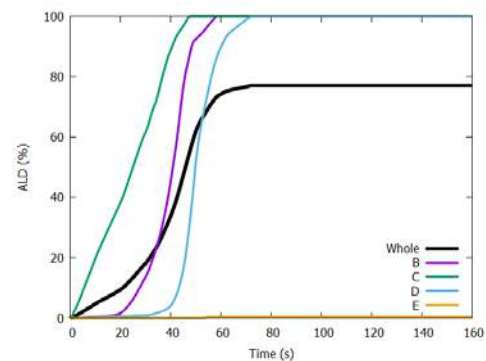


Figure 8: Degree of contribution to the change in the mean ALD by each source that creates RES

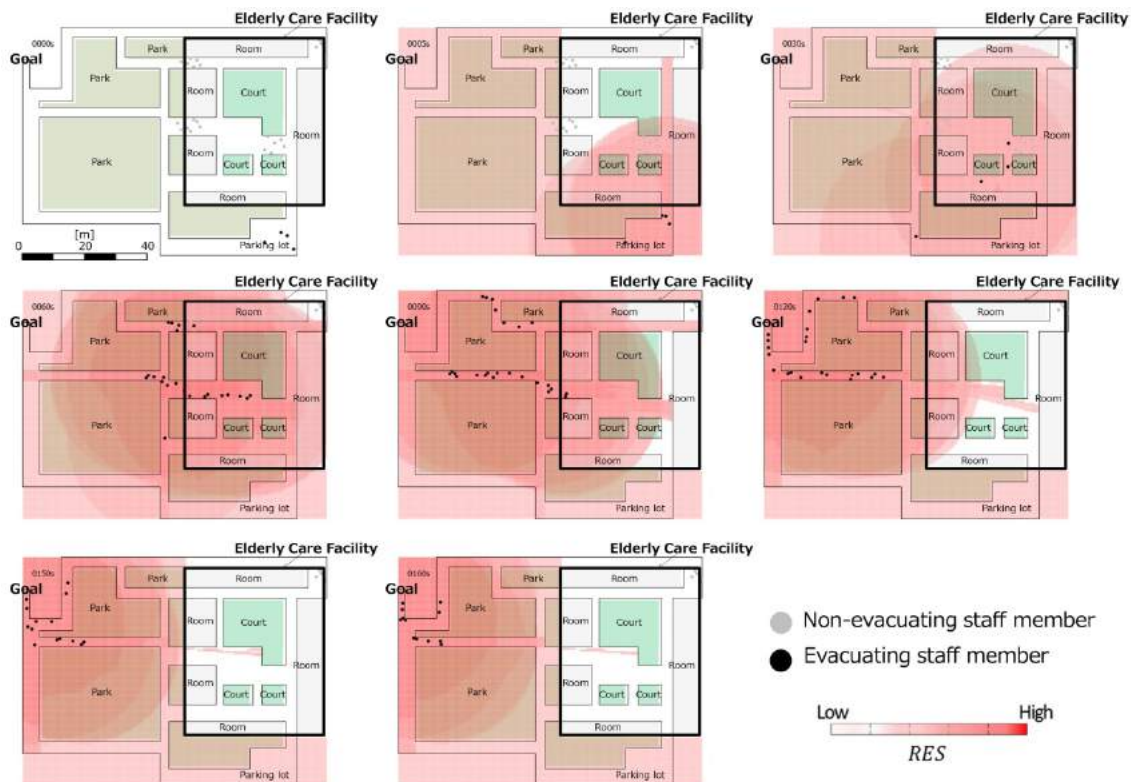


Figure 6: Snapshots of the tsunami evacuation simulation

staff members. Finally, she was washed away by the tsunami

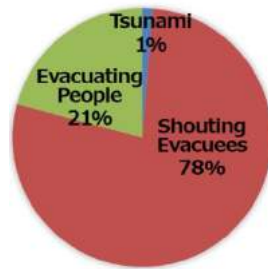


Figure 9: Sources that create RES during the last push of the start of evacuation

but, fortunately, was rescued.

Fig. 8 shows the degree of contribution to the change in the mean ALD by each source that creates RES. Fig. 9 shows the sources that create RES during the last push of the start of evacuation. The source of shouting evacuees is very effective for the start of evacuation in the facility, according to both figures. The source of evacuating people is less effective for the start of evacuation, according to Fig. 8. On the other hand, Fig. 9 shows that evacuating people is more or less effective as a last push of the start of evacuation. We can assume that many staff members increased their ALD by feeling RES created by shouting evacuees. Finally, they started evacuation as soon as they saw evacuating staff members. The tsunami itself is less effective for the start of evacuation, according to both figures. This is because the number of staff members who can see the tsunami is limited. Many staff members were in the facility and could not see the tsunami.

4. Conclusions

We used the tsunami evacuation simulation, which consists of the evacuee generation model and the evacuee behavior model, in the elderly care facility during the 2011 Tohoku tsunami. The main conclusions of this study are noted below:

1. We proposed the evacuee generation model based on the "cooperative creation of social reality." The basic concept of this model can be expressed as follows. First, the reality of evacuation start (RES) is created by various sources. Second, the awareness level of danger (ALD) of a person is increased gradually by feeling RES. Third, when ALD reaches the upper limit, the person starts evacuation and becomes a new source.
2. The simulation in the elderly care facility during the 2011 Tohoku tsunami is validated under the condition in which the sources that create RES were set as shown in Table 2, and the upper limit of ALD using a uniformly distributed random number was set.
3. The area of the route toward the goal and close to the goal was advantageous for the start of evacuation from the viewpoint of RES. On the other hand, it was difficult for the evacuation to start in the area that was not on the route toward the goal and was far from the goal (i.e., area E). RES was not created in area E at all. Staff members

there could not start evacuation because they could not feel any RES.

4. The start of the evacuation of the staff members in area C played an important role in effecting the start of the evacuation of others in the elderly care facility.
5. Shouting evacuees as a source that creates RES was very effective for the start of evacuation in the facility. It can be assumed that many staff members increased their ALD by feeling RES created by shouting evacuees. Finally, they started evacuation as soon as they saw evacuating staff members.

References

1. Cabinet Office (government of Japan) : The Questionnaire Survey to Residents about Evacuation behavior under the Great East Japan Earthquake, http://www.bousai.go.jp/jishin/tsunami/hinan/pdf/20121221_chousa1_3.pdf (in Japanese, accessed 2014-7-2).
2. Dohi, Y., Okumura Y., Koyama M. and 2016. Evacuee Generation Model of the 2011 Tohoku Tsunami in Ishinomaki, Journal of Earthquake and Tsunami, Vol.10, No.2, pp.1640010_1-1640010_17.
3. Kiyono, J., Miura, K., Takimoto, K. and Nakajima, Y., 1994. Evacuation Simulation in Emergency by Using DEM, Papers of the Annual Conference of the Institute of Social Safety Science, Vol.4, pp.321-327 (in Japanese).
4. Mikami, T., 2014, The Survey Analysis about the Victims by the Tsunami under the Great East Japan Earthquake - Yamada-Cho and Ishinomaki City -, Journal of Japan Society of Civil Engineers, Ser. A1 (Structural Engineering & Earthquake Engineering), Vol.70, No.4, pp.908-915 (in Japanese with English abstract).
5. Milgram, S., Bickman, L. and Berkowitz, L., 1969. Note on the Drawing Power of Crowds of Different Size, Journal of Personality and Social Psychology, Vol.13, pp.79-82.
6. National Police Agency, 2017. Countermeasures for the Great East Japan Earthquake, https://www.npa.go.jp/news/other/earthquake2011/pdf/higaijokyo_e.pdf (accessed 2017-9-12).
7. Okumura Y., Nakamichi N. and Kiyono, J., 2013. Evacuation Behavior from Unexpected Huge Tsunami: a Case Study of the 2011 Tohoku Tsunami in Shizugawa, Journal of Japan Society of Civil Engineers, Ser. B2 (Coastal Engineering), Vol.69, No.2, pp.1_1366-1_1370 (in Japanese with English abstract).
8. Okumura Y., Ogawa Y., Dohi, Y. and Kiyono, J., 2016. Numerical Analysis of Regional Difference for Start of Tsunami Evacuation, Journal of Japan Society of Civil Engineers, Ser. B2 (Coastal Engineering), Vol.72, No.2, pp.1_1603-1_1608 (in Japanese with English abstract).
- 10.

SEISMIC RISK ASSESSMENT OF HANOI USING THE JAPANESE METHOD

Takanobu Suzuki, Ha Thai Son

ABSTRACT

The seismic risk was assessed for a part of Hanoi by applying a ground motion prediction formula and a liquefaction assessment method developed in Japan. The analysis was performed for a target area of approximately 50 square kilometers using an elevation map. Bore holes data were also collected, and the ground of the areas lacking boring information was assessed using microtremor measurements. Ground motion prediction for an inland earthquake was calculated based on the ground assessment results. It was determined that the Mercalli intensity would be 7 or greater on the ground surface if an earthquake occurs at an epicentral depth of less than 30 km and that the loose sand stratum will be liquefied by this large shaking.

KEYWORDS: seismic risk, ground motion, liquefaction, bore hole data, microtremor measuring

DR. Takanobu Suzuki

Professor, Department of Civil and Environmental Eng., Toyo University, Japan

MR. Ha Thai Son

Former Graduate Student from Vietnam, Toyo University

1. Introduction

Although Vietnam has less seismic activity than Japan, there are reports of seismic damage, and according to Vietnam Academy of Science and Technology (VAST) there are several faults in northern Vietnam. An earthquake-resistant design code was introduced in Vietnam in 2006, and new buildings are designed with seismic forces taken into consideration. However, existing buildings do not have sufficient resistance to seismic forces, and if an earthquake occurs on one of these faults, substantial damage is expected near its epicenter.

Hanoi, the capital city of Vietnam, is located on a floodplain in the middle of the Red River, with large cities on almost-flat land. Just under Hanoi, a fault runs along the Red River, and in the worst case, an inland earthquake may occur. In such a case, the buildings without earthquake-resistant designs may collapse, resulting in significant damage. The vast Red River floodplain is not uniform, having areas of ground where the earthquake motion is particularly large or the sand may liquefy. Predicting the degree of damage through a prior assessment will allow disaster-reduction measures to be taken. Therefore, understanding the seismic risk by assessing Hanoi's ground condition will give us important information.

Japan is a country where earthquakes occur frequently, and seismic risk can be established based on ground assessment data that becomes the basic information for disaster-prevention measures. Japan Seismic Hazard Information System (J-SHIS) which is developed by National Research Institute for Earth Science and Disaster Resilience (NIED) is one source of publicly-available seismic risk data.

This data shows the predicted impact of future quakes based on seismic activity probabilities and the results of ground assessment across Japan. Although the ground assessment method and earthquake prediction methods used are based on data acquired in Japan, we assume that these methods can also be utilized in other countries. In Japan, the PL value represents the soil liquefaction risk index, and it is desirable to take measures to address potential liquefaction in areas where the PL value is large. The Ministry of Land, Infrastructure, Transport and Tourism (MLIT) has published a worksheet calculation program so that the soil liquefaction risk for a housing site can easily be assessed; the soil liquefaction risk is automatically calculated when values based on subsurface investigation data are entered.

This study attempts to assess the seismic risk of Hanoi by applying these Japanese disaster-prevention techniques to the ground data of several districts in Hanoi. The seismic activity is assumed to occur approximately once every 1,000 years, and by simulating the quake hypocenter at different depths, the size of an earthquake that may affect Hanoi can be assessed. We also attempted to assess the soil liquefaction risk using the PL value. The method used in this research could be developed to apply to all areas of Hanoi, and we believe that these risk assessment results will provide essential data for considering disaster prevention for Hanoi.

2. Earthquakes environment and landforms of Hanoi

According to studies by Vietnam, there are numerous fault zones running in the northwest to the southeast direction in Northern Vietnam, and the Red River fault zone, assessed to have moderate seismic activity, passes through Hanoi City. According to the published map from VAST, the magnitude of the earthquake predicted to occur once every 1,000 years in Hanoi is 6.2. Small- to medium-sized earthquakes have been confirmed along the fault zone. Although no large earthquake has been confirmed in the history of Hanoi, because it lies on a fault band, it is necessary to understand the risks anticipated when a future earthquake occurs.

In Vietnam, micro-topographic maps and subsurface geological maps of the entire country are available to the public. The scales are rough, but an outline of the ground conditions can be understood. The whole of Hanoi is located mostly in the floodplain, and the subsurface geology is a Thai Binh stratum throughout the city. Although this is a stratum in the floodplain that contains a large portion of clay, further detailed information could not be obtained.

Therefore, an elevation map was created using the DEM data. The area targeted in this study is 7 km × 7 km, centered on the Ba Dinh district of Hanoi. The Old City and government agencies of Hanoi are located in this district. Figure 1 shows the created elevation map. The elevation of the target area is 5 m to 15 m, and the map shows that most of the area has an elevation of 10 m or lower. Levees built along the rivers and lakes are 10 m or taller, and the levee built between the Ho Thai Lake and the Red River has an elevation of 15 m. The elevation near the Old City, where the government agencies are located, is approximately 10 m. Many ponds are scattered

in the lowland region of the area of interest, and this area may have once been a channel. Even terrain that may look flat at first glance has a height difference of about 10 m.

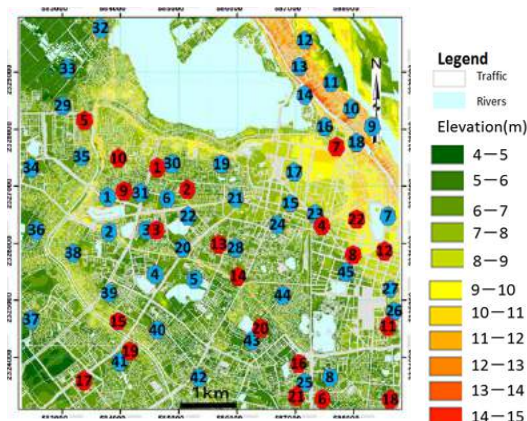


Figure1: Elevation map of the target area(red circle: bore data point, blue circle: micro tremor point)

3. Assessment of ground environment

We could acquire data from 22 bore holes in the area of interest which are shown in Figure1 as red numbers. Although the thicknesses of the strata differed, the bore holes data resulted in similar data. The area is composed of four strata, in order from the top: the Thai Binh and the Hai Hung strata, which are both alluvial clay, the Vinh Phuc stratum, consisting of alluvial sand, and the Hanoi stratum, which consists of diluvium. There are cases where clay and sand are mixed in the alluvium.

Next, we calculated the natural period of the ground TG. The natural period of the ground is assessment value required for construction design, and a longer natural period indicates softer ground. A formula from Specifications for Highway Bridges is used for this calculation. Equation (1) is the formula, and the natural period is four times the time it takes for a shear wave to pass through the subsurface.

$$TG = 4 \sum H_i / V_{si} \quad (1)$$

Where H_i is depth of each layer and V_{si} is the shear wave velocity of the layer numbered as i .

The shear wave velocity, V_s , can be estimated empirically from the N value of SPT. The resulting values are between 0.5 and 1.0 s, confirming that this ground requires caution when designing earthquake-resistant structures.

The average S-wave velocity, $AVS30$, as well as the natural period of the ground are important criteria for ground assessment. The $AVS30$ is the average value of the shear wave velocities up to 30 m below the surface, and the smaller the value is, the softer the ground. In J-SHIS, ground motion is predicted using a subsurface amplification factor that is based on the $AVS30$. The formula is beneath.

$$AVS30 = (\sum H_i \cdot V_{si}) / 30 \quad (2)$$

As with TG, the shear wave velocity can be estimated from the N value. $AVS30$ values calculated using the data from the 18 bore holes data that reached depths of 30 m or greater. The calculation results are between 170 m/s and 220 m/s, and the values are small due to the soft clay stratum in the central part of the target area.

Of the 22 bore holes data, 12 reached the diluvium. Because the amount of boring data is limited relative to the

surface area, the ground was also assessed using microtremor analysis to supplement the boring data. The H/V spectrum of the microtremor indicates the characteristics of a Rayleigh wave transmitted through the subsurface, and the peak frequency of the spectrum is similar to the normal-mode frequency. In this study, a velocity meter (NewPIC, System and Data Research Co., Ltd.) was used, and measurements were taken in 45 places shown in Figure 1 as blue numbers. The H/V spectrum is calculated by applying the Fourier transform to the measured waveforms in the vertical and horizontal directions, and, after smoothing using the moving average, the horizontal and vertical ratios were calculated, and the average of the two directions was calculated. A single measurement was approximately 40 seconds, and four to six measurements were taken per point. The average was calculated, excluding noisy data, and the H/V spectrum was determined for each observation point.

The natural period of the ground, TG, calculated from the boring data and the peak frequency acquired by the microtremor is compared with the predominant period obtained by converting the period. The predominant period obtained from the tremor is slightly larger; however, it is confirmed that the two are roughly consistent.

The ground vibration characteristic is assessed using both the TG from the boring data and the predominant period from the microtremor data. Figure 2 shows a map of the natural period of the ground. We can see that there is ground with a period of approximately one second in the downstream area of the Red River. Where the ponds are scattered, there is ground with a period of approximately one second that means to quake with large amplitude. From the tremor measurement results, it can be confirmed that the levee along the Red River has a period of approximately 0.7 seconds. The period around the Old City is relatively short, approximately 0.5 seconds.

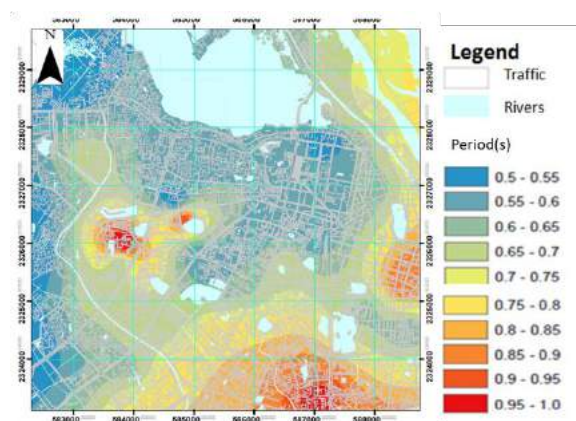


Figure 2: Distribution of estimated natural period TG

4. Prediction of ground motion during an inland earthquake

Ground motion is estimated using the prediction equation in J-SHIS and the results obtained in Chapter 3. The simple ground motion prediction formula in J-SHIS has two stages. First, $PGVb600$, which is the maximum velocity in the bedrock of a shear wave velocity of 600 m/s, is calculated using the attenuation formula from the fault, whose functions include the magnitude, seismic depth, and shortest fault length. For this calculation, the target area is assumed to have a

horizontal fault plane just beneath it, and the same values are used for the epicentral depth and fault length. A magnitude of 6.2 is used based on past research. The epicentral depth is unknown, so calculations are performed for three depths: 10 km, 20 km, and 30 km. In these simulations, the maximum velocity in the bedrock directly under the district of interest is calculated to be a constant value in each case.

Next, the maximum velocity of the ground surface is calculated by multiplying the amplification factor, R , calculated from the AVS30, times the estimated velocity in the bedrock. The formula of R is beneath.

$$\log R = 2.367 - 0.852 \log AVS30 \quad (3)$$

The greater the AVS30, the greater the maximum velocity. Although both the attenuation formula and the amplification factor are regression formulas based on Japanese data, we assume that they are used for Vietnam as they are the same in Vietnam. Figure 3 shows the map of amplification factor R .

Figure 4 shows the simulation results at the depths of 20km. The maximum velocity of the ground surface is approximately 30 cm/s. The results of depth of 10 km and 30km are about 40cm/s and 20cm/s respectively. In all three cases, the maximum velocity is greatest near the center of the target area, where the soft clay is deposited. We found that, when this maximum velocity is converted to the Mercalli intensity scale, it is a large quake of 7 to 8.

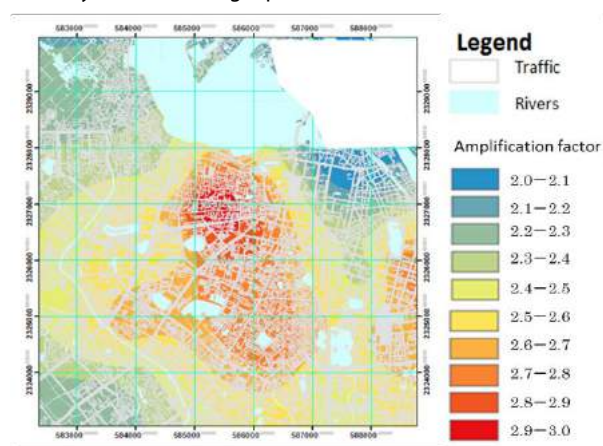


Figure 3: Distribution of amplification factor R

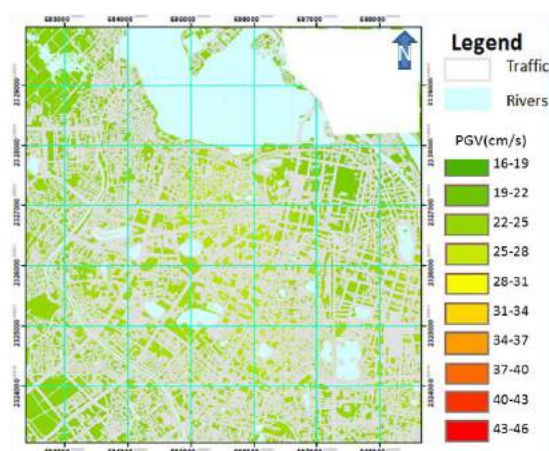


Figure 4: Estimated peak ground velocity at the time of inland earthquake in case of 20km depth

5. Assessing soil liquefaction risk using PL value

The target area may experience liquefaction when an earthquake occurs directly beneath it if there is a loose sand stratum. We performed a liquefaction assessment using the bore holes data obtained in this study. The criteria to determine is the PL value, and software released by the City Bureau and National Institute for Land and Infrastructure Management (NILM) of MLIT that determines the liquefaction risk of a housing site was used. This software provides assessments based on the Building Foundation Structure Design Guidelines and on Specifications for Highway Bridges, and in this study, we adopted the assessment calculation methodology of the latter.

In the liquefaction assessment calculation, the shear stress (L) acting on each stratum and the liquefaction resistance force (R) are calculated to determine the ratio such that $FL=R/L$. If the value of FL is 1 or smaller, the soil will liquefy, and if it is greater than 1, the soil will not liquefy. The smaller the FL value, the greater the soil liquefaction risk. The PL value is an index calculated, for those areas where $FL < 1$, by adjusting the calculated FL value from the ground surface to 20 m deep. The greater the PL value is, the greater the soil liquefaction risk is at that point. The formula is beneath.

$$PL = \int (1 - FL(z)) (10 - 0.5z) dz \quad (0 < z < 20m) \quad (4)$$

Where z means coordinate of vertical depth from the surface, and $FL(z)$ is FL Value at z m depth with the condition to be set to $FL = 1$, if the FL Value exceeds 1 at the depth. The thicker the liquefying stratum is, or the smaller the FL value is, the larger the PL value becomes.

The shear stress acting on the stratum is proportional to the acceleration of the ground surface. Per Specifications for Highway Bridges, the horizontal seismic coefficient, kh , is selected and used in the calculations. In this study, the calculations were performed for two cases: $kh=0.12$ and $kh=0.2$. The standard horizontal seismic coefficient for a Vietnamese building with an earthquake-resistant design is $kh = 0.12$, and $kh = 0.2$ is the standard horizontal seismic intensity for designs in Japan. According to the ground motion prediction for inland earthquakes, this degree of acceleration is assumed to be generated.

The calculation results for the PL values are shown in Figure 5. Twelve pieces of boring data were used. This map is roughly interpolated because only twelve data were used and liquefaction depends on local stratum condition. We assumed as the strata of surface gradually changed. The ground surface of the area of interest consists mainly of clay, but there are some sand strata mixed in some areas. For $kh = 0.12$, the PL value is small, and the soil liquefaction risk is low. On the other hand, for $kh = 0.2$, there are two areas with large PL values. The first, a point near Ho Thai Lake, although in an area of soft clay stratum, has a small plasticity index, I_p , which results in a high risk of liquefaction according to the Japanese judgement rule. The other, at a point along the Red River, the soft sand stratum is shallow, resulting in a large PL value.

In the case where a large earthquake occurs that significantly exceeds the horizontal seismic design coefficient for Vietnam, a possibility exists that the loose sand strata in the floodplain will liquefy, causing substantial damage. However, the assessment method used in this research is an estimation formula developed in Japan, and it is necessary to estimate Japanese formula and consider the application conditions. Additionally, the interpolated map is too rough,

because of the condition with one bore hole in four square kilometers. More detail estimation is needed about liquefaction.

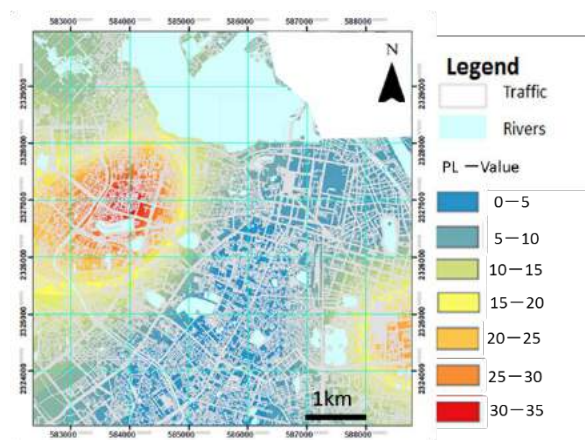


Figure 5: PL Value Map at the condition of horizontal seismic force $k_h = 0.2$

6. Conclusion

The seismic risk was assessed for a part of Hanoi by applying a ground motion prediction formula and a liquefaction assessment method developed in Japan. The analysis was performed for a target area of approximately 50 square kilometers using an elevation map. Bore holes data were also collected, and the ground of the areas lacking boring information was assessed using microtremor measurements. Although these assessments were conducted for a small area, the ground's characteristics differed.

In addition, ground motion prediction for an inland earthquake was calculated based on the ground assessment results. It was determined that the Mercalli intensity would be 7 or greater on the ground surface if an earthquake occurs at an epicentral depth within 30 km and that the loose sand stratum will also likely be liquefied by this large shaking. The risk of earthquakes and soil liquefaction are significantly influenced by the assumed earthquake, but it is necessary to think of the worst case because there is a fault zone beneath the city. Because only a part of Hanoi was analyzed in this study, it is desirable to study a larger area of the city. In addition, although the Japanese estimation formula was applied as-is, it is necessary to verify its validity for use in Vietnam.

Acknowledgements

We appreciate Dr. Nguyen Anh Duong in VAST for providing precious data and helpful advice.

References

1. Nguyen Sinh Minh, Pham Dinh Nguyen et al., 2014. Seismic hazard assessment for the expanded Hanoi city, establishing of detail seismic zoning map for Ha Dong, Son Tay, Hoa Lac areas by scaled 1:25.000, building of database of ground motion features according to the above maps. Final report of scientific research funding program supported by Hanoi city Government (in Vietnamese).
2. Shigeki Senna and Hiroyuki Fujiwara, 2011. Development of estimation tools for earthquake ground motion. Technical note of the National Research Institute for Earth Science and Disaster Prevention No.354, 2011 (in Japanese).

3. Japan Road Association, 2012. Specifications for highway bridges Part V: Seismic design.

4. City Bureau and National Institute for Land and Infrastructure Management, Ministry of Land, Infrastructure, Transport and Tourism, 2014. Calculation sheet for potential of liquefaction damage at housing site (in Japanese).

STUDY ON NUMERICAL ANALYSIS OF IMPACT RESPONSE OF CONCRETE PLATE SUBJECTED TO MEDIUM SPEED COLLISION OF STEEL PROJECTILE

Aiko Furukawa, Masato Goto, Junji Kiyono
and Hitoshi Nakase

ABSTRACT

Tokyo Electric Power Services Co. Ltd. and National Defense Academy of Japan conducted a medium speed collision experiment between a steel projectile and a concrete plate. In this study, numerical analysis of this collision experiment was conducted using a Refined DEM. In the experiment, three failure modes were observed, penetration, surface failure only, and backside failure. By improving a stress-strain model, the analysis results showed good agreements with the experiment.

KEYWORDS: Collision phenomena, Concrete plate, Steel projectile, Refined DEM

AIKO FURUKAWA

Associate Professor, Department of Urban Management, Graduate School of Engineering, Kyoto University, Japan.
E-mail: furukawa.aiko.3w@kyoto-u.ac.jp, **corresponding author**

MASATO GOTO

Master Course Student, Department of Urban Management, Graduate School of Engineering, Kyoto University, Japan.
Email: goto.masato.66a@st.kyoto-u.ac.jp

JUNJI KIYONO

Professor, Department of Urban Management, Graduate School of Engineering, Kyoto University, Japan.
Email: kiyono.junji.5x@kyoto-u.ac.jp

HITOSHI NAKASE

Engineer, Tokyo Electric Power Services Co. Ltd., Japan.

1. Introduction

The number of annual tornado occurrence is high in Japan. From 2012 to 2016, 87 tornadoes occur in average per year in Japan. In some cases, tornado was so strong that some people got injured or even killed by tornado. As an example, in 2013, 76 people got injured, and 247 houses were damaged due to tornado in Saitama prefecture [1]. Strong tornadoes can blow off even heavy objects such as steel pipes or vehicles. The velocity of a flying object is roughly around several ten m/s [2]. We define this velocity range as "medium speed" since this is larger than the earthquake shaking but smaller than the impact by missile.

If a strong tornado attacks a nuclear power plant and breaks some components, hazardous radioactive materials might come out. This will cause very severe damages. Therefore, a tornado is crucial especially for nuclear power plants. Nevertheless, researches on medium speed collision phenomena is not enough. For these reasons, Tokyo Electric Power Services Co. Ltd. conducted an experimental research on the impact response of a concrete plate subjected to medium speed collision by a steel projectile.

National Defense Academy of Japan developed a launch device [3,4]. This device can reproduce collision phenomena

under various values of the initial velocity of the projectile. Using this device, Tokyo Electric Power Services Co. Ltd. and National Defense Academy of Japan conducted an experiment, investigated the failure mode of concrete plates and measured the movement of the steel projectile [4].

In this research, the numerical analysis of collision phenomena is done with a refined DEM [5]. The objective is to improve stress-strain model of the refined DEM so that the analytical results match the experimental results.

2. Analysis Method

2.1 Refined DEM

This study employs a refined DEM [5] to simulate a series of structural dynamic behaviors from elastic to failure to collapse phenomena. A structure is modeled as an assembly of rigid elements, and interaction between elements is modeled with multiple springs and multiple dashpots that are attached to the surfaces of elements. Fig. 1(a) shows a spring for computing the restoring force (restoring spring), which models the elasticity of elements. The restoring spring is set between continuous elements. Fig. 1(b) shows a spring and dashpot for computing the contact force (contact spring and dashpot) and modeling the contact, separation and recontact between elements. The dashpots are introduced to express energy dissipation due to the contact. Structural failure is modeled as breakage of the restoring spring, at which time the restoring spring is replaced with a contact spring and a contact dashpot. Structural collapse behavior is obtained using these springs and dashpots. The elements shown in Figs. 1(a) and (b) are rectangular parallelepipeds, but the method does not limit the geometry of the elements. The surface of an element is divided into small segments as shown in Fig. 1(c). A segment in the figure is rectangular, but the method does not limit the geometry of the segment. The black points indicate the representative point of each segment, and the relative displacement or contact displacement between elements is computed for these points. Such points are referred to as contact points or master points in this study. One restoring spring and one combination of contact spring and dashpot are attached to one segment at each of the representative points in Fig. 1(c). The spring constant for each segment is derived on the basis of the stress-strain relationship of the material and the segment area.

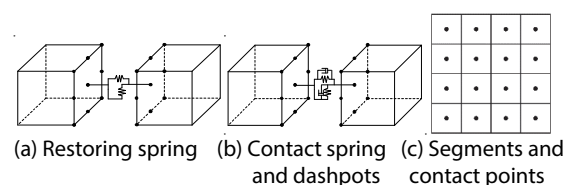


Figure 1: Basic concept of analysis method

Forces acting on each element are obtained by summing the restoring force, contact force and other external forces such as the gravitational force and inertial force of an earthquake. The behavior of an element consists of the translational behavior of the center of gravity and the rotational behavior around the center of gravity. The translational and rotational behaviors of each element are computed explicitly by solving Newton's law of motion and Euler's equation of motion.

2.2 Spring constant of each element

There are two types of springs, namely restoring and contact springs. It is considered that each segment has its own spring. The springs are set for both the normal and shear directions of the surface. The spring constants per area in the normal and shear directions, k_n and k_s , are obtained as follows.

$$k_n = \frac{E}{(1-\nu^2)\lambda}, \quad k_s = \frac{E}{2(1+\nu)\lambda} \quad (1)$$

where E is Young's modulus, ν is Poisson's ratio, and λ is the distance from the surface at which the spring is connected to the center of gravity.

2.3 Modeling of elastic behavior

It is assumed that two elements, A and B , are continuous, and that a contact point of element A is continuous with element B . Let G_A and G_B be the centers of gravity of elements A and B respectively. Let λ_A be the distance from G_A to the surface of element A in contact. Let λ_B be the distance from G_B to the surface of element B in contact. Let E_A and E_B be Young's moduli and ν_A and ν_B be Poisson's ratios of elements A and B .

The spring constants per area for the elements A and B are obtained from Eq. (1). Assuming that these springs are connected in series, the spring constants between elements per area, \bar{k}_n and \bar{k}_s , are

$$\bar{k}_n = \frac{1}{\frac{\lambda_A}{E_A/(1-\nu_A^2)} + \frac{\lambda_B}{E_B/(1-\nu_B^2)}}, \quad \bar{k}_s = \frac{1}{\frac{\lambda_A}{E_A/2(1+\nu_A)} + \frac{\lambda_B}{E_B/2(1+\nu_B)}} \quad (2)$$

The normal direction of forces is the direction perpendicular to the surface of the master point of element A .

Let σ and τ be the normal and shear stresses acting at the contact point, and u_n and u_s be the relative displacements between the adjacent master and slave points in the normal and shear directions. The relation between traction (σ , τ) and relative displacements (u_n , u_s) is then written as

$$\sigma = \bar{k}_n u_n, \quad \tau = \bar{k}_s u_s \quad (3)$$

The elastic behavior of structures is demonstrated by the multiple restoring springs between continuous elements until the restoring force of a spring reaches its elastic limit. The elastic limits are modeled using criteria of tension and compression failure. When a spring reaches one of these limits, it is judged that failure has occurred at the segment of the spring. After the failure, the restoring spring is replaced with a contact spring and dashpot at this segment.

2.4 Modeling of contact and recontact between elements

If a segment of an element is in contact with another element with which the segment is not continuous via the restoring spring, the contact spring and dashpot generate the contact force. Contact between a segment and the surface of another element is detected at each time step for

all segments that are not continuous with other elements via a restoring spring. The spring constant and the contact forces in the normal and shear directions are calculated in the same manner as for the restoring force. The differences from the case for the restoring force are that the contact force is generated only while the compression force acts. The dashpot is introduced to express the energy dissipation of the contact. The damping coefficient per area is calculated as follows.

$$c_n = 2h_n \sqrt{m_{ave} k_n}, \quad c_s = 2h_s \sqrt{m_{ave} k_s} \quad (4)$$

where h_n and h_s are the damping constants for the normal and shear directions. m_{ave} is the equivalent mass per area relevant to this contact. In this study, m_{ave} is calculated as

$$m_{ave} = \rho_A \lambda_A + \rho_B \lambda_B \quad (5)$$

where ρ_A and ρ_B are the mass densities of elements A and B . The damping constants should be evaluated according to the properties of the elements, but this study assumed damping ratio is zero ($h_n = h_s = 0.0$) since the experimental behavior could be traced without damping.

2.5 Equations of Motion

The equations of motion can be constructed using the restoring and contact forces and other external forces. The motion of each element is obtained by solving the two equations of motion. One is the equation for the translational motion of the center of gravity, and the other is the equation for the rotational motion around the center of gravity. By solving the equations of motion step by step, the position of each element can be traced, and the whole structural behavior can be obtained.

3. Numerical Analysis of the Collision Test

3.1 Overview of collision test

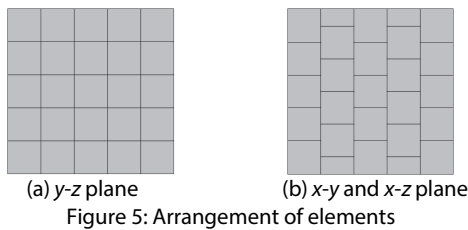
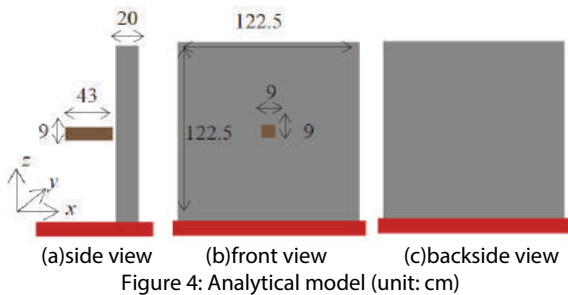
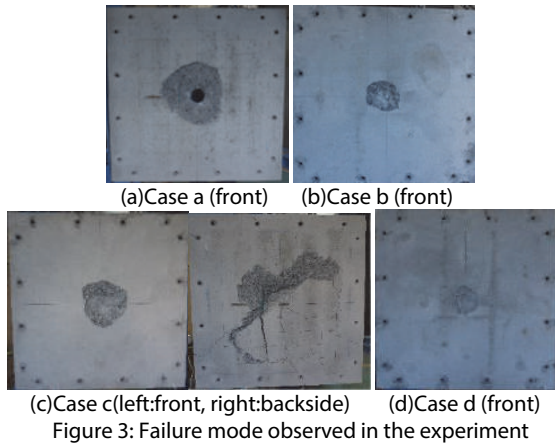
National Defense Academy of Japan developed a launch device (Figure 2). This device can create various collision phenomena using compressive air pressure. They caused several medium speed collision phenomena for various conditions, changing velocity of the projectile or thickness of the concrete plate (Table 1). For each case, failure mode of the concrete plate (Figure 3), movement of the steel projectile were measured.



Figure 2: Experiment setup
(left: launch device, right: projectile)

Table 1: Experimental case and its failure mode

Case	Thickness of concrete [cm]	Velocity [m/s]	Failure mode
a	10	69.7	Penetration
b	20	56.7	Front failure
c	20	81.2	Backside failure
d	30	81.9	Front failure



3.2 Analytical model

Analytical model is shown in Fig.4. A concrete plate is shown in gray, a projectile is shown in brown, and a fixed basement is shown in red. The concrete plate has the width and height of 122.5cm. The depth is 10cm for case a, 20cm for case b and case c, and 30cm for case d. The concrete was modeled as an assembly of small element with the width and height of 3.0625cm and depth of 2.5cm. Arrangement of elements for each plane is shown in Figure 5. The elements was arranged so that the boundary between elements in x-y and x-z plane is not in a straight line. Therefore, element size in the even column is halved.

A steel projectile was simply modeled with one rectangular parallelepiped element. The section size is 9cm × 9cm and the length is 43cm.

The distance between a projectile and a concrete plate at the initial condition is 2.6cm. The initial velocity shown in Table 1 was applied to the projectile.

3.3 Analytical model

Analytical parameters used was determined based on the element experiment. The projectile has the mass of 8.3kg, Young's modulus of 2.05×10^{11} N/m², poisson's ratio of 0. Concrete plate has the density of 2.3×10^3 kg/m³, Young's modulus 2.793×10^{10} N/m², and poisson's ratio of 0.2. As for concrete, the compression strength is $f_c = 4.5 \times 10^7$ N/m², the ultimate compression strength after compression failure is

$f_{c2} = 2.5 \times 10^7$ N/m², tensile strength is $f_t = 4.5 \times 10^6$ N/m². The fracture energy G_F [N/m] was estimated using the equation below [6].

$$G_F = 10(d_{max})^{1/3} f_{ck}^{1/3} \quad (6)$$

where d_{max} is largest size of coarse aggregate and the value of 20cm was assumed. f_{ck} is desing strength and the value of compression strength was used.

As for dashpot, the damping ratio of 0.0 was used since the analytical results matched the experimental results when zero value was used.

Time interval of 8.0×10^{-7} s was used.

3.4 Effect of stress-strain model in compression on analytical result

First, the analytical results using three different stress-strain models in compression as shown in Figure 6 were compared with the experimental result of case b. The tension softening was considered in all models. In the model of Figure 6(a), the compression softening was simply modled using the ultimate strength f_{c2} which is smaller than

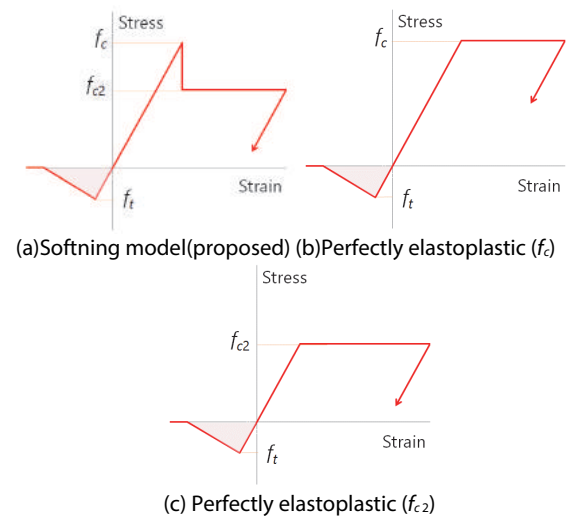


Figure 6: Comparison of stress-strain models in compression (Softening in tension is considered.)

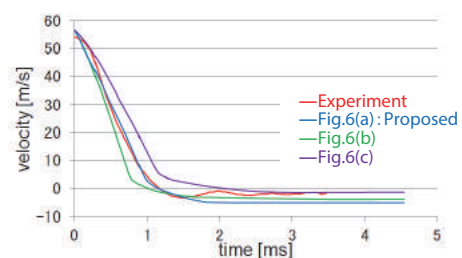
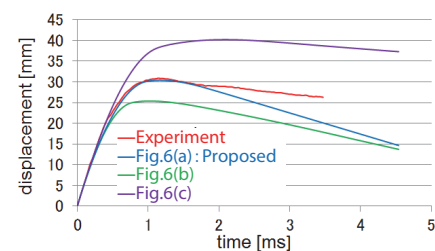
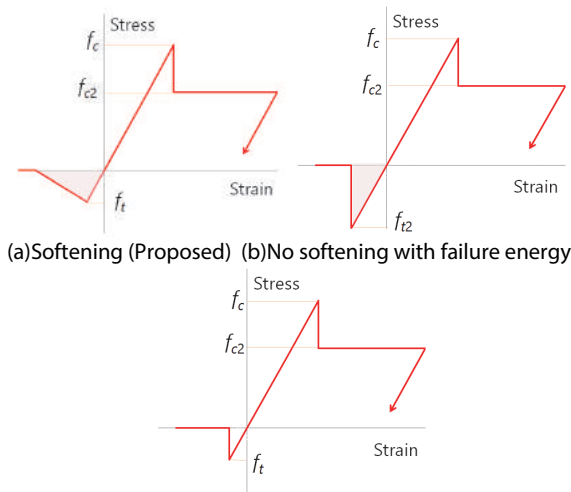


Figure 7: Effect of stress-strain model in compression



(a) Softening (Proposed) (b) No softening with failure energy
Figure 8: Comparison of stress-strain models in tension
(Softening in compression is considered.)

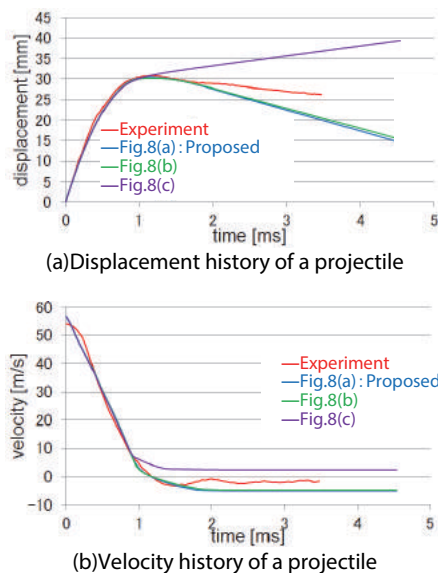


Figure 9: Effect of stress-strain model in tension

the compression strength f_c . In models of Figure 6(b) and (c), the perfectly elastoplastic model was used and no compression softening was considered. The model of Figure 6(b) has the strength of f_c and that of Figure 6(c) has the strength of f_{c2} .

The results are shown in Figure 7. The analytical result using compression softening model (Figure 6(a)) showed good agreement with the experiment compared to two perfectly elastic models (Figure 6(b)(c)). It was found that considering the compression softening was necessary and the validity of stress-strain model of Figure 6(a) was confirmed.

3.5 Effect of stress-strain model in tension on analytical result

Next, the analytical results using three different stress-strain models in tension as shown in Figure 8 were compared with the experimental result of case b. The compression softening was considered in all models. The model of Figure 8(a) is the same with the model of Figure 6(a), and the tension softening and the fracture energy was

both considered. In the model of Figure 8(b), the tension softening was neglected but the fracture energy was considered so that the hatched areas of Figure 8(a) and 8(b) become same. Therefore, the tensile strength of Figure 8(b) is larger than that of the model of Figure 8(a). In the model of Figure 8(c), the tensile strength was considered but the tension softening and fracture energy were both neglected.

The results are shown in Figure 9. The analytical results using Figure 8(a) and 8(b) models considering fracture energy were almost same and showed good agreement with the experimental one. However, the analytical results using Figure 8(c) model neglecting fracture energy overestimated the displacement. From these comparison, it was found that considering the fracture energy is very important in this simulation.

Based on the results, the stress-strain model considering both compression softening and tension softening was found to be the best choice.

3.6 Analysis of collision test

The stress-strain model of Figure 6(a) was used for all cases. The comparison of displacement and velocity histories of the steel projectile are shown in Figure 10. The concrete plate after collision is shown in Figure 11.

In case a where the projectile penetrated the concrete plate in the experiment, the analytical results also showed the “penetrating” behavior as shown in Figure 10(a) and Figure 11(a). The failure modes in Figure 3(a) and Figure 11(a) look very similar. Since the displacement and velocity

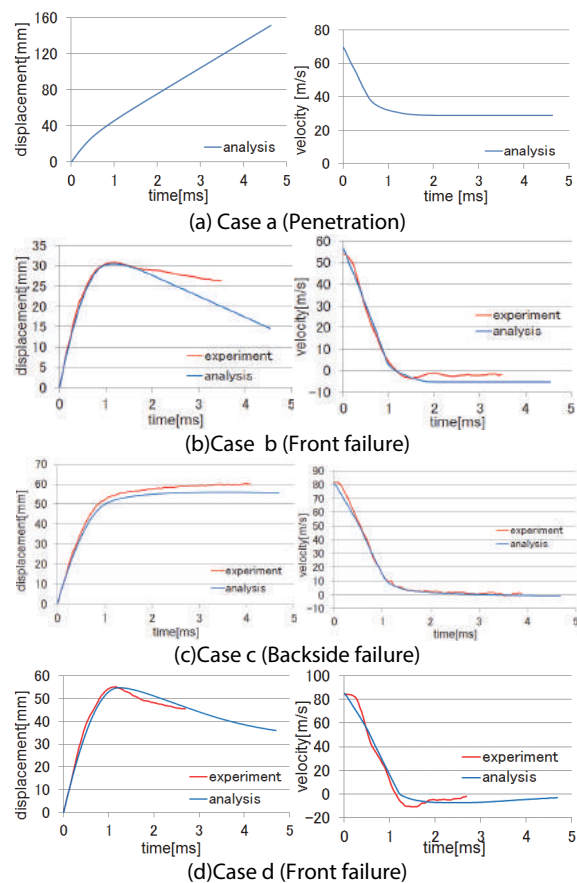


Figure 10: Comparison of analytical and experimental displacement and velocity histories

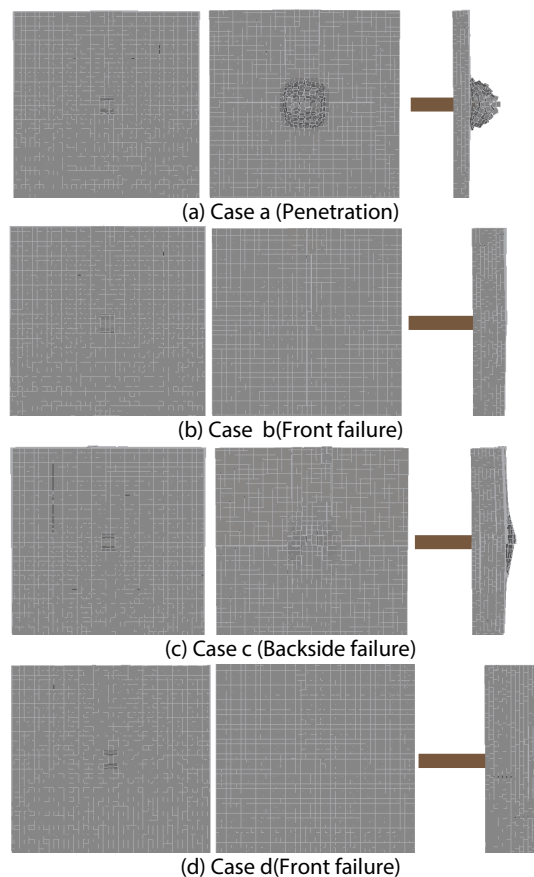


Figure 11: Analytical results

(left: front view, middle: backside view, right: side view)

histoires were not measured in the experiment, the analytical displacement and velocity histories are only shown in Figure 10(a).

For cases b and d where the front failure occurred in the experiment as shown in Figure 3(b) and 3(d), the analytical displacement and velocity histories showed very good agreement with the experimental ones as shown in Figure 10(b) and 10(d). Moreover, only failure occurred on the front side of the concrete in the analysis as shown in Figure 11(b) and 11(d). The concrete plates showed the same failure mode “front failure” in the analysis and experiment.

For case c where the backside failure occurred in the experiment as shown in Figure 3(c), the analytical displacement and velocity histories showed very good agreement with the experimental ones as shown in Figure 10(c). Moreover, the failure occurred both in the front and backside of the concrete in the analysis as shown in Figure 11(c). The concrete plate showed the same failure mode “backside failure” in the analysis and experiment.

As shown above, by introducing the stress-strain model with compression softening and tension softening into the refined DEM, the collision behavior could be traced by the simulation in good accuracy.

4. Conclusions

In this study, numerical analysis with the refined DEM was conducted for medium speed collision phenomena between a steel projectile and a concrete plate.

An improved stress-strain model for the refined DEM was proposed where the compression softening and tension softening of concrete were both taken into account.

Using the newly introduced stress-strain model, the collision experiment was simulated. Analytical results of the collision experiment showed good agreements with the experiment. Three failure modes of concrete plates, namely penetration, front failure and backside failure were all simulated. Moreover, the displacement and velocity histories of the steel projectile showed very good agreement in the analysis and experiment.

The validity of the newly introduced stress-strain model was confirmed and the applicability of the refined DEM into the collision phenomena was verified.

References

1. Japan Meteorological Agency: Database of tornado gust, <http://www.data.jma.go.jp/obd/stats/data/bosai/tornado/list/2011.html>.
2. Guidelines for evaluation of influence of tornado on nuclear power plant, Nuclear Regulatory Commission, 2013.
3. Masuhiro Beppu and Hironori Ueno, A Fundamental Study of the Local Damage of Concrete Plates Subjected to Medium Velocity Impact, Scientific and engineering reports of the National Defense Academy (Japanese), Vol.52, No.2, pp.21-30, 2015.
4. Shinnosuke Kataoka, Masuhiro Beppu, Hiroyoshi Ichino, Tatsuya Mase, Tatsuya Nakada and Ryo Matsuzawa: Failure behavior of reinforced concrete slabs subjected to moderate-velocity impact by a steel projectile, International Journal of Protective Structures, Vol.8, No.3 pp.384-406, 2017.
5. Aiko Furukawa, Junji Kiyono, and Kenzo Toki: Proposal of a Numerical Simulation Method for Elastic, Failure and Collapse Behaviors of Structures and its Application to Seismic Response Analysis of Masonry Walls, Journal of Disaster Research, Vol.6, No.1, pp.51-69, 2011.
6. Society for civil engineers: Design Volume of Standard Specifications for Concrete Structures 2007, 2008.

GEOSYNTHETIC ENCASED COLUMN – AN ALTERNATIVE OF TECHNICAL SOLUTIONS IN SOFT SOIL IMPROVEMENT FOR CONSTRUCTION WORKS IN VIET NAM

CỌC BỌC VẢI ĐỊA KỸ THUẬT – MỘT GIẢI PHÁP KỸ THUẬT TRONG CẢI TẠO NỀN ĐẤT YẾU CHO CÁC CÔNG TRÌNH XÂY DỰNG Ở VIỆT NAM

ME. Pham Tien Bach, Dr. Vo Dai Nhat, ME. Le Quan

ABSTRACT

Several technical solutions such as prefabricated vertical drain (PVD), surface and deep compaction, vacuum drainage, preloading as well as stone column with/without geotextile have been available in soft soil improvement for the construction of structures such as a heavy load building - power plant, storage tanks - petroleum refinery and so on. One of efficient solutions is to use geosynthetic encased columns transferring the loads of the large and rigid structures to stronger soil layers which reduce significantly not only settlement but also consolidation time. The paper presents a study on the use of geosynthetic encased column as an alternative solution for the land reclamation in cases of an extension of fabrication yard PTSC-MC and power plant Nhon Trach 2 (NT2) project. The proposed solution is also compared with other methods and the results are shown.

KEYWORDS: Geosynthetic encased column, soft soil improvement, settlement

TÓM TẮT

Nhiều giải pháp kỹ thuật như bắc thăm, nén chặt đất, bơm hút chân không, gia tải trước cũng như cọc đá kết hợp hoặc không kết hợp vải địa kỹ thuật được biết đến là các giải pháp cải tạo nền đất yếu cho các công trình xây dựng ví dụ như các công trình tải trọng lớn – nhà máy năng lượng, bồn chứa – nhà máy lọc dầu. Một giải pháp hiệu quả là sử dụng cọc bọc vải địa kỹ thuật có tác dụng truyền tải trọng của các công trình lớn, cứng xuống các lớp đất tốt nhằm giảm đáng kể độ lún và thời gian cố kết của đất nền. Bài báo giới thiệu nghiên cứu sử dụng cọc bọc vải địa kỹ thuật như một giải pháp kỹ thuật áp dụng cho dự án mở rộng bãi chế tạo PTSC-MC và dự án nhà máy điện Nhơn Trạch 2. Giải pháp đề xuất được so sánh với một số phương pháp khác và kết quả cũng được trình bày trong bài báo này.

TỪ KHÓA: cọc bọc vải địa kỹ thuật, cải tạo đất yếu, độ lún

ME. PHAM TIEN BACH

Department of Geotechnics, Faculty of Geology and Petroleum Engineering, HCMC University of Technology
Email: tienbachpham@gmail.com, **corresponding author**
Tel: 0902533853

DR. VO DAI NHAT

Lecturer, Department of Geotechnics, Faculty of Geology and Petroleum Engineering, HCMC University of Technology
Email: nhatvodai@hcmut.edu.vn
Tel: 0903013136

ME. LE QUAN

Department of Geotechnics, Faculty of Geology and Petroleum Engineering, HCMC University of Technology
Email: quanlepvp@gmail.com
Tel: 0903312936

1. Introduction

Vietnam has a large coastline area exceeding more than 3260 kms and the Mekong Delta is known as an area of complex river systems and is one of the areas with very poor subsoil. Soft soil is one of the biggest challenges for engineers because of low bearing capacity, high compressibility, low permeability etc. A lot of industrial parks, petroleum refinery, thermal power plants and infrastructure are under construction in the Mekong Delta and along-shore. Many ground improvement techniques are considered and applied in practice in these areas. These methods include precast drainage (PVD), surface and deep compression, vacuum drainage, preloading, stone/sand columns etc. Ground improvement techniques must be carefully investigated to provide the required performance, constructability, time and overall cost. A further development of well-known stone/sand column foundations is the geotextile encased stone/sand column, in contrast to conventional column foundations, encased columns can also be used as a ground improvement and bearing system in very soft soils with undrained shear strength $c_u < 5 \text{ kN/m}^2$. This method is used successfully worldwide in Germany, the Netherlands, Sweden, Italy, Russia, Brazil and Poland¹ but has not been researched and applied in Vietnam. This paper summarizes the results settlement of prefabricated vertical drains combined with vacuum and surcharging for improvement of foundation clays at a land reclamation site in powerplant NT2 and settlement of stone/sand columns for ground improvement at fabrication yard of PTSC-MC. Analytical settlement calculation of the encased stone/sand columns were made and compared with those methods above.

2. Methodology

The principle treatment stratum almost are soft clay or marine clay with high water content, and large void ratio, which has low ground bearing capacity and need to be improved. According to experiences, this stratum present poor drainage property, long consolidation duration and time for strength gain. Particularly, because of low permeability, long consolidation time will be expected. To meet all these highly requirements, some ground improvement technologies are widely applied in Vietnam as below:

2.1 Vertical Drain + Surcharge and Vacuum consolidation

Vertical drains are inserted into the soft soil layer and a sand blanket (draining layer) is installed above to convey water to the periphery of the treated zone before discharge in the environment.

1 Dimitar Alexiew, Marc Raithel

Surcharge material is then added to accelerate the consolidation process, but care shall be taken to the raising speed of the height of the embankment. At various stages of the consolidation, the consolidation layer can only stand a certain load bearing capacity and the critical raising speed shall never be exceeded for risk of general slope failure.

Vacuum preloading consolidation method is applicable to soft soils, especially deep soft soils with a high demand of post-treatment settlement. In this method, vacuum efforts are used to complete the consolidation of most soil masses, controlling post-treatment settlement of deep soils.

Vacuum consolidation method is a proprietary system used for preloading and consolidation soft and very soft saturated impervious soils. The procedure consists of installing vertical and horizontal drainage under an airtight impervious membrane and evacuating the air below the membrane thus imposing an atmospheric pressure on the soft soil.

This vacuum loading process creates an accelerated isotropic consolidation in the soil mass in a relatively short time thereby eliminating the need for long-term and potentially unstable surcharge loads.

2.2 Stone/Sand column

Stone/sand column acts both as a drainage column as well as an inclusion, with a modulus higher than the surrounding clay layer. The application of a surcharge is necessary to mobilize the friction and dissipate the pore pressure that is formed during the installation process. A layer of granular material of sufficient thickness is necessary

between the underface of shallow foundation and the top of the inclusion, so that an arch can develop.

2.3 Encased stone/sand column

To keep the drainage function, and to improve the stone columns as reinforcing elements, geosynthetics are used for column encasement. Encasing stone/sand column with geosynthetics was recommended to enhance the lateral column confinement which resulting on increasing load-bearing capacity. Additionally, encasement prevents the lateral squeezing of stones into the surrounding soil and vice versa.

3. Behaviors of Stone Column/Encased Stone Column, PVD/Encased Stone Column, A Case Study

3.1 Stone Column/Encased Stone Column at fabrication yard of PTSC-MC

Introduction of project

The ground improvement works are to provide a steady platform to support the operation of SL6000 (Kobelco) and the CC2800 (Terex Demag) cranes on the designated routes, which can support up to 500 kPa of transient loads and long term primary settlement should be less than 250mm. The soft clay is reinforced by the stone column with a diameter of 0.6 to 1.0m and depth of treatment from 8 to 14m. The stone columns are arranged in square grids with spacing from 2.2 to 2.4m.

For settlement analysis, the loading is based on service ability stage which is 370kPa at ground surface. The corresponding stress level at the top of soft clay layer i.e. 125kPa.

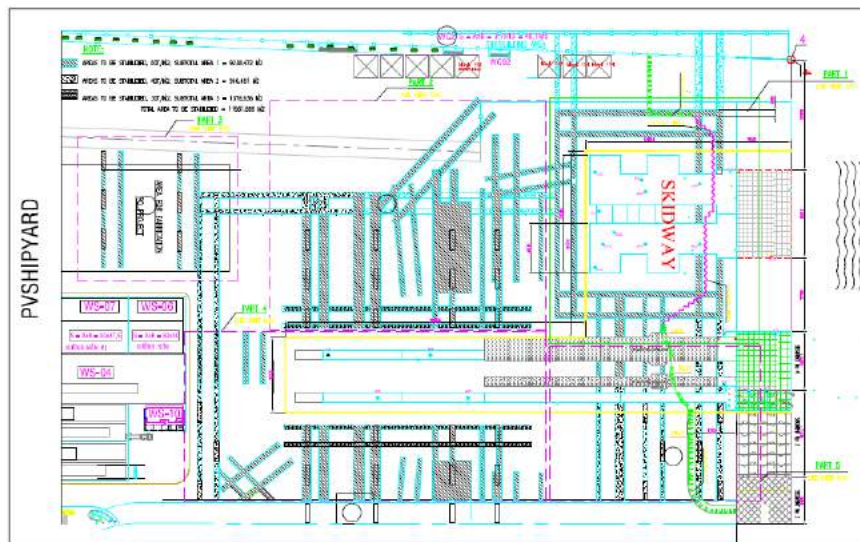


Figure 1: Crane route path layout and load requirements

Geological Condition

The soil layers and its parameters are shown in Table 1.

Table 1: Typical Subsoil Profile

Depth (m)	Soil Type	ϕ_{orig}	c'_{orig} (kPa)	D_{sorig} (kPa)
0 to 0.6	Gravel	40	0	40000
0.6 to 1.5	Sand	30	0	30000
1.5 to 2.5	Crust	0	35	5250
2.5 to 13.5	Soft Clay	0	20	3000

Settlement prediction of stone column

The settlement was calculated based on elastic theory and Priebe's improvement factor (Priebe 1995). The results are summarized as illustrated in Figure 2: The settlement without treatment is 370mm and with treatment is only 175mm.

Settlement prediction of encased stone column

The settlement was estimated based on Raithel and Kempfert's analytical calculation model (Raithel & Kempfert, 2000). This calculation is conducted using data obtained from stone column and soil parameters above. Based on obtained data by using analytical calculation model of stone column configured using geosynthetic encasement $J=3000 \text{ kN/m}$.

The settlement with alternative encased stone column is 125mm.

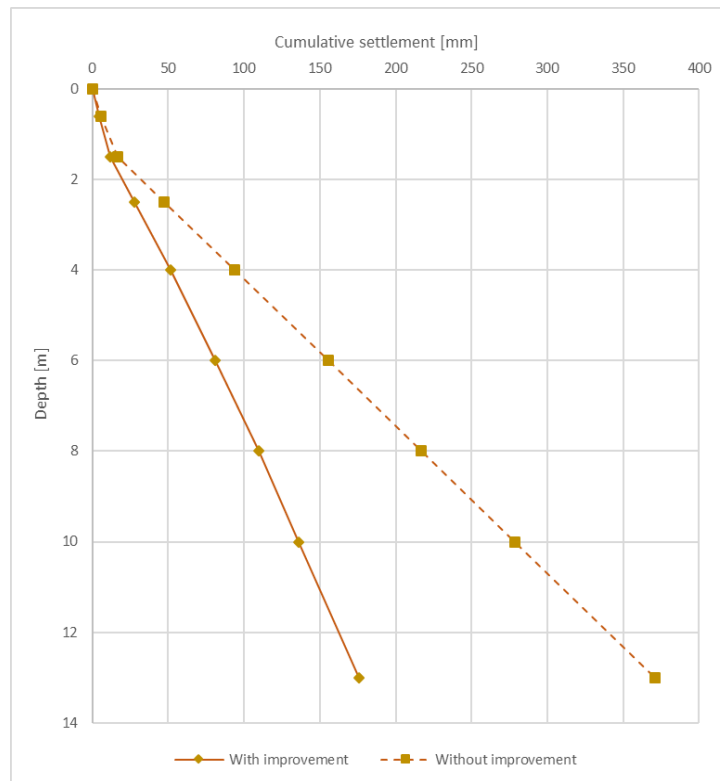


Figure 2: Settlement with and without Stone Column

3.2 The vacuum and surcharge preloading with PVD/Encased Stone Column at Nhon Trach 2

Introduction of project

The project of NT2 is to construct a Combined Cycle Power Plant of 750 MW, comprising two gas turbines and one steam turbine, and is part of a Power generation complex, whose ultimate capacity is meant to be 2640 MW. According to the load conditions 10 T/m^2 (100 kPa), soft soil treatment should improve the ground bearing capacity, control the residual settlement is less than 10 cm in 10 years.

Geological Condition

The two soft clay layers of NT2 and calculation data are summarized as follow:

- Layer 2: Fat clay, the average thickness is about 7.7m
- Layer 3: Silty clay, sometimes with fine sand, greenish grey, bluish grey, yellowish brown, stiff

to very stiff. The thickness varies from 5.5 m to 9.4m.

Settlement prediction

The immediate settlement and primary consolidation settlement are calculated according to the Vietnam code of practice (TCXD 245:2000). The design of the settlement and consolidation program is made as per Figure 5 & Table 2 and as follows:

- Calculation of the consolidation settlement that would occur under operation load if without any treatment during the considered period - immediate settlement as illustrated in Figure 3;
- Considering the available preloading, calculation of the necessary consolidation ratio to be reached to catch up the primary consolidation settlement – sand backfilling and vacuum load as illustrated in Figure 4;
- Calculations of the needed vertical drain mesh characteristics considering the available pre-consolidation period with result as per Figure 6.

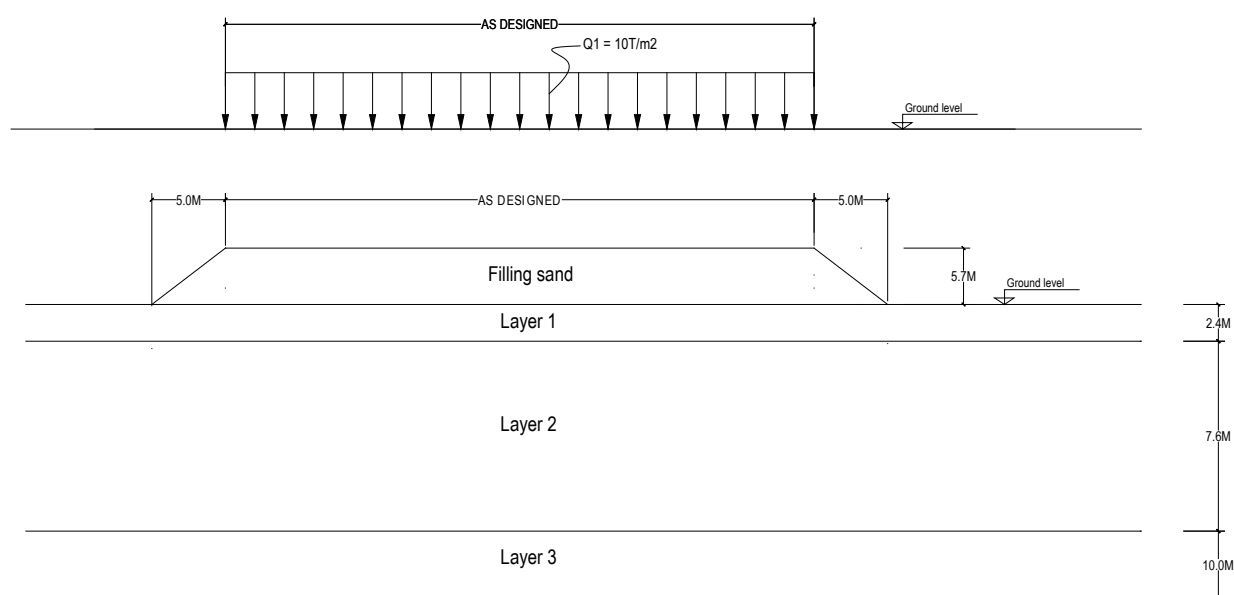


Figure 3: The calculation model under operation load without treatment

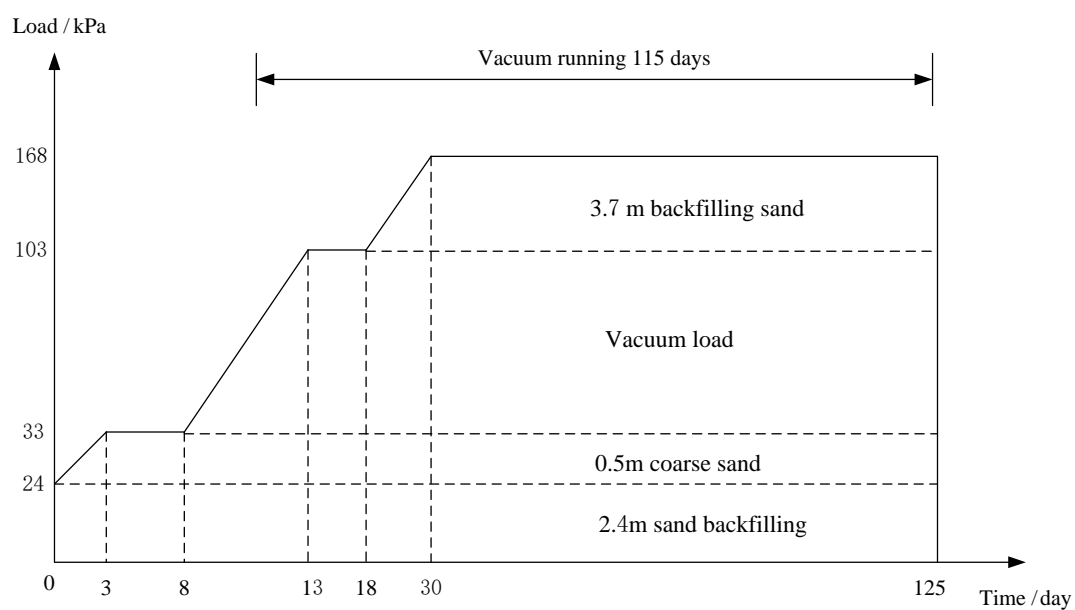


Figure 4: The calculation model under operation load with treatment

Table 2: Typical Soft Clay Profile

Soil Properties	Symbol	Unit	Layer 2			Layer 3		
			Average	Max	Min	Average	Max	Min
Moisture content	W	%	103.8	122.8	82.8	28.1	30.2	22.9
Wet Density	γ_w	g/cm ³	1.417	1.48	1.37	1.899	1.98	1.87
Dry Density	γ_d	g/cm ³	0.698	0.81	0.615	1.483	1.611	1.436
Specific Gravity	γ_s	g/cm ³	2.58	2.61	2.56	2.703	2.725	2.7
Void Ratio	e	%	2.715	3.171	2.174	0.823	0.88	0.688

Direct shear test	C	kG/cm ²	0.057	0.065	0.052	0.282	0.315	0.247
	φ	degree	2°19'	3°45'	2°00'	15°37'	18°10'	15°15'
<i>Consolidation test:</i>								
Pre-consolidation pressure	P _c	kG/cm ²	0.534	0.600	0.43	0.693	0.760	0.430
Coefficient of vertical consolidation	C _v	10 ⁻⁴ cm ² /s	2.61	4.330	0.195	4.710	6.570	0.387
Compression Index	C _c	-	1.172	1.351	0.933	0.110	0.119	0.076
Coefficient of Permeability	K ₂₀	10 ⁻⁷ cm/s	0.294	3.330	2.700	0.305	0.386	0.262
Swelling index	C _s	-	0.156	0.166	0.133	0.016	0.017	0.013
Coe. of horizontal consolidation	C _h	m ² /year	1.32	3.05	0.3	0.67	1.01	0.21
Coefficient of Modulus elasticity	E _{th}	kG/cm ²	56	67	49	473	473	473

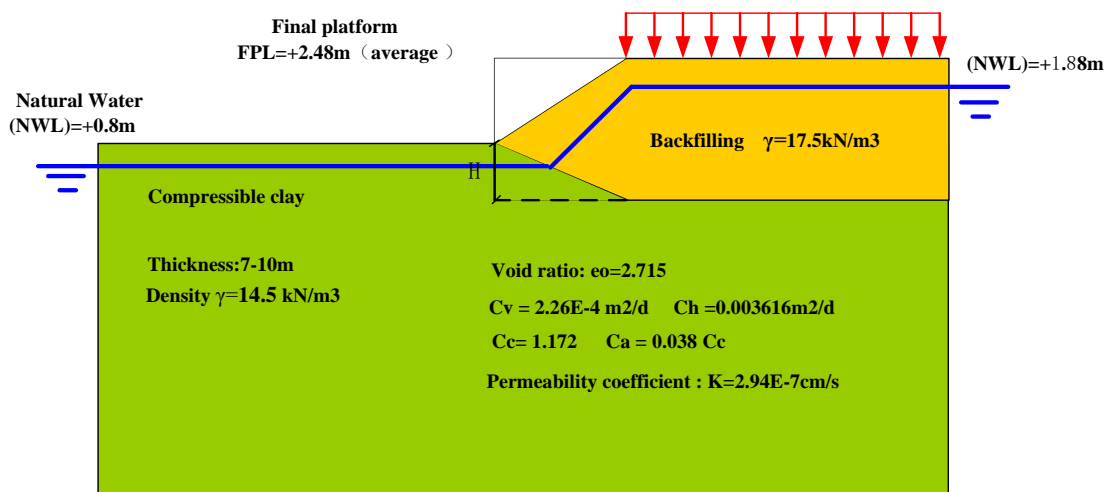


Figure 5: The calculation input data

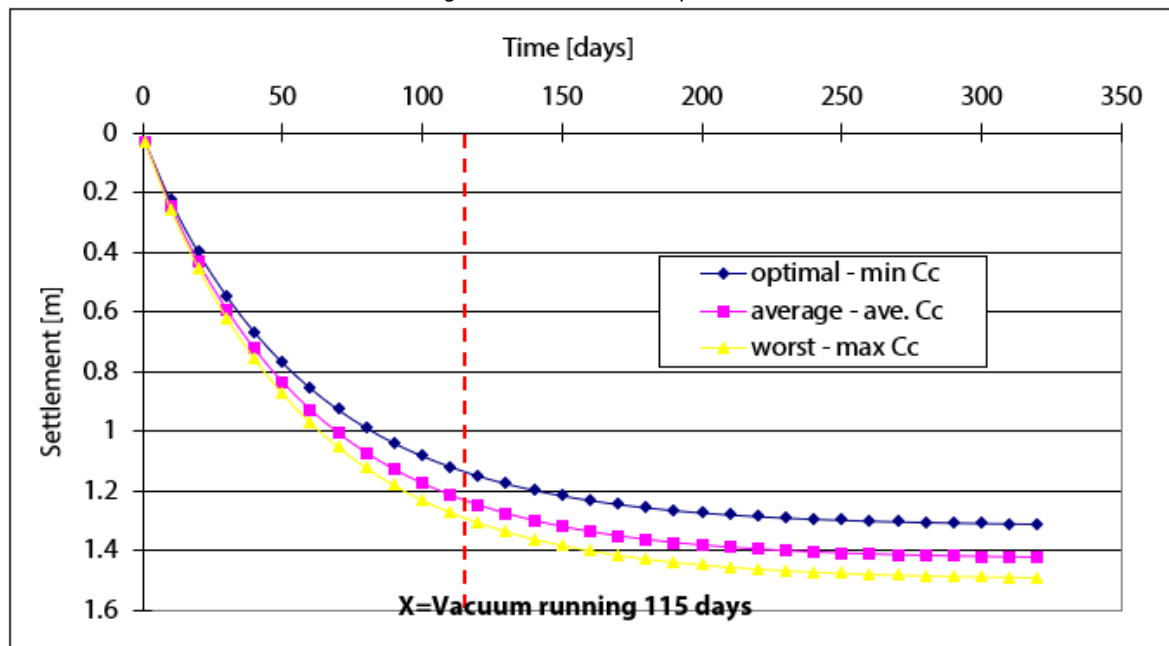


Figure 6: The consolidation settlement of 10T zone

- The post-construction settlements include two parts: the first is the secondary consolidation settlement of soft clay, the second is the immediate settlement under operation load.

$$s_s = C_a \frac{H}{1 + e_1} \log \frac{t_{sc}}{t_p} = C_a \frac{H}{1 + e_1} \log \frac{t_1 + t_r}{t_1}$$

Case	Unit	Optimal	Base	Worst
P	kPa	132.7	132.7	132.7
h₂	m	8	8	8
Eu₂	MPa	33.5	28	24.5
h₃	m	10	10	10
Eu₃	MPa	283.8	283.8	283.8
Si	m	0.040	0.047	0.052

$S_{\text{post-construction}} = 7.6 \text{ cm}$ (<10 cm requirement for soft soil)

Settlement prediction of encased stone column

The settlement was estimated based on Raithel and Kempfert's analytical calculation model (Raithel & Kempfert, 2000). The settlement with treatment is 84 mm with column diameter 1.0 m, spacing 2.3 m and the tensile stiffness of the geosynthetic encasement $J=3000 \text{ kN/m}$.

4. Results and Discussion

To evaluate the beneficial effects of providing stone columns encased with geosynthetics, a comparative calculation was carried out on encased stone columns/stone column and encased stone column/PVD with vacuum and surcharge preloading.

- Stone columns/encased stone columns and PVD are the most widely techniques used for ground improvement of soft soil in the world.
- Installation of stone columns/encased stone column considerably improves the constrained modulus of the weak soils.
- The case study shows that the settlement of soft soil reinforced with encased stone column is smaller than with stone columns.
- Encased stone columns/Stone columns are found to be an effective method of ground improvement, the time requirement is less as compared to PVD methods.
- Geosynthetic encased columns are optimal solution due to technical, technological and reasons of time for the land reclamation in Vietnam.

5. Conclusions

In this study, the settlement of stone columns encased with geogrid reinforcement was calculated and compared with the result of stone column and PVD with vacuum and surcharge preloading. The result shows that it fits into the studies and researches (Malarvizhi, S.N. and Ilamparuthi, K., 2007; Alexiew, D., Raithel, M., 2005). Many projects have been successfully executed worldwide (Alexiew, D., Raithel, M., 2015), the encased stone columns are the new direction research and application for the work of soil improvement in Vietnam.

6. References

1. Alexiew, D., Brokemper, D. and Lothspeich, S. (2005) *Geotextile Encased Columns (GEC): Load capacity, geotextile selection and pre-design graphs*. Geotechnical Special Publication, No. 130-142, Geo-Frontiers, 497-510.

2. Alexiew, D., Raithel, M., 2015. *Geotextile-encased columns: case studies over twenty years*. In: Indraratna, Chu, Rujikiatkamjorn (Eds.), *Embankments with Special Reference to Consolidation*.
3. Castro, J., Sagaseta, C., 2011. *Deformation and consolidation around encased stone columns*. Geotext. Geomembr. 29, 268-276.
4. Malarvizhi, S.N. and Ilamparuthi, K., (2007). *Comparative study on the behavior of encased stone column and conventional stone column*. Soils and Foundations Journal 47, No. 5, 873-885.
5. Priebe, H. J. (1995). *The design of vibro replacement*. Ground Engng. Dec., 31-37.
6. Raithel, M., Kempfert, H.-G. (1999). *Bemessung von geokunststoffummantelten Sandsäulen*. Die Bautechnik 76, Nr. 12.
7. Raithel, M., Kempfert, H.-G. (2000). *Calculation models for dam foundation with geotextile coated sand columns*. Proc. International conference on Geotechnical & Geological Engineering GeoEng. Melbourne.
8. *Practice for soft soil improvement with using vertical drains* – TCXD 245 – 2000.

ISOLATION RISK ANALYSIS OF RESIDENTIAL SETTLEMENTS IN MOUNTAINOUS REGION: CASE STUDIES FOR 2004 NIIGATA-KEN CHUETSU AND 2016 KUMAMOTO EARTHQUAKES

Yusuke Ono and Keishin Hibi

ABSTRACT

Road networks in mountainous areas are critical infrastructures to maintain social activities. Slope failures triggered by an earthquake often disrupt the functionality of road networks. For example, during the 2004 Niigata-ken Chuetsu Earthquake, in Japan, Yamakoshi village isolated due to distortion of the road network and all residents were forced to move to the disaster evacuation camps outside of the town. Isolation of a residential settlement affects the damaged region not only for the short-term but also for a long-term. Therefore, prediction and countermeasures in advance are necessary. In this study, a procedure to evaluate the isolation risk of residential settlements in a mountainous region where a strong earthquake strikes. First, the road network is modeled as a set of nodes and links by the graph theory. Second, the probability of failure for each node and link is computed considering slope failures under a given earthquake scenario. Finally, the isolation risk is evaluated by conducting the connectivity analysis with the Monte-Carlo simulation. For validation of the presented procedure, case studies for the 2004 Niigata-ken Chuetsu earthquake and the 2016 Kumamoto earthquake are conducted.

KEYWORDS: *isolation risk, slope failure, road network, earthquake*

DR. YUSUKE ONO

Professor, Department of Civil Engineering, Tottori University
Email: ysk@tottori-u.ac.jp, **corresponding author**
Tel: +81-857-31-5286

MR. KEISHIN HIBI

Graduate student, Graduate School of Sustainable Science, Tottori University
Email: m18j@edu.tottori-u.ac.jp
Tel: +81-857-31-5288

1. Introduction

Slope disasters such as a landslide, rockfall, et al. often cause road disruption in a mountainous region. Compared to a road disruption caused by a traffic accident or maintenance works, the influence of the road disruption due to slope failures tend to be severe and last for a long time. During an earthquake, slope failures may take place simultaneously in a mountainous area and result in severe damage to the road network. For instance, during the 2004 Niigata-ken Chuetsu earthquake, Yamakoshi village, which is currently a part of Nagaoka City because of the merger of municipals in 2005, suffered from many road disruptions caused by slope failures, and most of the village was isolated (Toyota et al. 2006). Due to the road disruptions, approximately 2,200 residents were rescued by a helicopter and forced to evacuate outside the village. On the other hands, during the 2016 Kumamoto earthquake, many slope

failures occurred in Minami Aso village, Kumamoto, and several small villages were isolated (Shirahama et al. 2016).

Some studies have devoted to investigating the performance of a road network under earthquake hazard. The method generally used is based on graph theory and can be described as follows: first, a concerning road network is modeled by a graph composed of nodes and links. Second, the probability of failure of each node and link are determined based on a specific seismic hazard. Finally, the probability of disconnection between a pair of two nodes is calculated.

In this study, a procedure to evaluate isolation risks of residential settlements in a mountainous area, concerning road disruption caused by earthquake-induced slope failures, are presented. Yamakoshi and Minami Aso villages which suffered from numerous road disruptions due to earthquake-induced slope failures are taken as examples and the evaluated probabilities of isolation are compared to the actual damage of these two villages for validation of the procedure.

2. Procedure for evaluating isolation risk of residential settlements

2.1 Graph of road network

In this study, the road networks in the target areas are modeled by the graph theory. A graph consists of links and nodes. Residential settlements are assigned to the nearest node.

2.2 Probability of isolation

If a node has no path leading to neighboring areas, the node is referred to be isolated. Figure 1 shows the isolated node schematically. In the figure, node A is isolated because there is no path to node D which connected outside the area. This means that residents living around node A do not have an access outside the area. On the other hand, nodes B and C have paths to the outside of the area.

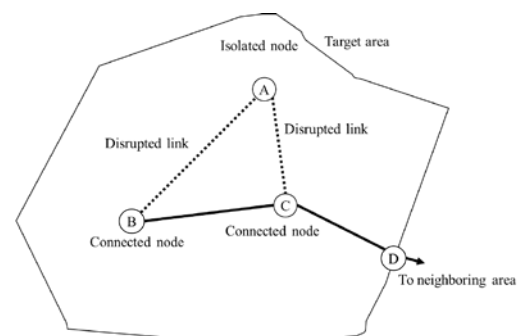


Figure 1: Schematic representation of isolated node

In this study, the isolation risk is evaluated as the probability of isolation, i.e., the probability of disconnection between the concerned node and nodes connecting

outside the area. For example, the probability of isolation for node A in Figure 1 is calculated as the probability of disconnection between nodes A and D.

2.3 Probability of node and link failure

The probability of failure of nodes and links are evaluated by overlaying geospatial analysis of raster and vector datasets. In this study, the occurrence probability of slope failure is provided as a raster data. On the other hand, the network graph which consists of nodes and links is prepared as a vector data. The probability of node failure is identical to the occurrence probability of slope failure at the raster cell where the node is located.

2.4 Occurrence probability of slope failure

Sakai et al. (2013) derived the equation to evaluate the occurrence probability of slope failure under a specified seismic ground excitation as follows.

$$p = \frac{1}{1 + \exp\{-(-7.89 + 0.09\phi + 0.0019a)\}} \quad (1)$$

where p is the occurrence probability of slope failure; ϕ is a slope angle; a is peak ground acceleration (PGA). The background data utilized to develop the equation was collected in Mt. Rokko after the 1995 Hyogo-ken Nanbu earthquake (Sakai, et al., 2013).

2.5 Calculating the probability of isolation

The procedure for calculating the probability of isolation is summarized in Figure 2. PGA, DEM and road network are dataset required for the analysis. All processes shown in Figure 2 are implemented by us, and the computer codes are written in Python programming language.

The Monte Carlo method (MCM) is utilized to evaluate the redundancy index; 10,000 sample networks are generated, and for every sample network it is examined if there is a path between considering nodes. In our implementation, NetworkX package (<https://networkx.github.io/>) for Python is utilized for the searching path.

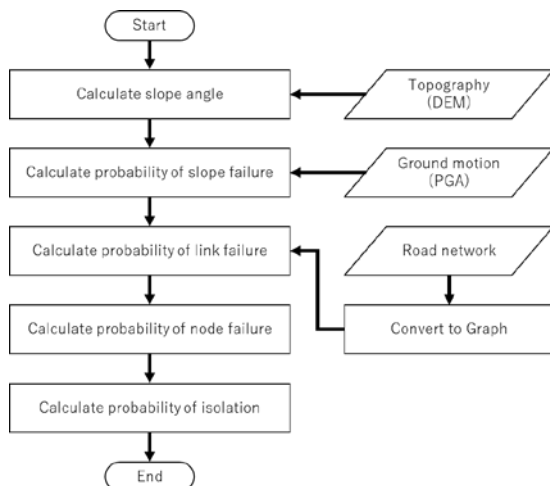


Figure 2: Procedure for calculating the probability of isolation

To calculate the probability of isolation, more computationally efficient algorithms (Ji and He, 2002; Javanbarg et al., 2009) than the MCM can be used. However,

the MCM is employed because of the simplicity of implementation.

3. Data preparation

3.1 Digital elevation model

For the topography, a dataset of the digital elevation model (DEM) with 10 m resolution was downloaded from the website (<http://www.gsi.go.jp/kiban/index.html>) operated by the Geospatial Information Authority of Japan, Ministry of Land, Infrastructure, Transport and Tourism. The DEM dataset with 5 m resolution is also available from the same website. However, the 10 m resolution version is utilized since Equation (1) was derived based on 10 m resolution topography.

3.2 Road network

The road network data for the study areas were downloaded from OpenStreetMap (<https://www.openstreetmap.org>) and converted into graphs with nodes and links by Python OSMnx package (Boeing, 2017). The OSMnx constructs nodes and links from the OpenStreetMap data structure and corrects network topology. Although the OpenStreetMap provides various kinds of road, such as a private service road, footpath, et al., only roads and streets where vehicles can pass through are utilized in this study.

3.3 PGA distribution

As described in the previous section, PGA distribution is required to calculate the probability of link or node failure. To evaluate the distribution of PGA, seismic hazard analysis considering the site amplification effect should be conducted. However, in general, a variation of PGA values in a mountainous region is relatively small and, therefore, we assume the uniform distribution of PGA value in the study area.

4 Results

4.1 Yamakoshi village

Yamakoshi village, which is currently a part of Nagaoka city, is in a mountainous region in Niigata prefecture, Japan. Yamakoshi village suffered from severe damage due to the 2004 Niigata-ken Chuetsu Earthquake of Mw 6.6. The event caused numerous slope failures and resulted in the disruption of the road network. All routes from the central part of the village to the outside of the village were disrupted. Therefore, all residents in the isolated region were forced to evacuate to refugee camps which are located outside the village.

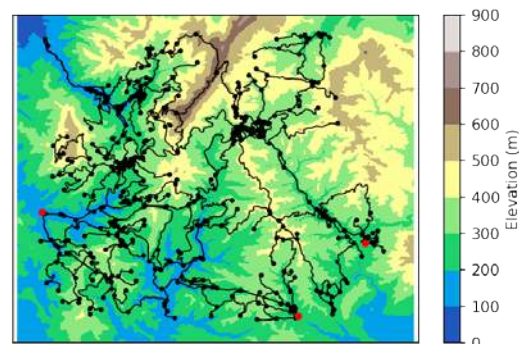


Figure 3: The topography and the road network of Yamakoshi

The topography and the road network of Yamakoshi village are shown in Figure 3. Nodes and links are represented by a solid black line and a black filled circle, respectively. The network consists of 494 nodes and 623 links. Each link is treated as a bi-directional since the normal traffic regulation could be ignored during an emergency such as an earthquake disaster. The red filled circle represents the terminal nodes which are connected to the outside of the village. The probability of isolation for each node is calculated as the probability of disconnection between the concerning node and one of the terminal nodes.

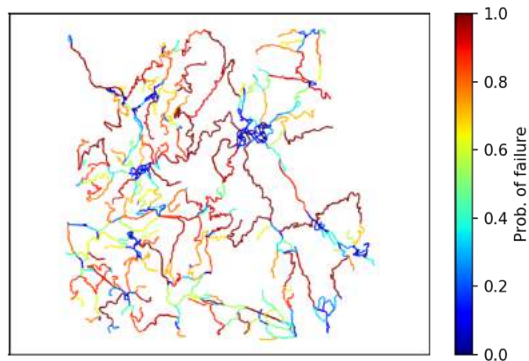


Figure 4: Probability of link failure for Yamakoshi

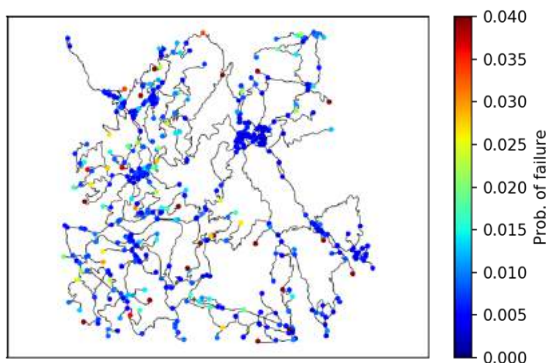


Figure 5: Probability of node failure for Yamakoshi

Figure 4 shows the calculated probabilities of link failure under the given uniform PGA distribution of 1000 cm/s/s. The links located in the flat area have small values of probability of failure. The longer links tend to have higher values of the probability of failure. On the other hands, the probability of node failure shown in Figure 5 takes a smaller value compared to the probability of link failure.

Based on the obtained probabilities of node failure and link failure shown in Figures 4 and 5, the probability of isolation for each node is evaluated by the Monte Carlo method with 10,000 generated samples. Figure 6 shows the probability of isolation. Figure 6(a) shows the spatial distribution of the probability of isolation in Yamakoshi village and that the nodes near the terminal nodes have relatively small values of the probability of isolation. Also, the probability of isolation for most of the nodes is close to unity. Figure 6(b) shows the histogram of the probability of isolation is shown. This result suggests that most of Yamakoshi village is prone to be isolated following the assumed earthquake event of PGA = 1000 cm/s/s.

4.2 Minami Aso village

Minami Aso village is in a mountainous region of Mt. Aso. The village was strongly shaken by the 2016 Kumamoto Earthquake of Mw 7.0 and suffered from severe damage including numerous slope failures. The foreshock of Mw 6.2 took place one day before the mainshock, which may extend the damage consequently. The districts around Tokai University Aso campus and Jigoku-Onsen were isolated respectively due to the road disruptions, and approximately 1000 residents in total were affected.

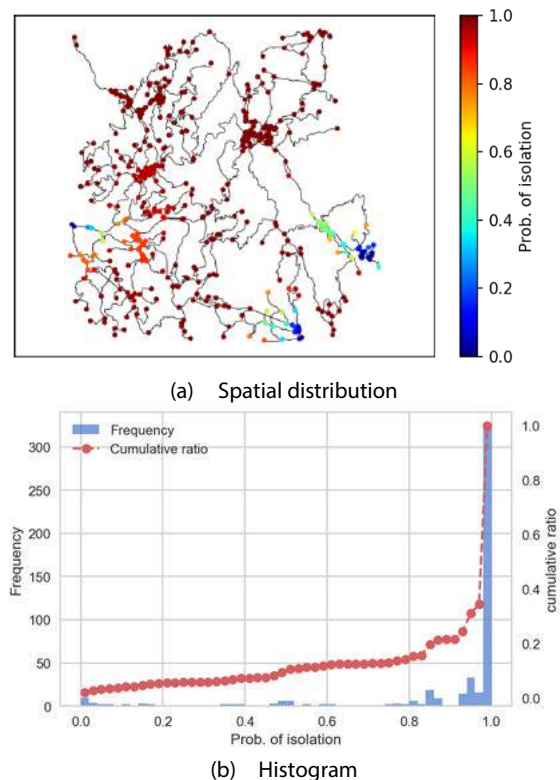


Figure 6: Probability of isolation for Yamakoshi

Figure 7 shows the topography of Minami Aso village and its road network downloaded from OpenStreetMap. The three nodes represented by red fill circles are the terminal nodes assumed. The road network consists of 1644 nodes and 2155 links. The uniform distribution of PGA=927 cm/s/s is assumed for calculating the failure probability of nodes and links.

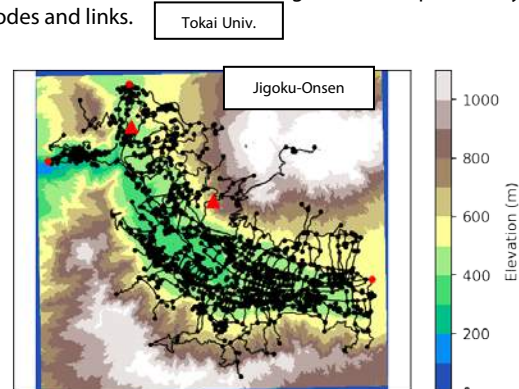


Figure 7: The topography and the road network of Minami Aso

Figure 8 shows the probability of link failure. The probabilities of link failure in a flat place of the basin are smaller than those of the higher places. On the other hands, Figure 9 shows the probabilities of node failure. Compared to the links, the probabilities of node failure are generally small. The value of the probability of node failure is at most 0.10.

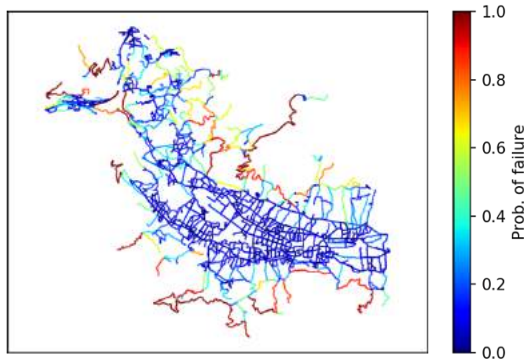


Figure 8: Probability of link failure for Minami Aso

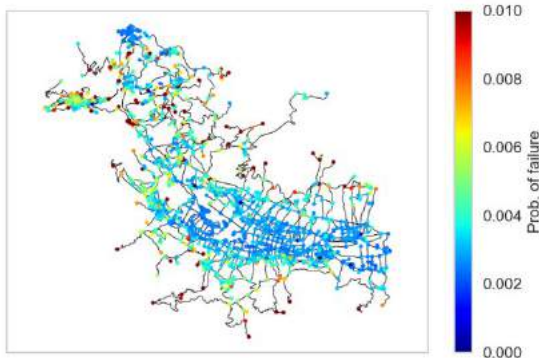


Figure 9: Probability of node failure for Minami Aso

The probability of isolation for each node is calculated by the Monte Carlo method with 10,000 samples as well as the case of Yamakoshi village and shown in Figure 10. The nodes in the higher altitude places tend to take higher values of the probability of isolation than those of the nodes in the flat area. For about 80% of nodes, the probability of isolation is lower than 0.2.

Table 1: Probability of isolation for the residential settlements isolated during the 2016 Kumamoto earthquake

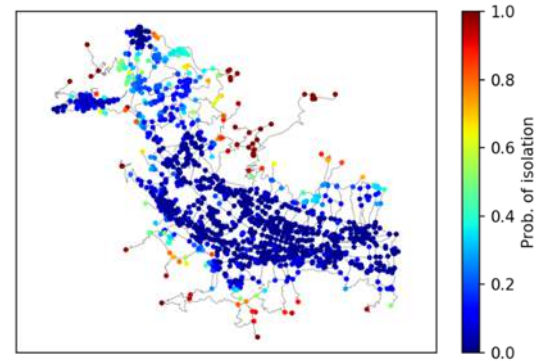
Place	Probability of isolation
Distinct around Minami Aso	0.224
Campus of Tokai University	
Distinct around Jigoku Onsen	0.775

5. Discussion and conclusion

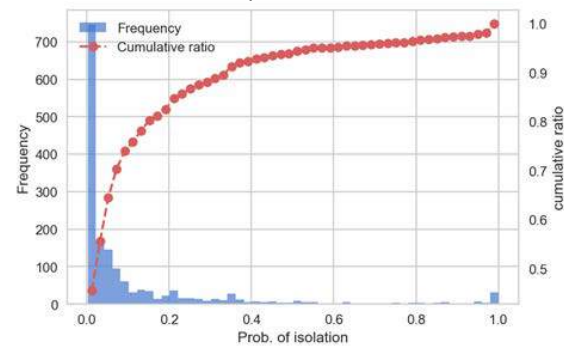
Due to the 2004 Niigata-Ken Chuetsu Earthquake, road disruption occurred everywhere in Yamakoshi village, and approximately 2,200 residents were rescued by a helicopter and evacuated outside the village. As shown in Figures 6, the computed probability of isolation for all nodes in Yamakoshi village is relatively high.

On the other hands, two districts around Tokai University Aso campus and Jigoku-Onsen in Minami Aso village were isolated, respectively, due to the road disruption in the 2016 Kumamoto earthquake. The locations of these districts are plotted by red triangles in Figure 7. Table 1 summarizes the probabilities of isolation for the nodes corresponding to these districts. For both, the value of the probability is relatively high compared to other nodes.

These results shows that the probability of isolation evaluated in this study can explain the occurrence of actual damage appropriately.



(a) Spatial distribution



(b) Histogram

Figure 10: Probability of isolation for Minami Aso

References

1. Toyota, H., Wang, J., Nakamura, K., and Sakai, N., (2006). *Evaluation of natural slope failures induced by the 2004 Niigata-ken Chuetsu earthquake*, Soils and Foundations, 46(6), 727-738.
2. Shirahama, Y. et al., (2016). *Characteristics of the surface ruptures associated with the 2016 Kumamoto earthquake sequence, central Kyushu, Japan*, Earth, Planets and Space, 68(19).
3. Boeing, G., (2017). *OSMnx: New methods for acquiring, constructing, analyzing, and visualizing complex street networks*, Computers, Environment and Urban Systems, 65, 126-139.
4. Javanbarg, M.B., Scawthorn, C., Kiyono, J., and Ono, Y., (2009). *Minimal path sets seismic evaluation of lifeline networks with link and node failures*, Proc. of the 2009 ASCE Technical Council on Lifeline Earthquake Engineering Conference.
5. Li, J. and He., J., (2002). *A recursive decomposition algorithm for network seismic reliability evaluation*,

Earthquake Engineering and Structural Dynamics,
48(3), 234-246.

6. Sakai, H., et al., (2013). *A fundamental study on simplified method for calculating earthquake-induced slope collapse ratio*, Journal of Structural and Earthquake Engineering, JSCE, 69(4), 142-147 (in Japanese).

EFFECT OF DRILLING MUDS AND CUTTINGS DISCHARGED TO THE ENVIRONMENT

ẢNH HƯỞNG CỦA MÙN KHOAN VÀ Vụn KHOAN XẢ THẢI ĐẾN MÔI TRƯỜNG

Do Quang Khanh, Hoang Trong Quang, Tran Thi Mai Huong, Kieu Phuc

ABSTRACT

The offshore drilling process uses drilling fluids and generates waste fluids and cuttings. Drilling fluids used in offshore drilling operations are water based drilling fluids (WBF), oil based fluids (OBF) and synthetic based fluids (SBF). The wastes generated in the largest volumes during drilling oil and gas wells are drilling muds and cuttings. Several options to manage offshore drilling wastes were presented in this paper such as offshore discharge, offshore downhole injection and onshore disposal.

KEY WORDS: *Offshore drilling, drilling fluids, waste management, EU standards*

TÓM TẮT

Quá trình khoan ngoài khơi sử dụng dung dịch khoan và tạo ra chất thải và vụn khoan. Dung dịch khoan được sử dụng trong các hoạt động khoan ngoài khơi là dung dịch khoan gốc nước (WBF), dung dịch khoan gốc dầu (OBF) và dung dịch khoan tổng hợp (SBF). Các chất thải được tạo ra với khối lượng lớn nhất trong các giếng khoan dầu khí là mùn khoan và vụn khoan. Một số tùy chọn để quản lý chất thải khoan ngoài khơi đã được trình bày trong bài báo như là xả thải ngoài khơi, bơm ép xuống đáy biển và xử lý trên bờ.

TỪ KHÓA: *Khoan ngoài khơi, dung dịch khoan, quản lý chất thải, tiêu chuẩn EU*

DR. DO QUANG KHANH

Lecturer, Faculty of Geology and Petroleum Engineering,
HCMC University of Technology (HCMUT)
Email: dqkhanh@hcmut.edu.vn, **corresponding author**
Tel: 0936 39 77 33

M.E. HOANG TRONG QUANG

Lecturer, Faculty of Geology and Petroleum Engineering,
HCMC University of Technology (HCMUT)
Email: htquang@hcmut.edu.vn
Tel: 0913 678 400

M.E. TRAN THI MAI HUONG

Lecturer, Faculty of Geology and Petroleum Engineering,
HCMC University of Technology (HCMUT)
Email: ttmhuong@hcmut.edu.vn
Tel: 0989 051 923

B.E. KIEU PHUC

Lecturer, Faculty of Geology and Petroleum Engineering,
HCMC University of Technology (HCMUT)
Email: kieuphuc@hcmut.edu.vn
Tel: 0934 058 158

1. Introduction

Until several decades ago, the seas and oceans were considered as limitless dumping grounds. However, during the 1970s and 1980s there have been evidences that some types of drilling waste discharges could have undesirable effects on local ecology, particularly in shallow water.

Offshore platforms can impact the environment in three ways: the physical presence of the platforms, waste discharges from the platforms and accidental discharges. The impact of offshore oil & gas exploration and production on the marine ecosystem varies from disturbing sea mammals during acoustic exploration research activities to chemical, physical and toxicological effects of residual waste streams. Operational discharges include:

- + Cuttings contaminated with oil and chemicals (from drilling platforms)
- + Production water contaminated with oil and chemicals (from production platforms)
- + Rainy-, scrub- and cleaning water contaminated with oil and chemicals. Accidental discharges may be as a consequence of blowouts and damage of pipelines, discharges due to flaring.

2. Drilling fluids and drill cuttings

Drilling fluids (muds) consist of a continuous liquid phase, to which various chemicals and solids have been added to modify the operational properties of the resulting drilling system. Because of that the composition of drilling fluids is complex and varies widely depending on the specific down-hole conditions such as downhole temperature and pressure, geology, and other factors. Drilling fluids fall into one of three types depending on their principal liquid-phase component: water-based fluids (WBFs), oil-based fluids (OBFs), and synthetic-based fluids (SBFs)^{1,6}.

2.1 Water based fluids

A water-based fluid is a suspension of particulate minerals, dissolved salts, and organic compounds in freshwater, seawater, or concentrated brine. When water-based fluids (WBFs) are used, only limited environmental harm is likely to occur. WBF ingredients can be divided into 18 functional categories¹². Each category of additives may contain several alternative materials with slightly different properties (Table 1).

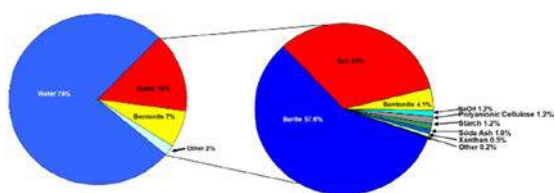


Figure 1. Composition of typical water based drilling (WBM) and of the additives to a typical WBM

Table 1. Functional categories of materials used in WBF, their functions, and examples of typical chemicals in each category⁹

Functional Category	Function	Typical Chemicals
Weighting materials	Increase density (weight) of mud, balancing formation pressure, preventing a blowout	Barite, hematite, calcite, ilmenite
Viscosifiers	Increase viscosity of mud to suspend cuttings and weight agent in mud	Bentonite or attapulgite clay, carboxymethyl cellulose, and other polymers
Thinners, dispersants, and temperature stability agents	Deflocculate clays to optimize viscosity and gel strength of mud	Tannins, polyphosphates, lignite, lignosulfonates
Flocculants	Increase viscosity and gel strength of clays or clarify or de-water low-solids muds	Inorganic salts, hydrated lime, gypsum, sodium carbonate and bicarbonate, sodium tetraphosphate, acrylamide-based polymers
Filtrate reducers	Decrease fluid loss to the formation through the filter cake on the wellbore wall	Bentonite clay, lignite, Na-carboxymethyl cellulose, polyacrylate, pregelatinized starch
Alkalinity, pH control additives	Optimize pH and alkalinity of mud, controlling mud properties	Lime (CaO), caustic soda (NaOH), soda ash (Na ₂ CO ₃), sodium bicarbonate

		(NaHCO ₃), and other acids and bases
Lost circulation materials	Plug leaks in the wellbore wall, preventing loss of whole drilling mud to the formation	Nut shells, natural fibrous materials, inorganic solids, and other inert insoluble solids
Lubricants	Reduce torque and drag on the drill string	Oils, synthetic liquids, graphite, surfactants, glycols, glycerin
Shale control materials	Control hydration of shales that causes swelling and dispersion of shale, collapsing the wellbore wall	Soluble calcium and potassium salts, other inorganic salts, and organics such as glycols
Emulsifiers and surfactants	Facilitate formation of stable dispersion of insoluble liquids in water phase of mud	Anionic, cationic, or nonionic detergents, soaps, organic acids, and water-based detergents
Bactericides	Prevent biodegradation of organic additives	Glutaraldehyde and other aldehydes
Defoamers	Reduce mud foaming	Alcohols, silicones, aluminium stearate (C ₅₄ H ₁₀₅ AlO ₆), alkyl phosphates
Pipe-freeing agents	Prevent pipe from sticking to wellbore wall or free stuck pipe	Detergents, soaps, oils, surfactants
Calcium reducers	Counteract effects of calcium from seawater, cement, formation anhydrites, and gypsum on mud properties	Sodium carbonate and bicarbonate (Na ₂ CO ₃ and NaHCO ₃), sodium hydroxide (NaOH), polyphosphates
Corrosion inhibitors	Prevent corrosion of drill string by formation acids and acid gases	Amines, phosphates, specialty

		mixtures
Temperature stability agents	Increase stability of mud dispersions, emulsion and rheological properties at high temperatures	Acrylic or sulfonated polymers or copolymers, lignite, lignosulfonate, tannins

If permitted by local regulations, the cuttings may be discharged to the sea. Periodically, some of the drilling fluid may be discharged as well. The total mass of WBF and cutting discharged per exploratory well is about 2000 metric tons/well and somewhat less for most development wells⁹.

When WBF and cuttings are discharged to the sea, the larger particles and flocculated solids, representing about 90% of mass of the mud solids, form a plume that settles quickly to the bottom. The remaining 10% of the mass of the mud solids consisting of fine-grained unflocculated clay-sized particles and a portion of the soluble components of the mud from another plume in the upper water column that drifts prevailing currents away from the platform and is diluted rapidly in the receiving waters. In well-mixed sea waters, drilling fluids and cuttings are diluted by 100-fold within 10 m of the discharge and by 1000-fold after a transport time of about 10 minutes at a distance of about 100 m from the platform⁹. Because of rapid dilution of the drilling mud and cuttings plume in the water column, harm to communities of water column plants and animals is unlikely and has never been demonstrated.

WBF and cuttings solids settle to and accumulate on the sea floor. If discharged at or near the sea surface, the mud and cuttings disperse in the water column over a wide area and settle as a thin layer of a large area of the sea floor. If mud and cuttings are discharged just above the sea floor the drilling solids may accumulate in a large, deep pile near the discharge pipe. The accumulation of mud and cuttings on the bottom, the cutting pile, may contain higher concentrations of several metals, particularly barium (from drilling mud barite), and sometimes petroleum hydrocarbons than nearby uncontaminated sediments. Chromium, lead, and zinc are the metals, in addition to barium, that are most often enriched in cutting pile sediments. The metals associated with drilling mud barite or cutting piles have a low bioavailability to marine animals; they do not accumulate in the tissues of bottom-living animals⁹.

WBF are non-toxic or partially non-toxic to marine animals, unless they contain elevated concentrations of petroleum hydrocarbons, particularly diesel fuel. Most drilling mud ingredients are non-toxic or used in such small amounts in WBF that they do not contribute to its toxicity. Chrome and ferrochrome lignosulfonates are the most toxic of the major WBF ingredients. Although used frequently in the past, these deflocculants are being replaced in most

WBF by non-toxic alternatives to reduce the ecological risk of drilling discharge.

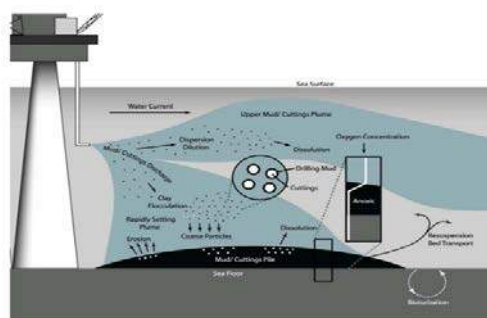


Figure 2. Dispersion and fates of water based drilling mud (WBM) following discharge to the ocean.

2.2 Oil based fluids

Oil based-fluids have traditionally been used to improve lubricity, reduce friction and address site-specific conditions such as: high down hole temperatures, hydratable shales, high angle drilling, and extended reach wells. An oil based-fluid has diesel, mineral oil, or some other oil as its continuous phase, with water as the dispersed phase. Other constituents are barite, clays, emulsifiers, water, CaCl_2 , lignite, lime and other additives. Discharge of OBF cuttings has far greater toxicity than waste from WBFs and poses the most severe environmental impact on the seafloor of the three fluid types. The use of OBFs are declining because of the added cost of transporting waste fluids to shore, regulatory restrictions, and the development of SBFs. Cuttings piles, created when oil-based fluids (OBFs) are used on deeper sections of wells, impair zones beneath and adjacent to the platforms. Piles of oil-based cuttings can affect the local ecosystem in three ways: by smothering organisms, by direct toxic effect of the drilling waste, and by anoxic conditions caused by microbial degradation of the organic components in the waste (Figure 1)⁸.

3. Biological effects of WBM and cuttings in the ocean.

Bioavailability is the extent to which a chemical can be absorbed (bioaccumulated) by a living organism by active (biological) or passive (physical or chemical) processes (Neff, 2002a). A chemical is said to be bioavailable if it can move through or bind to a permeable surface coating (e.g., skin, gill epithelium, gut lining, cell membrane) of an organism (Newman and Jagoe, 1994). Metal bioavailability from sediments (cuttings piles) can be divided into 2 components: environmental accessibility and environmental bioavailability. Environmental accessibility is a measure of the fraction of the total chemical that is in a form or location in the environment that is accessible for bioaccumulation by organisms. Environmental bioavailability depends on the interactions of a marine organism with its environment. Exposure occurs at the interface between environmental media (water, sediment, and food) and permeable biological membranes of the marine organism in contact with the different media

Mercury is the metal of greatest environmental concern in drilling wastes discharged to US waters (Neff, 2002b), and sometimes is found at higher concentrations in drilling mud barite and WBM than in clean marine sediments. Lead is the metal of greatest concern in drilling wastes discharged to the North Sea, because some North Sea drilling mud barite contains high concentrations of easily leached lead. The US EPA (1993) set limits on maximum acceptable concentrations of mercury and cadmium in drilling mud barite in 1993, in an effort to decrease the amounts of metals discharged to the ocean in drilling wastes. Drilling mud barite discharged offshore must contain less than 1 mg/kg (ppm) mercury and 3 ppm cadmium

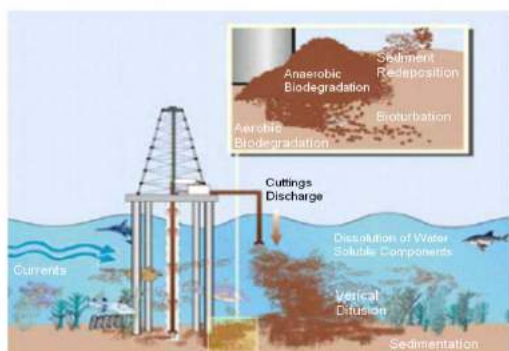


Figure 3. Effect of drill cuttings discharge on marine environment⁴

4. Waste minimization hierarchy

IPPC Directive of 1996. IPPC stands for Integrated Pollution Prevention and Control. In essence, the IPPC The permits must be based on the concept of Best Available Techniques (or BAT).

In many cases BAT means quite radical environmental improvements and sometimes it will be very costly for companies to adapt their plants to BAT. The waste minimization hierarchy is described in the IPPC Directive. The first step is investigate options that prevent waste generation, next is to reduce waste, then reuse and recycle as much as possible, while the last and the least preferred option is to deposit residues. Waste minimization in drilling operations starts in the preplanning phase. The selection of BAT solutions, when balancing drill cuttings, had to take into account following issues¹¹: drilling technology (well design, drilling fluid, solids handling equipment on rig), drilling waste (disposal options, transport and logistics, drilling waste treatment technology), impact of different waste disposal options, and cost. Integrated fluids engineering helps to achieve several benefits: reduced health, safety and environmental risks, environmental compliance, reduced waste volumes, reduced fluid-disposal costs, optimized product usage, reduced site-closure costs, maximized pollution prevention.

5. Drilling waste disposal options

There are three options to manage offshore drilling wastes (Figure 4):

Offshore discharge – fluids and/or cuttings are discharged overboard from the drilling platform after undergoing treatment by solids control equipment designed to remove solids and recover fluids,

Offshore downhole injection –cuttings are ground to fine particle sizes and disposed of, along with entrained fluids, by injection into permeable subsurface formations,

Onshore disposal – cuttings and the associated fluids are collected and transported for treatment if necessary and final disposal.

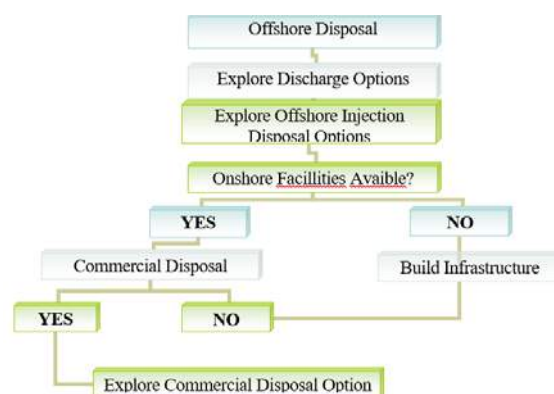


Figure 4. Offshore waste disposal options decision three.

All options have advantages and disadvantages with regard to total life cycle environment impact, safety, cost, and operational performance. In making decisions regarding disposal options, one should establish a framework to compare the pros and cons for each alternative option in this framework factors other than potential environmental impacts should be considered (Table 2).

Table 2. Framework of parameters for evaluating disposal options¹¹

ECONOMIC	OPERATIONAL	ENVIRONMENTAL
Immediate costs	Safety	Air emissions from drilling and supporting operations
\$/m ³ for disposal	Human health issues/chemical exposure	Power requirements
Energy cost	Processing rate	Reduction in volume of waste
Maintenance cost	Mechanical reliability	By-products of process
Labor cost	Size and portability of unit (s)	Compliance with regulations
Equipment cost	Space availability	Receiving physical environment
Transportation costs	Energy requirements	Marine species potentially at risk
Disposal costs of end products	Condition of end products	Potential environmental stressors
Future liabilities	Method of disposal after processing	Removal of hydrocarbons, heavy metals and salts from solids and water

6. Environmental legislation concerned with offshore platform discharges

Regarding the maritime environment, the United Nations Convention of the Law of the Sea (UNCLOS, 1982) is the key overall regulatory framework at global level for all activities at sea. Conventions supporting this at global level are¹ :

The International Convention for the Prevention of Pollution from Ships (MARPOL, 1973/78),

The Framework for prevention of dumping of pollutant material (London Dumping Convention, 1972) and

The International Convention on Pollution Preparedness, Response and Cooperation (OPRC, 1990).

Regarding to chemicals used and discharged offshore OSPAR agreed on two lists of chemicals: the list of "chemicals for priority action" (i.e. the most hazardous ones), and "PLENOR" list, the list of chemicals which have been considered as "posing little or no risk to the environment".

At present time no "chemicals for priority action" is intentionally used offshore; substances listed on the PLENOR list do not request further investigation^{3,10,11}.

7. Conclusions

The disposal of drill cuttings and produced water has become a major concern for operators and environmental controls have been tightened by regulatory authorities.

Most oil and gas operators today develop and implement an environment management system (EMS) for all operations which is in line with international standards.

Through the adoption and implementation of an EMS, potential environment impacts and consequences are identified, managed and minimized where possible.

References

1. APPEA, Framework for the Environmental Management of offshore discharge of drilling fluid on cuttings in Australia, March 1998.
2. Barcelona Convention - Convention for the Protection of the Mediterranean Sea against Pollution, 1976. Protocol for the Protection of the Mediterranean Sea Against Pollution Resulting from Exploitation of the Continental Shelf and the Seabed and its Subsoil (14 October, 1994.)
3. Garland, E.: Environmental Regulatory Framework in Europe: An Update, SPE 93796, the 2005 SPE/EPA/DOE Exploration and Production Environmental Conference, pp.1-10, Galveston, Texas, 2005.
4. Gaurina-Međimurec, N., Krištafor, Z.: Offshore Drilling Wastes Management and EU Regulations, 6th International Symposium on Mine Haulage and Hoisting, Budva, May 23-25. 2005.

5. Helsinki Convention - Convention on the Protection of the Marine Environment of the Baltic Sea. Helcom Recommendations 9/5, 1974

6. Jones, F.V., Leuterman, J.J., Still, I.: Discharge Practices and Standards for Offshore Operations Around the World, Presented at 7th International Petroleum Environmental Conference Albuquerque, New Mexico, November 7-10, 2000.

7. Kuwait Regional Convention for Co-operation on the Protection of the Marine Environment from Pollution (1 July, 1979). Kuwait Protocol - Concerning Marine Pollution Resulting from Exploration and Exploitation of the Continental Shelf (29 March, 1989).

8. Melton, H.R., Smith, J.P., Mairs, H.L., Bernier, R.F., Garland, E., Glickman, A.H., Jones, F.V., Ray, J.P., Thomas, D., Campbell, J.A.: Environmental Aspects of the Use and Disposal of Non-aqueous Drilling fluids Associated with Offshore Oil&Gas Operations, SPE 86696, The Seventh SPE International Conference on Health, safety, and Environment in Oil and Gas Exploration and production, pp. 1-10, Calgary, Alberta, Canada, 2004.

9. Neff, J.M.: Composition, Environmental Fates, and Biological Effect of Water Based Drilling Muds and Cuttings Discharged to the Marine Environment: A Synthesis and Annotated Bibliography; Prepared for Petroleum Environmental Research Forum and API, pp. 73, Duxbury, MA, 2005.

10. OSPAR Convention, Convention for the Protection of the Marine Environment in the North East Atlantic. 1992.

11. Paulsen, J.E., Omland, TH., Igeltjorn, H., Aas, N., Solvang, S.A.: Drill Cuttings Disposal, Balancing Zero Discharge and Use of Best Available Technique, SPE/IADC 85296, SPE/IADC Middle East Drilling Technology Conference&Exhibition, pp.1-11, Abu Dhabi, UAE, 2003.

FORCE-DISPLACEMENT ANALYSIS OF BURIED STEEL PIPELINES FOR STRIKE-SLIP FAULTING

Farzad Talebi, Junji Kiyono

ABSTRACT

In the present study, FE-based models of buried steel pipeline at strike-slip fault are analyzed. And FEM models have been verified by use of analytical solution and experiment results. FEM models have been used for evaluating, in particular, the effect of axial pipe-soil interaction on force-displacement fields of the pipeline, due to different fault-pipeline crossing angles.

The first aim of this study is to present a verification method for FEM analysis of pipeline crossings strike-slip fault problems and the second one is an evaluation of the importance of axial pipe-soil interaction in pipeline crossings strike-slip fault problems.

These analyses show that changes in the axial component of pipe-soil interaction effect on the magnitude of the maximum bending moment, maximum axial force and maximum shear force of pipeline. It has shown that by decreasing of fault-pipeline crossing angle, pipeline axial force increases a lot and this increase of axial force decreases bending moment and shear force magnitude. Simultaneously the removing of the axial component of soil-pipe interaction from calculation makes increase in the maximum bending moment, maximum shear force and the horizontal displacement of pipeline and also makes very large decreasing in axial force of pipeline. Finally, we found the axial component of pipe-soil interaction very effective on the force-displacement field of the pipeline subjected to the earthquake. Additionally the presented verification method has been found very accurate and valuable in simplicity point of view.

KEYWORDS: *buried pipeline, Fault intersection, Strike-slip fault,*

FARZAD TALEBI

Doctoral candidate, Graduate school of Engineering, Kyoto University, Japan.

Email: talebi.farzad.57z@st.kyoto-u.ac.jp,

Tel: +81-9041361945

Corresponding author

PROF. JUNJI KIYONO

professor, Graduate School of Engineering, Kyoto University, Japan

Email: kiyono.junji.5x@kyoto-u.ac.jp

Tel: +81-753833249

1. Introduction

Assessment of the buried pipelines at fault crossings point is among top design priorities. This is because the bending moments and axial forces subjected to the pipeline by ground deformation at pipe-fault intersection zone become large and even cause to damages and rupture on the pipeline. Beyond the damaging effects that such rupture can have on the operation of vital lifeline network systems (EERI Kocaeli Earthquake Report, 1999; J. Uzarski and C. Arnold, 2001), an irreparable environmental damage may cause the leakage of ecologically harmful stuff such as chemical liquids or gas, natural gas, fuel or liquid waste. Nowadays the Finite element method based analysis

could expose an appropriate solution to the pipeline crossing fault problem (ASCE 2001). Nonetheless, creating a FEM model with the accurate non-linear behavior of the pipeline material, the nonlinear pipe-soil interactions, and the second-order effects is tough, and also it is possible during modeling some mistakes appear. Therefore the use of analytical methodologies, for design and verification purpose, is essential.

Pipelines damage and ruptures in the past earthquakes have been reported, such as the 1971 San Fernando earthquake (P.C. Jennings, 1971; M.A. McCaffrey and T.D. O'Rourke, 1983; T.P. Desmod et al., 1995), the 1995 Kobe earthquake (T. Nakata and K. Hasuda, 1995), the 1999 Kocaeli earthquake (EERI, 1999), the 1999 Chi-Chi earthquake (S. Takada et al., 1999) and more recently the Sarpole-Zahab Earthquake 2017 (M. Miyajima et al., 2018). Majority of damage to buried pipelines have observed due to ground deformations such (e.g. fault movements, landslides, liquefaction), whereas only a few cases of pipelines were damaged by wave propagation (T. Ariman and G.E. Muleski., 1981; J. Liang and S. Sun., 2000). The first attempt on the evaluation of fault response crossing fault was proposed by Newmark and Hall at 1975 based on a simplified analytical model of the pipeline with behavior of cable for small displacement (N.M. Newmark and W.J. Hall., 1975). The most known method for evaluation of pipeline at the intersection of both strike-slip and normal faults is proposed by Kennedy et al in 1977 (R.P. Kennedy et al., 1977) and consequently adopted by the ASCE guidelines for the seismic design of pipelines (ASCE., 1984). The bending stiffness of the pipeline at high curvature zone is neglected (D. Karamitros et al., 2007). Kennedy et al work, by revising of the bending stiffness of pipeline have extended for strike-slip fault crossings by Wang and Yeh (L.R.L. Wang and Y.A. Yeh., 1985). Wang and Yeh could solve one the bending stiffness problem at high curvature zone, but they also neglected the inappropriate contribution of axial forces on bending stiffness of pipeline. Karamitros et al (2007) more improved prior researches and developed a method for strike-slip faults in which, the pipeline is partitioned into four segments, which are analyzed according to the beam-on-elastic foundation and elastic beam theories and also took second-order effects into account in the calculation of bending strains (D. Karamitros et al., 2007). Trifonov et al extended Karamitros et al (2007) model for normal fault crossings, they removed symmetry conditions about the intersection point and contributed transverse displacements for estimation of the axial elongation of In this study, an analytical analysis based on the theory of beam on an elastic foundation is implemented besides experimental result for verification of the finite element method based model of the pipeline at the intersection point with a strike-slip fault of the 90-degree angle.

The FEM models by taking pipe-soil interaction in axial and transverse directions into account are very accurately validated with the analytical solution besides experiment results. The FEM-based model is imposed

for accurate reproduction of pipe crossings strike-slip fault with different angles for two situations of with and without axial pipe-soil interaction effect to compare the force-displacement field outputs for all of the cases and figure out the importance of axial pipe-soil interaction on this problems. The first aim of this study is to present a verification method for FEM analysis of pipeline crossings strike-slip fault problems and the second is an evaluation of the importance of axial pipe-soil interaction in pipeline crossings strike-slip fault problems.

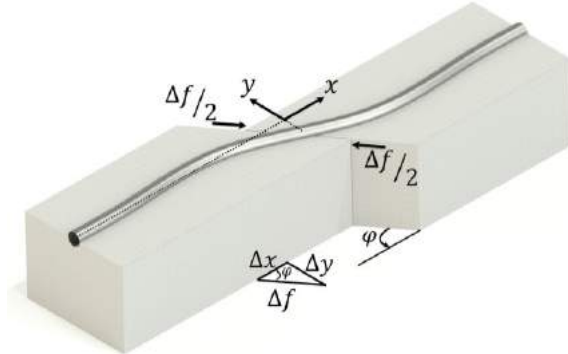


Figure 1: Deformation of axes x and y and fault displacement of Δx , Δy and Δf for oblique strike-slip fault crossing.

2. Analytical solution

In this part an analytical solution for steel pipeline subjected to strike-slip fault based on elastic beam on foundation theorem has been implemented. Since in this analytical solution the axial pipe-soil interaction effect has not conducted and also in boundary conditions only fault transverse displacements (not axial displacements) could be implemented, for getting good accuracy in results, analytical solution of pipeline crossings strike-slip faults problem is conducted only for 90° degree case which has only transverse deformation components in input ground deformation.

The differential equilibrium equation for the pipeline crossing strike-slip with 90° angle in elastic response is presented in Eq. (1) and by having boundary condition imposing $w=0$ for $x \rightarrow -\infty$ and $w=\Delta f/2$ for $x=0$ and $M=0$ for $x=0$, Eq. (1) yields:

$$-EI \frac{d^4 w}{dx^4} - kw = 0 \quad (1)$$

$$w(x) = \frac{\Delta f}{2} e^{\beta x} \cos \beta x \quad (2)$$

$$\beta = \sqrt[4]{\frac{k}{4EI}} \quad (3)$$

Here, w is transverse displacement of the pipeline, E is Young's modulus of the pipeline steel, I is the moment of inertia of the pipeline cross section, Δf is fault displacement and k is elastic constant of the transverse soil springs.

3. FEM analysis results and Verification of pipeline response with analytical solutions

To evaluate the pipeline response at strike-slip fault crossings, a number of representative numerical analyses were conducted by FEM using the commercial

code ABAQUS (ABAQUS., 2017). A typical steel pipeline was simulated in models, with an external diameter of 0.0572m and thickness of 0.0023m. A total length of 1km was simulated, for gaining higher accuracy in results symmetrically pipeline in both sides of the fault discretized gradually from fine meshes to a little bigger sizes.

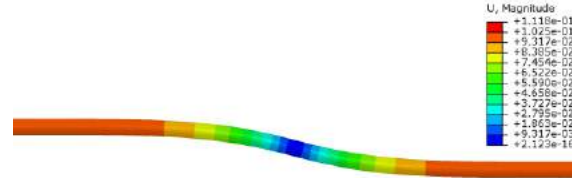


Figure 2: Displacement counters of pipeline due to 0.2m dislocation of strike-slip fault from Finite Element analysis.

Various cases with different pipe-soil interaction and different faulting angles by FEM analyzed (Table 1).

Table 1: Cases details and Pipe-Soil interaction spring properties

Case No.	Solver	Soil name	Spring type	k (GN/m ³)	Angle
1	Analytical	Soft T.	Transverse Axial	0.0018 -	90°
2	FEM	Soft T.	Transverse Axial	0.0018 -	90°
3	FEM	Soft T.A.	Transverse Axial	0.0018 0.0009	90°
4	FEM	Soft T.	Transverse Axial	0.0018 -	60°
5	FEM	Soft T.A.	Transverse Axial	0.0018 0.0009	60°
6	FEM	Soft T.	Transverse Axial	0.0018 -	45°
7	FEM	Soft T.A. Soft T.	Transverse Axial	0.0018 0.0009	45°

Table 2: distance between maximum bending moments of pipeline on experiment and analysis

type	Distance (m)
Experiment (N. Hasegawa., 2016)	1.90
FEM	2.35
Analytical	2.34

3-1. Verification of pipeline response

FEM based model respect to the mentioned analytical solution in the prior section has been created. In this part two FEM cases 2 and 3 of pipeline crossings of strike-slip fault with 90° degree angle analyzed and results are presented in comparison with analytical solution results at Fig. 3.

With regard to Table 1, case 1 and case 2 are exactly the same models without pipe-soil axial interaction but with a different method of solution. The results of FEM analysis of case2 is meticulously validated by analytical solution of case1. And additionally, the distance between 2 maximum moment points on the pipeline in the FEM verified by analytical solution results as well as experimental results in Table 2. There is a 45cm

difference between our analysis results and experiment result; it is because of non-linear effects of soil and steel pipe on the experiment which is not conducted in analytical and FEM analysis. Based on FEM analysis, the response of pipeline in both of case 2 and 3 observed as same.

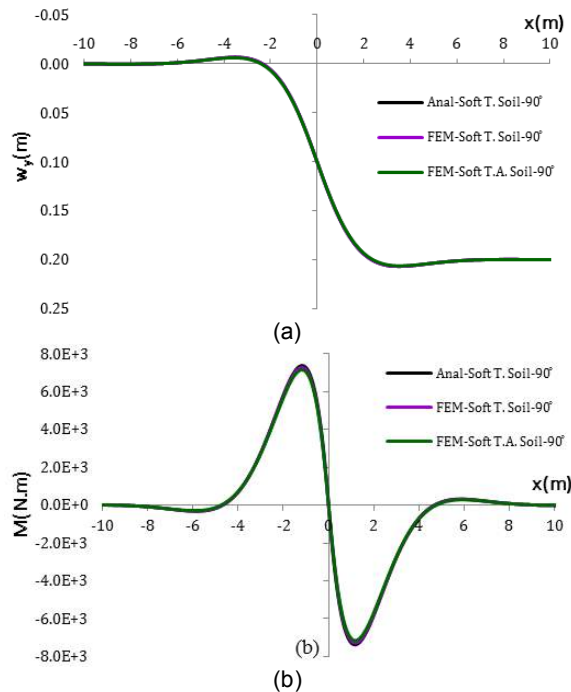


Figure 3: FEM & Analytical analysis results of pipeline subjected to strike-slip fault with 90° angle. (a) Transverse Displacement curve (b) Bending moment curve.

3-2 Results FEM analysis

By use of FEM based simulations, force-displacement fields of the pipeline crossings a strike-slip fault was studied. The mechanical behavior of the pipeline in several cases of strike-slip fault with different faulting angles and with and without axial pipe-soil interaction has been evaluated. In particular, the effect of axial soil-pipe interaction spring in pipeline behavior in various structural responses of the pipeline has been investigated in following figures.

By conducting of axial pipe-soil interaction in FEM base models, 6 different cases have been analyzed and

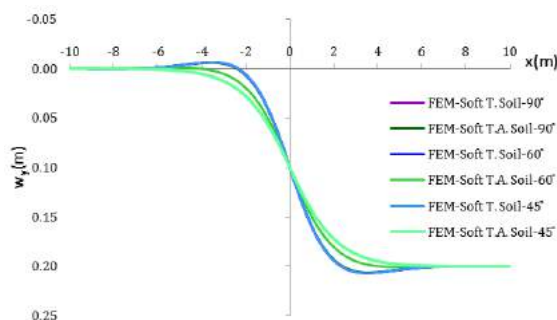


Figure 4: Transverse displacements of pipeline crossings strike-slip fault.

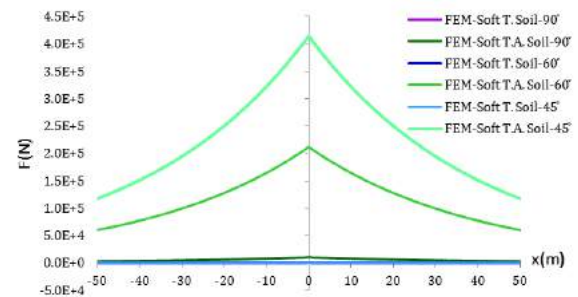


Figure 5: Axial forces of pipeline crossings strike-slip fault.

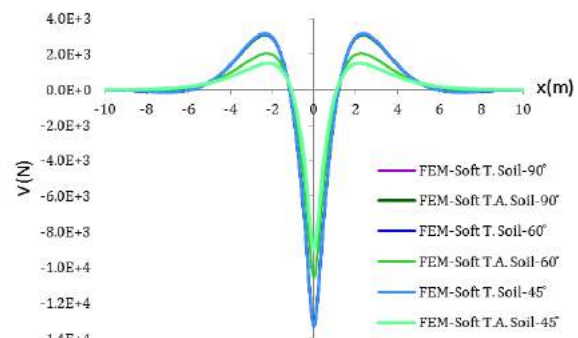


Figure 6: Shear Forces of pipeline crossings strike-slip fault.

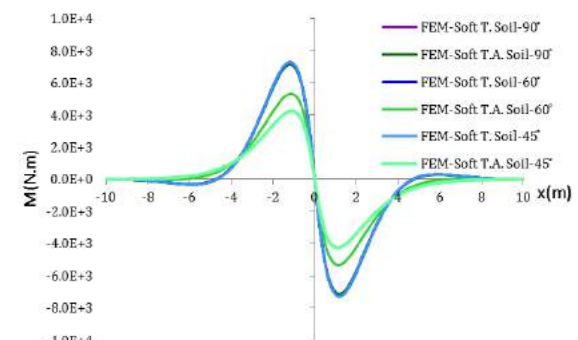


Figure 7: Bending moment of pipeline crossings strike-slip fault.

the pipeline response has been evaluated. Based on the results of the FEM analysis we obtain the following findings:

- Maximum axial force response of pipeline in crossings strike-slip fault with implementing of axial pipe-soil interaction in comparison with same case without axial pipe-soil interaction effect, in $\phi=45^\circ$ strike-slip fault 41 times and in case of $\phi=60^\circ$ strike-slip fault 21 times has been increased.
- Maximum shear force response of pipeline in crossings strike-slip fault with implementing of axial pipe-soil interaction in comparison with same case without axial pipe-soil interaction effect, in $\phi=45^\circ$ strike-slip fault 33% and in case of $\phi=60^\circ$ strike-slip fault 20% has been decreased.
- Maximum bending moment response of pipeline in crossings strike-slip fault with implementing of axial pipe-soil interaction in comparison with same case without axial pipe-soil interaction effect, in $\phi=45^\circ$ strike-slip fault 42% and in case of $\phi=60^\circ$

strike-slip fault 27% has been decreased.

- Force-displacement responses of pipeline in cases crossings 90°, 60° and 45° strike-slip faults without implementation of axial pipe-soil interaction effect were exactly same as the case of pipeline crossings 90° strike-slip fault with implementing of the axial pipe-soil interaction effect (scenario3). Hence without axial pipe-soil interaction effect, all of the cases of pipeline crossings strike-slip fault with every faulting angle will have the same response with pipeline crossings 90° strike-slip fault. Consequently, the faulting angle is very significant for pipe-soil interaction parameter. In particular, there is a direct relationship between axial pipe-soil interaction and the axial component of fault displacement (Δx).

4. Conclusions

The pipe-soil interaction and the performance of pipelines subjected to permanent strike-slip fault movement have been investigated using 2D FEM models and analytical solution. Additionally, the results of FEM analysis has been validated and verified based on the analytical solution besides experimental result. In this study we have focused on the presentation of a validation method for FEM models of pipeline crossings strike-slip faults and at second evaluated axial pipe-soil interaction importance on pipeline crossings strike-slip problems. The numerical FEM study corresponding to various values of faulting angle θ was concocted with and without implementing of axial pipe-soil interaction has been evaluated. Based on the results of FEM analysis and analytical solution, we found that:

- 1) The presented analytical solution of pipeline crossings strike-slip fault has is an accurate and feasible method for verification of the validity of FEM based models for the case of pipeline crossings 90° degree strike-slip fault in elastic range. The simplicity of this method is the main advantage. After verification of the FEM-based model for 90° fault in the elastic range, this FEM-based model could be extended and use for other cases (with different angles and etc.,) with valid results.
- 2) Decreasing of faulting angle (having oblique fault to the pipeline) makes a large increase in maximum axial force response of pipeline and makes an effective decreasing in shear force and bending moment response of pipeline crossings strike-slip fault.
- 3) A direct relation between pipeline and fault crossing angle θ and axial pipe-soil interaction without axial pipe-soil interaction has observed. The pipeline responses were similar even in different faulting angles. In another word, the main parameter on implementing of faulting angle effect is axial pipe-soil interaction.
- 4) The Axial pipe-soil interaction on pipeline crossings strike-slip fault problems has found very effective and important, which has made a big change in force-displacement responses of

the pipeline.

- 5) In The response of pipeline in FEM cases without axial pipe-soil interaction spring in comparison with the cases with the axial pipe-soil interaction, in maximum axial force response of pipeline were several times less, in maximum shear force response of pipeline 20% to 35% was more and in maximum bending moment 25% to 45% were more. Therefore for having an economic and realistic design method for controlling the damage of pipeline crossings strike-slip fault problems, it's very important to take accurately axial pipe-soil interaction effect into account.

References

1. EERI. The Izmit (Kocaeli), Turkey Earthquake of August 17, 1999. EERI Special Earthquake Report, (1999)
2. J. Uzarski and C. Arnold., (2001). Chi-Chi, Taiwan, Earthquake of September 21, 1999, Reconnaissance Report. Earthquake Spectra, Professional J EERI (2001);17(Suppl. A).
3. American Lifelines Alliance-ASCE. Guidelines for the Design of Buried Steel Pipe, (2001) (with addenda through February 2005).
4. P.C. Jennings., (1971). Engineering features of the San Fernando earthquake February 9, 1971, California Institute of Technology Report, EERL (1971) 71–02, Pasadena, CA.
5. M.A. MacCaffrey and T.D. O'Rourke., (1983). Buried pipeline response to reverse faulting during the 1971 San Fernando Earthquake. ASME, PVP conference 77 (1983) 151–9.
6. T.P. Desmod, M.S. Power, C.L. Taylor and R.W. Lau., (1995). Behavior of large-diameter pipeline at fault crossings. ASCE, TCLEE (1995) (6):296–303.
7. T. Nakata and K. Hasuda., (1995). Active fault 1995 Hyogoken Nanbu earthquake. Kagaku (1995) 65:127–42.
8. S. Takada, M. Nakayama, J. Ueno and C. Tajima., (1999). Report on Taiwan Earthquake. RCUSS, Earthquake Laboratory of Kobe University, 1999. p. 2–9.
9. M. Miyajima, A. Fallahi, T. Ikemoto, M. Samaei, S. Karimzadeh, H. Setiawan, F. Talebi and J. Karashi., (2018). Site Investigation of the Sarpoole-Zahab Earthquake, Mw 7.3 in SW Iran of November 12, 2017. JSCE Journal of Disaster FactSheets, 2018.
10. T. Ariman and G.E. Muleski., (1981). A review of the response of buried pipelines under seismic excitations. Earthquake Engineering and Structural Dynamics 1981;9:133–51.
11. J. Liang and S. Sun., (2000). Site effects on seismic behavior of pipelines: a review. ASME Journal of Pressure Vessel Technology 2000;122(4):469–75.
12. N.M. Newmark and W.J. Hall., (1975). Pipeline design to resist large fault displacement. In: Proceedings of the U.S. national conference on earthquake engineering, Ann Arbor, University of Michigan, 1975. p. 416–25.
13. R.P. Kennedy, A.M. Chow and R.A. Williamson., (1977) Fault movement effects on buried oil pipeline. ASCE Transportation Engineering Journal

- 1977;103(5):617–33.
14. ASCE Technical Council on Lifeline Earthquake Engineering. Differential ground movement effects on buried pipelines. Guidelines for the Seismic Design of Oil and Gas Pipeline Systems; 1984.
 15. D. Karamitros, G. Bouckovalas and G. Kouretzis., (2007) Stress analysis of buried steel pipelines at strike-slip fault crossings. *Soil Dynamics and Earthquake Engineering* 2007;27:200–11.
 16. L.R.L. Wang and Y.A. Yeh., (1985). A refined seismic analysis and design of buried pipeline for fault movement. *Earthquake Engineering & Structural Dynamics* 1985;13(1):75–96.
 17. O.V. Trifonov and V.P. Cherniy., (2010) A semi-analytical approach to a nonlinear stress– strain analysis of buried steel pipelines crossing active faults. *Soil Dynamics and Earthquake Engineering* 2010;30(11):1298–308
 18. ABAQUS/CAE 2017. Dassault Systems Simulia Corp, release 2017 documentation, 2017.
 19. N. Hasegawa (2016). Seismic design approach for steel pipeline crossing active faults, Doctoral thesis Kyoto University (Supervisor: Prof. Kiyono), 2016, 60p.,

DAMAGE ANALYSIS OF WATER SUPPLY SYSTEM IN HEAVY RAIN DISASTERS

N. Iwamoto¹ and M. Miyajima²

¹Graduate School of Natural Science and Technology, Kanazawa Univ., Kakuma-machi, Kanazawa, Ishikawa, 920-1192, Japan

²School of Environmental Design, Kanazawa Univ., Kakuma-machi, Kanazawa, Ishikawa, 920-1192, Japan. E-mail: miyajima@se.kanazawa-u.ac.jp

ABSTRACT

This paper examines the characteristics of damage to water supply system in heavy rain disasters in order to take effective measures against heavy rain. Firstly, a database of damage to water supply system in heavy rain disaster was made. The data include the damage to water supply facilities induced by heavy rain in Japan from 1999 to 2015. Thirty-six heavy rain disasters are picked up here because sufficient information of water stoppage and amount of rainfall are available from the database. The relation between water stoppage and amount of rainfall was clarified by using the database.

INTRODUCTION

Recently, frequency of heavy rain that is more than 50mm/h or 200mm/day has increased, therefore disasters frequently occurred in Japan. Water supply systems were also damaged by heavy rain. In the Kanto and Tohoku heavy rain disaster in 2015, two of the three purification plants in Joso city, Ibaragi prefecture were flooded and the water supply of many households stopped for about two weeks. There is every possibility of failure of water supply system by heavy rain in everywhere. However, water supply system was thought that it has not strong relation to heavy rain disaster, thus countermeasures against heavy rain was not taken positively. The water supply system was damaged by heavy rain so often in the past. Nevertheless, there are few studies that compare and review the damage to water supply system in heavy rain. The lessons learned from the disasters were, therefore, not opened and not used. This paper examines the characteristics of damage in heavy rain disasters in order to take effective measures against heavy rain.

CHARACTERISTICS OF DAMAGE IN HEAVY RAIN DISASTERS

Comparison with earthquake disaster: First of all, a database of damage to water supply system in heavy rain disasters was made by using the data of newspapers and statistics issued by government. The data include the damage to water supply facilities induced by heavy rain in Japan from 1999 to 2015. The damage by heavy rain is compared with that by earthquake to clarify the characteristics of the damage. Table 1 lists a number of incidence and water stoppage by heavy rain and by earthquake, respectively. According to Table 1, the number of water stoppage by earthquake is much bigger than that by heavy rain. However, the number of water stoppage per one incidence is almost the same as in heavy rain as in earthquake if the number in Tohoku earthquake is neglected because of very rare incidence. Therefore, it indicates that the damage by heavy rain is also very severe.

The differences of the damage by heavy rain and that by earthquake are examined. The damage depends on the seismic intensity at installation place in case of earthquake. However, when there is large precipitation at water resource and the upper stream of a river, water stoppage

may be occurred even if there is small precipitation at installation place in case of heavy rain. Figure 1 shows the relation between period of water stoppage and precipitation, that is, maximum hourly precipitation and cumulative precipitation in each local municipality. This figure indicates that the period of water stoppage does not depend on the precipitation directly.

Table 1. Comparison of water stoppage in earthquake and heavy rain.

	EQ	Heavy Rain (incl. Typhoon)
Number of incidents	5	32
Total number of water stoppage [household]	2,661,038	490,094
(Except Tohoku EQ) [household]	93,828	
Average number of water stoppage [household/incident]	18,766	15,315
Average period of water stoppage [day/incident]	20	16

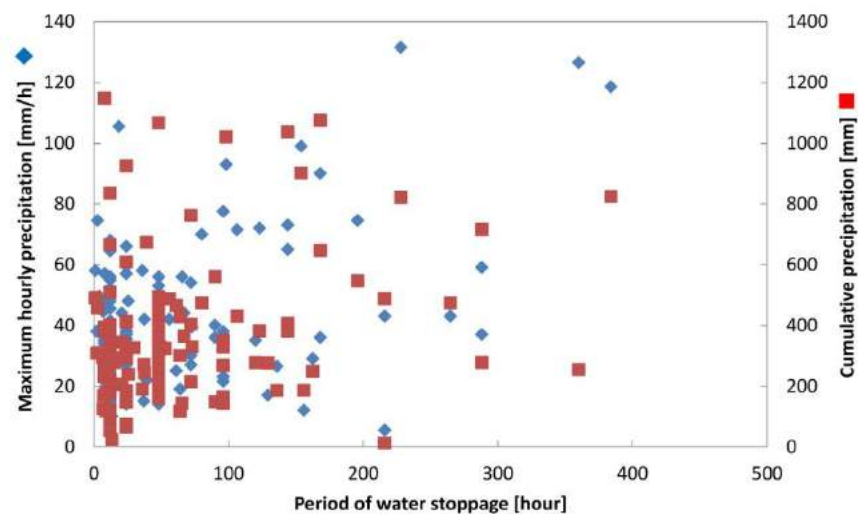


Figure 1. Relation between maximum hourly precipitation and period of water stoppage

Duration of each hazard is different. When heavy rain starts, then water level of a river rises and flows out or inundation inside a levee may occur, it takes longer time in comparison with earthquake. The flooded damage in heavy rain, particularly by river flood may be, therefore, forecasted.

A sanitation problem may be created in heavy rain disaster such as a river flood or inundation inside a levee. The water-demand in heavy rain disaster is not only daily life water but also water for cleaning. A waterworks bureau therefore must prepare emergency water-supply not only for daily life use but also for cleaning in early restoration in heavy rain disaster.

Flowchart of occurrence of damage in heavy rain: Figure 2 shows a flowchart that indicates how the damage occurs to water supply facilities by heavy rain. First step is whether water level of a river rises or not. When water level of a river rises, a water pipe bridge and/or a bridge-attached pipe may flow out or may be damaged. If a waterworks bureau uses river water for raw water, a water intake may be blockaded and raw water condition become heavily muddy. Furthermore, if a river is flooded, each water supply facility is inundated and water stoppage may occur with high probability. The extent of damage depends on inundation height. Water pipes buried close to a river bank may be damaged by scour of surface ground.

Even when sediment disaster occurs in mountainous areas, water supply facilities and pipes nearby the disaster may be damaged seriously. When water supply facilities sustain structural

damage, water stoppage may occur with high probability in case of no bypass pipe or no connecting pipe to other municipality.

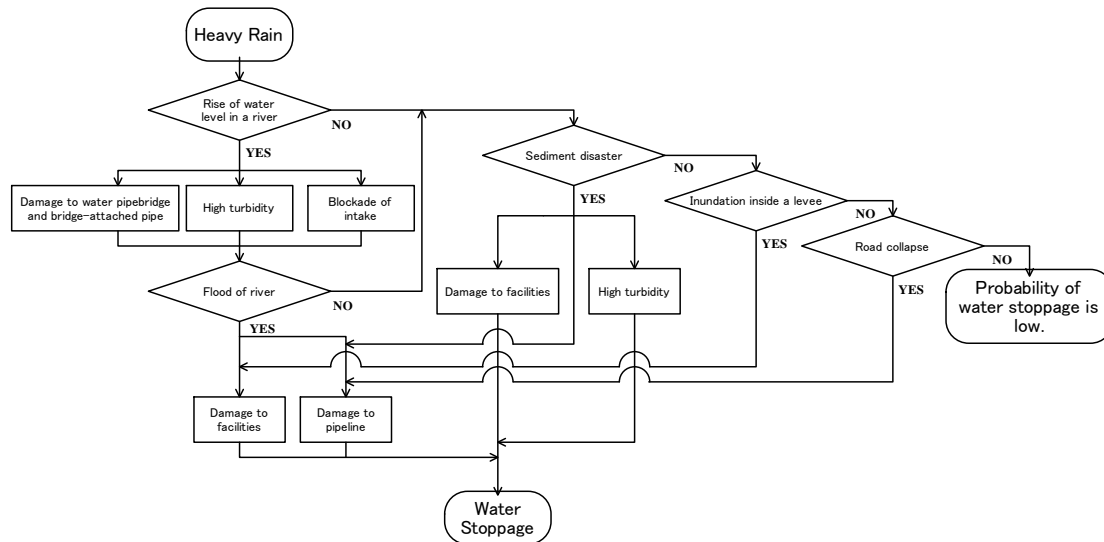


Figure 2. Flowchart of occurrence of damage to water supply system by heavy rain.

When inundation inside a levee occurs, water supply facilities are damaged functionally and structurally, and then water stoppage may occur. Furthermore, when a road collapses by heavy rain, water pipes may be damaged, broken away or flow out.

RELATION BETWEEN AMOUNT OF RAINFALL AND WATER STOPPAGE

The data of water stoppage and amount of rainfall such as precipitation from 1999 to 2015 are analyzed here. Thirty-six heavy rain disasters are picked up because sufficient information of water stoppage and amount of rainfall are available from the database. The data is arranged in each local municipality. When water stoppage is related to a river, data of rainfall is used not at areas where water stoppage occurred but at upper stream area of the river. The maximum hourly precipitation, cumulative precipitation and cumulative precipitation until water stoppage are used as a fundamental statistics of rainfall.

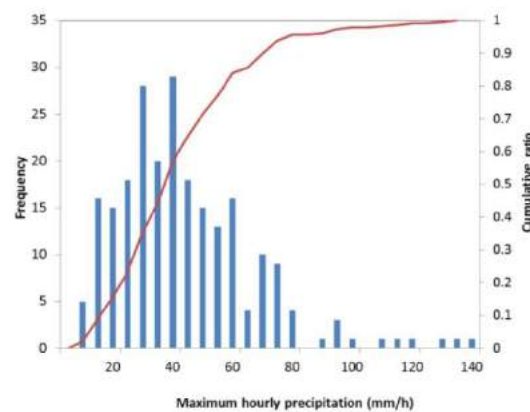


Figure 3. Histogram of maximum hourly precipitation in each water stoppage.

Figure 3 shows a histogram of maximum hourly precipitation of each municipality in each

water stoppage in heavy rain disaster. According to Figure 3, a rank of 35-39mm/h is the most frequently and its cumulative ratio is over 50%. A cause of water stoppage is not related to precipitation directly, but related to power stoppage or high waves during heavy rain disaster in 17 cases and maximum hourly precipitation is less than 15mm/h in eight cases of them. Since most of causes of water stoppage was not related to precipitation in case of a value of less than 15mm/h, 15mm/h of hourly precipitation is set as an index of water stoppage in this study. An hourly precipitation of 15mm/h is cumulative ratio of 10% in Figure 3.

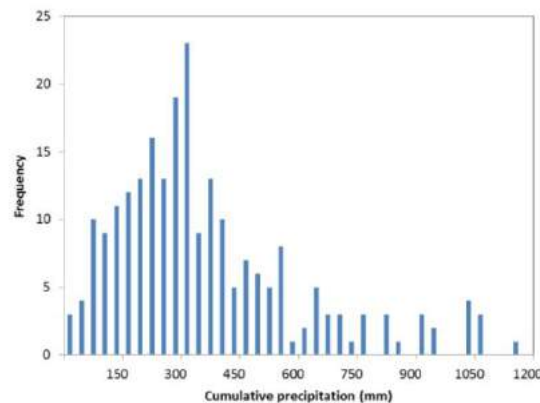


Figure 4. Histogram of cumulative precipitation in each water stoppage.

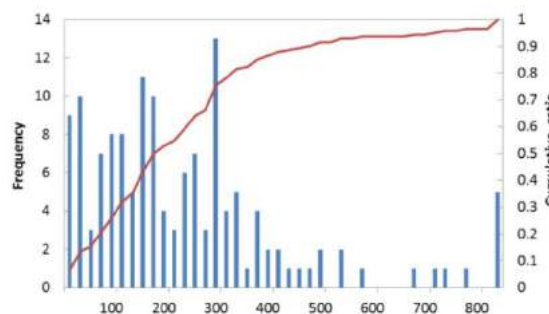


Figure 5. Histogram of cumulative precipitation until water stoppage in each water stoppage.

Figure 4 shows a histogram of cumulative precipitation of each municipality in each water stoppage in heavy rain disaster. A rank of 300-329mm is the most frequently and its cumulative ratio is over 50%. However, a cumulative precipitation is a precipitation from beginning to end of rainfall thus we cannot use it for advance preparation for disaster. Figure 5 shows a cumulative precipitation until water stoppage. A rank of 280-299mm is the most frequently and cumulative ratio of a rank of 160-179mm is over 50%. A cause of water stoppage is not directly related to precipitation, but related to failure of aged pipe, power stoppage or high waves during heavy rain disaster in case of a value less than 59mm. Therefore, 60mm of cumulative precipitation is set as an index of water stoppage in this study.

IMPACT OF DAMAGE TO EACH FACILITY TO WATER STOPPAGE

Impact of damage to each water supply facility is discussed by using number and period of water stoppage here. Table 2 lists number and period of water stoppage, maximum hourly

precipitation, cumulative precipitation and cumulative precipitation until water stoppage if damage occurs at purification plant, pipeline, pump station, or intake.

Table 2. Number and period of water stoppage by damage to each facility.

		Number of water stoppage [household]	Period of water stoppage [hour]	Max. hourly precipitation [mm/h]	Cumulative precipitation [mm]	Cumulative precipitation until water stoppage [mm]
Purification plant	Mean	3877	118.4	40.2	377.5	293.8
	Median	2539	64.0	33.0	324.0	296.3
	S.D.	3463.2	129.6	27.5	219.7	141.8
	Number of data	11	9	11	11	10
Pipeline	Mean	1043	41.5	43.5	319.8	166.3
	Median	83	24.0	41.0	302.0	154.0
	S.D.	3241.8	43.1	20.6	176.3	118.9
	Number of data	63	50	63	63	49
Pump station	Mean	3808	88.1	47.2	493.8	284.8
	Median	1171	56.1	33.3	389.0	292.5
	S.D.	6966.7	95.8	46.7	382.7	109.1
	Number of data	6	4	6	6	4
Intake	Mean	4690	67.0	37.8	367.6	262.7
	Median	462	64.0	35.3	303.8	179.0
	S.D.	8422.8	45.7	19.8	236.9	221.5
	Number of data	32	23	32	32	29
Other	Mean	367	50.1	25.6	225.4	157.4
	Median	66	12.0	25.5	176.0	119.0
	S.D.	636.3	105.0	8.4	202.7	121.9
	Number of data	9	7	9	9	7

Table 3. Number and period of water stoppage in each pipe.

		Aqueduct	Transmission pipe	Distribution pipe
Number of water stoppage [household]	Mean	162	1,978	1,666
	Median	158	1,000	32
	Number of data	4	5	27
Period of water stoppage [day]	Mean	35.3	61.3	39.1
	Median	48	13.5	24
	Number of data	3	3	24

Median of a number of water stoppages is bigger if damage occurs at purification plant or pump station than those at other facilities. This means that those two functions strongly influence water stoppage. Median of a number of water stoppages in pipelines is the smallest and a difference between the mean and median of water stoppage in pipelines is large. The reason is seems whether main pipes is damaged or not. Table 3 shows a comparison in each pipe. This table indicates that damage to transmission pipe most influence water stoppage because mean of number and period of water stoppage are largest.

Median of a period of water stoppage is larger if damage occurs at purification plant or intake than those at other facilities according to Table 2. This means that those two functions strongly influence period of water stoppage. Median of a period of water stoppage in pipelines is the smallest. The reason seems that the pipeline is able to be restored a short period. According to Table 3, transmission pipes strongly influence a period of water stoppage.

Finally, resistance of each facility against heavy rain was discussed by using each precipitation data in Table 2. The mean of hourly precipitation is the smallest in case of damage to intake. The function of intake is weak for momentary heavy rain. On the other hand, the

function of pump station is strong for momentary heavy rain because the mean is the biggest. The mean of cumulative precipitation until water stoppage is the biggest of purification plant thus the resistance of this function seems to be strong.

Table 4. Number and period of water stoppage induced by inundation of purification plant and high turbidity of water resource.

		Number of water stoppage [household]	Period of water stoppage [hour]	Max. hourly precipitation [mm/h]	Cumulative precipitation [mm]	Cumulative precipitation until water stoppage [mm]
High turbidity	Maximum	33400	241	93	1021	717
	Minimum	0	0	6	39	0
	Median	2900	64	19	217	95
	Mean	8731	82	28.9	345.0	261.2
	Number of data	9	7	7	7	5
Inundation of plant	Maximum	35377	465	288	569	472
	Minimum	40	62	26	59	259
	Median	3578	143	43	429	323
	Mean	8409	168.9	65.6	381.7	345.0
	Number of data	14	11	11	11	8

From the above, resistance of purification plant is strong but if damage to purification plant occurs, number and period of water stoppage become comparatively large. On the other hand, resistance of function of pipelines is relatively small but number of and period of water stoppage is not so large.

Damage to purification plants strongly influences water stoppage in heavy rain disaster. Influence of inundation of purification plant and high turbidity of water resource in floods are compared. Table 4 lists number and period of water stoppage induced by inundation of purification plant and high turbidity of water resource. The mean of number of water stoppage is almost same but median of that induced by inundation of plant is one point two times larger than that by high turbidity. Median of period of water stoppage by inundation of plant is two times longer. Because when a water purification plant is covered by water, not only the function of purification but also transmission, distribution and draining is damaged.

DIFFERENCE OF DAMAGE BY FLOODS AND SEDIMENT DISASTERS

Influence of damage by floods and sediment disaster on water supply system is discussed. Table 5 lists number and period of water stoppage by floods and sediment disasters during heavy rain. Median of number of water stoppage in floods is two times larger than that in sediment disasters. Median of period of water stoppage in floods is also longer than that of sediment disasters. Cumulative precipitation until water stoppage in both disasters is compared. The mean of cumulative precipitation until water stoppage in floods is smaller than that of sediment disasters. Thus, water stoppage in floods occurs easily. Table 6 shows number of water stoppage induced by damage to each facility. According to this table, water stoppage induced by damage to pipelines is occurred in sediment disaster rather than in floods. Furthermore, damage to pipeline or purification plant easily causes water stoppage in floods and damage to pipeline or intake easily causes water stoppage in sediment disasters.

Table 5. Number and period of water stoppage by floods and sediment disasters.

		Number of water stoppage [household]	Period of water stoppage [hour]	Max. hourly precipitation [mm/h]	Cumulative precipitation [mm]	Cumulative precipitation until water stoppage [mm]
Floods	Mean	1909	65.2	40.1	334.1	242.9
	Median	355	48	37.8	324.8	164.0
	S.D.	3086.7	71.5	15.1	184.2	155.3
	Number of data	18	17	18	18	15
Sediment disasters	Mean	1644	52.6	40.7	375.3	274.0
	Median	176	24.8	36.5	298.5	237.5
	S.D.	4078.5	63.1	20.7	231.1	172.1
	Number of data	42	30	42	42	33

Table 6. Number of water stoppage induced by the damage to each facility.

	Purification plant	Pipeline	Pump station	Intake	Other	Sum
Floods	5 26%	7 37%	2 11%	4 21%	1 5%	19 100%
Sediment disasters	2 4%	28 56%	1 2%	14 28%	5 10%	50 100%

From the above, number and period of water stoppage in floods are larger than those in sediment disasters. Nevertheless, period of water stoppage in sediment disaster is longer than that in floods in case of damage to pipelines. Furthermore, water stoppage in floods easily occurs than that in sediment disaster because cumulative precipitation until water stoppage in floods is smaller than that in sediment disaster.

CONCLUSION

The damage to water supply system by heavy rain is analyzed in this study. Firstly, a database of damage to water supply system in heavy rain was made by using the data of newspapers and statistics issued by government in Japan from 1999 to 2015. Then the relation between water stoppage and amount of rainfall was discussed by using the database. The results of this study are summarized as follows.

- 1) 15mm/h of hourly precipitation is an index of occurrence of water stoppage and 60mm of cumulative precipitation is another index of occurrence of water stoppage.
- 2) A resistance of purification plant for heavy rain is strong but if damage to purification plant occurs, number and period of water stoppage become comparatively large. On the other hand, the resistance of function of pipelines is relatively small but number and period of water stoppage is not so large.
- 3) Number and period of water stoppage in floods are larger than those in sediment disasters. Nevertheless, period of water stoppage in sediment disasters is longer than that in floods in case of damage to pipelines.
- 4) Water stoppage in floods easily occurs than that in sediment disaster because cumulative precipitation until water stoppage in floods is smaller than that in sediment disaster.

ACKNOWLEDGEMENT

We deeply appreciate to Mr. Masa-aki Fukushima, the director and chief editor of the newspaper of waterworks industry in Japan for his kind offer of database of the articles of the newspaper.

REFERENCES

- Cabinet Office. “Catalog of disaster information” <http://www.bousai.go.jp/updates/index.html> (Oct., 2014).
- Japan Meteorological Agency. “Meteorological data in past” <http://www.data.jma.go.jp/obd/stats/etrn/> (June, 2015).
- Ministry of Land, Infrastructure, Transport and Tourism. “Hydrological data and water quality data” <http://www1.river.go.jp/> (June, 2015).

DEVELOPING AN ANALYTICAL METHOD FOR DETERMINING THE RADIUS OF FAILURE ZONE OF SINGLE PILE IN SAND

PHÁT TRIỂN PHƯƠNG PHÁP GIẢI TÍCH XÁC ĐỊNH BÁN KÍNH VÙNG PHÁ HOẠI CỦA CỌC ĐƠN TRONG CÁT

Tran Van Tuan, Bui Huu Trong, Vo Van Dau, Le Tuan Anh

ABSTRACT

Bearing capacity of single pile is an essential part of foundation engineering field. The bearing capacity includes shaft friction along the pile shaft length and end-bearing capacity under the pile tip. The end-bearing capacity intensely depends on failure zone around the pile tip and it has been proposed by several authors. Failure zone has a shape of spherical cavity expansion is a remarkable proposal on which this research focused. An analytical method based on cavity expansion theory was developed to determine the radius of failure zone under the piled tip for single pile in sand. Finite element method (FEM) was also used for comparing purpose. The radius of failure zone obtained from proposed method approximated to FEM. Results indicated that the radius of failure zone of single pile in sand can be determined using this proposed method.

KEYWORDS: *analytical method, pile in sand, bearing capacity, failure zone, cavity expansion.*

TÓM TẮT

Sức chịu tải của cọc đơn là một phần quan trọng trong lĩnh vực nền móng. Sức chịu tải này bao gồm ma sát bên theo chiều dài thân cọc và sức kháng dưới mũi cọc. Sức kháng mũi phụ thuộc vào vùng phá hoại xung quanh mũi cọc, vùng phá hoại này đã được đề xuất bởi nhiều tác giả. Bài báo này tập trung nghiên cứu vùng phá hoại có dạng hình cầu theo lý thuyết mở rộng lỗ rỗng. Một phương pháp giải tích dựa trên lý thuyết mở rộng vùng phá hoại dạng này được phát triển để xác định bán kính của vùng phá hoại cho cọc đơn trong đất cát. Phương pháp phần tử hữu hạn cũng được sử dụng với mục đích so sánh. Bán kính của vùng phá hoại tìm được từ phương pháp giải tích xấp xỉ kết quả tìm được từ phương pháp phần tử hữu hạn. Kết quả cho thấy bán kính vùng phá hoại của cọc đơn trong đất cát có thể xác định bằng cách sử dụng phương pháp được đề xuất này.

TỪ KHÓA: *phương pháp giải tích, cọc trong cát, sức chịu tải, vùng phá hoại, lý thuyết mở rộng vùng phá hoại.*

DR. TRAN VAN TUAN

Lecturer, Department of Civil Engineering, Can Tho University (CTU)
Email: tvantuan@ctu.edu.vn **corresponding author**
Tel: 0901088944

BUI HUU TRONG

Master student, Transportation Management Center, Department of Transportation, An Giang, Vietnam.
Email: trongm4216046@gstudent.ctu.edu.vn
Tel: 0945151447

VO VAN DAU

Lecturer, Department of Civil Engineering, Can Tho University (CTU)

Email: vvdau@ctu.edu.vn

Tel: 0947180418

LE TUAN ANH

Bachelor student, Can Tho University (CTU).

Email: anhlee1015@gmail.com

Tel: 01225830517

1. Introduction

Many proposals for estimating bearing capacity of a single pile have been used for a long time. These proposals depend on the assumption of failure zone around the piled tip. Randolph's method, which is based on the analogy between spherical cavity expansion and bearing failure, is the same as the assumption in Fig.1 (d), as in [7]. Bearing capacity of the single pile in sand was revealed in Randolph's method [5] but the radius of the failure zone was not determined.

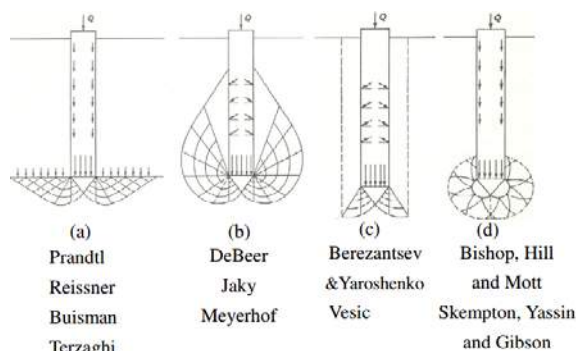


Fig. 1 Assumed failure patterns [7]

In this study, an analytical method was developed to determine the radius of the failure zone under the pile tip of single pile in sand. The analytical method was based on cavity expansion theory. Beside the analytical method, finite element method was performed using 2D Plaxis.

Through this analytical study, it is expected the radius of single pile in soils could be determined more accurately and the new reliable results would be obtained. Some discussions and recommendations were also presented.

2. Literature review

In Terzaghi's assumption (1943), the failure surfaces developed between the edges of the pile tip and the horizontal plane as show in Fig. 1(a). In Meyerhof's bearing capacity theory (1951), the failure zone was assumed as in Fig. 1(b). In Fig. 1(c), the failure surface at ultimate load under a single pile is termed as punching shear failure by

Vesic (1963). As per the theory of cavity expansion, the failure zone is analogous to spherical cavity expansion. This research has focused on the assumption as shown in Fig. 1(d).

3. Analytical method

3.1 Equilibrium condition

In cylindrical coordinate: Notation for normal and shear stresses in cylindrical coordinate is in Fig. 2. The stresses are acting on an elemental soil mass. For equilibrium, summing forces in z direction. The equation of equilibrium for forces in the radial direction

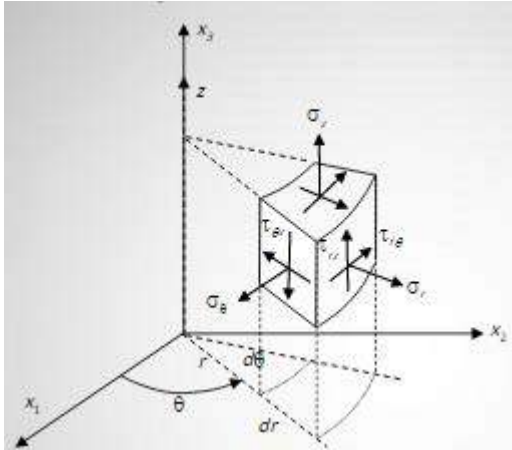


Fig. 2 Forces for an elemental soil mass in cylindrical coordinate system

$$\frac{\partial \sigma_r}{\partial r} + \frac{\sigma_r - \sigma_\theta}{r} + \frac{1}{r} \frac{\partial \tau_{r\theta}}{\partial \theta} + f_r = 0$$

Neglecting $f_r, \tau_{r\theta} \Rightarrow \frac{\partial \sigma_r}{\partial r} + \frac{\sigma_r - \sigma_\theta}{r} = 0$

In spherical coordinate:

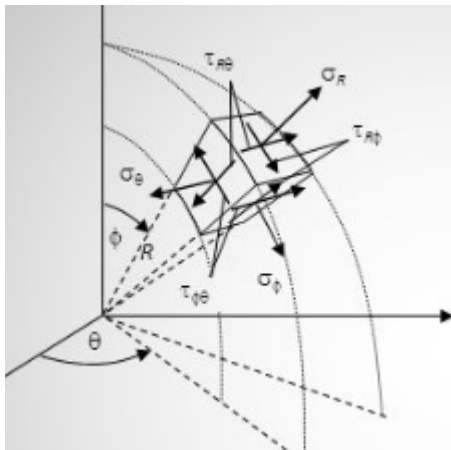


Fig. 3 Forces for an elemental soil mass in spherical coordinate system

Summing up forces in the radial direction, neglecting body force per unit volume in the radial direction, the equation of equilibrium can be obtained

$$\frac{\partial \sigma_r}{\partial r} + \frac{1}{r} \frac{\partial \tau_{r\theta}}{\partial \theta} + \frac{1}{r \sin \theta} \frac{\partial \tau_{r\phi}}{\partial \phi} + \frac{2\sigma_r - \sigma_\theta - \sigma_\phi + \tau_{r\theta} \cot \theta}{r} = 0$$

For θ is infinitesimal: $\sin \theta = \cot \theta = \theta$

The axial symmetry that for the spherical cavity: $\sigma_\phi = \sigma_\theta$

Neglecting $\tau_{r\theta}$ and $\tau_{r\phi}$. Neglecting

$$\Rightarrow \frac{\partial \sigma_r}{\partial r} + \frac{2(\sigma_r + \sigma_\theta)}{r} = 0$$

In summary $\frac{\partial \sigma_r}{\partial r} + k \frac{(\sigma_r + \sigma_\theta)}{r} = 0$ (1)

where : $k=1$ for cylindrical cavity ; $k=2$ for spherical cavity

3.2 Cavity expansion problem

Initially, at time $t=0$: the cavity has a radius a_0 and an internal pressure $p_0 = \sigma_1 = \sigma_2 = \sigma_3$ with $\sigma_1, \sigma_2, \sigma_3$ are the principal stress components. At time t later: the cavity has a radius a , internal pressure p . In the radius direction: $\sigma_1 = p$ when $r = a$; $\sigma_r = p_0$ when $r = \infty$

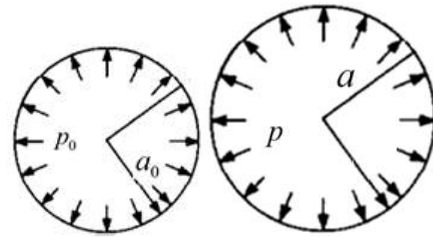


Fig. 4 Cavity expansion radius [2]

3.3 Plane strain and axial symmetric conditions

The expansion in cylindrical cavity occurs under plane strain conditions. The plane strain state obeys Hooke's law. There is no components of plastic strain in z direction and plane strain conditions provide that $\Delta \epsilon_3 = 0$.

$$\Delta \epsilon_3 = \frac{1}{E} (-\nu \Delta \sigma_1 - \nu \Delta \sigma_2 + \Delta \sigma_3) = 0$$

$$\Rightarrow \Delta \sigma_3 = \nu (\Delta \sigma_1 + \Delta \sigma_2)$$

In cylindrical coordinate: $\Delta \sigma_z \equiv \Delta \sigma_3$, $\Delta \epsilon_z \equiv \Delta \epsilon_3$

$$\Rightarrow \Delta \sigma_z = \nu (\Delta \sigma_r + \Delta \sigma_\theta) \quad (2)$$

From axial symmetric conditions we have $\sigma_\phi = \sigma_\theta$ (3)

3.4 Hooke's law

Relationship between the rates of change of stress and strain is based on Hooke's law:

$$\dot{\sigma} = D \dot{\epsilon} \quad (4)$$

where: $\dot{\sigma} = (\dot{\sigma}_r, \dot{\sigma}_\theta)^T$; $\dot{\epsilon} = (\dot{\epsilon}_r, k \dot{\epsilon}_\theta)^T$

$$\epsilon_r = -\partial u / \partial r; \epsilon_\theta = -u / r; u = r - r_0$$

Differentiation with respect to time:

$$\dot{\epsilon}_r = -\partial \dot{u} / \partial r; \dot{\epsilon}_\theta = -\dot{u} / r$$

The coefficients of the matrix D depend on the type of material analysis, as in [2]

For purely elastic deformations

$$D_E = \begin{bmatrix} \lambda + 2\mu & \lambda \\ \lambda & \lambda + 2\mu / k \end{bmatrix} \quad (5)$$

For deformations, involve plastic yielding

$$D = \frac{2G}{\chi} \begin{bmatrix} 1 & 1/M \\ 1/N & 1/MN \end{bmatrix} \quad (6)$$

where: G is elastic shear modulus,

$$\chi = \frac{k(1-\nu) - k\nu(M+N) + [(k-2)\nu + 1]MN}{[(k-1)\nu + 1]MN}$$

ν is Poisson's ratio for the ideal material,
 $M = (1 + \sin \psi)(1 - \sin \psi)$, ψ is dilatancy angle.

The total strain includes elastic and plastic strain:

$$\dot{\epsilon} = \dot{\epsilon}^E + \dot{\epsilon}^P \quad (7)$$

In plane strain condition: $\frac{\dot{\epsilon}_1^P}{\dot{\epsilon}_3^P} = -\frac{1}{M}$; $\dot{\epsilon}_2^P = 0$

In symmetry condition: $\frac{\dot{\epsilon}_3^P}{2\dot{\epsilon}_3^P} = -\frac{1}{M}$; $\dot{\epsilon}_2^P = \dot{\epsilon}_3^P$

$$\text{In summary: } \frac{\dot{\epsilon}_r^P}{\dot{\epsilon}_\theta^P} = -\frac{k}{M} \quad (8)$$

3.5 Mohr-Coulomb criterion

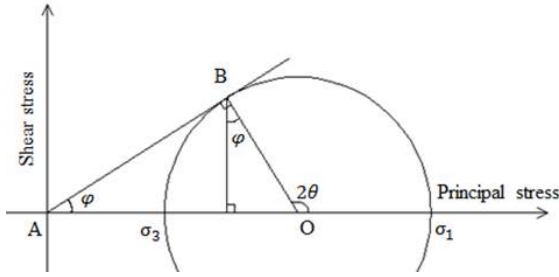


Fig. 5 Mohr circle (purely frictional material)

$$\sin \phi = \frac{OB}{OA} = \frac{\sigma_1 - \sigma_3}{\sigma_1 + \sigma_3} \Rightarrow \sigma_1 = \frac{1 + \sin \phi}{1 - \sin \phi} \sigma_3 \Rightarrow \sigma_1 = N \sigma_3$$

where $N = (1 + \sin \phi) / (1 - \sin \phi)$

σ_r and σ_θ are the major and minor principal stresses during cavity expansion

$$\Rightarrow \sigma_1 = N \sigma_3 \quad (9)$$

3.6 Radius of failure zone

Plastic yield is occurring throughout the region $a \leq r \leq R$. Beyond the elasto-plastic interface ($r > R$) the material remains elastic, as in [2].

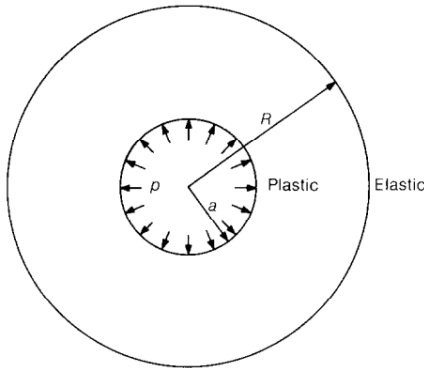


Fig. 6 Cavity expansion problem

$$u = \epsilon_R \left(\frac{R}{r} \right)^k \quad (10)$$

$$\text{where: } \epsilon_R = (\sigma_R - p_0) / 2Gk \quad (11)$$

At the elastic-plastic boundary, radial stress and circumferential strain:

$$\text{Radial stress: } \sigma_R = \frac{1+k}{N+k} N p_0 \quad (12)$$

$$\text{Circumferential strain: } \epsilon_R = \frac{N-1}{N+k} \frac{p_0}{2G} \quad (13)$$

3.6.1 Equilibrium condition in plastic zone

From Eq.(1) and Eq.(9)

$$\begin{aligned} \Rightarrow \frac{d\sigma_r}{dr} + k \frac{\sigma_r - \sigma_\theta}{r} &= 0 \\ \Leftrightarrow \frac{d\sigma_r}{dr} + k \frac{N-1}{N} \frac{\sigma_r}{r} &= 0 \end{aligned} \quad (14)$$

Eq.(14) can be solved: $\sigma_r = C r^{-k \frac{N-1}{N}}$;

when $r=R$: $\sigma_r = \sigma_R \Rightarrow \sigma_R = C R^{-k \frac{N-1}{N}}$

$$\frac{\sigma_r}{\sigma_R} = \left(\frac{r}{R} \right)^{\beta-1} \quad (15)$$

where: $\beta = 1 - k(N-1)/N$

The constitutive relation in the plastic zone:

From Eq. (6) and Eq. (4)

$$\begin{aligned} \begin{bmatrix} \dot{\sigma}_r \\ \dot{\sigma}_\theta \end{bmatrix} &= \begin{bmatrix} 1 & 1/M \\ 1/N & 1/MN \end{bmatrix} \frac{2G}{\chi} \begin{bmatrix} \dot{\epsilon}_r \\ k \dot{\epsilon}_\theta \end{bmatrix} \\ \Rightarrow \dot{\sigma}_r &= \frac{2G}{\chi} (\dot{\epsilon}_r + \frac{k}{M} \dot{\epsilon}_\theta) \Leftrightarrow \dot{\sigma}_r \frac{\chi}{2G} = -\frac{\partial \dot{u}}{\partial r} - \frac{k}{M} \frac{\dot{u}}{r} \\ \Leftrightarrow \frac{\partial \dot{u}}{\partial r} + \frac{k}{M} \frac{\dot{u}}{r} &= -\chi \frac{\dot{\sigma}_r}{2G} \\ \Rightarrow \frac{\partial \dot{u}}{\partial r} + \alpha \frac{\dot{u}}{r} &= -\chi \frac{\dot{\sigma}_r}{2G} \end{aligned} \quad (16)$$

where: $\alpha = k/M$, $M = (1 + \sin \psi) / (1 - \sin \psi)$

ψ is dilatancy angle.

Combining Eq. (15) and Eq. (16):

$$\frac{\partial \dot{u}}{\partial r} + \alpha \frac{\dot{u}}{r} = -k(k+1) \epsilon_R \chi \left(\frac{r}{R} \right)^{\beta-1} \frac{\dot{R}}{R} \quad (17)$$

In addition, when $r = R$, Eq.(10) becomes

$$\dot{u} = (k+1) \epsilon_R \dot{R} \quad (18)$$

Now, Eq.(17) can be solved:

$$\dot{u} = -(k+1) \epsilon_R \frac{k\chi}{\alpha + \beta} \left(\frac{r}{R} \right)^\beta \dot{R} + r^{-\alpha} C \quad (17')$$

Applying the appropriate boundary condition at the elastic-plastic interface ($r = R$) and Eq. (18)

$$\begin{aligned} (k+1) \epsilon_R \dot{R} &= -(k+1) \epsilon_R \frac{k\chi}{\alpha + \beta} \left(\frac{R}{R} \right)^\beta \dot{R} + R^{-\alpha} C \\ \Leftrightarrow C &= (k+1) \epsilon_R \dot{R} \left[1 + \frac{k\chi}{\alpha + \beta} \right] R^\alpha \end{aligned}$$

Equation (17') can be written:

$$\dot{u} = \epsilon_R \left[T \left(\frac{R}{r} \right)^\alpha - Z \left(\frac{r}{R} \right)^\beta \right] \dot{R} \quad (19)$$

where $T = (k+1) \left(1 + \frac{k\chi}{\alpha + \beta} \right)$; $Z = (k+1) \frac{k\chi}{\alpha + \beta}$

Equation (19) can be rewritten as

$$\frac{\dot{u}}{\dot{R}} = \epsilon_R \left[T \left(\frac{R}{r} \right)^\alpha - Z \left(\frac{r}{R} \right)^\beta \right] \quad (20)$$

For steady state deformation, ratio $\dot{u} / \dot{R} \rightarrow r / R$
Eq. (20) becomes

$$1 = \epsilon_R \left[T \left(\frac{R}{r} \right)^{1+\alpha} - Z \left(\frac{R}{r} \right)^{1-\beta} \right] \quad (21)$$

From Eq.(21) and Eq.(13):

$$\Rightarrow \frac{2G}{p_0} = \frac{N-1}{N+k} \left[T \left(\frac{R}{r} \right)^{1+\alpha} - Z \left(\frac{R}{r} \right)^{1-\beta} \right] \quad (22)$$

When $r = a$ the radial stress is treated as limit pressure:
 $\sigma_r = p_L$. Equation (22) becomes

$$T \left(\frac{R}{a} \right)^{1+\alpha} - Z \left(\frac{R}{a} \right)^{1-\beta} - \frac{2G}{p_0} \frac{N+k}{N-1} = 0 \quad (23)$$

Henceforth, the radius of failure zone of single pile in sand now can be determined using Eq.(23).

3.6.2 Geometry and properties

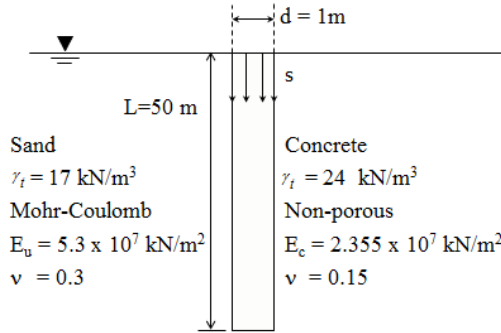


Fig.7 Geometry parameters

Table 1 Properties of sand and pile

Description	Sand	Pile
Young's modulus, E (kN/m ²)	5.3×10^4	2.355×10^7
Weight, γ (kN/m ³)	17	24
Poisson's ratio ν	0.3	0.15
Friction angle ϕ (degree)	35.5	-
Dilatancy angle ψ (degree)	0	-
Diameter, d (m)	-	1
Embedded length of pile (m)	-	50

The geometry in Fig.7 described a single concrete pile 1 m in diameter and 50 m long driven into a homogeneous sand layer. The sand layer was modelled with Mohr-Coulomb criterion while the pile was treated as a non-porous material. For the pile, the Young's modulus, E , is equal $5.3 \times 10^4 \text{ kN/m}^2$ and for the sand layer equal $2.355 \times 10^7 \text{ kN/m}^2$. Some other parameters of the pile and the sand layer were written in Table 1.

The radius could be determined by using Eq.(24).

Internal pressure: $p_0 = \gamma \times L = (17 - 10) \times 50 = 350 \text{ (kN/m}^2\text{)}$

$$N = (1 + \sin \phi) / (1 - \sin \phi) = 3.77$$

$$M = (1 + \sin \psi) / (1 - \sin \psi) = 1$$

$$\alpha = k / M = 2; \beta = 1 - k(N - 1) / N = -0.47; \chi = 0.471$$

$$T = 4.846; Z = 1.846$$

$$\text{Thus, } T \left(\frac{R}{a} \right)^{1+\alpha} - Z \left(\frac{R}{a} \right)^{1-\beta} - \frac{2G}{p_0} \frac{N+k}{N-1} = 0$$

$$\Rightarrow 38.768R^3 - 5.114R^{1.47} - \frac{20.385}{0.35} \frac{3.77+2}{3.77-1} = 0$$

$$\Rightarrow R \approx 1.875 \text{ (m)}$$

4. Finite element method (FEM)

4.1 Mohr-Coulomb Model.

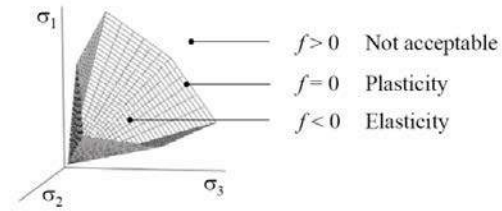


Fig. 8 Yield surfaces for the model perfectly plastic model

The basic principle of elasto-plasticity is that strains and strain rates are decomposed into an elastic part and a plastic part:

$$\varepsilon = \varepsilon^E + \varepsilon^P; \dot{\varepsilon} = \dot{\varepsilon}^E + \dot{\varepsilon}^P; \dot{\varepsilon}^P = \lambda (\partial g / \partial \sigma')$$

The following parameters must be provided.

E : Young's modulus (kN/m²);

ν : Poisson's ratio;

c : Cohesion (kN/m²);

ϕ : Friction angle (degree)

ψ : Dilatancy angle (degree)

4.2 Analysis Of Single Pile In Sand

A geometry model was built according to Fig.7 and Table 1. Material models are linear elastic for pile and Mohr-Coulomb for sand. The models has 1348 elements using the 15-noded style (Interface element adhesion factor valued of 0.75). The mesh was generated with the global coarseness set to "very fine". The model has a width of 50 m, depth of 100 m and 11106 nodes.

Applying vertical settlement: $s = (5\% - 10\%)d$. There was only a half of the pile geometry was built because this is an axisymmetrical problem. Boundary condition was set as standard fixities. The interface between pile and sand around pile shaft was patterned with contact elements. The interface factor of sand was supposed to be 0.75. The mobilization settlement varies from 5% to 10% of the pile diameter. The results are plotted in Fig.9, Fig.10 and Fig.11.

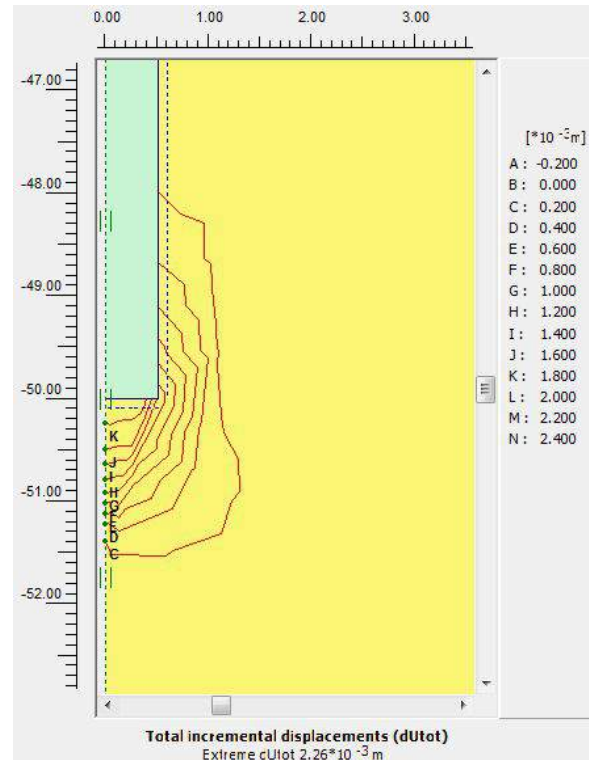


Fig. 9 Failure zone under the pile tip ($s = -0.05 \text{ m}$; $5\% d$)

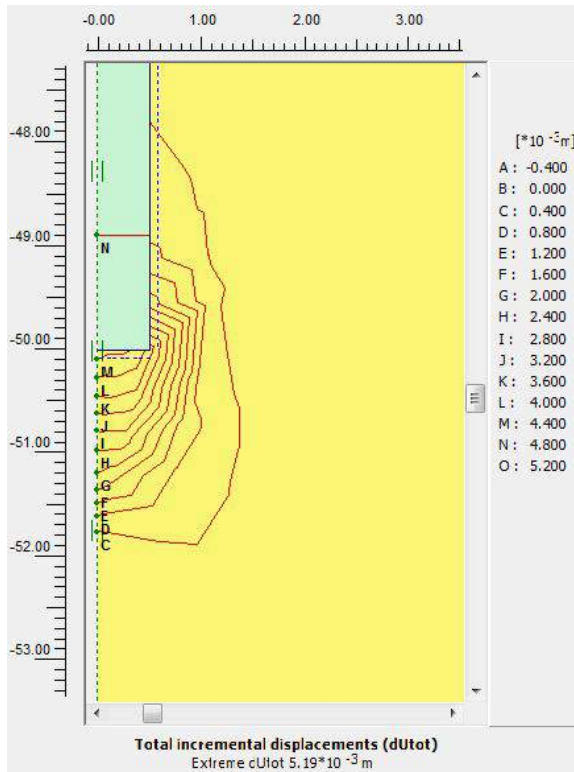


Fig. 10 Failure zone under the pile tip ($s=-0.075\text{m}$; $7.5\%d$)

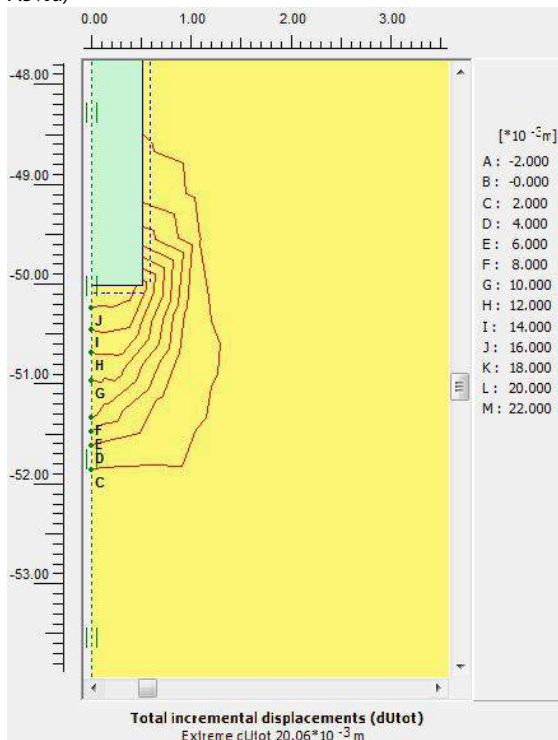


Fig. 11 Failure zone under the pile tip ($s=-0.1\text{m}$; $10\%d$)

5. Comparison of results

Accuracy of the analytical method can be assessed by comparing results. Bearing capacity of the pile has not already mobilized when vertical settlement s is equal 5% or 7.5% of diameter d . Geometry of glide was approaching spherical shape. The value of radius R was acquired from

analytical method and FEM (with $s = 10\%d$) are 1.875m and 1.850m respectively. The two results shown this analytical method is acceptable.

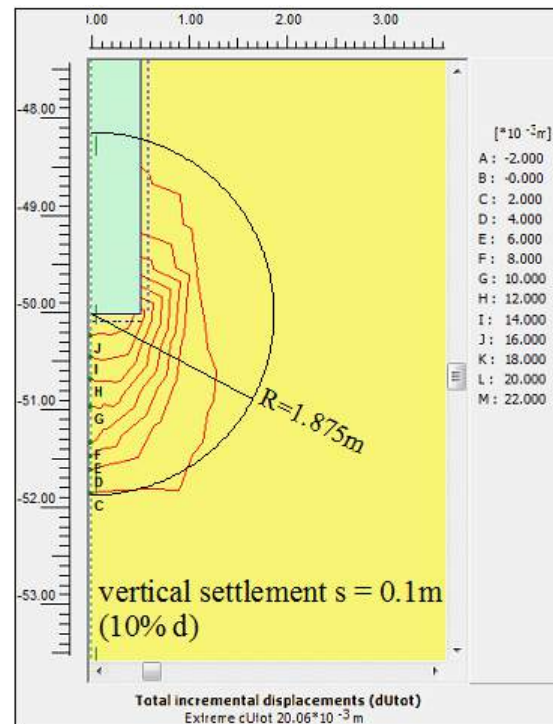


Fig. 12 Radius of failure zone – Analytical method & FEM

6. Conclusions

Radius of failure zone under pile tip of single pile in sand can be determined using this method. The radius was found in analytical method approximates to the radius was found in FEM.

The formula for calculating the radius of single pile in sand could be developed into the one for calculating the radius of single pile in general soil.

7. References

1. Braja M.Das. (1983). Principles of foundation engineering. United States of America. Global Engineering: Christopher M. Shortt.
2. Cater, J. P., Booker, J.R & Yeung, S.K. 1986. Cavity expansion in cohesive frictional soils. Geotechnique 36, No. 3, 349-353.
3. Muni Budhu. (2011). Soil mechanics and foundations. The United States of America. John Wiley & Sons, Inc.
4. Poulos, H. G. & Davis, E. H. (1974). Elastic Solutions for Rock and Soil Mechanics. Sydney. John Wiley & Sons, Inc.
5. Randolph, M. F., Dolwin, J., & Beck, R. 1994. Design of driven piles in sand. Geotechnique 44, No. 3, 427-488.
6. Timoshenko, S. & Goodier, J. N. (1951). Theory of Elasticity. New York. McGraw-Hill book company, Inc.
7. T.V. Tran., M. Kawamura., & T.Boonyatee. 2009. An Analytical Study on Failure Zone around Concrete Piles under Ultimate Loads. The 22nd KKCNN Symposium on Civil Engineering, 31 October - 2 November, 2009, Chiang Mai, Thailand. 527 – 533.

STRONG GROUND MOTION SIMULATION OF THE MAINSHOCK OF THE 2016 KUMAMOTO EARTHQUAKES WITH MULTIPLE POINT SOURCES AND NEAR SURFACE RUPTURES

Yosuke Nagasaka and Atsushi Nozu

ABSTRACT

We conducted strong ground motion simulation for the main shock of the 2016 Kumamoto earthquakes (Mw7.0). In the simulation, near surface rupture area (0-3 km deep) was newly added to the point source model by Nagasaka and Nozu (2017). Near and intermediate-field terms were evaluated for the near surface slip area, which can be predominant in near fault area, however, has often been ignored in semi-empirical strong ground motion simulations. These terms were evaluated by correcting Green's functions that consist of only far-field terms, based on elastic wave theory. Then synthetic Fourier spectra and velocity waveforms were compared with observations. The result showed that near surface slip was necessary to explain low frequency components below 0.5 Hz at stations very close to the fault, indicating that near surface ruptures are important for large structures with lower natural frequencies.

KEYWORDS: Strong ground motion simulation, the 2016 Kumamoto earthquakes, source model

MR. YOSUKE NAGASAKA

Researcher, Engineering Seismology Group, Earthquake Disaster Prevention Engineering Division, Port and Airport Research Institute

Email: nagasaka-y@pari.go.jp **corresponding author**

Tel: +81468445085

DR. ATSUSHI NOZU

Director, Disaster Prevention Engineering Division, Port and Airport Research Institute

Email: nozu@pari.go.jp

Tel: +81468445085

1. Introduction

The main shock of the 2016 Kumamoto, Japan, earthquakes occurred at 01:25 on April 16, 2016 (JST), with Mw 7.0. The ruptures started at a depth of 12 km and reached the surface, resulting in 34 km of surface ruptures (Y. Shirahama et al., 2016). Source process analyses by waveform inversion technique have been conducted for the earthquake (Asano and Iwata, 2016; Kubo et al., 2016; Yoshida et al., 2017; Nozu and Nagasaka, 2017). They revealed detailed slip distribution using relatively low frequency components below 1 Hz except for Nozu and Nagasaka (2017), which used 0.2-2 Hz. For engineering purposes, it is also important to develop a strong motion model that is sufficiently simple and applicable to higher frequency components as well as low frequency components.

Nagasaka and Nozu (2017) conducted strong ground motion simulation using a pseudo point-source model (Nozu, 2012), which consists of point sources, path effect, empirical site amplification factor, and empirical phase characteristics. In spite of its simplicity, the model well reproduced the observed Fourier spectra and velocity

waveforms of the Kumamoto earthquake. On the other hand, Nagasaka and Nozu (2017) underestimated low frequency components below 0.5 Hz, which can be a problem when the simulated ground motions are used as the design ground motion of large structures such as quay walls or high rise buildings. The underestimation in the low frequency range can be attributable to the effect of near surface slip, which were not considered in the point source model.

The effect of near surface slip can be seen as permanent displacements in observed records because near and intermediate-field terms are significant in the near fault region. In fact, over 100 cm of permanent displacement and over 100 cm/s of peak velocity were observed at the KiK-net station KMMH16 (Aoi et al., 2004; Okada et al., 2004) as shown in Figure 1. This fact shows that near surface ruptures affected the strong ground motions for the earthquake although near surface slips have often been ignored in semi-empirical strong ground motion simulations.

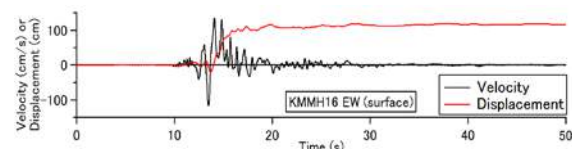


Figure 1: Estimated velocity and displacement at KMMH16 during the 2016 Kumamoto earthquake

In the semi-empirical strong motion models, recorded or simulated weak-motions are used as Green's functions and these weak-motions usually do not include permanent displacement. Nagasaka and Nozu (2017) also considered only far-field terms in their simulation with point sources. Thus, considering near surface slips in the strong ground motion simulation can potentially improve our strong motion model for the Kumamoto earthquake.

In this study, strong ground motion simulation model by Nagasaka and Nozu (2017) was revised by incorporating a near surface slip area to the point sources, and the effect of the near surface slip was examined.

2. Methods

2.1 Pseudo point-source model

The pseudo point source model is a source model for strong ground motion simulations. In the pseudo point source model, synthetic Fourier transform at a target site from a point source is modeled using the source, path, site amplification, and phase spectra, which can be written as

$$A(f) = S(f)P(f)G(f) \frac{o(f)}{|o(f)|_p},$$

where f is the frequency, $A(f)$ is the synthetic Fourier transform at a target site, $S(f)$ is the source spectrum, $P(f)$ is

the path spectrum, $G(f)$ is the site amplification factor, $O(f)/|O(f)|_p$ is the phase spectrum. $S(f)$ and $P(f)$ are given by Boore (1983):

$$S(f) = R_{\theta\phi} \cdot PRTITN \cdot FS \cdot \frac{M}{4\pi\rho\beta^3} \cdot \frac{(2\pi f)^2}{1 + (f/f_c)^2},$$

$$P(f) = \frac{1}{r} \exp\left(-\frac{\pi r f}{Q\beta}\right),$$

where $R_{\theta\phi}$ is the radiation coefficient, $PRTITN$ is the coefficient to divide the seismic energy into two horizontal directions, FS is the amplification factor due to the free surface (=2 in this study), M is the seismic moment, ρ and β are the density and shear wave velocity in source region. f_c is the corner frequency, r is the distance from the point source to the site, Q is the quality factor. $S(f)$ follows the omega-square model and $P(f)$ includes geometrical spreading and inelastic damping.

For $G(f)$, in this study, we used empirical site amplification factors that were evaluated by spectral inversion technique using many observed records (Nozu et al. 2006). Velocity profiles are not necessary to evaluate the empirical site amplification factors. They are simply derived from the observed records and, therefore, they are consistent with the characteristics of observed records. $S(f)P(f)G(f)$ corresponds to the synthetic Fourier amplitude at the target station.

$O(f)$ is the Fourier transform of a weak motion record at the target station to evaluate the phase characteristics. $|O(f)|_p$ is the absolute value of $O(f)$, to which a Parzen window of 0.05 Hz bandwidth is applied. $O(f)/|O(f)|_p$ is a complex spectrum whose absolute value is almost one. The absolute value of $O(f)/|O(f)|_p$ is not a constant value, but has ripples because the Parzen window is applied in the denominator. The ripples are necessary for generating causal ground motions (Nozu and Sugano, 2008). Synthetic waveforms are the sum of sinusoidal waves with various frequency and each sinusoidal waves is not causal. Causal synthetic waves can be obtained by summing sinusoidal waves with appropriate combination of amplitudes and phases. Thus, we need to keep the ripples in $O(f)$.

In the pseudo point-source model, only six parameters are necessary for each point source, namely, longitude, latitude, depth, seismic moment, corner frequency, and relative rupture time. The model does not explicitly consider the spatiotemporal extension of the source for simplicity. Instead, the finiteness of the point source is implicitly considered by f_c , which is inversely proportional to the square root of the area. In spite of the simplicity, the model has successfully been applied to large earthquakes including the 2011 Tohoku earthquake.

2.2 Near surface slip area

For the near surface slip area, we need to evaluate the near and intermediate field-terms, which become predominant over the far-field terms when the target site is close enough to the fault. Nozu (2006) proposed a simple method to evaluate the near and intermediate-field terms. In the method, Green's functions consisting of only far-field terms for P and S waves are firstly evaluated by multiplying $S(f)$ and $P(f)$. The Green's functions include source spectrum that follows the omega-square model, geometrical spreading, and inelastic damping. For P-waves, P-wave velocity α is used instead of S-wave velocity β and appropriate $R_{\theta\phi}$ is used for S waves and P waves.

Then theoretical expression for the elastic waves from a dislocation point source in an unbounded uniform medium is used to evaluate the near and intermediate-field terms from the far-field terms.

$$u(x, t) = \frac{M}{4\pi\rho} \left[\begin{aligned} &R_{\theta\phi}^N \frac{1}{r^4} \int_{-\frac{r}{\beta}}^{\frac{r}{\beta}} \tau f(t-\tau) d\tau + R_{\theta\phi}^{IP} \frac{1}{r^2\alpha^2} f\left(t-\frac{r}{\alpha}\right) \\ &+ R_{\theta\phi}^{IS} \frac{1}{r^2\beta^2} f\left(t-\frac{r}{\beta}\right) + R_{\theta\phi}^{FP} \frac{1}{r\alpha^3} \dot{f}\left(t-\frac{r}{\alpha}\right) + R_{\theta\phi}^{FS} \frac{1}{r\beta^3} \dot{f}\left(t-\frac{r}{\beta}\right) \end{aligned} \right],$$

where $u(x, t)$ is the displacement at coordinate x and time t , $f(t)$ is the normalized source time function. $R_{\theta\phi}$ is the radiation coefficient and the superscripts of $R_{\theta\phi}$ are the abbreviations for the Near, Intermediate-field P, Intermediate-field S, Far-field P, and Far-field S waves, respectively. α is the P-wave velocity.

After applying Fourier transform to $u(x, t)$, the ratios of all the terms to far-field P and S terms are calculated respectively. The ratio is calculated for the θ and ϕ components and the r component separately because far-field S wave has θ and ϕ components and far-field P wave has only r component. It can be theoretically shown that the ratio is not dependent on θ and ϕ . The ratio can be expressed as follows.

For the θ and ϕ components:

$$\frac{N_{\theta\phi} + IP_{\theta\phi} + IS_{\theta\phi} + FS}{FS} =$$

$$6i\left(\frac{\beta}{r\omega}\right)^3 \left[1 - e^{-i\omega r\left(\frac{1}{\alpha}-\frac{1}{\beta}\right)}\right] - 6\left(\frac{\beta}{r\omega}\right)^2 \left[1 - \frac{\beta}{\alpha} e^{-i\omega r\left(\frac{1}{\alpha}-\frac{1}{\beta}\right)}\right]$$

$$+ 2i\left(\frac{\beta}{r\omega}\right)\left(\frac{\beta}{\alpha}\right)^2 e^{-i\omega r\left(\frac{1}{\alpha}-\frac{1}{\beta}\right)} - 3i\left(\frac{\beta}{r\omega}\right) + 1,$$

for the r component:

$$\frac{N_r + IP_r + IS_r + FP}{FP} =$$

$$9i\left(\frac{\alpha}{r\omega}\right)^3 \left[1 - e^{-i\omega r\left(\frac{1}{\beta}-\frac{1}{\alpha}\right)}\right] - 9\left(\frac{\alpha}{r\omega}\right)^2 \left[1 - \frac{\alpha}{\beta} e^{-i\omega r\left(\frac{1}{\beta}-\frac{1}{\alpha}\right)}\right]$$

$$- 4i\left(\frac{\alpha}{r\omega}\right) + 3i\left(\frac{\alpha}{r\omega}\right)\left(\frac{\alpha}{\beta}\right)^2 e^{-i\omega r\left(\frac{1}{\beta}-\frac{1}{\alpha}\right)} + 1,$$

where ω is the angular frequency ($=2\pi f$), i is the imaginary unit. For the θ and ϕ components, $S(f)P(f)$ for far-field S term is multiplied by the ratio of θ and ϕ components to obtain the Green's function including all terms; for r component, $S(f)P(f)$ for far-field P term is multiplied by the ratio of r component.

Finally, empirical site amplification factors and empirical site phase characteristics are incorporated into the Green's functions. In this study, our target frequency range is 0.2 to 10 Hz because the empirical site amplification factors used in the study are valid in that particular frequency range according to Nozu et al. (2006).

3. Simulation for the 2016 Kumamoto earthquake

3.1 Settings

Target stations and the modeled fault geometry of this study are shown in Figure 2. Eight K-NET and KiK-net stations around the fault were selected from the stations used in nagasaka and Nozu (2017). Among the eight stations, KMM006, KMMH16, and KMM005 are especially close to the fault. The point sources, the near surface slip area, and its slip distribution used in this study are also shown in Figure 2.

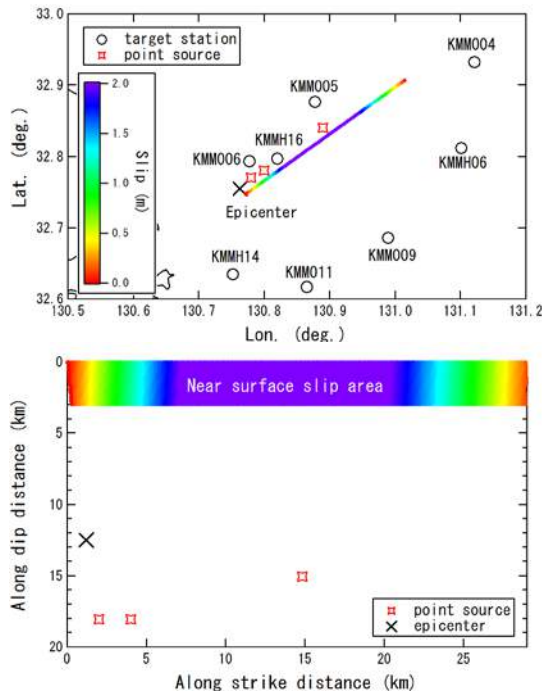


Figure 2. Target stations and the modeled fault geometry used for the simulation

Table 1. Parameters of the pseudo point source model

	Point source 1	Point source 2	Point source 3
Longitude	130.78°	130.80°	130.89°
Latitude	32.77°	32.78°	32.84°
Depth	18.0 km	18.0 km	15.0 km
Seismic Moment	4.0×10^{17} Nm	7.0×10^{17} Nm	8.0×10^{18} Nm
Corner Frequency	0.50 Hz	0.60 Hz	0.12 Hz
Relative Rupture Time	0.0 s	1.1 s	5.7 s

Parameters for the pseudo point source model are the same as in Nagasaka and Nozu (2017). The point sources were aligned on a single fault plane with a strike of 232° and dip of 84° . Density of 2400 kg/m^3 and S wave velocity of 3.55 km/s were used. Parameters for each point source are shown in Table 1. We used the empirical site amplification factors evaluated by Nozu et al. (2006) with the generalized inversion technique, using weak motions. The site amplification factors for KMM006 and KMMH16 were revised by Nagasaka and Nozu (2017). The records of the earthquake of April 16, 2016 occurred at 04:51 (JST) were used to evaluate the phase characteristics for all the target stations.

For the near surface slip area, P and S wave velocities were assumed to be 5.10 km/s and 3.00 km/s , respectively. Rise time was 3 s, and the rupture velocity was assumed to be 2.1 km/s from Nozu (2017), in which source process analysis of the Kumamoto main shock was conducted based on the method by Hartzell and Heaton (1983). In Nozu (2017), 3 s of rise time (12 time windows with an interval of 0.25 s) was assumed and 2.1 km/s of rupture velocity minimized the residual. The length of the area was

29 km and the slip distribution was determined to be consistent with the field survey by Shirahama et al. (2016). We used the average radiation coefficient and thus rake angle was not necessary. Q was assumed to be $114f^{0.63}$ from Kato (2001). Finally, the width for the near surface slip area was determined so that the Fourier spectrum error defined by the following equation was minimized.

$$\text{Fourier spectrum error} = \int_{0.2 \text{ Hz}}^{0.5 \text{ Hz}} (\log_{10} FS_{\text{obs}} - \log_{10} FS_{\text{syn}})^2 d(\log_{10} f)$$

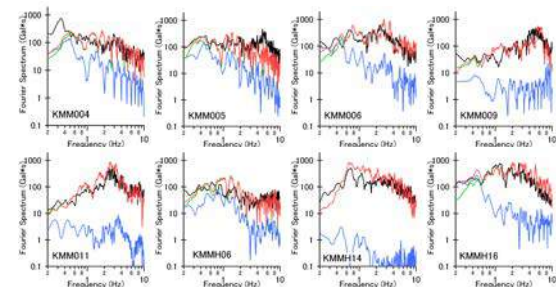
The Fourier spectrum error was calculated using only three stations closest to the fault (KMM005, KMM006, and KMMH16) where the effect of near surface slip was significant. As a result, the width was determined to be 3 km. The site amplification factors and phase characteristics were considered in the same way as for the pseudo point source model using the same weak motion records.

3.2 Results

The synthetic and observed Fourier spectra at the target stations are shown in Figure 3. In general, the synthetic Fourier spectra with only point sources (green lines) well reproduced the observed spectra, and the contribution from the near surface slip (blue lines) was not predominant. However, there are some exceptions. Among the stations close to the fault (KMM005, KMM006, and KMMH16), at KMM006 and KMMH16, the effect of the near surface slip (blue lines) well compensated for the insufficient contributions from the point source model (green lines) in the low frequency range. In contrast, the point source model remained predominant in the low frequency range at KMM005.

This result can be due to the difference in the distance from the surface rupture. KMM005 locates farther from the surface rupture than KMM006 and KMMH16. The effect of near surface slip attenuates rapidly with distance. Another possibility is that the assumed total near-surface slip in the simulation might be too small. We determined the slip distribution based on the field survey, however, the surface ruptures do not necessarily reflect the actual slip on the fault. In a future work, other approaches to determine the slip on the near surface slip area should be considered. The near surface slip area had little effects on the simulation results at the other five stations because those stations are not very close to the fault.

The synthetic and observed velocity waveforms (0.2-2 Hz) at KMM006 and KMMH16, where the effect of the near fault slip area was significant, are shown in Figure 4. Figure 4 shows that the synthetic velocities with only near surface slip area (blue lines) mainly contributed to the low frequency range and the large velocity pulses were generated by the point sources. This tendency corresponds to that seen in Figure 3.



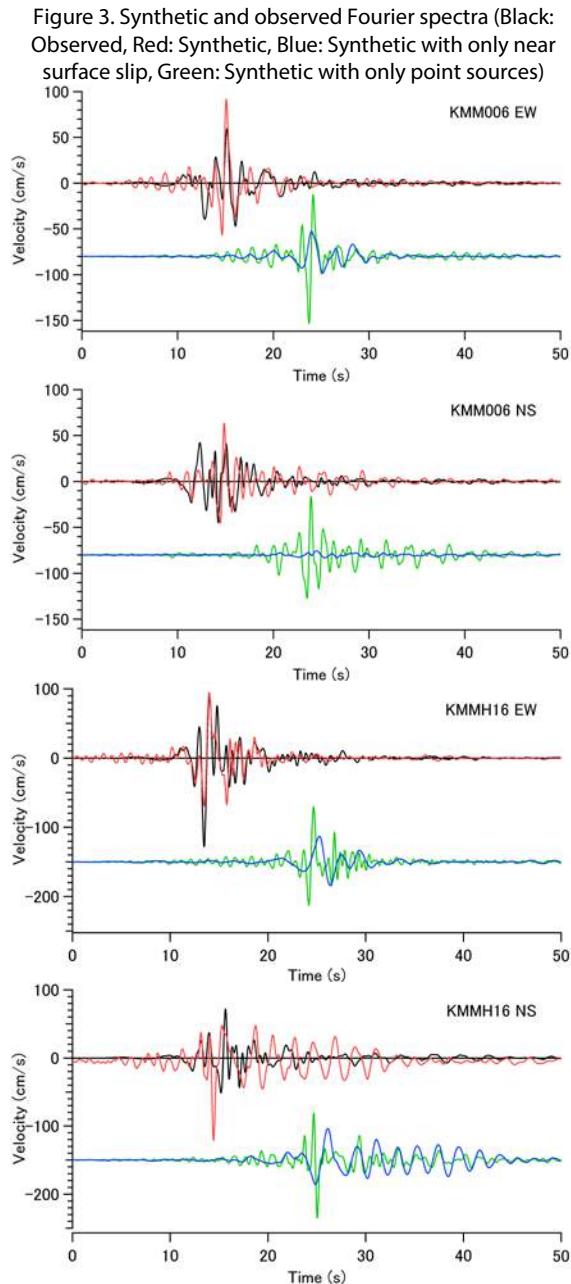


Figure 4. Synthetic and observed velocity waveforms (Black: Observed, Red: Synthetic, Blue: Synthetic with only near surface slip, Green: Synthetic with only point sources)

4. Conclusion

We conducted strong ground motion simulations for the main shock of the 2016 Kumamoto earthquakes with point sources and a near surface slip area. The point source model by Nagasaka and Nozu (2017) and a newly added near surface slip area was considered in this study. Near and intermediate-field terms were considered for the near surface slip. Near and intermediate-field terms were evaluated by a simple method in which the Green's functions consisting of far-field terms are corrected based on theoretical elastic waves. The synthetic Fourier spectra and velocity waveforms showed that the near surface slip had considerable effects in the low frequency range below

0.5 Hz at KMM006 and KMMH16, which locate very close to the fault. Strong motions from the point sources were predominant at the other stations. This result shows that slip in a shallow area should be considered in the near fault region especially when the simulation is intended to generate design ground motions for large structures such as quay walls or high rise buildings. One of the future tasks is to examine the validity of the slip distribution for the near fault slip area. Investigating the applicability of this model to other earthquakes is also important.

Acknowledgements

We used the waveform data from K-NET and KiK-net operated by the NIED.

References

1. A. Aoi, T. Kunugi and H. Fujiwara, (2004). *Strong-motion seismograph network operated by NIED: K-NET and KiK-net*, Journal of Japan Association for Earthquake Engineering, 4: 65-74.
2. K. Asano and T. Iwata, (2016). *Source rupture processes of the foreshock and mainshock in the 2016 Kumamoto earthquake sequence estimated from the kinematic waveform inversion of strong motion data*, Earth Planets Space, 68:147.
3. D.M. Boore, (1983). *Stochastic simulation of high-frequency ground motions based on seismological models of the radiated spectra*. Bulletin of the Seismological Society of America, 73, pp 1865-1894.
4. S. Hartzell and T. Heaton, (1983). *Inversion of strong ground motion and teleseismic waveform data for the fault rupture history of the 1979 Imperial Valley, California, earthquake*. Bulletin of the Seismological Society of America, 73, pp 1553-1583.
5. K. Kato, (2001). *Evaluation of source, path, and site amplification factors from the K-NET strong motion records of the 1997 Kagoshima-Ken-Hokuseibu earthquakes*, J. Struct. Constr. Eng, 543: 61-68. (in Japanese with English abstract)
6. H. Kubo, W. Suzuki, S. Aoi and H. Sekiguchi, (2016). *Source rupture processes of the 2016 Kumamoto, Japan, earthquakes estimated from strong-motion waveforms*, Earth Planets Space, 68:161.
7. Y. Nagasaka and A. Nozu, (2017). *Strong ground motion simulation of the 2016 Kumamoto earthquake of April 16 using multiple point sources*, Earth Planets Space, 69:25.
8. A. Nozu, (2006). *A simple scheme to introduce near-field and intermediate-field terms in stochastic Green's functions*, Proceedings of the 12th Japan Earthquake Engineering Symposium, pp.190-193. (in Japanese with English abstract)
9. A. Nozu A, T. Nagao and M. Yamada, (2006). *Simulation of strong ground motions based on site-specific amplification and phase characteristics*, Proceedings of the Third International Symposium on the Effects of Surface Geology on Seismic Motions, Grenoble.
10. A. Nozu and T. Sugano, (2008). *Simulation of strong ground motions based on site-specific amplification and phase characteristics-accounting for causality and multiple nonlinear effects*, Technical Note of the Port and Airport Research Institute, 1173. (in Japanese with English abstract)
11. A. Nozu, (2012). *A simplified source model to explain strong ground motions from a huge subduction earthquake -simulation of strong ground motions for the*

- 2011 off the Pacific Coast of Tohoku Earthquake with a pseudo point-source model*, Zisin2, 65: 45-67.
12. A. Nozu and Y. Nagasaka, (2017). *Rupture process of the main shock of the 2016 Kumamoto earthquake with special reference to damaging ground motions: waveform inversion with empirical Green's functions*, Earth Planets Space, 69:22.
 13. Y. Okada, K. Kasahara, S. Hori, K. Obara, S. Sekiguchi, H. Fujiwara and A. Yamamoto, (2004). *Recent progress of seismic observation networks in Japan—Hi-net, F-net, K-net and KiK-net*, Earth Planets Space, 56: xv-xxviii.
 14. Y. Shirahama, M. Yoshimi, Y. Awata, T. Maruyama, T. Azuma, Y. Miyashita, H. Mori, K. Imanishi, N. Takeda, T. Ochi, M. Otsubo, D. Asahina and A. Miyakawa, (2016). *Characteristics of the surface ruptures associated with the 2016 Kumamoto earthquake sequence, central Kyushu, Japan*, Earth Planets Space, 68:191.
 15. K. Yoshida, K. Miyakoshi, K. Somei and K. Irikura, (2017). *Source process of the 2016 Kumamoto earthquake (Mj7.3) inferred from kinematic inversion of strong motion records*, Earth Planets Space, 69:64.

EFFECTS OF MAJOR NATURAL DISASTERS IN VIETNAM, GOVERNMENTAL SOLUTIONS AND PEOPLE'S ATTITUDES DEAL WITH THE NATURAL DISASTERS ẢNH HƯỞNG CỦA MỘT SỐ LOẠI THIÊN TAI CHÍNH Ở VIỆT NAM, GIẢI PHÁP CỦA CHÍNH PHỦ VÀ QUAN ĐIỂM CỦA NGƯỜI DÂN ĐỐI VỚI THIÊN TAI

Nguyen Van Tho

ABSTRACT

Vietnam is one of the countries severely affected by natural disasters and climate change, causing great damage to people and property as well as to socio-economic development. The country is mainly affected by natural disasters such as storms, floods, droughts, salinity intrusion and landslides, all of which have frequent and severe impacts. This article discusses the effects of these natural disasters, governmental solutions and people's attitudes deal with them.

KEYWORDS: *natural disasters, climate change, Vietnam*

TÓM TẮT

Việt Nam là một trong những nước chịu ảnh hưởng nặng nề của thiên tai và biến đổi khí hậu, gây thiệt hại lớn cho người dân và tài sản cũng như phát triển kinh tế xã hội. Đất nước bị ảnh hưởng chủ yếu bởi thiên tai như: bão, lũ lụt, hạn hán, xâm nhập mặn và lở đất - có tác động thường xuyên và nghiêm trọng. Bài viết này thảo luận ảnh hưởng của những thảm họa thiên nhiên này, các giải pháp của chính phủ và quan điểm của người dân đối phó với thảm họa thiên nhiên.

TỪ KHÓA: *thiên tai, biến đổi khí hậu, Việt Nam*

DR. NGUYEN VAN THO

Department of Environment, Faculty of Urban Infrastructure Engineering, Mien Tay Construction University, 20B, Pho Co Dieu Street, Ward 3, Vinh Long City, Vinh Long Province.

Email: nguyenvantho@mtu.edu.vn

Tel: 01262.214279

Introduction

Viet Nam is located in Southeast Asia, and has 63 cities and provinces. Vietnam's population reached about 95 million in 2017 (WB, 2018). Vietnam's mainland stretches from 23°23' to 08°02' north latitude and widens from 102°08' to 109°28' east longitude. Vietnam's total land area is approximately 329,314 square kilometres and its coast line is approximately 3,200 kilometres (UN, 2018). Viet Nam is extremely vulnerable to climate change impacts given its extensive coastline and river deltas (ADB, 2015). Approximately 28% of Viet Nam's total land area is suitable for agriculture, although there are significant variations by region, with the highest production capacity in lowland areas. The agriculture sector is dominated by rice production, which comprises approximately 75% of total national crop production value (ADB, 2015). The two large deltas which contribute importantly to the national food production of Vietnam are The Red Delta in the north and Mekong Delta in the south. The Mekong Delta, with more than 16 million people representing 22% of the national population, is extremely important for national agriculture,

producing half of the national food requirements and 60% of the exported aquaculture goods (Käkönen, 2008). Vietnam is one of the countries most affected by natural disasters and climate change, especially storms, floods, droughts and saline intrusion. Annually, natural disasters kill over 300 people, with economic losses ranging from 1-1.5% of GDP, equivalent to nearly 1.3 billion USD (Xuan Tuyen, 2017). The country is preparing for more severe and adverse impacts associated with global warming and climate change, especially rising sea levels and increasingly frequent natural disasters. In this context, 70 percent of Viet Nam's population lives in rural areas and about 60 percent of the agriculture labor forces are considered most vulnerable (FAO, 2011). A 2017 World Bank report listed Vietnam among the five countries likely to be most affected by climate change, in large part due to its location and the economy's dependence on sectors such as agriculture (WB, 2017). This article presents typical natural disasters, their effects on the country, governmental solutions and people's attitudes deal with them.

Storms

Typhoons appear to pose the biggest threat to coastal communities in Vietnam. In particular, the northern coast is hit by typhoons more frequently than any other part of the country and the possibility of a large typhoon taking place in southern Vietnam is considerably smaller than in the northern and central parts of the country (Takagi et al., 2014). Large scale typhoons that originate in the Pacific, often strike the Vietnamese coast, causing storm surges and flooding that affects hundreds thousand of people (Thieffry, 2018). Annually, there are on average about 12 tropical storms on the East Sea, of which about 45 % form in the East Sea and 55 % stem from the Pacific Ocean. About seven storms affect Vietnam annually, five of which hit or directly affect the country's mainland (Schmidt-Thomé et al., 2015).

The current rainy season tends to end later than before and many typhoons show signs of moving southwards in recent years (IMHEN and UNDP, 2015). Normally, in the East Sea, there are only about 10 to 11 storms operating each year (Nhan Dan, 2017). In 1964, the meteorological industry recorded 16 storms and tropical depressions operating in the East Sea. But at that time, records did not distinguish between storm and tropical depression, and referred to all as storms. In 2017, a record number of 16 storms and 6 tropical depressions were recorded (Nhan Dan, 2017).

One of the most devastating storms in Vietnam was typhoon Linda (a very violent tropical storm). It occurred in November 1997. It landed mainly in Ca Mau and Kien Giang provinces - two provinces in the Mekong Delta, causing severe damage to people and property with over 3,000 dead or missing, and over 3,600 fishing boats sunk or damaged (OCCA, 2018). Linda was considered to be the

worst storm to hit Vietnam the last century, and its consequences were compounded by the storm landing at high tide in a place where there was little experience with typhoons and few means to communicate to fishermen at sea (McElwee et al., 2010). Despite fewer human losses compared to typhoon Linda in 1997, another typhoon, Ketsana, which hit the central region of Vietnam in 2009, caused severe flooding and extensive property damage, with nearly 20,000 homes collapsed or swept away completely. Over 165,000 houses sustained damaged roofs, about 120,000 houses were submerged, and 50,000 ha of rice and crops were lost. Nearly 13,000 clinics communal people's committees, schools and public buildings were damaged. Important transit routes were cut off in many places and the electrical grid system was also badly damaged in many areas (OCCA, 2017).

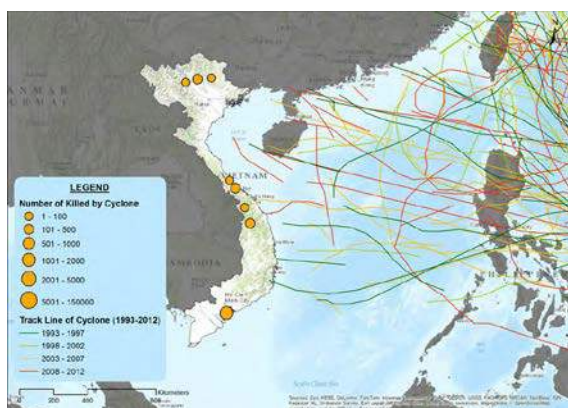


Figure 1: Locations of cyclones in Vietnam and human loss (AHA Center and JICA, 2015)

Another devastating typhoon which swept through the Central and South-East region of Vietnam on 4th November 2017 was Typhoon Damrey. With wind speeds of up to 135 kilometres per hour, it caused massive damage to people, agriculture, aquaculture, infrastructure and housing. More than 4.33 million of people were affected with over 100 people killed. More than 130,000 houses were destroyed and several thousand hectares of agricultural land was damaged. The typhoon also caused widespread damage to roads, water and electricity infrastructure (Thieffry, 2018). In summary, it has been estimated that up to 80-90% of Vietnam's population is affected by typhoons (AHA Center and JICA, 2015). Locations of cyclones are showed in the Figure 1.

Floods

The high flood risk in Vietnam is due to its tropical monsoon climate and dense river systems (Chau et al., 2014). Depending on the climate (monsoon) regime and the geographic zones, floods in Vietnam occur at different times of the year. For the northern part of Vietnam, the flood season is mainly from April to October. In the central coastal part and the highlands, floods predominantly occur between July and November. In the southern part of Vietnam, flood season occurs in the period between July and the end of November (Chinh et al., 2016).

The country experiences both riverine and coastal flooding, due to its topography and socio-economic concentration. Vietnam's coastline is 3,200 kilometres long and 70 percent of its population lives in coastal areas and low-lying deltas (Bangalore et al., 2015). In the Mekong

Delta, most of the deltaic plain is less than 5m above sea level, so during the rainy season a large area of the delta is inundated (Fujihara et al., 2016). The major causes of floods in the Mekong Delta are heavy rainfall in upstream catchments, flood discharges from upstream hydroelectric dams, deforestation, improper planning of irrigation canal and dykes, and urban development etc., (IMHEN and UNDP, 2015).

Vietnam has been extensively impacted by flooding over the years, sustaining heavy losses in human life and damage to housing, agriculture, and transportation. Floods have had severe impacts on communities in Vietnam with at least 14,927 deaths and economic damage equivalent to 1% of GDP between 1989 and 2015 (Luu et al., 2018). The following are the damages caused by the effects of typical floods that have occurred in different regions of Vietnam in recent years.

In the Mekong Delta, the flood in 2000 was a historic flood, equivalent to the floods in 1961 and 1978. This flood affected 5 million people, with 448 deaths, estimated damage of about 285 million USD. Another severe flood occurred in 2001, killing 539 people, injuring 219 people, with millions affected. It caused damage estimated at about 300 million USD (IMHEN and UNDP, 2015).

In the Central region of Vietnam, the flood which occurred in 1999 was in the most catastrophic ever recorded for this area, causing 718 deaths. Damage was estimated at about 300 million USD, causing severe long-term social and economic consequences in the central provinces (IMHEN and UNDP, 2015)

The flood that occurred on 6-7 October 2009 in the North of Vietnam was considered the largest in recent decades, causing loss of life (51 dead and 14 missing) and property (60,000 houses were submerged in water, 6,000 houses were collapsed, 25,000 hectares of rice and 95,000 hectares of crops were damaged) (OCCA, 2017).

Droughts and salinity intrusion

Vietnam is one of the most drought-prone countries in the East Asia and Pacific region, with both drought and saltwater intrusion occurring often in recent years. Drought and associated saltwater intrusion of 2015–2016 severely affected 18 provinces in Vietnam as shown in the Figure 2, resulting in direct economic losses of VND 15,032 billion (about 674 million USD), representing 0.35 percent of national GDP and resulting in negative agricultural growth for the first time in decades (WB, 2017).



Figure 2: Provinces affected by drought and saltwater intrusion (World Bank, 2017)

There are two seasons, dry season (November–April) and rainy season (May– October). Drought, including monthly and seasonal drought, seems to have varying patterns among different climate regions. Hot and sunny weather has shown signs of increasing dramatically in various regions in the country, particularly in the North Central and in southern regions (Schmidt-Thomé et al., 2015).

In the Mekong Delta, most of the deltaic plain is less than 5m above sea level, so the coastal area is affected by saltwater intrusion during the dry season (Fujihara et al., 2016). The rainy season in 2015 was late but it ended early, and the total rainfall was low compared to the average for many years. Meanwhile, in the early months of 2016, the water flow from Mekong River declined and the most severe saline intrusion ever recorded occurred in the Mekong Delta (on the Vam Co River, saline intrusion extended upstream for up to 93 km, and in other estuaries for up to 50 to 70 km), (MARD, 2016a). Due to the impact of saline intrusion, many economic sectors and people's lives in 10 of 13 provinces and cities in the region (Long An, Tien Giang, Ben Tre, Tra Vinh, Soc Trang, Bac Lieu, Kien Giang, Ca Mau, Hau Giang and Vinh Long) were severely affected (Figure 3)

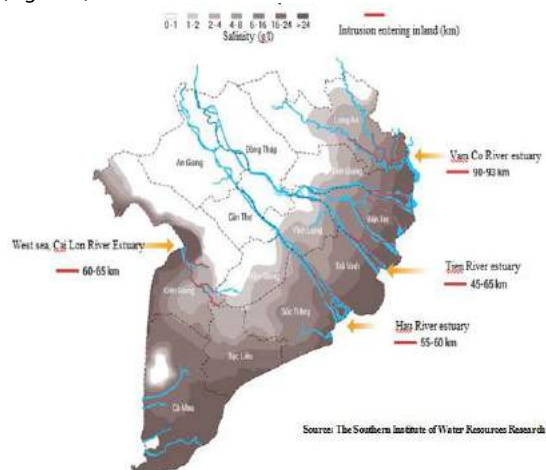


Figure 3: Saltwater intrusion in the Mekong Delta until March 2016 (MARD, 2016)

Saline intrusion has also affected the availability of freshwater for domestic consumption and agricultural use, especially in many parts of Ca Mau, Kien Giang, Ben Tre, Tra Vinh, and Soc Trang which rely on groundwater for these purposes. There are about 208,394 households (about 800,000 people) with water shortage and many schools, clinics, hotels, factories affected by droughts and saline intrusion (MARD, 2016b).

Landslides

Landslides are common in northern and central areas, especially in Lao Cai and Bac Kan provinces. A landslide in Lao Cai province in 2004 killed 22 people and injured 16. Another landslide in Pac Nam commune, Bac Kan province in 2009 resulted in 13 people dead or missing and 5 injured (CCDPC, 2014).

Landslides also occur in the Mekong Delta, where serious riverbank and coastal erosion occurs in 13 provinces and cities in the Mekong Delta, the most serious

being in Vinh Long, An Giang, Dong Thap, Ca Mau, Bac Lieu. On average riverbank and coastal erosion are responsible for the loss of about 500 ha annually and directly threaten the lives and property of people. The whole area has 562 landslide areas with a total length of 786 km, of which 42 areas with a total length of 148 km are particularly dangerous, and require careful management to ensure the safety of the lives and property of the people and the State (MONRE, 2018). One of the reasons for the accelerating rate of riverbank erosion in some areas is sand mining (Takagi et al., 2014), carried out to meet the growing demand for construction materials.

Effects of the natural disasters

In recent years, Vietnam has suffered from many types of natural disasters, with high intensity, wide scope and more severe consequences, causing serious damage to people and property. As examples, human and economic losses from natural disasters for the period 2011–2017 are shown in Figure 4. In 2017 alone, natural disasters left 386 dead or missing and 664 injured. Total damage in the same year was estimated at more than 2.6 billion USD (equivalent to more than 60 trillion VND).

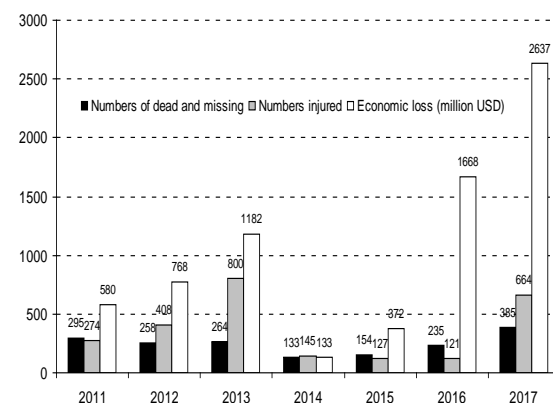


Figure 4: Numbers of dead, missing and injured and economic loss from 2011 to 2017 by the natural disasters (Nhan Dan, 2017)

Over the past two decades, natural disasters in Vietnam have caused more than 13,000 deaths as well as property damage in excess of 6.4 billion USD (WB, 2017). According to Hoai (2017), in 2017 alone natural disasters caused more than 8,666 houses to collapse or be washed away. Over 588,139 houses were flooded and damaged, while 363,502 ha of rice and crops, 169,640 hectares of industrial crops and fruit trees, and 143,438 hectares of forest were destroyed or damaged. The natural disasters also caused the death of 69,757 livestock and 2 million poultry, 41,375 fish cages and 60,392 ha of aquaculture area were damaged, and 3,682 boats were sunk or destroyed at their moorings. In addition, the natural disasters caused landslides along about 1,145 km of dykes, embankments, ditches, river banks and 1,586 km of roads (Hoai, 2017).

Governmental solutions and people's attitudes deal with the natural disasters.

Natural disasters are becoming increasingly complex and unpredictable, in terms of both intensity and frequency of occurrence. In 2013, the National Assembly

passed the Law on Natural Disaster Prevention and Control as a basis for Ministries and localities to implement effective measures for natural disaster prevention and control. The Government always attaches great importance to the prevention, mitigation and overcoming of consequences caused by natural disasters. Considering prevention is the responsibility of the State, organizations and individuals, in whom the State plays the leading role, organizations and individuals take action actively and community help each other. The Government has issued decisions, programs and established agencies to advise the Government on the control and mitigation of consequences after natural disasters. On July 4, 2014, the Government issued Decree No. 66/2014 / ND-CP detailing and guiding the implementation of a number of articles of the Law on Natural Disaster Prevention and Control. Two years later on 17th March, 2015, the Prime Minister signed the Decision No. 367/QĐ-TTg establishing the Central Steering Committee for Natural Disaster Prevention and Control which coordinates the inter-sectoral assistance to the Government and the Prime Minister in organizing, directing and managing the prevention, response and overcoming of the consequences of natural disasters in the whole country. On 3rd July, 2017, the Prime Minister decided to establish the General Department of Disaster Prevention under the Ministry of Agriculture and Rural Development to advise the Ministry of Agriculture and Rural Development, the Steering Committee Disaster preparedness for disaster prevention more effectively. The Government and the Central Steering Committee for Natural Disaster Prevention and Control always promptly take part in organizing and directing the response before and after the storm, promptly inform people about the level of danger of storms and support the overcoming of consequences. In addition, National Centre for Hydro-Meteorological Forecasting (NCHMF), a governmental organization belonging to Vietnam Meteorological Hydrological Administration, was established under Decision 696/QĐ-BTNMT on March 8, 2018 of the Ministry of Natural Resources and Environment with authority to issue forecasting/warning information for weather, climate, hydrology, water resource, marine weather (i.e. hydro-meteorology) for all provinces, and areas in Vietnam (Figure 5).



Figure 5: Weather forecast map for all areas in Vietnam.
(NCHMF, 2018)

People can also access to the website of NCHMF to know warnings of natural disasters for example, typhoons or tropical depressions which are forecasted in advance for

10 days to have good solutions to deal with (NCHMF, 2018).

The Government also coordinates with advanced countries on natural disaster prevention and international organizations such as UN organizations in Viet Nam, development partners, donors such as World Bank, Asian Development Bank in training skills to deal with disasters for the community, and jointly with other localities to continuously bring information and skills to the community in disaster prevention. To monitor and control the landslides, to raise the capacity to cope with and to take initiative in preventing and restricting the damage and stabilizing people's livelihoods along the rivers and coastal areas in the Mekong Delta, the Ministry of Agriculture and Rural Development has reviewed, evaluated and classified river bank erosion, coastal erosion in the Mekong Delta, made the map of landslides. So, people can access the website: <http://satlodbscl.phongchongthientai.vn> to know how many serious landslides, the location of landslides and the characteristics and scales of these erosion sites.

Over the years, people always take care of natural disaster prevention to minimize damages to people and property. However, the awareness of people in coastal areas of Vietnam on natural disasters is high but not comprehensive. In addition, the level of preparedness of the people is still low. People do not pay proper attention to the dangers that directly threaten their lives (Nguyen Danh Thao and Le Tuan Anh, 2015). In the case of dangerous natural disasters such as typhoons, the authorities evacuate people in the affected area to safe places, but some households in the affected area do not follow evacuation orders from the authorities.

Conclusions

Vietnam is severely affected by many natural disasters, including storms, floods, droughts, saline intrusion and landslides, which have frequent and severe impacts on people and property, as well as serious damage to the economy of the country. The Government has issued many decrees, documents as well as the establishment of functional agencies to help the government to prevent and mitigate the consequences of natural disasters and to help the people affected by the disasters. In addition, the Government has also coordinated with advanced countries and international organizations on natural disaster prevention. People are increasingly aware of the prevention of natural disasters, but the awareness of natural disasters of many people who live in coastal areas of Vietnam is not comprehensive

Acknowledgements

I gratefully acknowledge Dr. Barry Clough for very constructive comments and for reading the English manuscript.

References

- ADB (Asian Development Bank), (2015). Viet Nam: Environment and climate change assessment. Asian Development Bank, Mandaluyong City, Philippines. ISBN 978-92-9254-132-3
- AHA Center and JICA, (2015). Country Report Vietnam. Natural disaster risk assessment and area business continuity plan formulation for industrial agglomerated areas in the ASEAN Region. The ASEAN Coordinating

- Centre for Humanitarian Assistance on disaster management (AHA Center) and The Japan International Cooperation Agency (JICA)
- Bangalore M., Smith A., Veldkamp T., (2015). Exposure to Floods, Climate Change, and Poverty in Vietnam. Policy Research Working Papers. World Bank
- CCDPC (National Steering Center for Natural Disaster Prevention and Control), (2014). Báo cáo tổng quan tình hình thiệt hại do lũ, lũ quét, sạt lở đất và công tác chỉ đạo phòng tránh, tháng 08/2014
- Chau V. N., Holland J and Cassells S., (2014). Institutional structures underpinning flood management in Vietnam, International Journal of Disaster Risk Reduction 10, 341–348
- Chinh D. T., Bubeck P., Dung N. V., and Kreibich H, (2016). The 2011 flood event in the Mekong Delta: preparedness, response, damage and recovery of private households and small businesses. Disasters 40 (4): 753–778
- FAO (The Food and Agriculture Organization of the United Nations), (2011). Viet Nam and FAO Achievements and success stories. <http://www.fao.org/docrep/015/an165e/an165e00.pdf>, accessed 15/5/2018
- Fujihara Y., Hoshikawa K., Fujii H., Kotera A., Nagano T and Yokoyama S, (2016). Analysis and attribution of trends in water levels in the Vietnamese Mekong Delta. Hydrol. Process. 30, 835–845
- Hoai T. Q., (2017). Looking back on disaster prevention in 2017. Ministry of Agriculture and Rural Development (MARD), the article was in Vietnamese language. <https://www.mard.gov.vn>, accessed 2/06/2018
- IMHEN and UNDP, (2015). Summary report serves policy makers. In the Special Report of Vietnam on Disaster Risk Management and Extreme Events to Promote Adaptation to Climate Change (the Report in Vietnamese language). Viet Nam Publishing House of Natural Resources, Environment and Cartography, pp. 2–27.
- Käkönen M., (2008). Mekong Delta at the crossroads: more control or adaptation? Ambio 37(3): 205–212.
- Luu C., Meding J. V., Kanjanabootra S., (2018). Flood risk management activities in Vietnam: A study of local practice in Quang Nam province. International Journal of Disaster Risk Reduction 28, 776–787
- MARD (Ministry of Agriculture and Rural Development), (2016a). Hạn, mặn tiến công đồng bằng sông Cửu Long. <http://mtnn.mard.gov.vn/5/chi-tiet-tin-tuc-229/han-man-tien-cong-dong-bang-song-cuu-long>, accessed 04/06/2018
- MARD (Ministry of Agriculture and Rural Development), (2016b). Tình hình hạn hán, xâm nhập mặn ở đồng bằng sông Cửu Long, Nam Trung Bộ và Tây Nguyên năm 2016, nguyên nhân và các giải pháp ứng phó. MARD (Ministry of Agriculture and Rural Development).
- McElwee P., Hue L. T. V., Huong V. T. D, Be N. V., Tri L. Q., Trung N. H., Tuan L. A., Dung L. C., Duat L. Q., Phuong D. T., Dung N. T., Adutt G., (2010). The Social Dimensions of Adaptation to Climate Change in Vietnam. The World Bank, Washington, D. C, USA
- MONRE (Ministry of Natural Resources and Environment), (2018). 2,500 billion VND to overcome landslide in the Mekong Delta. <http://www.monre.gov.vn>, accessed 12/05/2018
- NCHMF (National Centre for Hydro-Meteorological Forecasting), (2018). Weather forecast map, <http://www.nchmf.gov.vn/web/en-US/43/Default.aspx>, accessed 20/07/2018
- Nguyen Danh Thao and Le Tuan Anh, (2015). An assessment of awareness and preparedness of people against coastal disaster in Viet Nam. Journal of Water Resources and Environmental Engineering 49 (6/2015), p 22–28
- Nhan Dan, (2017). 2017 - The Year of Big Disaster (the article in Vietnamese language). Nhan Dan Online. <http://www.nhandan.com.vn>, accessed 10/05/2018
- OCCA (The Steering Committee for Climate Change Mitigation and Adaptation), (2017). Assessment of the economic loss and life of the fishermen community due to the impact of climate change and natural disasters (the article in Vietnamese language). <http://occa.mard.gov.vn>, accessed 06/05/2018
- OCCA (The Steering Committee for Climate Change Mitigation and Adaptation), (2018). Assessment of impacts of climate change and natural disasters on fishery production (the article in Vietnamese language). <http://occa.mard.gov.vn>, accessed 06/06/2018
- Schmidt-Thomé P., Nguyen H., Pham L., Jarva J., Nuottimäki K., (2015). Climate change adaptation measures in Vietnam: Development and Implementation. Springer. 100 p, ISBN 978-3-319-12346-2
- Takagi H., Esteban M and Thao N. D., (2014). Coastal Disasters and Climate Change in Vietnam: Engineering and Planning Perspectives. Elsevier. Pages 424. ISBN: 9780128004791
- Thieffry M. F, (2018). Climate Change Resilience in Viet Nam: Viet Nam's typhoon season and changing vulnerability. UNEP (United Nations Development Programme). <http://www.vn.undp.org>, accessed 05/06/2018
- UN (United Nations), (2018). Viet Nam at a Glance. <http://www.un.org.vn>, accessed 7/06/2018
- WB (World Bank), (2017). Toward Integrated Disaster Risk Management in Vietnam: Recommendations Based on the Drought and Saltwater Intrusion Crisis and the Case for Investing in Longer-Term Resilience. World Bank, Washington D. C, USA
- WB (World Bank), (2018). Vietnam country profile. World Bank. <https://data.worldbank.org>, accessed 10/07/2018
- Xuan Tuyen, (2017). Online Newspaper of the Government of the Socialist Republic of Viet Nam. <http://baochinhphu.vn/Hoat-dong-cua-lanh-dao-Dang-Nha-nuoc/Hoan-thien-Chien-luoc-quoc-gia-phong-chong-giam-nhe-thien-tai-lay-phong-ngua-la-chinh/320724.vgp>, accessed 05/06/2018

VERIFICATION OF DYNAMIC RESPONSE OF A LONG-PERIOD BRIDGE SUBJECTED TO AN EXTREME GROUND EXCITATION

Gaku Shoji, Ryota Harigaya, Sumika Miura

ABSTRACT

In this study, for the Tsurumi Tsubasa cable-stayed bridge in Tokyo Metropolitan Expressways, that is classified in long-period infrastructure with first natural period of more than about 2.0s, the dynamic characteristics were discussed based on analysis of the seismic records by the aftershock of the 2011 off the Pacific coast of Tohoku earthquake.

The dynamic characteristics of natural frequencies and vibration modes were estimated by spectral analysis of the recorded acceleration, and modal parameters of the bridge were also identified by using multi-degree-of-freedom-system model consisting of super-structures, piers, and foundations. Finally, the natural frequencies and damping coefficients of the bridge were verified by analyzing the transfer functions of main-girder and main tower records with respect to the foundation record, compared with the theoretical transfer functions.

KEYWORDS: *long-period bridge, seismic record, dynamic characteristic, the 2011 off the Pacific coast of Tohoku earthquake*

DR. GAKU SHOJI

Associate Professor, Department of Engineering Mechanics and Energy (EME), Faculty of Engineering Information and Systems, University of Tsukuba
Email: gshoji@kz.tsukuba.ac.jp, **corresponding author**
Tel: +81-298-853-6190

MR. RYOTA HARIGAYA and MS. SUMIKA MIURA

Former Undergraduate Student, College of Engineering Systems, University of Tsukuba

1. Introduction

Observation records by the aftershock of the 2011 off the Pacific coast of Tohoku Earthquake were provided in the Tsurumi Tsubasa cable-stayed bridge in Tokyo Metropolitan Expressways at 2:56:18 on March 13, 2011. The Tsurumi Tsubasa Bridge is grouped in long-period infrastructure with first natural period of more than about 2.0s, which might be suffered by amplified dynamic response of a long-period bridge subjected to a long-period component of seismic ground motion. Hence, verification of dynamic response of a long-period bridge by use of associated observation records is substantially important in view of the rarity of observation records in an extreme ground excitation.

From the reason above, in this study, the dynamic characteristics of the Tsurumi Tsubasa Bridge are verified based on analysis for the dynamic responses by use of the observed records while estimating vibration modes of the bridge and comparing them with the results provided in previous research (H.Yamaguchi et al., 1996; Y. Yamamoto, Y. Fujino and M. Yabe; 2009).

2. Subject bridge and observation records

The Tsurumi Tsubasa Bridge shown in Figure 1 is a three-span cable-stayed bridge with a continuous steel box main-girder, which crossing Tsurumi Channel of Quay Daikoku and Ohgishima in Bayshore line of Tokyo Metropolitan Expressways (Metropolitan Expressway Public Corporation, 1994). Two reverse Y-shaped steel main towers stay a reversely trapezoidal flat steel box-girder.

A tower base, that is P2 and P3, downward two thirds from the position of a steel cross beam section at the upper portion of P2 and P3 shows an octagonal two-emptiness cross section of steel reinforced concrete (SRC), as well as an edge pier of P1 and P4 of reinforced concrete (RC).

At the top of P2 and P3, vertical bearings and horizontal ones, and two elastic restraint cables and a vane-type oil damper are installed. At the top of P1 and P4, rocking bearings and horizontal ones are also installed. The vertical bearings are set free of the motion both in the longitudinal (LG) direction and in the transverse (TR) direction. The horizontal bearings are set free in the LG direction and in contrast fixed in the TR direction. The rocking bearings resist the associated vertical (UD) loads and are moveable in the LG direction. The elastic restraint cables are adopted in the support of the LG direction to tie a main tower and a main-girder, and the vane-type oil dampers are installed in the main tower base for damping improvement of the bridge total system. The class of soil at the cross-linked point of the bridge is classified into Type II (medium stiff soil) at P1 and Type III (soft soil) at P2, P3, and P4, which are specified in Design Specifications for Highway Bridges by Japan Road Association (JRA).

Associated 27 seismometers are installed in the bridge, observing acceleration of 50 components in total and displacement as illustrated in Figure 1. The sampling frequency of each waveform is 100Hz and the measurement duration is 174.50s.

Based on time-series and frequency-domain analysis for observed data, it was found that the acceleration record observed with the Tsurumi Tsubasa Bridge basically contained a rich long-period component of more than 1.5s accompanying a shorter period component of less than 1.0s. It was also found that the P3 main tower top showed largest acceleration response of 0.28m/s^2 whereas the intermediate part of the P2 main tower showed largest as be 0.38m/s^2 . It is considered that the P3 main tower excited dominantly by the typical first mode, whereas in contrast the P2 main tower by the second vibration mode.

3. Characteristics of dynamic properties

Figure 2 shows the frequency of a normal vibration mode of the Tsurumi Tsubasa Bridge estimated by Fourier spectrum analysis for the LG/TR/UD component of the observation records in the main-girder between P3 and P4. Compared with the results by pioneering research (H.Yamaguchi et al., 1996; Y. Yamamoto, Y. Fujino and M. Yabe; 2009), the peak at 0.330Hz in the Fourier spectrum of the LG direction is estimated to be the main-girder swinging pole mode, and the peak at 0.317Hz in the Fourier

spectrum of the TR direction is more likely to be the first

symmetry horizontal bending mode of the main-girder.

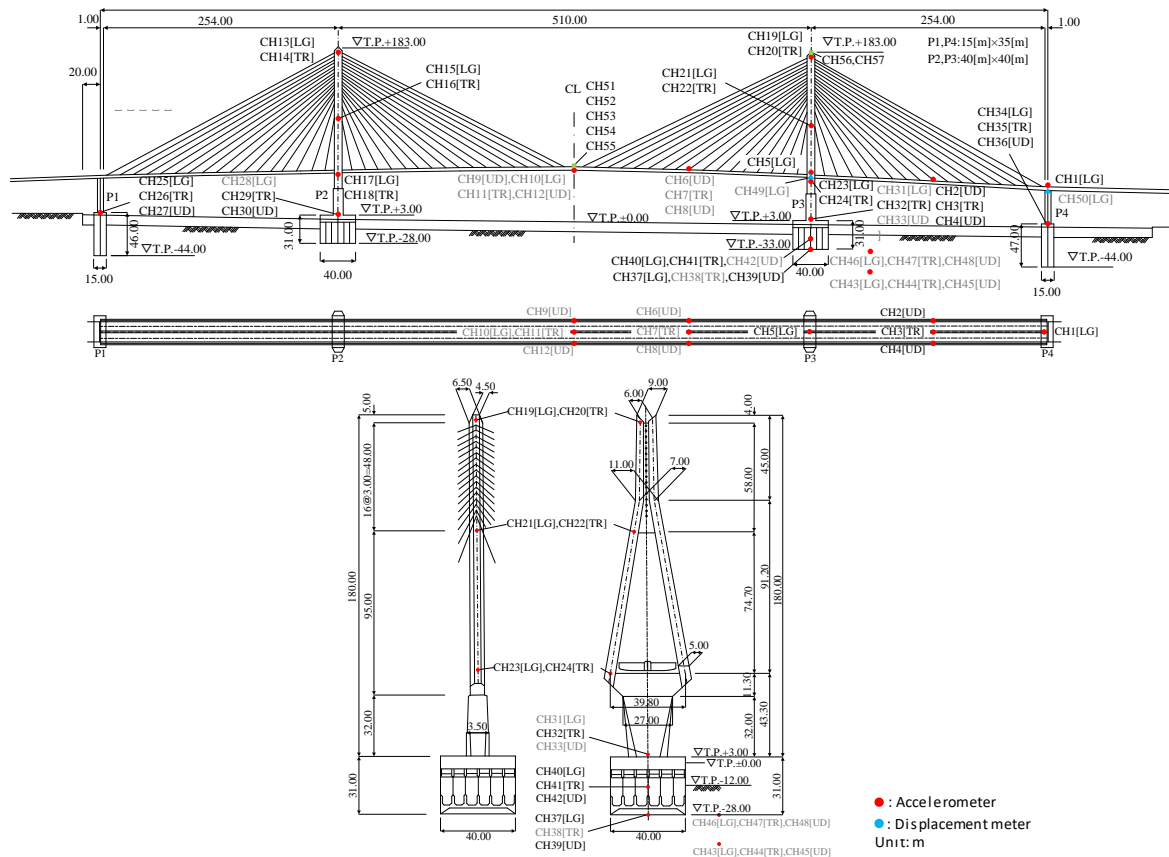


Figure 1: Tsurumi Tsubasa cable-stayed bridge

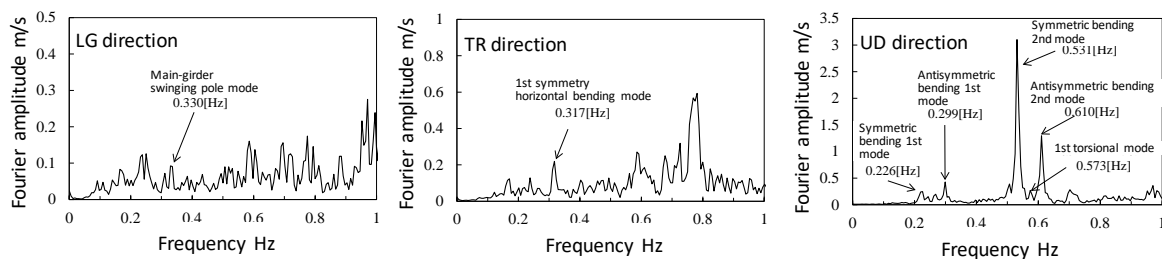


Figure 2: Fourier spectra for the LG/TR/UD component of the observation records in the main-girder between P3 and P4

In addition, the main-girder vertical (UD) vibration mode could be confirmed as the symmetric bending primary mode of 0.226Hz and second of 0.531Hz, the antisymmetric bending primary mode of 0.299Hz and second of 0.610Hz, and the primary torsional mode of 0.573Hz. From these, in particular the main-girder vertical dynamic characteristics could be accurately identified from the observed data on unstationary seismic response of the bridge compared with the horizontal and transverse ones. This is caused by the lower rigidity in the plane of the main-girder characterizing the dynamic property of the bridge total system.

4. Estimation of vibration modes

Figure 3 shows amplitude and phase characteristics of transfer functions computed by use of the observed data in the LG direction, setting the waveform at the gravity center position in the P3 foundation (CH40) as be input data and

those at the top (CH19), the intermediate (CH21), and the bottom (CH23) in the P3 main tower, at the main-girder on P1 (CH1) and P3 (CH5) as output data. From these transfer functions, the vibrational mode shapes for the P3 main tower and P3-P4 main-girder of the Tsurumi Tsubasa Bridge in the LG direction are estimated as shown in Figure 4 demonstrating the maximum amplitude to be normalized as 1.0 with respect to the others.

In similar way, the transfer functions about the TR direction of the bridge were calculated by setting the waveform on the top in the P3 foundation (CH32) as input and those at the top (CH20), the intermediate (CH22), and the bottom (CH24) in the P3 main tower, and at the main-girder between P3 and P4 (CH3) as output in particular to draw the transverse vibration mode shapes of the P3 main tower as shown in Figure 4. It is noted that the transfer functions were calculated based on the time series

waveform data with the duration of 302.08s, and smoothing

was carried out by Parzen window of band width of 0.01Hz.

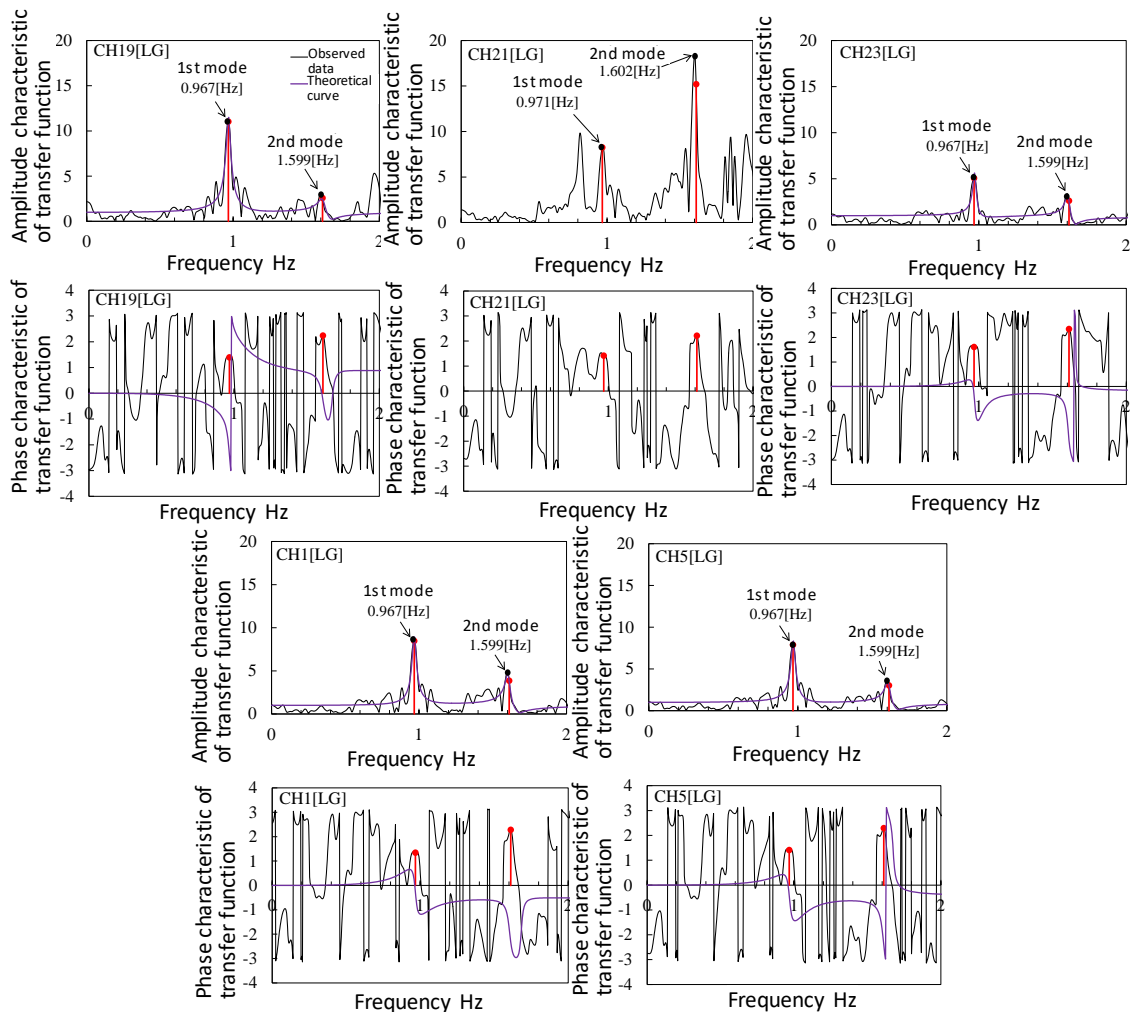


Figure 3: Amplitude and phase characteristics of transfer functions computed by use of the observed data in the LG direction of the bridge

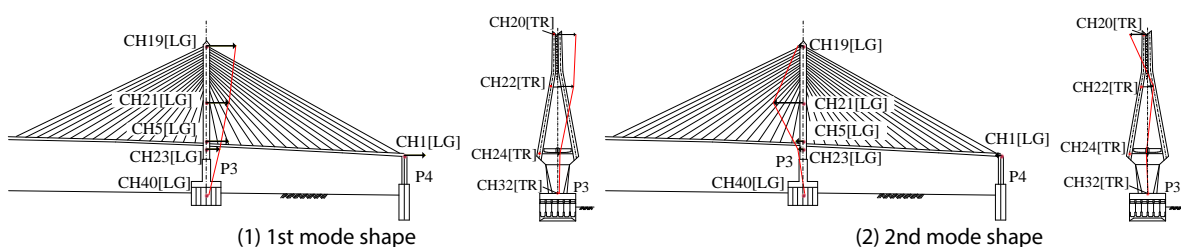


Figure 4: Estimated vibrational mode shapes for the P3 main tower and P3-P4 main-girder in the LG direction of the bridge

From these figures the primary mode in the LG direction of the P3 main tower was estimated to be 0.969~0.971Hz, and the second mode to be 1.606~1.616Hz. In addition, the primary mode in the TR direction of the P3 main tower was also estimated to be 0.891-0.980Hz, and the second mode to be 1.640-1.643Hz.

In terms of the Yokohama Bay Bridge which is a cable-stayed bridge like the Tsurumi Tsubasa Bridge, the previous study has revealed the first antisymmetric mode and the first symmetric one in the plane of the main tower to be 0.403Hz and 0.418Hz respectively based on the observation records in the 1990 Izu-Oshima Kinkai earthquake.

Although the height of the main tower in the Yokohama Bay Bridge is T.P.175.0m and is 8.0m lower than that in the Tsurumi Tsubasa Bridge of T.P.183.0m, it is thought that the rigidity in the plane of the main tower in the Yokohama Bay Bridge is lower than that in the Tsurumi Tsubasa Bridge since the hanging cables in the Yokohama Bay Bridge are adopted nearly in parallel from the main tower to connect the main-girder. Hence, it is considered to be valid that the primary mode of the P3 main tower in the Tsurumi Tsubasa Bridge shows the higher natural frequencies compared with those in the Yokohama Bay Bridge.

5. Conclusions

In this study, the dynamic characteristics of the Tsurumi Tsubasa cable-stayed bridge as be one of typical long-period bridges were verified based on analysis for the dynamic responses by use of the observation records by the aftershock of the 2011 off the Pacific coast of Tohoku earthquake, while estimating vibration modes of the bridge and comparing them with the results provided in previous research (H.Yamaguchi et al., 1996; Y. Yamamoto, Y. Fujino and M. Yabe; 2009). The Fourier spectrum analysis and the computation of transfer functions for the LG/TR/UD component of the observed time-series acceleration waveforms in the P3 main tower, the P3-P4 main-girder and the P3 foundation can be resulted as follows:

1. The acceleration waveforms recorded at the Tsurumi Tsubasa Bridge contained a rich long-period component of more than 1.5s accompanying a shorter period component of less than 1.0s.
2. As for the main-girder dynamic characteristics, the LG dynamic motion contained the main-girder swinging pole mode of 0.330Hz and the TR dominant mode was the first symmetry horizontal bending mode of 0.317Hz. The vertical UD vibration mode was estimated as the symmetric bending primary mode of 0.226Hz and second of 0.531Hz, the antisymmetric bending primary mode of 0.299Hz and second of 0.610Hz, and the primary torsional mode of 0.573Hz.
3. The primary mode and the second one of the LG direction of the P3 main tower were estimated to be 0.969~0.971Hz and 1.606~1.616Hz, respectively. In addition, the primary mode of the TR direction was also estimated to be 0.891-0.980Hz, and the second mode to be 1.640-1.643Hz.
4. These identified natural frequencies are thought to be sufficiently valid compared with the results by previous research above.

Acknowledgements

We would like to say special thanks to the associated division of Metropolitan Expressway Company Ltd. for their offering valuable observed data recorded in the Tsurumi Tsubasa Bridge. We also appreciate Mr. Mizoguchi at Metropolitan Expressway Company Ltd. and Dr. M. Yabe at Chodai Co., Ltd. for their giving sincerely technical advices to our research.

References

1. Metropolitan Expressway Public Corporation., (1994). Construction Historical Document on Tsurumi Tsubasa Bridge.
2. H. Yamaguchi, H. Takano, M. Ogasawara, T. Shimosato, M. Kato and J. Okada., (1996). *Identification of dynamic characteristics by field vibration test in Tsurumi Tsubasa Bridge*. Journal of JSCE, 543/I-36, 247-258, 1996
3. Y. Yamamoto, F. Fujino and M. Yabe., (2009). *Comparison of seismic records with seismic response of long-span cable-supported bridges identified using a dynamic analytical model*. Journal of JSCE, A, 65(3), 738-757, 2009

NATURAL DISASTERS AND THEIR EFFECTS ON LIVELIHOODS OF THE PEOPLE IN VINH LONG PROVINCE

CÁC THẢM HỌA TỰ NHIÊN VÀ ẢNH HƯỞNG CỦA CHÚNG ĐẾN SINH KẾ CỦA NGƯỜI DÂN Ở TỈNH VĨNH LONG

Ha Chi Tam and Nguyen Van Tho

ABSTRACT

Vinh Long is one of the provinces in the Mekong Delta affected by natural disasters. Some of them (salinity intrusion, droughts, floods and landslides) have greatly affected the livelihoods of the people in the province. Field survey, data collection and analysis of official statistics showed that in 2017 flooding and tidal inundation affected 27.03% (24,497.27 ha) of agricultural land. Droughts also affected about 30% of the rice land area (equivalent to 17,600 ha). Drought together with salinity intrusion from the east entering inland caused salinity up to 5.5‰. Cyclones also occurred with low frequency, affected about 102 hectares of crops. River bank landslide and erosion of four major river mouths and several small branches in the province were also revealed. Many sections of the rivers experienced landslides of more than 2.7km in length and erosion up to 32m.

KEYWORDS: Natural disaster, livelihood, Vinh Long province

TÓM TẮT

Tỉnh Vĩnh Long là một trong số những tỉnh ở Đồng Bằng Sông Cửu Long bị ảnh hưởng bởi các thiên tai. Trong số chúng (xâm nhập mặn, hạn hán, lũ lụt và sạt lở) đã ảnh hưởng rất nhiều đến sinh kế của người dân trong tỉnh. Bằng phương pháp thu thập khảo sát thực địa, thu thập dữ liệu và phân tích thống kê cho thấy trong năm 2017 lũ lụt và triều cường đã ảnh hưởng đến 27.03% (24.497,27 ha) diện tích đất nông nghiệp. Hạn hán cũng đã ảnh hưởng khoảng 30% diện tích đất trồng lúa (tương đương 17,600ha). Hạn hán cùng với sự xâm nhập mặn từ hướng biển đông xâm nhập vào đất liền làm cho độ mặn tăng lên đến 5.5‰. Lốc xoáy cũng có xảy ra nhưng với tần suất thấp, ảnh hưởng khoảng 102 ha hoa màu. Sạt lở bờ sông và xói mòn của 4 con sông chính và một vài nhánh sông nhỏ đã được đánh giá. Có nhiều đoạn sông chiều dài sạt lở bờ đến hơn 2.7km, xâm thực vào đất liền có đoạn đến 32m.

TỪ KHÓA: Thảm họa tự nhiên, Sinh kế, Tỉnh Vĩnh Long

Ha Chi Tam, PhD

Committee Division of Environment and Natural Resources,
the People Committee of Vinh Long City. 9/24, 30/4 Street,
Ward 1, Vinh Long City, Vinh Long Province

Email: hachitam78@gmail.com,

Tel: 090.9946464

Nguyen Van Tho, PhD

Department of Environment, Faculty of Urban
Infrastructure Engineering, Mien Tay Construction
University. 20B, Pho Co Dieu Street, Ward 3, Vinh Long City,
Vinh Long Province.

Email: nguyenvantho@mtu.edu.vn.

Tel: 01262.214279

1. Introduction

The Mekong Delta, one of the largest agricultural centers in the south of Vietnam (Le Van Khoa, 2003), consists of 13 provinces. In recent years, natural disasters such as floods, droughts, saline intrusion, landslides, storms, etc. have occurred in a dense frequency which severely affects the environment, people and development in the Mekong Delta (Mekong Delta). This is the land of the lower Mekong, characterized by low land, soft and quite flat with a system of dense rivers. Therefore, the Mekong Delta is vulnerable to natural disasters.

Vinh Long is located in the Mekong Delta. It has a total natural area of 47.82 km² (149,680.74 ha) and is divided into 08 administrative areas (01 city, 01 town and 06 districts) (Figure 1). Flat terrain with a slope of less than 20% is lowered from north to south, along with four major rivers (Hau River, Tien River, Co Chien River and Mang Thit River) which supply water for people's economic and social activities in the area. Annual average temperature is from 27-28°C, lowest temperature is 16.7°C and highest is 38.3°C. The rainy season usually lasts for 7 months, from May to the end of November. Annual average rainfall is from 1,300 to 1,600 mm. Hydrology is affected by the rainfall so the flow rates of the rivers are often changing and complex.

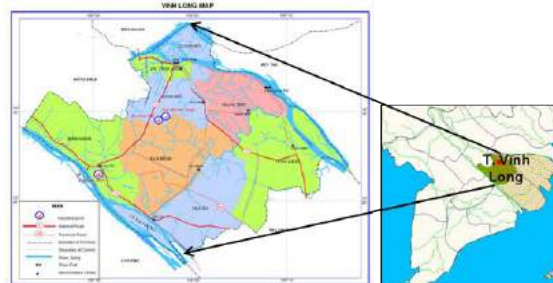


Figure 1: Vinh Long Province in the Mekong Delta

Due to the meteorological, geographical and ecological changes, natural disasters have caused great losses to the natural environment and livelihoods of the people in the province. However, over the past time, the province has no statistics on natural disasters and impact on people's livelihoods in the province. The study "Natural disasters and their effects on livelihoods of the people in Vinh Long province" was conducted to: (i) survey on natural disasters that occurred Vinh Long province and (ii) to assess effects of natural disasters on people's livelihood.

2. Research methodology

Data and information about natural conditions, geographic location, hydrological regime and natural disasters were collected from the Department Resources and Environment of Vinh Long Province. Data on land use, agricultural production, crop calendar and natural disasters and damages caused by natural disasters were collected from the Department of Agriculture and Rural Development,

Steering Committee for Natural Disaster Prevention and Search and Rescue in Vinh Long Province.

Field survey was conducted in areas affected by natural disasters to collect data related to socio-economic damage. Local government officials and people affected by natural disasters were also interviewed to assess the impact of natural disasters. Salinity, and submerged depth during inundation were also measured.

The MIKE-GIS model was carried out and a spatial map that shows the locations and extent of saltwater intrusion of areas submerged was formed. Data collected was aggregated, coded and analyzed using the Microsoft Excel and presented through tables and charts.

3. Results and discussion

3.1. Natural disaster statistics and frequency of occurrence

From the reports in the last 10 years showed that natural disasters occurred in Vinh Long Province included inundation, drought, saline intrusion, river bank erosion, thunderstorms and cyclones. Among them, drought and flooding occurred annually with 1 - 2 times per year and the time lasting several months. Riverbank erosion, thunderstorms, storms and cyclone were determined as unexpected and the occurred frequency listed in Table 1.

Table 1: Statistical frequency of natural disasters caused by riverbank erosion, thunderstorms and tornadoes

Years	The occurred frequency of disaster natural (counts)	
	Riverbank erosion	Thunderstorms, storms and cyclone
2007	5	7
2008	4	10
2009	-	4
2010	3	6
2011	4	10
2012	9	10
2013	10	15
2014	6	5
2015	39	5
2016	110	10
2017	125	16
Total	315	98

(Source: Department of Agriculture and Rural Development of Vinh Long province, 2007 – 2017)

Note: “-” Data not yet available

Table 1 showed that the riverbank erosion disaster increased every year and occurred with more than 300 times in the past 10 years. Besides that, the total length of riverbank erosion measured more than 31.396m, in which

the largest length was up to 2.700m. The largest width of erosion into the mainland was 32m and the largest depth up to 12m. Thunderstorms, storms and cyclone were occurred at least 4 times per year (2009), at most 16 times per year (2017); and the total number in the past 10 years was 98 times.

3.2. Impact assessment by natural disaster

3.2.1. Riverbank erosion

River erosion caused damage to property (such as loss of residential land, ruining houses, crops, and the damaged riverine routes caused to disrupting travel and freight) and risk to harm to human's life. The statistical results from 2007 to 2017 showed that there were 1094 houses affected by riverbank erosion, in which there were more than 59 houses where residents were forced to move to another place; the total damage was estimated over 31.5 billion Vietnam Dong (VND) (Table 2). The cause was mainly determined by the effect of flow, the natural vortex, the topography of the meandering river, and human impact (such as river sand mining, riverbed dredging, and dam construction...).

Table 2: The statistics on damage caused by riverbank erosion during 2007 - 2017

Years	The damage caused by riverbank erosion		
	The number of the affected houses and facilities	The number of the displaced houses	Estimated damage amount (million VND)
2007	11	2	1.000,00
2008	11	3	475,00
2009	20	10	15,00
2010	8	-	-
2011	1	-	-
2012	26	7	12,00
2013	7	3	56,00
2014	24	-	-
2015	22	-	-
2016	105	-	12.347,91
2017	859	34	17.665,54
Total	1.094	59	31.571,45

(Source: Department of Agriculture and Rural Development of Vinh Long province, 2007 – 2017)

3.2.2. Thunderstorms, storms and cyclone

Vinh Long province was less directly affected by storms, but was often affected by the fringe storm and tropical depressions, thunderstorms and cyclone. The statistical results by Flood Prevention Board in Vinh Long province showed that thunderstorms, storms and cyclone caused damage to houses, facilities and the life of the people. From 2007 to 2017 years, there were more than 3.000 houses collapsed, lost roofs and fire; killed 11 people and injured 14

people; the total damage was estimated at over 31 billion VND (Table 3).

Table 3: The statistics on damage caused by thunderstorms, storms and cyclone

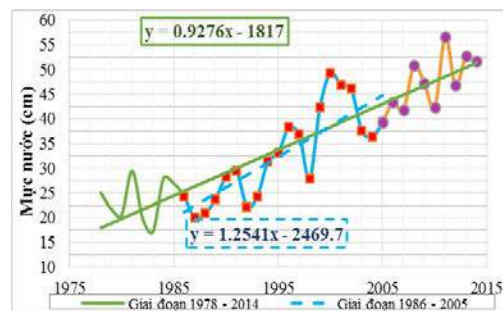
Years	Damage by tropical depressions, thunderstorms, storms and cyclone			
	The number of houses collapsed, lost roofs and fire	The number of dead	The number of injured	Estimated damage amount (million VND)
2007	363	2	-	1.335,00
2008	80	1	4	1.081,00
2009	113	4	1	1.569,00
2010	80	2	-	1.301,00
2011	345	1	2	2.664,00
2012	835	1	6	9.698,00
2013	210	-	-	3.147,50
2014	185	-	-	1.946,00
2015	140	-	-	1.488,35
2016	297	-	-	3.086,80
2017	363	-	1	3.969,80
Total	3.011	11	14	31.286,45

3.2.3. Floods

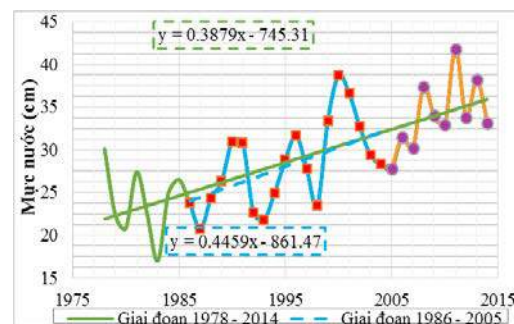
Vinh Long province was located in the area that affected by floods and tides of the Mekong River. Floods began to appear when water from rivers raised and affected the area of Vinh Long province. Flood comes from the upstream water of the Mekong Delta river systems that flow down through the Tien and Hau rivers and the northern part of the Vinh Long province area. Annual, flooding was usually occurred in mid-August, culminating in late September and mid-October.

Inundation often occurs when floods combine with high tides that have affected some land areas of Vinh Long province. This is due to the flat topography and low-lying areas, multiple and complex from the flow systems, some poor drainage areas. Inundation was assessed through the annual water level measurements on large rivers and the inundated locations that were shown on the map from survey data.

The annual water level measurements were done at two stations (Cho Lach and Can Tho) on two large rivers of Mekong river that flowing through Vinh Long province. The results showed that the average water level at stations increased to 0.93 cm per year (Figure 2). In 2017, the measured water level was higher than the average for many years 0.20 - 0.40 m. Results proved that the water level in the rivers has been increasingly rising in the stage of 1978 to 2017. The results were similar to previous research by the Irrigation Science Institute of Vietnam, besides that, the cause is determined by climate change and causing the water level rise (Pham Thi Huyen Trang, 2016).



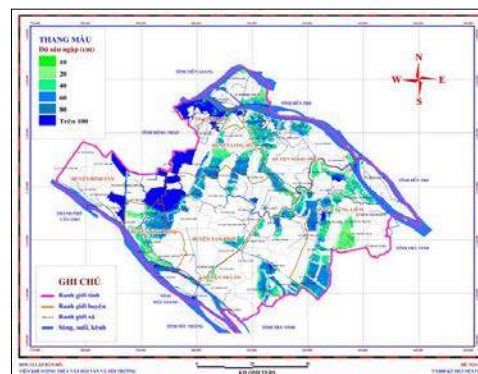
(a)



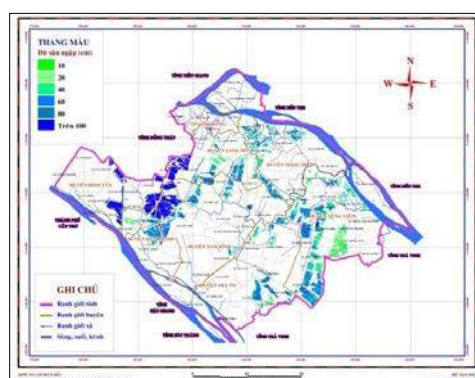
(b)

Figure 2: Water level trends at the monitoring stations
(a) Can Tho station, (b) Cho Lach station

Through MIKE 11 - GIS calculation model, the results were described the inundated areas map in Vinh Long province (Figure 3). It was showed that the inundated areas mainly occurred in Vinh Long city, Binh Tan and Binh Minh districts with the inundated areas up over 1m, the remaining districts inundated with average 0.1 - 1m.



(a)



(b)

Figure 3: Maps of the inundated depth calculation in 2016
(a) When the highest tide and (b) inundated rice paddy land

In the recent years, many roads, houses, buildings and farmland have been inundated by flood and tides which affected to the livelihood of people in Vinh Long province. The inundated depth was determined to be about 15 – 50 cm (Department of Natural Resources and Environment of Vinh Long province, 2015).

In the inundated depth maps (Figure 3) showed that many areas were inundated. Specially, the Vinh Long city area most cared because this is an urban area with the densely populated place. The remaining inundated areas were located near canals and rural areas. The statistical results indicated that the agricultural land group was most affected with inundated land area accounting about 27.03 % (the inundated area about 24.497,27 ha); the estimated damage about 1 – 5 billion VND/ha; The area of industrial land, house and office building were inundated about 24.76% (about 8.769,29 ha). Specific data on the inundation land area of each district in Vinh Long province was presented in the Table 4.

3.2.4. Drought

Annual, droughts occurred at Vinh Long province during the low tide period from January to April every year. The drought has affected people living in high terrain areas, areas without water. In the past, natural disasters due to the occurred drought have not been adequately considered. In the past, natural disasters due to the occurred drought were less considered, therefore, the statistical data related to the impact level of the livelihood was little unrecorded. The affected areas by droughts were often agricultural land areas. The statistical results in the recent years were done on the damaged rice area which was shown in Figure 4.

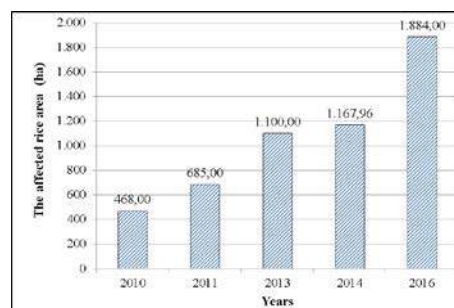


Figure 4: The affected rice area by drought

Figure 4 showed that the affected rice area by drought was increased from 2010 to 2016. However, due to a severe drought occurred in 2016 the affected rice area was increased. In 2016, there were 1,884 hectares of plants died due to lack of water, the estimated damage nearly 300 billion VND; In which, three districts were most damaged as Vung Liem, Mang Thit, and Tra On. The occurred drought in 2016 with two causes were identified as (1) The impact of the El Nino phenomenon causes severe sunshine, the lowly rainfall and the rainy season ended sooner than every year; and (2) The amount of water from upstream of the Mekong River flowing through the rivers of Vinh Long was sharply reduced. This is due to the hydropower dam systems that built on the mainstream of Mekong River. In addition, the upstream countries of the Mekong River have increased using water due to forming new agricultural lands, establishing industrial clusters along the Mekong River.

3.2.5. Salinization

Salinization occurred during the period of the appeared drought in combination with the low tide, the saltwater intrusion deep into the mainland. The salinity on Co Chien river was monitored at Vung Liem station, the results showed many fluctuations and increased over 10 years observation with the measured salinity from 1.6‰ up to 5.5‰ (Figure 5).

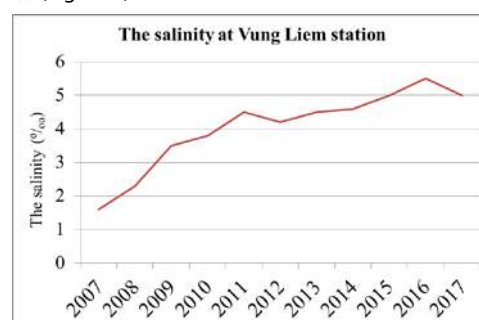


Figure 5: The salinity at Vung Liem station

Table 4: The inundation land area of each district in Vinh Long province

	Binh Minh	Binh Tan	Long Ho	Mang Thit	Tam Binh	Vinh Long city	Tra On	Vung Liem	Total
The total area of the agriculture land (ha)	5.528,22	10.631,30	10.345,09	8.999,07	18.902,81	1.700,10	16.524,84	17.991,59	90.623,04
The inundated agriculture land area (ha)	2.345,22	2.165,89	3.866,65	2.117,27	3.174,92	685,29	2.815,55	7.326,50	24.497,27

	Binh Minh	Binh Tan	Long Ho	Mang Thit	Tam Binh	Vinh Long city	Tra On	Vung Liem	Total
The inundated ratio (%)	42,42	20,37	37,38	23,53	16,80	40,31	17,04	40,72	27,03
The total area of industrial land, house and office building (ha)	2093,86	2.394,20	5.458,56	3.578,4	6.692,32	1.777,39	6.273,85	7.149,96	35.418,54
The inundated area of industrial land, house and office building (ha)	908,39	437,55	1829,79	807,18	1151,63	986,51	954,23	1694,01	8.769,29
The inundated ratio (%)	43,38	18,28	33,52	22,56	17,21	55,50	15,21	23,69	24,76

The salinity distribution maps of Vinh Long province were constructed by using the GIS tool in combination with the MIKE 11 model from the highest salinity data of 2007, 2010, 2013 and 2016 years (Figure 6). As the results indicated that the salinity has changed in overtime and invaded deep into the mainland in Vinh Long province. The highest salinity in Vinh Long up to 8‰ in 2016 on Co Chien river. The trend of salinity in Tien River was higher than Hau River. The salinity 1 ‰ covered almost all of Vung Liem district and a small part of Mang Thit district. The boundary salty 0.5 ‰ on Co Chien and Song Hau rivers measured at the boundary of My Phuoc commune, Mang Thit district and Vinh Long - Tra Vinh boundary, respectively.

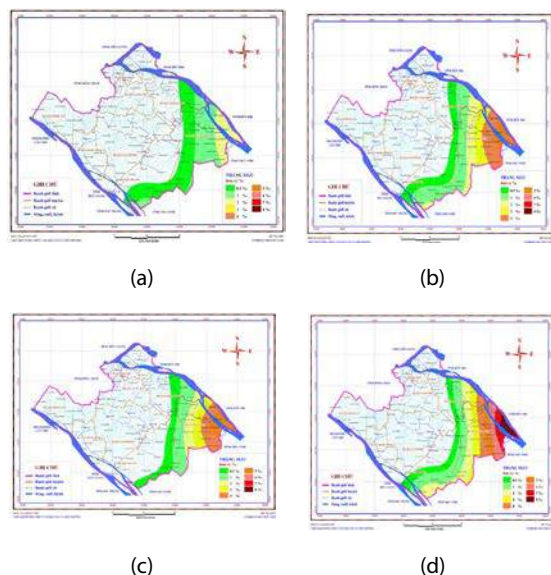


Figure 6: Highest salinity in years at main river branches in Vinh Long Province (a) 2007, (b) 2010, (c) 2013 and (d) 2016

Increased salinity affected the local people's water supply and agricultural production. Salty water intruding into the agricultural areas caused the flowering of crops failed and death of the young plants. As a consequence, the acreage of the arable land was reduced and the yield of the crop was decreased. According to the survey results and statistics showed that in 2016 there were 23,179.63 hectares of rice land affected by saline intrusion, estimated

losses of more than 250 billion VND. The results of the interviews showed that the rice crop was mainly damaged in the period of waiting for harvest. In addition, prolonged salinity intrusion also affected the crop calendar of the next crop due to not enough fresh water source to irrigate crop. Causes were determined by the salty water coming soon, the decreased fresh water from the upstream, prolonged hot weather.

4. Conclusions

Main natural disasters in Vinh Long province were floods, droughts, storms, saline intrusion, and river bank erosion. The results showed that over the past 10 years, there were more than 300 cases of river bank erosion (in which the most in 2017 up to 125 cases). Some areas landslide occurred more than 2.7km, erosion into the inland more than 32m in length and up to 12m in depth. There were 98 cyclones and storms occurring at least 4 times a year. Floods occurred during the three months of the year (August - October each year), with the highest flooding level over 1m. Droughts also occurred from January to April every year, resulting in the salinity intrusion entering inland with the highest salinity determined to be over 5.5‰. Statistics showed that the natural disasters caused a great damage, affecting people's livelihood, health, farming land and property.

References

1. Le Van Khoa, (2003). *The compaction in land for intensive rice cultivation at the Mekong Delta, Vietnam*, Scientific journal of Cantho University, 95-101 (Vietnamese version).
2. Pham Thi Huyen Trang, (2016). *Floods in the Mekong Delta: Causes and solutions*, Scientific journal of Pedagogical University Ho Chi Minh City, No. 3(81) (Vietnamese version).
3. Department of Agriculture and Rural Development of Vinh Long province, (2007 – 2017). *The annual report of the steering committee of flood prevention* (summation from reports) (Vietnamese version).
4. Department of Natural Resources and Environment of Vinh Long province, (2015). *Report on environmental status in 2015* (Vietnamese version).
5. Department of Natural Resources and Environment of Vinh Long province, (2016). *Climate change action plan* (updates version) (Vietnamese version)

EFFECTS OF OVERBURDEN LOADS ON LIQUEFACTION-INDUCED SETTLEMENTS WITH SAND BOILING

Tetsuo Tobita and Yuya Yoshimura

ABSTRACT

Effect of overburden loads on the amount of settlements associated with sand boiling is investigated with model testing. Loose saturated sand deposit is made in a transparent acrylic cylinder and torsional shaking is given to reproduce liquefaction. To mimic non-liquefiable layer on top of the liquefiable layer, an aluminum circular plate whose diameter is slightly smaller than the inner diameter of the cylinder is placed on the model ground surface. Boiled sand through the gap between the side wall of the cylinder and the plate was monitored from the side, and 4 excess pore pressure transducers recorded transient variations of the water pressure, and 1 laser displacement sensor measured the settlement of the plate. The overburden loads is varied by attaching an extra-mass on the rod connected with the aluminum container. Major findings include; 1) The amount of settlements sharply increases when the boiled sands are piled up on the surface of the non-liquefiable layer. 2) The amount of settlement is largely influenced by the overburden loads when sand boiling is manifested. 3) Width of the gap through which boiled sand is passing has less influence on the amount of settlement.

KEYWORDS: *liquefaction, sand boiling, settlements, physical modeling*

DR. TETSUO TOBITA

Associate Professor, Department of Civil, Environmental and Systems Engineering, Kansai University, 3-3-35, Yamate-cho, Suita, Osaka, 564-8680, Japan.

Email: tobita@kansai-u.ac.jp, **corresponding author**

Tel: +81-6-6368-0898

1. Introduction

Sand boiling or sands ejected from the ground has been recognized as a clear evidence of liquefaction occurrence (e.g., Seed and Idriss, 1967; Bardet and Kapuskar 1991, Wakamatsu, 2011; Ishihara, 2012; Yasuda et al., 2012). In 2010 and 2011 Canterbury, New Zealand, earthquake, huge amount of liquefied soil, which was naturally deposited, was ejected in the area along the Avon river (Cubrinovski and Green, 2010, Cubrinovski, et al., 2012). It had not been anticipated that such a huge amount of soil could be ejected and that caused relocation of residents from the area. In the 2011 Off the Pacific Coast of Tohoku, Japan, Earthquake, Urayasu, Chiba Pref., suffered similar sand ejecta of reclaimed soil (Yasuda et al., 2012; Ishihara, 2012).

The amount of ejected soil or the way of sand boiling may be inferring some basic and important information of the ground shaking and properties of the ground. However, it has been so far used merely as an evidence of liquefaction. Numata et al. (1999) conducted detailed study on the trench where liquefaction occurred and found that liquefied soils were sorted by their diameter or weight before ejecting from the ground. Numata and Someya (2004) accessed the effect of the sorting in model tests. Yamaguchi et al (2008) studied pattern of sand boiling and developed a method to evaluate

the thickness of a liquefied layer. They reported that the porewater was trapped between liquefied and non-liquefiable layer. There are numbers of studies which investigated mechanism of sand boiling (e.g., Wibawa et al. 1990; Okawa, 1997; Yamaguchi et al., 2008ab; Ishikawa and Yasuda, 2012). However, there are seldom researches which studied a relationship between the amount of settlements and sand boiling. Through physical model testing, effect of overburden stress on the amount of settlements associated with sand boiling is investigated quantitatively.

2. Model testing for sand boiling

Mechanism of settlements associated with sand boiling was investigated through a series of the model testing. Loose saturated sand deposit was made in a transparent acrylic cylinder (Table 1 and Fig. 1). Toyoura sand ($G_s=2.66$, $\rho_{dmax}=1.638 \text{ g/cm}^3$, $\rho_{dmin}=1.329 \text{ g/cm}^3$) of 24.1 kg was poured into the cylinder. Then by boiling method the height of the surface of the model ground was adjusted at 950 mm from the bottom to obtain the relative density of $Dr=40\%$.

Torsional shaking along the vertical center axis of the cylinder was given by an electrical motor to reproduce liquefaction, whose rotation angle was about ± 0.5 degrees under 50 Hz. Duration of the input motion was about 2 seconds with which, as shown later, complete liquefaction was realized. Note that shear stress and strain thus induced might vary radially. However, it may be reasonable to assume that those effect may vanish after complete liquefaction.

To mimic the existence of a non-liquefiable layer on top of the liquefiable layer, an aluminum circular plate (called "loading plate" in Fig. 2) whose dimensions are given in Table 1, was placed on the surface of model ground. To make liquefied sand boil through the gap between the side wall of the cylinder and the plate, a diameter of the plate (144 or 146 mm) was made slightly smaller than the inner diameter of the cylinder (150 mm). Through this gap (3 mm or 2mm), liquefied sand could be ejected. The plate was equipped with a sidewall (Fig. 2) to catch the boiled sands. The elevation of the sidewall of the plate was varied (20 or 40 mm) to see the buoyancy effect of the plate on the settlement due to sand boiling. Overburden stress is given by attaching an extra-mass (100 or 250 g) on the rod connected with the plate whose self-weight is 500 g. Inclination of the plate from horizontal ground surface was restricted by limiting the horizontal movement of the rod with a lid attached on top of the cylinder (Figs. 1 and 2).

Two accelerometers on the base plate were attached in either radial or tangential directions. Three pore pressure transducers were installed on the side wall of the cylinder with 400 mm intervals (Fig. 1). Another pore pressure transducer was installed at the bottom of the plate to measure excess pore water pressure just beneath the plate where squeezed pore water from the liquefied and then consolidated ground may be trapped. One laser

displacement transducer is installed for measuring the settlement of the plate (Fig. 1). Also, to visually monitor the process of settlements with sand boiling, video image was recorded from the side of the cylinder.

Table 1: Dimensions of testing equipment and model sand deposit.

	Parameter	Unit	Value
Acrylic cylinder	Inner diameter	mm	150
	Length	mm	1,400
	Depth of the sand deposit	mm	950
Aluminum plate	Diameter	mm	144 / 146
	Elevation of sidewall	mm	20 / 40
	Self weight	gf	500
	Added weight	gf	0 / 100 / 250

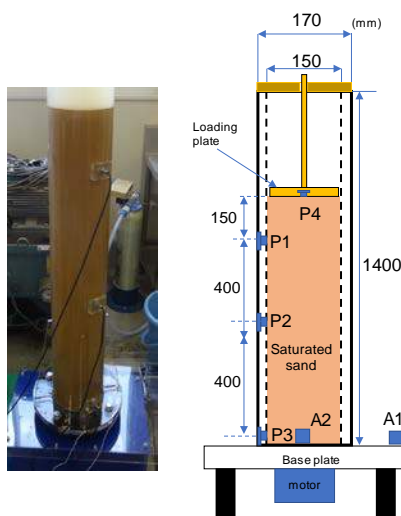


Figure 1: Schematics of an acrylic cylindrical container for sand boiling test

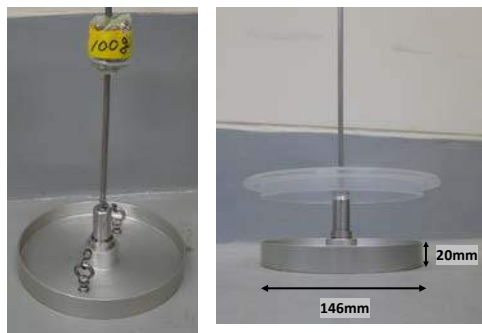


Figure 2: View of an aluminum plate with 100 gf of additional weight and a lid to cover the cylinder.

Figure 3 explains how each test case can be identified by the given case ID. For example, as shown in Fig. 3, the case "PT20-146-WL20.250" uses the plate whose sidewall height is 20 mm, diameter is 146 mm, the ground water level is 20mm from the surface of the sand, and added mass is 250g.

Time histories of the excess pore water pressure ratio of with/without the loading plate (Fig. 4) clearly show that whole sand deposit is liquefied, i.e., all the excess pore water pressures measured by P1, P2 and P3 reach $r_u=1$.

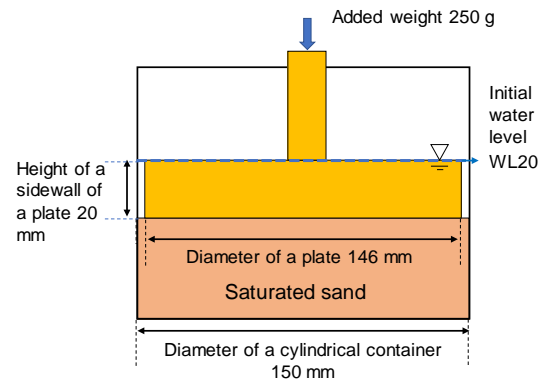


Figure 3: Example of the case ID of PT20-146-WL20.250.

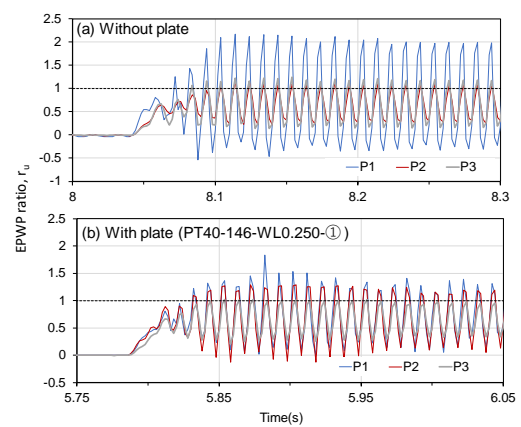


Figure 4: Time histories of the excess pore water pressure ratio: (a) without a loading plate, (b) with the loading plate; PT20-146-WL20.250.

3. Test results

By varying above mentioned parameters on testing, total 70 tests were conducted. Figure 5 depicts an example of sand boiling and settlements of the plate for the case of PT20-146-WL20.250. After a brief interval from the shaking, sand surface started to rise in the gap with minor settlement of the plate (Fig. 5b). The settlement of the plate was accelerated with the ejected sand flown into the plate, which gave an additional mass to the plate (Fig. 5c).

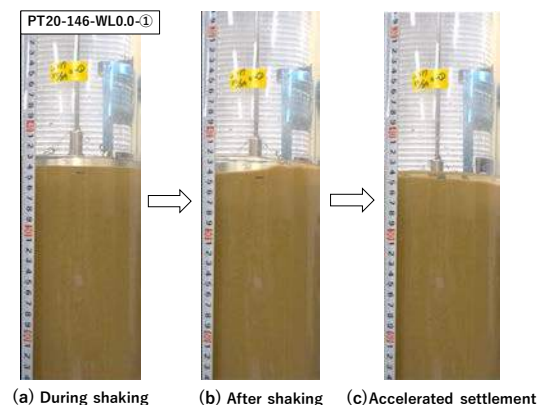


Figure 5: Transdition of boiled sand and the loading plate: PT20-146-WL20.250.

Figure 6 shows time histories of the settlement of the plate for the cases of various overburden loads (500, 600, and 750 g). In Fig. 6, the case with no plate (PT0-0-WL0.0) is plotted as a solid marker for which continuous measurement of settlement was not made. The largest settlement of about 130 mm is observed for the case of the heaviest case (initial total overburden mass: 750 g), which is more than 4 times of settlement than that of the case of without a plate. Figure 6 indicates that the amount of residual settlement is in proportion to the initial overburden loads.

Also, in Fig. 6, the speed of settlement increases after a brief interval from the shaking. That timing is indicated by up-pointing arrows in Fig. 6. From the video images, they correspond to the timing when the ejected sand flew into the plate. That is, heavier the overburden mass is, faster the sand boiling occurs. Fig. 6 also indicates that the rate of settlement after sand boiling (slope of the curves after the arrows in Fig. 6) is slightly larger for the cases of a larger overburden mass. Hence, the ground settlements are largely influenced by the overburden loads due to a non-liquefiable layer when the sand boiling is manifested.

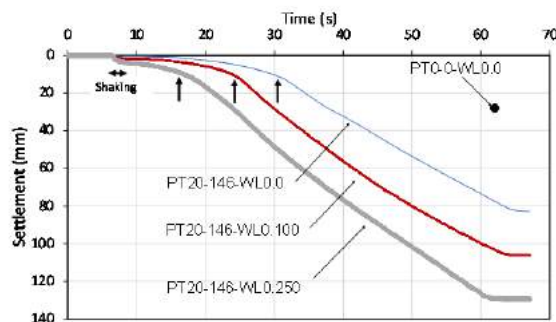


Figure 6: Time histories of ground settlements for no plate (0 N/m²) (PT0-0-WL0), with the plate of 500 g (301 N/m²) only, with the plate and additional weight of 100 g (361 N/m²) and with the plate and additional weight of 250 g (452 N/m²).

Figure 7 shows variation of residual settlements versus the initial overburden mass for the use of the plates of different diameters and sidewall elevation. Here, in Fig. 7, the initial water depth is undistinguishing. As expected, the residual settlement increases with the total initial overburden mass. Compared the settlements of PT20-146 with those of PT20-144, average settlements of the plate are nearly identical. When the elevation of the sidewall is larger, PT40-146, the settlement is reduced about 30% on average from the cases of PT20-146. This might be due to a larger buoyancy of the plate which reduced the overburden loads. Also, the high sidewall might hinder inflow of the boild sands in the plate.

4. Conclusions

A series of dynamic model testing to study the influence of overburden loads on the amount of settlements due to the boiled sand of liquefied soil was conducted. The model ground was constructed in an acrylic cylinder of the inner diameter of 150 mm. Loosely saturated model ground

(Dr=40%) with Toyoura sand was made by the boiling method. Sand boiling was replicated from the gap between the side wall of the cylinder and the plate placed on top of the model ground surface to mimic non-liquefiable layer. Dynamic motion was given in the torsional direction along the center axis of the cylinder with +/- 0.5 deg. of 50Hz. Major findings are;

1. The amount of settlements sharply increases when the boiled sands are piled up on the surface of the non-liquefiable layer.
2. The amount of settlement is largely influenced by the overburden loads when sand boiling is manifested.
3. Width of the gap through which boiled sand is passing has less influence on the amount of settlement.

Fundamental data to predict the amount of settlement due to sand boiling was obtained through the small-scale model testing. Next step may be to construct analytical procedure for predicting the amount of boiled sand and associated settlements.

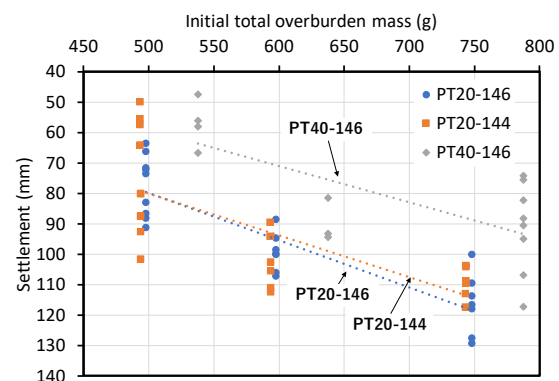


Figure 7: Initial overburden mass versus settelement of the plate.

References

1. J. P. Bardet and M. Kapuskar., (1991). *The liquefaction sand boils in the San Francisco Marina district during the 1989 Loma Prieta Earthquake*, International Conferences on Recent Advances in Geotechnical Earthquake Engineering and Soil Dynamics, 1687-1691.
2. M. Cubrinovski, and R. A. Green., (2010). *Geotechnical reconnaissance of the 2010 Darfield (Canterbury) earthquake*, Bulletin of the New Zealand Society for Earthquake Engineering, Vol. 43, No. 4, December 2010, pp. 243-320.
3. M. Cubrinovski, D. Henderson and B. Bradly., (2012). *Liquefaction impacts in residential areas in the 2010–2011 Christchurch Earthquakes*, Proceedings of the International Symposium on Engineering Lessons Learned from the 2011 Great East Japan Earthquake, 811-824.
4. K. Ishihara., (2012). *Liquefaction in Tokyo Bay and Kanto Region in the 2011 Great East Japan Earthquake*, Proceedings of the International Symposium on Engineering Lessons Learned from the 2011 Great East Japan Earthquake, 63-81.

5. K. Ishikawa and S. Yasuda., (2012). *Study of sand boiling characteristics along Tokyo bay during the 2011 Tohoku-Pacific Ocean earthquake*, 15WCEE, No. 1651.
6. T. Iwasaki., (1985). Soil liquefaction studies in Japan: state-of-the-art, *Soil Dynamics and Earthquake Engineering*, 5(1), 2-68.
7. A. Numata and N. Someya., (2004). *Simplified model experiment of sand dike due to liquefaction*, 39th Japan National Conference on Geotechnical Engineering, D-07.
8. A. Numata, S. Mori, I., Tohno and K. Endo., (1999). *A study on sand dikes and sand boils caused by liquefaction*, *Journal of JSCE*, 638(III-49), 311-324 (inJapanese).
9. H. Ohkawa., (1997). *Consideration on the mechanism of liquefaction*, *Journal of JSCE*, 568(III-39), 13-20.
10. H. B. Seed and I. M. Idriss., (1967). *Analysis of soil liquefaction: Niigata earthquake*, *Journal of the Soil Mechanics and Foundations Division, ASCE*, 1967, Vol. 93, Issue 3, Pg. 83-108.
11. K. Wakamatsu., (2012). Recurrent liquefaction induced by the 2011 Great East Japan Earthquake compared with the 1987 earthquake. *Proceedings of the International Symposium on Engineering Lessons learned from the 2011 Great East Japan Earthquake*, Tokyo, 675-686.
12. B. Wibawa, H. Ohta, and T. Okuma., (1990). *An experimental study of sand boiling due to liquefaction*, *J. JSNDS*, 9-3, 42-59.
13. A. Yamaguchi, N. Yoshida, and Y. Tobita., (2008a). *Estimation of thickness of liquefied layer from sand boiling pattern*, *Journal of JSCE*, 64(1), 79-89 (inJapanese).
14. A. Yamaguchi, N. Yoshida, and Y. Tobita., (2008b). *Experimental study about liquefaction mechanism*, *The Japan Association for Earthquake Engineering (JAEE) Journal*, 8(2), 46-62 (inJapanese).
15. S. Yasuda, K. Harada, K. Ishikawa, and Y. Kanemaru., (2012). *Characteristics of liquefaction in Tokyo Bay area by the 2011 Great East Japan Earthquake*, *Soils and Foundations*, 52(5), 793-810.

Evaluation of The Joint Characteristics Distribution in The Exploratory Adit

Đánh Giá Sự Phân Bố Khe Nứt Trong Hầm Ngang Khảo Sát

Nguyen Thi Kieu Mi, Nguyen Huynh Thong, Naotoshi Yasuda

ABSTRACT

Dong Nai 4-2 exploratory adit is one in four exploratory adits for Dong Nai 4 hydropower dam, 80m length, 2m diameter, and 140° direction. In exploratory adit, the joints are complex and most of the joint spacing is less than 0.6m. Most of the joint roughness is smooth, but the joint separation is small causing the infilling such as sandy silt, calcite, and quartz that control entirely the shear strength of the joint, that obstructs collapse of the exploratory adit. However, from these characteristics don't yet accurately assess the stability of exploratory adit, it also depends on an important factor that is the orientation of joints in the exploratory adit. Therefore, in order to evaluate the stability of the exploratory adit, the paper used rose diagram and stereonet method to statistic the joints, that easily find out the main development and the pole density of the joints. Therefrom, evaluating their effect on the excavation direction. Considering the 5-10m section of the Dong Nai 4-2 exploratory adit, it's through 30 joints, with 6 joint systems. From the rose diagram and stereonet method show that the axis of the 5-10m section is perpendicular to the main development direction of the joints, but the excavation direction drive against the dip of these joints, with density > 50%. According to Bieniawski (1989), the 5-10m is unfavorable. Especially, in the case where many joints cross. So, there should excavate another direction to ensure stability.

KEYWORDS: joint, rose diagram, stereonet, Dong Nai 4-2 exploratory adit

TÓM TẮT

Hầm ngang Đồng Nai 4-2 là một trong 4 đường hầm khảo sát đập thủy điện Đồng Nai 4, dài 80m, đường kính 2m, hướng hầm 140°. Trong hầm ngang, các khe nứt phân bố phức tạp, khoảng cách của các khe nứt đều nhỏ hơn 0.6m. Phần lớn bề mặt các khe nứt nhẵn nhưng độ mở nhỏ làm cho các vật chất lấp nứt như cát, canxit và thạch anh cũng tham gia vào sự cản trở lực cắt xảy ra và tăng sự liên kết tại các bề mặt khe nứt, từ đó làm cản trở sự biến dạng hay sập hầm. Tuy nhiên, yếu tố quan trọng là thể nằm của khe nứt trong hầm ngang rất phức tạp nên từ các đặc tính trên vẫn chưa đưa ra được đánh giá chính xác ổn định của hầm. Vì vậy, nhằm đánh giá sự ổn định của hầm ngang, bài báo đã sử dụng phương pháp vẽ đồ thị hoa hồng và stereonet nhằm thống kê lại các khe nứt, để dễ dàng tìm ra phương phát triển chính và mật độ của khe nứt. Xét đoạn 5-10m của hầm ngang Đồng Nai 4-2, đoạn hầm đi qua 30 khe nứt, trong đó có 6 hệ thống khe nứt. Từ đồ thị hoa hồng và

stereonet cho thấy các khe nứt này chủ yếu vuông góc và có hướng cắm ngược lại với hướng đào hầm, với mật độ > 50%. Theo Wickham (1972) thì hướng đào hầm đoạn 5-10m sẽ không thuận lợi. Đặc biệt là tại vị trí có nhiều khe nứt cắt nhau. Vì vậy, cần phải thay đổi hướng đào để đảm bảo sự ổn định của hầm.

TỪ KHÓA: khe nứt, đồ thị hoa hồng, stereonet, hầm ngang Đồng Nai 4-2

NGUYEN THI KIEU MI

Student, Department of Earth Resources and Environment, Faculty of Geology and Petroleum Engineering, HCMC University of Technology (HCMUT)
Email: 1412248@hcmut.edu.vn
Tel: 01229189077

DR. NGUYEN HUYNH THONG

Lecturer, Department of Earth Resources and Environment, Faculty of Geology and Petroleum Engineering, HCMC University of Technology (HCMUT)
Email: nhthong@hcmut.edu.vn, corresponding author
Tel: 0908782913

DR. NAOTOSHI YASUDA

Lecturer, Department of Civil and Earth Resources, Faculty of Engineering, Kyoto University

1. Introduction

Today, according to the development of the word, underground projects are more and more developed to meet needs of economic life and national security. These projects are affected by the geological structure; especially underground projects in rock. So the geological survey is very important. In there, the joint factor must be evaluated first.

In rock, the joint exists a lot, our orientation is complex, this is one of the main factors affecting the material rock as increasing weathering grade, decreasing compressive strength of the rock. Therefrom, the issues as collapse happen easily. So, to make specifically the effect of the joint on projects, with the subject " Evaluation of the joint distribution in the exploratory adit" for Dong Nai 4-2 exploratory adit, this is one in four survey exploratory adits of the Dong Nai 4 hydropower dam (Dak Nong), to evaluate the strain degree and stability of the project items as water tunnel, dam shoulder, electrical generating plant, main dam, minor dam,...that is a necessary subject, giving the evaluation method of the effects of distribution and orientation of the joint on the stability exploratory adit. And the evaluation process is more exact.



Figure 1: Location of Dong Nai 4 hydropower dam (investinvietnam.vn)

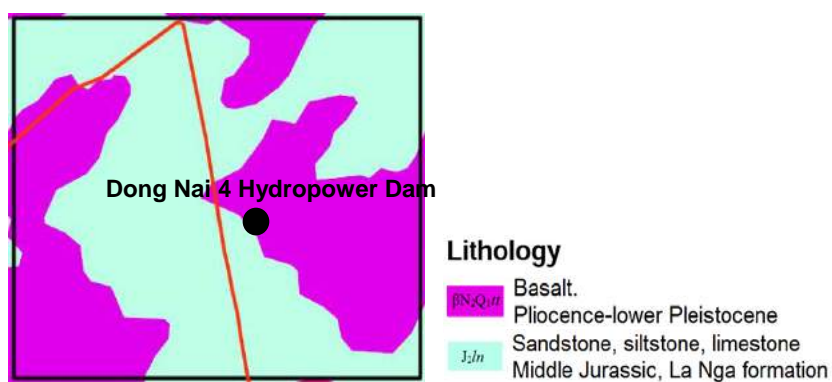


Figure 2: Regional geology of Dong Nai 4 hydropower dam

2. Research methods

2.1 Theoretical basic

In engineering, according to Bieniawski (1989), the characteristic joints includes spacing and orientation, roughness of the joint surfaces, their separation, their length or continuity, weathering of the wall rock of the planes of weakness, and the infilling material. Therein, the orientation of the joints importantly affect the stability tunnel and they are expressed as Table 1.

Table 1: Effect of joint strike and dip orientation in tunneling (Wickham, 1972)

Strike perpendicular to tunnel axis			
Drive with dip		Drive against dip	
Dip 45-90°	Dip 20-45°	Dip 45-90°	Dip 20-45°
Very favorable	Favorable	Fair	Unfavorable
Strike parallel to tunnel axis			Irrespective of strike
Dip 45-90°	Dip 20-45°	Dip 0-20°	
Fair	Very unfavorable	Fair	

So, If the excavation direction is perpendicular to strike and driving with dip of the joints, the excavation direction is favorable. In contrast, if the excavation direction is perpendicular to strike and driving against dip, or the excavation direction is parallel to strike, and irrespective of strike, the excavation direction is unfavorable.

The rose diagram (Figure 3) is set up by the method that assembles joints having the certain direction in the diagram. To conduct this, all the measurement is divided into groups of 5° or 10°. Example, if using groups 5, all the joints have the strike of 1-5, as well as all the joints have the strike of 181°-185° and forming a group, the joints have the strike of 6°-10° (186°-190°) forming the next group,...Processing to count the number of each group 5 and setting up the statistical table.

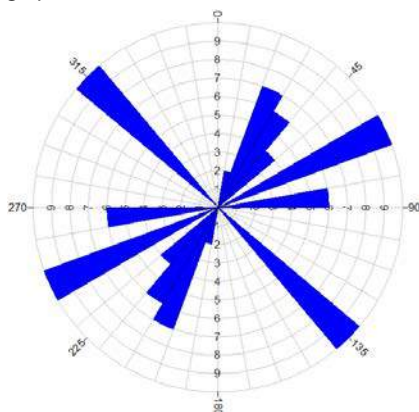


Figure 3: Rose diagram

Differs from the rose diagram just uses strike, dip direction, or dip, the stereonet (Figure 4) uses all three of the factor (strike, dip direction and dip) forming the pole on the Wulff net. When the joint data is a lot or there are the

joints having the same parameter, the evaluation is different by the pole. So the joint distribution is evaluated by the contour zone on the stereonet with the scale color.

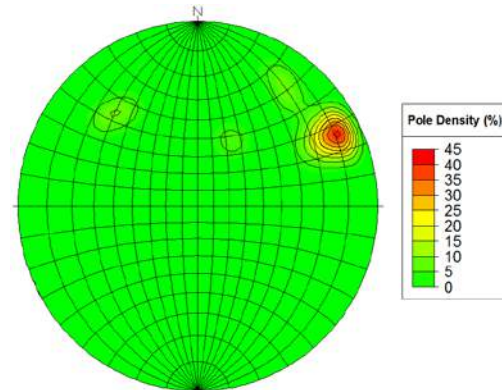


Figure 4: Stereonet

Thus, the paper uses the rose diagram to define the main development direction of the joints, then using the stereonet to define the pole density and the orientation of the joints according to the main development direction. Therefrom, the joint distribution characteristic will be shown fully and evaluated easily the effect of the joint distribution on the excavation direction of the exploratory adit.

2.2 Project characteristics

Due to the geological conditions are complex, the Dong Nai 4-2 exploratory adit is excavated on the south bank of Dong Nai River to survey the geology at the outlet of the headrace tunnel, to learn about rock characteristics in the headrace tunnel and conduct field tests to learn about rock material properties or friction between concrete and ballast.

The Dong Nai 4-2 exploratory adit is excavated in the sandstone of the La Nga formation as Figure 2, with 140° direction, 2m diameter, 80m length, in the elevation of 300-370m as Figure 5.

To sure for the evaluation process is full of rock properties, the exploratory adit is dug to fresh rock and stopped. So, it throughs four weathering grades as Figure 6 and Table 2.

Table 2: Weathering grades of rock in the length of the Dong Nai exploratory adit

Grades	Length (m)	Characteristics
IA ₁	0-5	Highly weathered zone. More than half of the rock material is decomposed or disintegrated to a soil with grey, grey-yellow, mix 40% breccia < 6cm.
IA ₂	5-30	Moderately weathered zone. Less than half of the rock material of sandstone is decomposed or disintegrated to a soil with grey, grey-black.
IB	30-55	Slightly weathered zone. Some part of sandstone may be discolored by weathering with grey, grey-black.
II	55-80	Fresh rock zone of sandstone

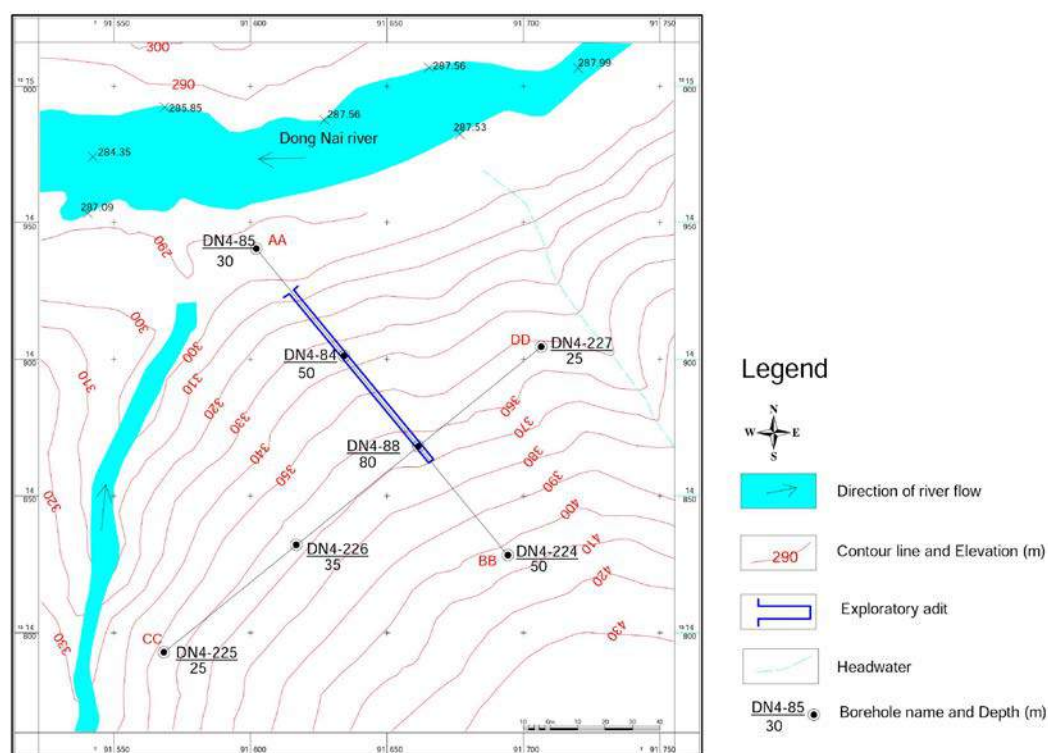


Figure 5: Dong Nai 4-2 exploratory adit (Southern General Investigation Enterprise, 2007)

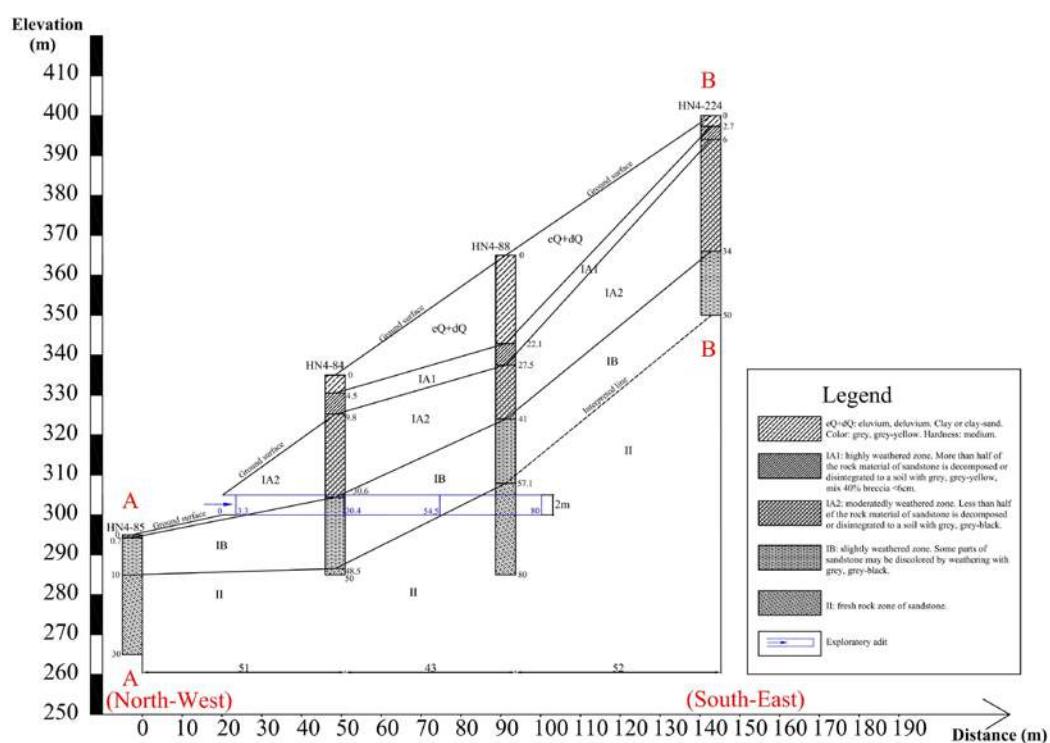


Figure 6: Section of the weathering grade of the Dong Nai 4-2 the exploratory adit

The exploratory adit is divided into each 5m section to evaluate. However, 0-5m is in the highly weathered rock (HW), so the evaluation process is started from 5m.

Considering 5-10m section, the joint distribution is expressed by 3D and 2D models as in Figure 7, and made a statistical table in Table 3. In this section has 30 joints with 6 joint systems. Most of the joint roughness is smooth, but the joint separation is small, causing the infilling such as sandy silt, calcite, and quartz that control entirely the shear strength of the joint, so the joint surfaces are connected together more. However, at the positions where there are many joints cross when the exploratory adit through them, it appears small blocks and wedge-shaped blocks, causing

instability as collapse exploratory adit.

Same for other sections, the joints in the Dong Nai 4-2 exploratory adit are a lot, having 349 joints with 83 joint systems distributing complexly. Most of the joint surfaces in the exploratory adit are smooth, but the separation is small (< 10mm), causing the infilling such as sandy silt, calcite, and quartz that control entirely the shear strength of the joint that obstructs deformation and collapse of the exploratory adit. However, the orientation characteristics are complex, so needing to use the rose diagram and stereonet to have an overview for the joint distribution in the exploratory adit, then evaluating the effects of them on the excavation direction.

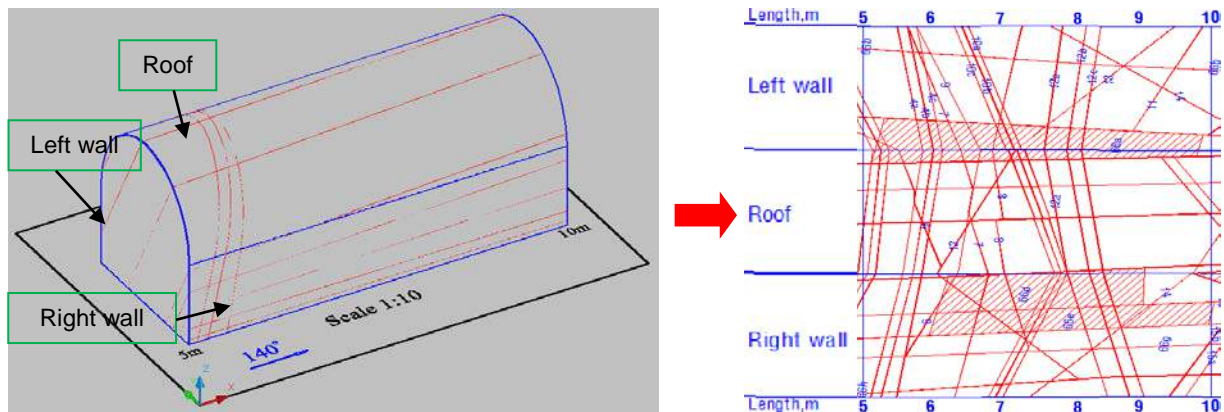


Figure 7: Joint distribution in the 5-10m section

Table 3: Joint characteristics in the 5-10m section

Symbol	Number of joints	Strikes	Dip directions	Dips	Separation (mm)	Roughness	Infillings	Length (m)
4	3	240-245	330-335	75-80	2-3	Smooth	Sand	6.3
5	3	240-245	330-335	65-70	2-3	Smooth	Sand	6.5
6	1	205-210	295-300	30-35	2-3	Smooth	Sand	6.4
7	1	210-215	300-305	70-75	1-2	Smooth	Sand	6.5
8	1	215-220	125-130	70-75	2-5	Smooth	Sand	5.4
9	1	240-245	330-335	55-60	5-10	Smooth	Sand	5.8
10	3	200-205	290-295	65-70	1-2	Smooth	Sand	6.6
11	1	210-215	120-125	60-65	2-5	Smooth	Sand	1.9
12	3	220-225	130-135	75-80	5-10	Smooth	Sand	6.2
13	1	260-265	170-175	45-50	2-5	Smooth	Sand	7.8
14	1	265-270	355-360	35-40	2-5	Smooth	Sand	8.9
15	2	190-195	280-285	65-70	2-3	Smooth	Sand	4.5
23	1	140-145	230-235	80-85	10-20	Smooth	Quartz, sand	18.5
66	8	130-135	40-45	55-65	5-20	Rough	Quartz, sand, calcite	> 20

2.3 Analysis and results

Considering 5-10m section, from the orientation joints in the left wall and the right wall, the results of the rose

diagram and the stereonet are expressed in Figure 8 and Table 4-5.

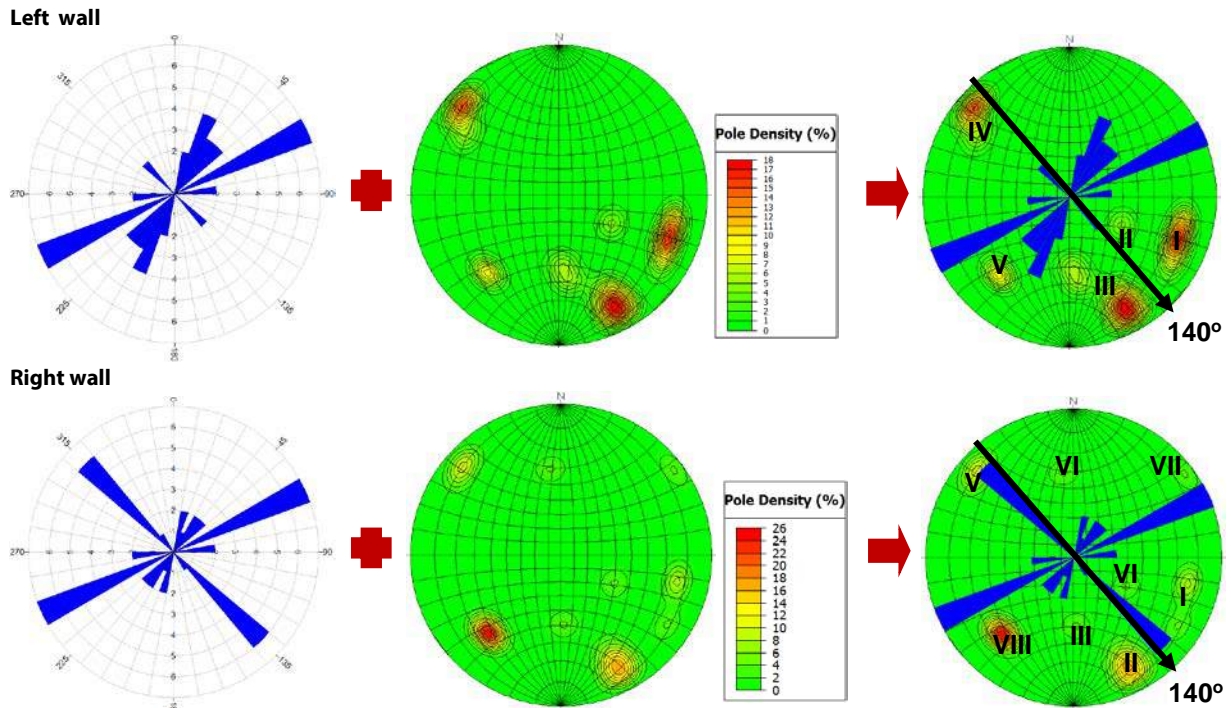


Figure 8: Results of the rose diagram and the stereonet of the 5-10m section

Table 4: Results of the rose diagram and the stereonet of the left wall of the 5-10m section

Development direction of joints	Regions	Density (%)	Dip directions (°)	Dips (°)	140° excavation direction to orientation of joint	Effect of joint on excavation direction
Northeast-Southwest	I	26	290 ± 5	75 ± 5	Perpendicular, drive against	Unfavorable
	II	37	335 ± 5	80 ± 5		
	III	7	300 ± 5	45 ± 5	Perpendicular, drive with	Favorable
Northwest-Southeast	V	9	45 ± 5	65 ± 5	Parallel	Unfavorable

Table 5: Results of the rose diagram and the stereonet of the right wall of the 5-10m section

Development direction of joints	Regions	Density (%)	Dip directions (°)	Dips (°)	140° excavation direction to orientation of joint	Effect of joint on excavation direction
Northeast-Southwest	I	16	285 ± 5	80 ± 5	Perpendicular, drive against	Unfavorable
	II	30	335 ± 5	75 ± 5		
	III	4	360 ± 5	50 ± 5		
	IV	4	300 ± 5	40 ± 5	Perpendicular, drive with	Favorable
Northwest-Southeast	V	12	135 ± 5	80 ± 5		
	VI	4	170 ± 5	50 ± 5	Parallel	Unfavorable
	VII	4	230 ± 5	85 ± 5		
	VIII	26	45 ± 5	65 ± 5		

Through the analysis results of the left wall and the right wall in the 5-10m section, the joints almost develop in the northeast-southwest, the excavation direction is perpendicular to their strikes and driving against with their dips, with density > 50%. So the excavation direction is

unfavorable.

Similar to the joint distribution evaluation in the 5-10m section, through the evaluation of other sections of the Dong Nai 4-2 exploratory adit, the results of the rose diagram and the stereonet are combined as Table 6.

Table 6: Results of the rose diagrams and the stereonets of the sections of the Dong Nai 4-2 exploratory adit

Length (m)	Left wall							Right wall							Results
	Main development direction of joints		Joint density perpendicular to excavation direction		Dip directions (°)	Dips (°)	Effect of joints on exca- vation direction	Main development direction of joints		Joint density perpendicular to excavation direction		Dip directions (°)	Dips (°)	Effect of joints on exca- vation direction	
Main develop- ment direction	To exca- vation direction	Excavation direction to dip directions	Density (%)				Main develop- ment direction	To exca- vation direction	Excavation direction to dip directions	Density (%)					
0-5	—	—	—	—	—	—	—	—	—	—	—	—	—	—	—
5-10	NE-SW	Pe	DW	70	335 ± 5	80 ± 5	Uf	NE-SW	Pe	DW	54	335 ± 5	75 ± 5	Uf	Uf
			DA	21	135 ± 5	75 ± 5				DA	16	135 ± 5	75 ± 5		
10-15	NE-SW	Pe	DW	32	295 ± 5	85 ± 5	F	NE-SW	Pe	DW	32	290 ± 5	75 ± 5	F	F
			DA	51	165 ± 5	85 ± 5				DA	39	165 ± 5	55 ± 5		
15-20	NE-SW	Pe	DW	77	300 ± 5	80 ± 5	Uf	NE-SW	Pe	DW	68	300 ± 5	80 ± 5	Uf	Uf
			DA	0	—	—				DA	6	115 ± 5	40 ± 5		
20-25	NE-SW	Pe	DW	70	320 ± 5	50 ± 5	Uf	NE-SW	Pe	DW	77	320 ± 5	50 ± 5	Uf	Uf
			DA	4	105 ± 5	70 ± 5				DA	0	—	—		
25-30	NE-SW	Pe	DW	67	305 ± 5	85 ± 5	Uf	NE-SW	Pe	DW	63	335 ± 5	80 ± 5	Uf	Uf
			DA	2	130 ± 5	55 ± 5				DA	8	130 ± 5	55 ± 5		
30-35	NE-SW	Pe	DW	84	315 ± 5	75 ± 5	Uf	NE-SW	Pe	DW	100	315 ± 5	75 ± 5	Uf	Uf
			DA	0	—	—				DA	0	—	—		
35-40	NE-SW	Pe	DW	82	315 ± 5	75 ± 5	Uf	NE-SW	Pe	DW	81	315 ± 5	75 ± 5	Uf	Uf
			DA	0	—	—				DA	0	—	—		
40-45	NE-SW	Pe	DW	83	325 ± 5	75 ± 5	Uf	NE-SW	Pe	DW	79	325 ± 5	75 ± 5	Uf	Uf
			DA	0	—	—				DA	0	—	—		
45-50	NE-SW	Pe	DW	79	315 ± 5	85 ± 5	Uf	NE-SW	Pe	DW	78	315 ± 5	85 ± 5	Uf	Uf
			DA	0	—	—				DA	2	170 ± 5	65 ± 5		
50-55	NE-SW	Pe	DW	62	315 ± 5	85 ± 5	Uf	NE-SW	Pe	DW	64	315 ± 5	85 ± 5	Uf	Uf
			DA	12	140 ± 5	85 ± 5				DA	16	140 ± 5	85 ± 5		
55-60	NE-SW	Pe	DW	83	310 ± 5	75 ± 5	Uf	NE-SW	Pe	DW	70	310 ± 5	75 ± 5	Uf	Uf
			DA	0	—	—				DA	6	115 ± 5	85 ± 5		
60-65	NE-SW	Pe	DW	73	295 ± 5	85 ± 5	Uf	NE-SW	Pe	DW	47	315 ± 5	80 ± 5	Uf	Uf
			DA	14	135 ± 5	85 ± 5				DA	24	135 ± 5	85 ± 5		
65-70	NE-SW	Pe	DW	78	315 ± 5	60 ± 5	Uf	NE-SW	Pe	DW	68	310 ± 5	75 ± 5	Uf	Uf
			DA	10	135 ± 5	85 ± 5				DA	18	135 ± 5	85 ± 5		
70-75	NE-SW	Pe	DW	83	315 ± 5	85 ± 5	Uf	NE-SW	Pe	DW	82	135 ± 5	85 ± 5	Uf	Uf
			DA	12	165 ± 5	85 ± 5				DA	8	165 ± 5	85 ± 5		
75-80	NE-SW	Pe	DW	90	315 ± 5	55 ± 5	Uf	NE-SW	Pe	DW	84	310 ± 5	75 ± 5	Uf	Uf
			DA	0	—	—				DA	0	—	—		

NE-SW: Northeast-Southwest
Pe: Perpendicular

DW: Drive with
DA: Drive against

F: Favorable
Uf: Unfavorable

The results show that most of the joints of each section have the main development direction is northeast-southwest. The strikes of these joints are perpendicular and the dips are against the excavation direction, with density > 50%. So the joint distribution almost affects unfavorably on the excavation direction. Except for the excavation direction of the 10-15m section, it is perpendicular to the strikes and driving with the dips of the joints, so the excavation direction is favorable. Therefore, in general, the joint distribution in the Dong Nai 4-2 exploratory adit make the excavation direction is unfavorable.

3. Conclusions

Through the analysis results show that the joint distribution in the Dong Nai 4-2 exploratory adit has the development direction is northeast-southwest and perpendicular to the excavation direction. Most of the dips of these joints are against the excavation direction (140°), with density > 50%. Causing the excavation direction is unfavorable.

Therefore, the solutions are to change to 320° direction is the most favorable. Or have to conduct research and lean detailly about characteristic joints, hydrogeology, RMR, or Q to ensure the projects are stable and favorable.

The research result of the subject has contributed to confirm that is a sensible method to evaluate the effects of the joint distribution of this exploratory adit as well as tunnels in general, and providing a method for the first evaluations of tunnel stability. Making premise for the next research as deformation and tunnel stability quality. And confirming the statistical methods by rose diagram and stereonet, that will support to quickly and easily evaluate the directional factors.

References

1. Barton N. and Choubey V. "The shear strength of rock joints in theory and practice", *Rock Mechanics*, 1977, vol. 10, pp.1-54.
2. Bieniawski ZT. *Engineering rock mass classifications*. Canada, A Willey-Interscience Publication, 1989, 29-91.
3. Power Engineering Consulting Joint Stock Company 2-Southern General Investigation Enterprise. *Project of Dong Nai 4 Hydropower Dam*, Ho Chi Minh City, 2009.
4. Binh.V.H, Hao.P.L. "Hệ thống phân loại đất đá phục vụ cho xây dựng các công trình thủy điện khu vực Tây Nguyên". *Journal of Science and Technology Development*, 2007. Vol. 10, 69-79.
5. John A.Hudson and John P.Harrison. *Engineering rock mechanics-An Introduction to the Principle*. London, Imperial College of Science and Technology and Medicine University, 1989, pp. 114-116.
6. Chich.T.L and Long.H.L. *Địa chất kiến trúc và Đo vẽ bản đồ địa chất và Một số vấn đề cơ bản của Địa kiến tạo*. Ho Chi Minh City, Vietnam National University Press, 2011, pp.146-167.
7. Wickham, G.E., H.R. Tiedemann, and E.H. Skinner. "Support Determination Based on Geologic Predictions". *Proc. Rapid Excav. Tunneling Conf.*, AIME, New York, 1972, pp. 43-64.

VERIFICATION OF THE CORRECTED EMPIRICAL GREEN'S FUNCTION METHOD – EFFECTS OF FREE SURFACE ON FLING STEPS –

Shuanglan Wu, Atsushi Nozu, Yosuke Nagasaka

ABSTRACT

Generally, the near-fault ground motions are characterized by impulsive velocity and/or permanent displacement, which might cause serious damages to near-fault structures. Toward more reliable assessments on seismic response of structures, it is highly required to obtain more precise displacement waveforms including fling-steps. The corrected empirical Green function (EGF) method is advantageous in incorporating site effects precisely and has widely been used in the design of port and airport structures in Japan. It was originally designed to consider only far-field S-wave, however, it was recently modified to include permanent displacements and has been verified for homogeneous full-space (Nozu and Nagasaka, 2017). In this research, we continue their research to verify its applicability to a half space where the near-fault fling-steps are affected by the existence of free-surface. In particular, we are interested in the applicability of the simplified coefficient $FS = 2.0$ to account for the effect of free surface. For this important issue, a comparative study was made for fling step waveforms for typical three types of faults (strike-, dip- and oblique-slip faults) by three different methods: the corrected empirical Green's function method (2017), Hisada's (2003) method and Okada's (1992) method, and the effects of free surface was discussed. It resulted that, the $FS = 2.0$ can't always reflect the effects of free surface on the permanent displacement waveforms, especially for the reverse and oblique fault models, which indicated that further modifications are required.

KEYWORDS: *Near-fault ground motions, Corrected empirical Green's function method, Theoretical Green's function method, Okada's method, fault models*

Shuanglan Wu

Postdoctoral Researcher, Port and Airport Research Institute, Japan (PARI)
Email: u-shu@pari.go.jp, **corresponding author**
Tel: 011-81-46-844-5058

Atsushi Nozu

Director of the Earthquake Disaster Prevention Engineering Division, Port and Airport Research Institute (PARI)
Email: nozu@pari.go.jp
Tel: 011-81-46-844-5058

Yosuke Nagasaka

Researcher, Port and Airport Research Institute (PARI)
Email: nagasaka-y@pari.go.jp
Tel: 011-81-46-844-5058

1. Introduction

Near-fault ground motions often contain strong directivity pulses and permanent ground displacements (fling steps). For example, during the main shock of the 2016 Kumamoto earthquake sequence, strong ground motions with fling steps up to 1.5 m were observed in the

near-source region, which could potentially affect the seismic behaviors of near-fault structures significantly. Thus, it is necessary to consider near-fault ground motions with fling steps in the design of infrastructures.

There are some methods for near-fault ground motion simulations, for example, the theoretical Green function method proposed by Hisada and Bielak (2003), while its application is limited to layered-half space. The analytical solution by Okada (1985, 1992) is widely used, however, it can evaluate only static displacements. On the other hand, the corrected empirical Green function method (Nozu and Sugano, 2008; Nozu et al., 2009) is advantageous in incorporating site effects precisely and it successfully simulated some strong earthquakes, for example, the 1995 Kobe earthquake (Nozu and Sugano, 2008) and the 2011 off the pacific coast of Tohoku earthquake (Nozu, 2012). Based on these results, the method has widely been used in the design of port and airport structures in Japan. The method was originally designed to consider only far-field S-wave, however, it was recently modified to include near-fault fling steps (Nozu and Nagasaka, 2017). Their method uses a correction function, which can be used to introduce near- and intermediate-field terms into Green's functions. Their numerical solutions agreed quite well with the analytical solutions for the displacement time history for a circular fault in an infinite homogeneous elastic medium (Nozu and Nagasaka, 2017). However, their method has not been verified for more complicated situation, i.e., the half space including the free surface, which is closer to the practical condition. In their method, amplification factor of 2.0 (namely $FS = 2.0$) (Boore, 1983) was used to account for the effect of free surface. While main advantage of the assumption lies in its simplicity, the value might not be applicable depending on various incident angles and wave types (SH or SV waves). In order to investigate this issue, a comprehensive verification of this method was conducted in this study. A comparative study was made for fling step waveforms for typical three types of faults (strike-, dip- and oblique-slip faults) by three different methods: the corrected empirical Green's function method (2017), Hisada's (2003) method and Okada's (1992) method and the effects of free surface will be discussed.

2. Methodology

In this section, we briefly describe the method by Nozu and Nagasaka (2017), where the corrected empirical Green's function (EGF) method (Nozu and Sugano, 2008; Nozu et al., 2009) was modified to include near- and intermediate-field terms, based on complete solutions for elastic wave field.

The corrected empirical Green's function method (Nozu and Sugano, 2008; Nozu et al., 2009) can be summarized as follows: Firstly, it considers a small earthquake occurring on the fault plane of the target earthquake and obtains the ground motions at the target sites (which are called the "Green's functions"). Secondly, based on the same superposition method as the conventional Empirical green's function method (Irikura et al., 1997), the green functions are superimposed to evaluate ground motions

caused by the large earthquake according to the fault model of the large earthquake.

The Green's functions are calculated as the inverse Fourier transform of the spectrum $F(f)$ at a target site. $F(f)$ is represented by Eq. (*):

$$F(f) = \left| \frac{R_s \cdot FS \cdot PRTITN_s}{4\pi\rho\beta^3} \cdot M_0 \cdot \frac{(2\pi f)^2}{1+(f/f_c)^2} \right| \frac{1}{r} \exp(-\pi f r / Q_s \beta) |G(f)| \frac{O(f)}{|O(f)|_p} \quad (*)$$

where, R_s is the radiation coefficient of S-wave, FS is the amplification factor accounting for the effects of free-surface, $PRTITN_s$ is the reduction factor that accounts for the partitioning of S-wave energy into two horizontal components, ρ is the density of seismological bedrock, M_0 is the seismic moment of the small earthquake, f_c is the corner frequency of the small earthquake, and Q_s is the Q value of S wave. $|G(f)|$ is the site amplification factor, $O(f)$ is the Fourier transform of a record of small earthquake, and $|O(f)|_p$ is its amplitude, processed through a Parzen window with a band width of 0.05 Hz (Nozu and Sugano, 2008). More details could be obtained in Nozu and Nagasaka (2017).

Generally, in terms of FS , the simplified value of $FS = 2.0$ has conventionally been used to account for the effects of free surface in the field of engineering seismology. However, investigation is needed in terms of whether such simplified expression for the effects of free surface is suitable for calculating fling-step displacements. Thus, this study was focused on how to consider the effects of free surface within the framework of the corrected empirical Green's function method. Because the results should be verified by the analytical solutions, the site-specific

amplification and phase characteristics have not been considered in this study.

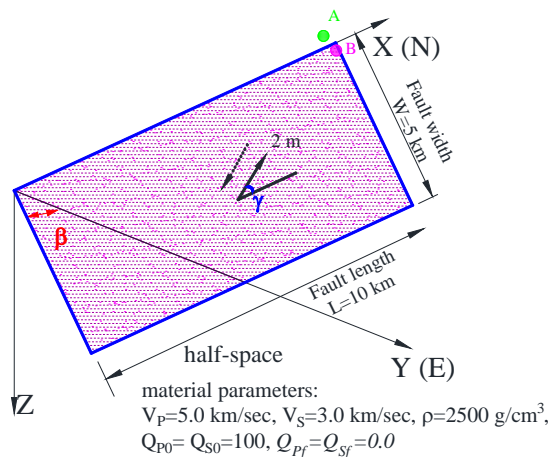
3. Verification

When Nozu and Nagasaka (2017) applied the corrected empirical green function method to near-fault ground motions, they simply used the value of $FS = 1.0$ because their target was a homogeneous full-space. In this study, we are interested in the applicability of the simplified coefficient $FS = 2.0$ to account for the effects of free surface. To investigate this issue, we investigated three typical types of faults, the strike-slip (rake 0°), oblique-slip (rake 45°) and dip-slip (rake 90°) faults under various dip angles.

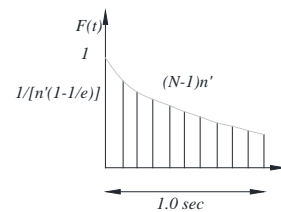
We assumed a fault model with 10km long and 5km wide, embedded in a homogeneous half -space with the parameters listed in Figure 1 (a). The dip angle was varied from 15° to 90° with an interval of 15° . The slip-velocity function for the corrected EGF method and Hisada's method are listed in Figure 1 (b) and (c), separately. The fault parameters are summarized in Table 1. The displacement waveforms including fling steps for two near-fault observation sites (named A and B, 0.1 km away from the surface fault trace as shown in Figure 1 (a)) are synthesized by the corrected EGF method and compared with the results by Okada's (1985, 1992) method and Hisada's (2003) method.

Table 1 Fault parameters for verification

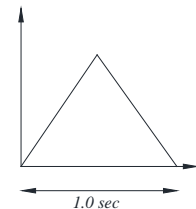
M_0 (dyne.cm)	Strike ($^\circ$)	Dip β ($^\circ$)	Rake γ ($^\circ$)	Length (km)	Width (km)	Rise time (s)
1.1225×10^{25}	0	$15 \sim 90$	0, 45, 90	10.0	5.0	1.0



(a) Fault model with various dip- and rake-angle



(b) Slip velocity function for the corrected EGF method



(c) Slip velocity function for Hisada's method

Figure 1 fault model and 2 observation sites in the near fault area

Due to the limited spaces, only the comparisons of displacement waveforms for the strike-slip fault with the dip

angle of 90° and the dip-slip fault with the dip angle of 45° are shown in Figure 2 and Figure 3.

The good agreements among these three methods for the strike-slip fault in Figure 2 well demonstrated that the FS value of 2.0 can well approximate the effects of free-surface in the half-space; the slight differences between the corrected EGF method and Hisada's method are due to the difference of the slip velocity functions (as shown in Figure

1 (b) and (c)) used in the calculation. However, for the dip-slip fault model, remarkable differences were observed between the results of the corrected EGF method and the analytical solutions (Okada method) as shown in Figure 3, both for the foot wall site (Figure 3 (a)(b)) and the hanging wall site (Figure 3 (c)(d)).

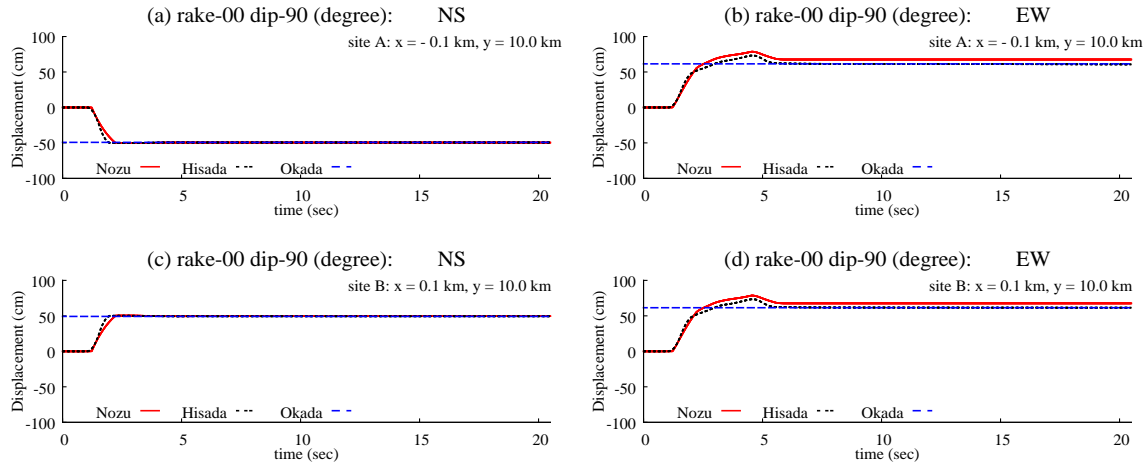


Figure 2 displacement waveforms for strike-slip fault with dip angle 90°

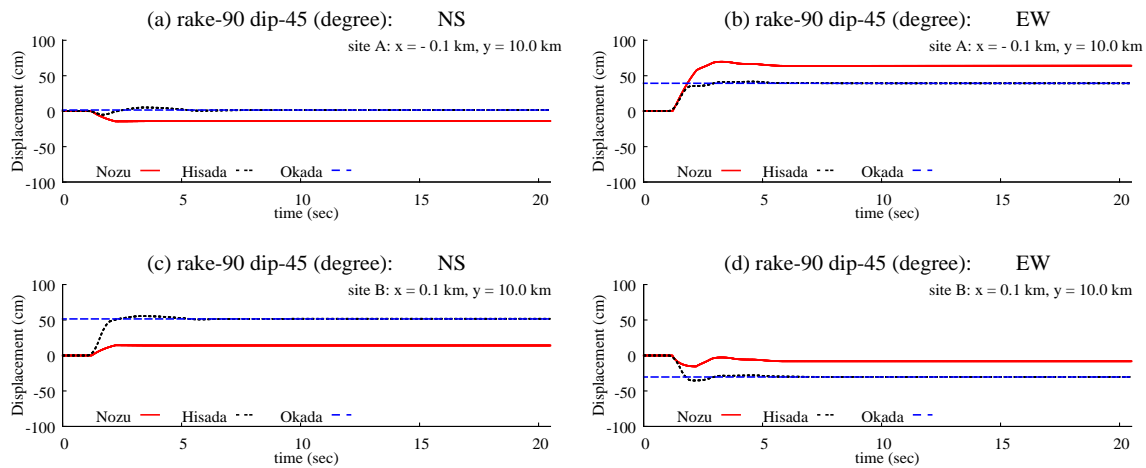


Figure 3 displacement waveforms for dip-slip fault with dip angle 45°

In order to make clear the applicability of the simplified value of FS=2.0 for typical types of faults, the strike-slip (rake 0°), oblique-slip (rake 45°) and dip-slip (rake 90°) faults, the differences of permanent displacement for all the cases calculated in this analysis between the corrected EGF method and Okada's method are presented in Figure 4, which illustrated the following:

(1) For the strike-slip fault, as shown by the red lines in Figure 4 (a) and (b), good agreement between the two methods was found both for the sites located on the hanging wall and foot wall both for the NS and EW components; the difference between the methods was within 10 cm.

(2) For the dip-slip fault, as shown by the magenta lines, the EW and NS components exhibited different tendencies. For the EW-component, the difference increased with the increasing dip angles, both for the sites on the foot wall and

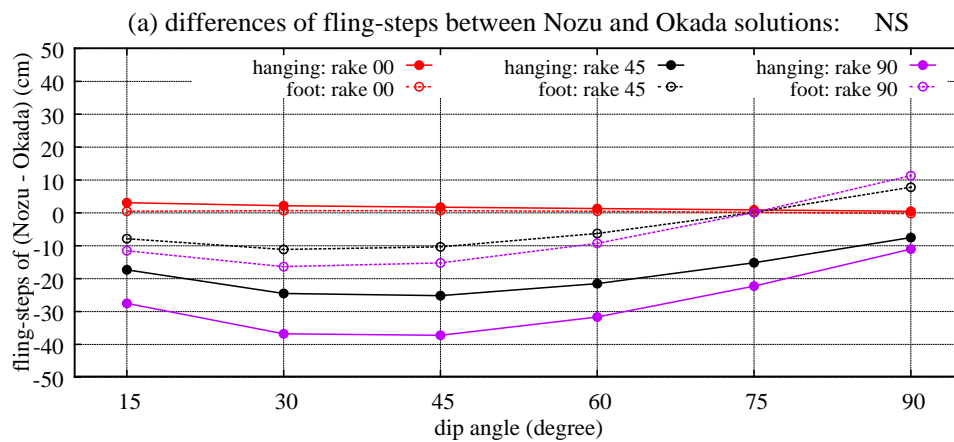
hanging wall; the largest differences were greater than 30cm and slightly different in between the hanging wall and foot wall sites as shown in Figure 4 (b). On the other hand, for the NS-component, the greatest difference of 38cm was found for the dip angle of 45°. For this case, the corrected EGF method with the FS value of 2.0 remarkably underestimated the fling-steps for the hanging wall site while overestimated for the foot wall site.

(3) For the oblique-slip fault, as shown by the black lines in Figure 4 (a) and (b) the tendency was between the strike-slip and dip-slip faults.

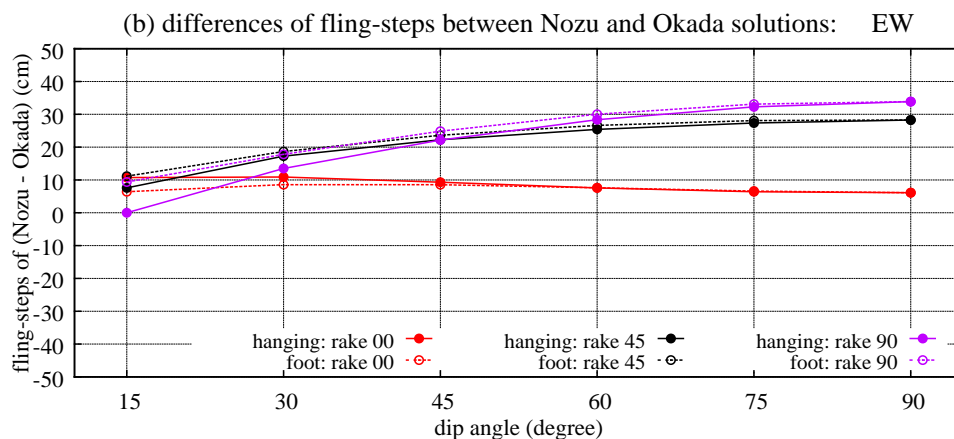
Theoretically speaking, the amplification due to the existence of free surface is strictly equal to 2.0 for the SH waves, while it takes a different value for the SV and P waves, which also depends on the incident angle. For the strike slip case, the FS value of 2.0 lead to good results because the SH waves are predominant in this case, while

the discrepancy was significant for the dip slip case because the SV and P waves are predominant in this case.

Based on the results above, the simplified FS value of 2.0 could not correctly reflect the effects of free-surface on the fling-steps in the half-space.



Note: the positive difference stands for underestimated and negative differences shows overestimated for foot wall site and inverse for hanging wall by Nozu method as compared with analytical solutions.



Note: the positive difference stands for overestimated and negative differences shows underestimated for foot wall site and inverse for hanging wall by Nozu method as compared with analytical solutions.

Figure 4 the differences of permanent displacement between the corrected EGF method and Okada's method

4. Conclusions

In this study, we continue to verify the corrected empirical green's function method for near-fault ground motions including fling steps in the half-space, where the fling steps are affected by the existence of the free-surface. In particular, we were interested in exploring the applicability of the conventional FS value of 2.0 to fling-step displacement. Comparisons of the fling-steps with the results of two other methods (Hisada's and Okada's methods) were conducted for three typical types of faults under various dip angles. The result indicated that the FS = 2.0 could well approximate the effects of free surface on fling-steps for the strike-slip faults; while it is not suitable for oblique-slip and dip-slip faults. It is presumably due to the fact that the amplification due to the existence of free surface is strictly equal to 2.0 for the SH waves, while it takes a different value for the SV and P waves, which also depends on the incident angle.

The site-specific amplification and phase characteristics have not been considered in this study, which will be considered in the future research; and new FS value will be proposed in the future research.

Acknowledgement

We would like to express our gratitude to program for homogeneous half-space by analytical method, which is open in the link: http://www.bosai.go.jp/study/application/dc3d/DC3Dhtm1_J.htm and Professor Hisada of Kogakuin University for his open program of the theoretical Green's function.

References

1. Okada, Y., (1985). *Surface deformation due to shear and tensile faults in a half-space*, Bull. Seism. Soc. Am., 75 (1985) 1135-1154.
2. Okada, Y., (1992). *Internal deformation due to shear and tensile faults in a half-space*, Bull. Seism. Soc. Am., 82 (1992) 1018-1040.
3. Boore DM., (1983). *Stochastic simulation of high-frequency ground motions based on seismological*

- models of the radiated spectra*. Bull Seism Soc Am 73 (1983) 1865–1894.
4. Hisada, Y, and J. Bielak, (2003). *A Theoretical Method for Computing Near-Fault Strong Motions in Layered Half-Space Considering Static Offset due to Surface Faulting, with a Physical Interpretation of Fling Step and Rupture Directivity*, Bull. Seism. Soc. Am 93(3) (2003) 1154-1168.
 5. Nozu, A. and Y. Nagasaka, (2017). *Verification of the empirical Green's function method with near-field and intermediate-field terms*. [Online]. Available: <http://www.pari.go.jp/bsh/jbn-kzo/jbn-bst/taisin/research_jpn/research_jpn_2017/jr_51.pdf> . (in Japanese)
 6. Nozu, A., T. Nagao and M. Yamada, (2009). *Simulation of strong ground motions using empirical site amplification and phase characteristics - modification to incorporate causality-*, Journal of JSCE (A), Vol. 65(3) (2009) 808-813. (in Japanese with English abstract)
 7. Irikura, K., T. Kagawa and H. Sekiguchi, (1997). *revision of the empirical Green's function method by Irikura (1986)*, Programme and abstracts, the Seismological Society of Japan, No. 2, B25. (in Japanese)
 8. Nozu, A. and T. Sugano, (2008). *Simulation of strong ground motions based on site-specific amplification and phase characteristics- accounting for causality and multiple nonlinear effects*, Technical note of the port and airport research institute, No. 1173 (2008) (in Japanese with English abstract)
 9. Nozu, A. (2012). *A super asperity model for the 2010 Off the Pacific coast of Tohoku earthquake*. Journal of JAEE, 12 (2012) 221-240. (in Japanese with English abstract)

STUDY, ANALYSIS AND ASSESS EFFECTIVENESS OF SOFT SOIL IMPROVEMENT USING PVD COMBINE VACUUM PRELOADING AT HYOSUNG VINA CHEMICALS PROJECT AT BA RIA VUNG TAU PROVINCE, VIET NAM BASED ON MONITORED RESULTS AND SOIL INVESTIGATION BEFORE AND AFTER GROUND IMPROVEMENT.

**Phan Thanh Tien¹⁾ and Nguyen Tan Son²⁾ Dang Hoang Thai³⁾ Dao Ba Linh⁴⁾
Tran Van Dung⁵⁾ Hoang Minh Phuong⁶⁾ Tran Thanh Vu⁷⁾ Luu Ba Giap⁸⁾
Truong Thanh Can⁹⁾ Nguyen Van Tinh¹⁰⁾ Nguyen Phu Tay¹¹⁾**

(1) Phan Thanh Tien, General Director of GeoSmart Consultants JS Company (GeoSmart).
Email: geosmartco@yahoo.com; Website: geosmart.vn; Handphone: (+84)93 212 8081

(2) Nguyen Tan Son, General Director of Nam Mien Trung Co, Ltd.
Email: nammientrungltd@gmail.com; sondct43@gmail.com; Handphone: (+84) 918428273

(3) Dang Hoang Thai Director- Branch of inspection engineering of Binh Phuoc Construction Department
thaibk92@gmail.com; Handphone: (+84) 903 000 198

ABSTRACT

This paper reports on geotechnical monitoring results of pore- pressure and study engineering geology inspection by in-situ: Field Vane Shear Test, and in lab test results. Study and analysis collected data could be assess Degree of Consolidation after treatment and also effect of ground improvement, comment and analysis causes of disagreement or/and difference achieved results rate of consolidation and basic for reasonable data selection.

KEYWORDS: settlement, soft clay, soil improvement, PVD, surcharge, vacuum, Monitoring.

CONTENT

1. INTRODUCTION:

Harmony in the trend of economic development of the sea in Southern Vietnam, Hyosung Vina Chemicals port in Cai Mep, Ba Ria, Vung Tau is under constructions stage.

Soft ground improvement method using Prefabricated Vertical Drains (PVD) combined preloading surcharge is used commonly in more than a recent in Viet Nam especially in southern VietNam. However the challenges for soft soil treatment for Hyosung Vina Chemicals Project are overlaid on very soft marine clay with thickness about 12m very low shear strength and very high water content over 100% with organic approximately 10%; filling height: + 5.5m from ground level; Insufficiency of fine sand source and requirement of short time consolidation; complicated in controlling stability protection of inside project area may cause as a side of project face to a long with very deep Thi Vai Cai Mep riverbank.

Thus Soft ground improvement method using Prefabricated Vertical Drains (PVD) combined preloading surcharge is not used and PVD combined vacuum is adapted and adopted for Hyosung Vina Chemicals Project. Three main aspects of tests will be presented, and namely, instrumentation and field investigation geotechnical program (FVST, SPT), calculation of consolidation settlement and testing of soil properties to see the difference before and after ground improvement.

2. SITE NATURAL CONDITIONS

2.1. Location:

Hyosung Port Vina Chemicals is located in Cai Mep Industrial Zone, Tan Phuoc Commune, Tan Thanh District, Ba Ria - Vung Tau Province.



Figure 2: Location: Hyosung Port Vina Chemicals

2.2. Topographic features:

The surface site before construction is the flooded area and was influent by both tidal area and regional navigation system (Figure 2).

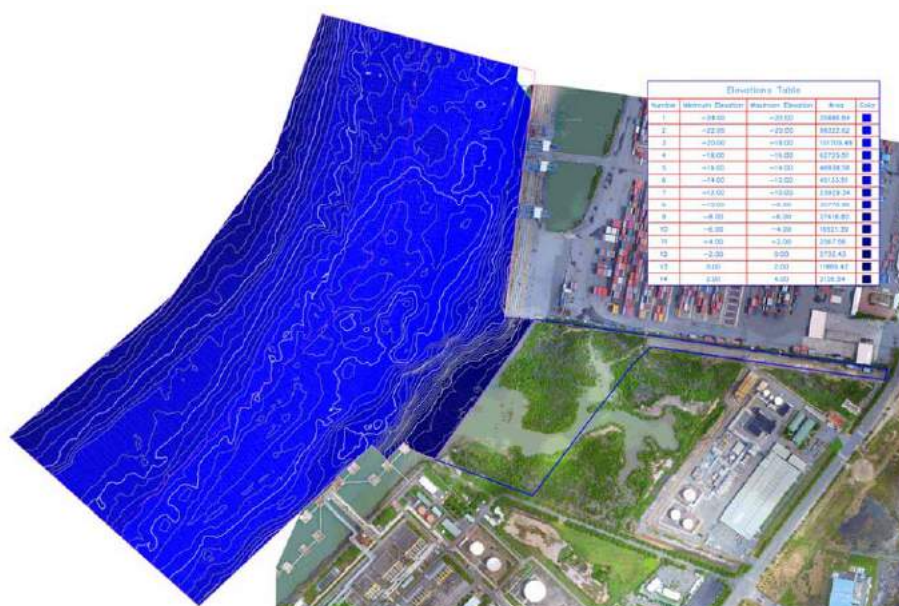


Figure 3: Topographic project site

2.3. Climate conditions:

Monsoon tropical climate, divided into two distinct seasons: rainy season, hot, humid, from May to October; dry season, cold from November to April.

3. GROUND IMPROVEMENT WORKS

Soil profile at project site as details:

3.1. Geology condition at Project site

Layer 1: (CH, MH) Clay with organic, dark grey, bluish grey, very soft, the depth of about 10m; thickness about 5-18m and vary on project site area: Container ground yard Area near Hyosung Factory varies from 10 to 18m soft clay thickness, offshore area near jetty varies from 5 to 8m soft clay thickness

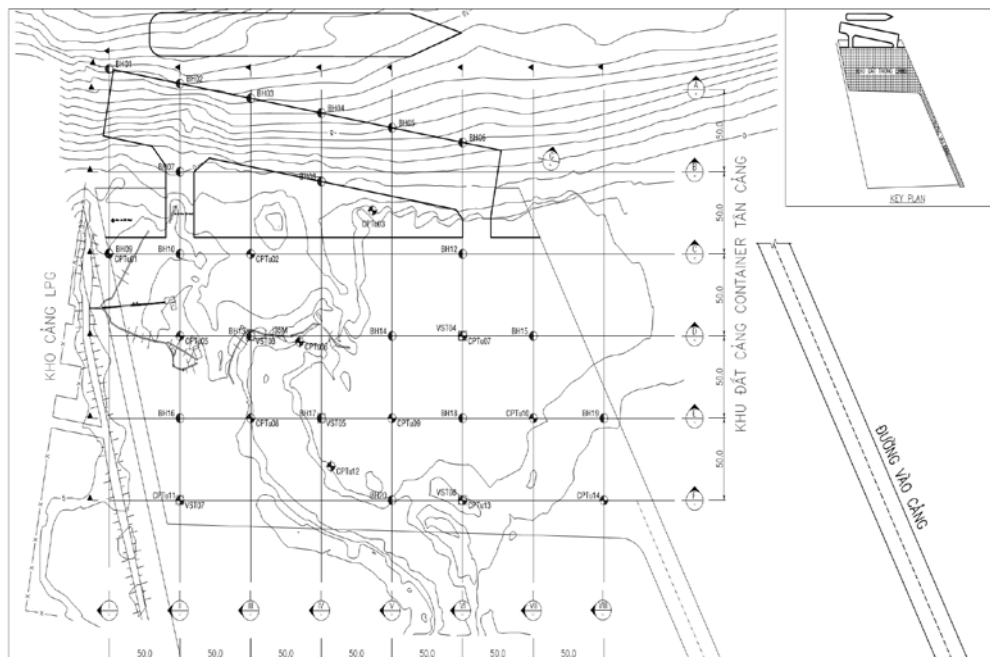
Layer 2: Underlying layer 1 to the depth of about 43m, thickness about 38m (SM,SC) Silty sand, clayey sand, yellowish grey, whitish grey, dark grey, reddish brown, loose to medium dense, very loose at somewhere.

Layer 3: (CH) Clay, yellowish grey, bluish grey, stiff, the depth of about 45m, thickness about 2m

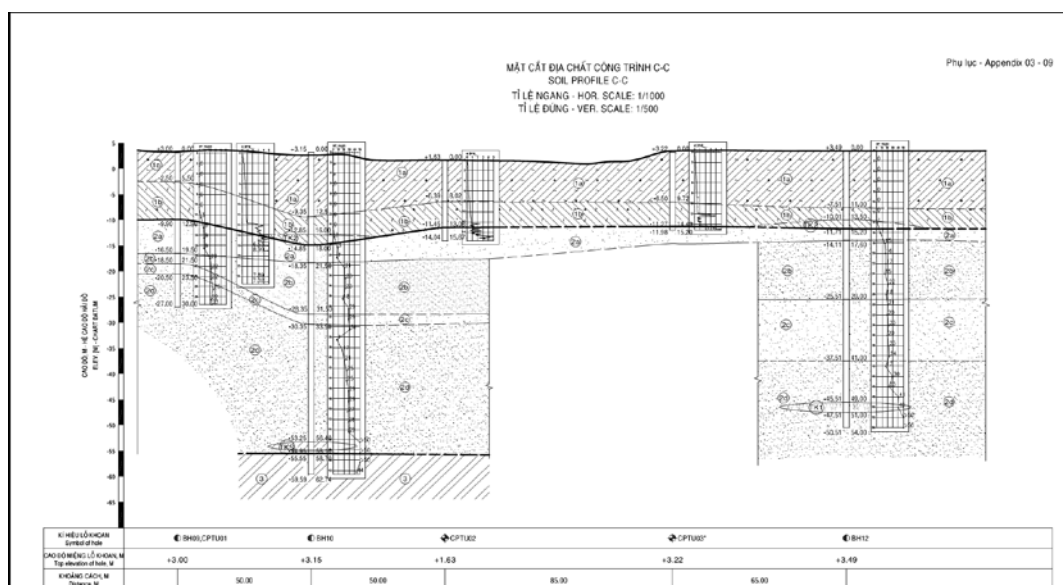
Layer R1: Weathered Granite, bluish grey, whitish grey, dark grey (RQD<75%).

Layer R2: Fresh Granite, bluish grey, whitish grey, dark grey (RQD>75%).

Soil profile and soil properties obtained from soil investigation in this stage (Portcoast Geo, 2016 & 2017) are generalized in Figure 4



Distribution of soft soil thickness on site is shown in Figure 5



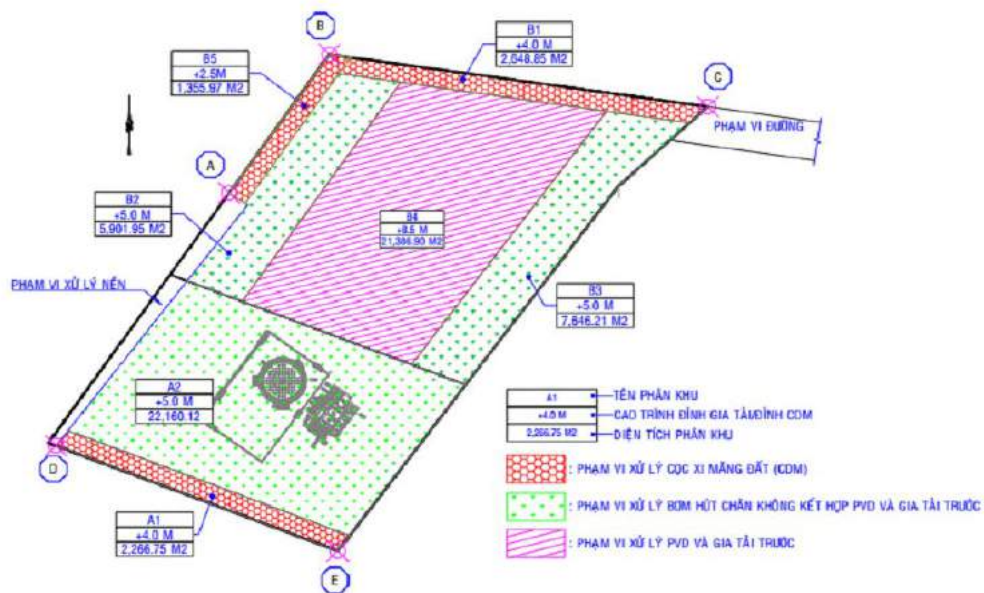
Soil properties		Unit	Layer							
			1a	1b	2a	2b	2c	2d	3	5
Grain size	Clay	%	64.8	64.2	18.7	13.5	14.1	6.4	34.7	-
	Silt	%	34.3	34.1	8.4	7.5	13.4	11.3	54.8	-
	Sand	%	0.9	1.7	72.6	78.2	72.5	81.6	10.5	-
	Gravel	%	-	-	0.3	0.8	-	0.7	-	-
Wet density (γ_w)		g/cm ³	1.45	1.48	1.97	2.05	2.02	2.04	2.07	2.70
Moisture Content (w)		%	97.6	88.9	21.1	16.3	18.1	15.1	24.8	0.2
Liquid limit (LL)		%	92.8	92.0	-	-	-	-	72.4	-
Plastic limit (PL)		%	37.5	35.1	-	-	-	-	29.2	-
Plasticity index (PI)		-	55.4	56.9	-	-	-	-	43.2	-
Specific gravity (Gs)		-	2.67	2.67	2.67	2.67	2.67	2.67	2.69	2.72
Void ratio (e)		-	2.645	2.397	0.640	0.515	0.556	0.506	0.621	0.008
Shear strength										
Direct shear test	c	kPa	-	-	2.2	2.2	1.5	2.0	-	-
	ϕ	(°)	-	-	27°00'	29°20'	29°40'	33°30'	-	-
	c_1 ($\alpha=0.95$)	kPa	-	-	0.7	0.2	0.0	0.0	-	-

Soil properties		Unit	Layer							
			1a	1b	2a	2b	2c	2d	3	5
	ϕ_I ($\alpha=0.95$)	(°)	-	-	26°00'	28°40'	29°00'	32°50'	-	-
	c_{II} ($\alpha=0.85$)	kPa	-	-	1.3	0.9	0.0	0.0	-	-
	ϕ_{II} ($\alpha=0.85$)	(°)	-	-	26°20'	28°50'	29°10'	33°10'	-	-
UC Strength, q_u (UC test)		kPa	21.0	27.5	-	-	-	-	-	-
Undrained shear strength, s_u (UU test)		kPa	13.8	14.6	-	-	-	-	-	-
UC Strength for rock		MPa	-	-	-	-	-	-	-	82.6
Compression characteristics										
Consolidation test										
Compression index C_c		-	0.923	0.767	-	-	-	-	-	-
Recompression index C_r		-	0.182	0.125	-	-	-	-	-	-
Swelling index C_s		-	0.155	0.132	-	-	-	-	-	-
Coeff. of consol, C_{v90}	OC	m ² /yr	5.4	5.0	-	-	-	-	-	-
	NC	m ² /yr	1.2	1.3	-	-	-	-	-	-

No	Name of works	Purpose of monitoring works	Quantities
1	Surface Settlement plate monitoring	Settlement monitoring on surface of improved soil layers	22
2	Extensometer monitoring	Settlement monitoring at each varies depths	6
3	Piezometer monitoring	Pore pressure in improved soil layers	6
4	Water level underground monitoring	Underground water level monitoring during ground improvement stage	6
5	Inclinometer monitoring	Inclination monitoring a long with thickness of improved soft soil layer	12

3.2. Detail ground improvement works

Site ground area of project as Figure 6

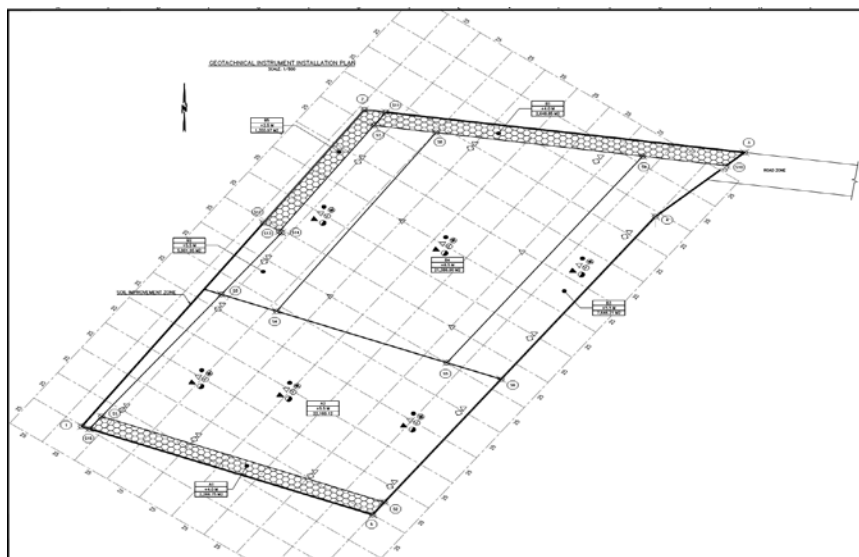


Site plan was surcharged 1.5m for convenience of PVD and CDM construction. Yard area was improved by PVD with 1x1m into bed of layer 1

3.3. Geotechnical monitoring works

Geotechnical monitoring works started from April 2018 to September 2018 with detail quantities as below:

Figure 7. Plan of monitoring system



3.4. Re- field soil investigation:

Perform with works as: Drilling, sampling, Vane shear test and in- lab test: physical& mechanical properties index, Incremental Loading Consolidation Test, Constant Rate of Strain Consolidation Test, UU Triaxial Shear Strength Test, CIU Triaxial Shear Strength Test with Pore Pressure Measurements.

Figure 8. Field soil investigation after treatment
Drilling and sampling works after ground improvement



Field vane shear test after ground improvement

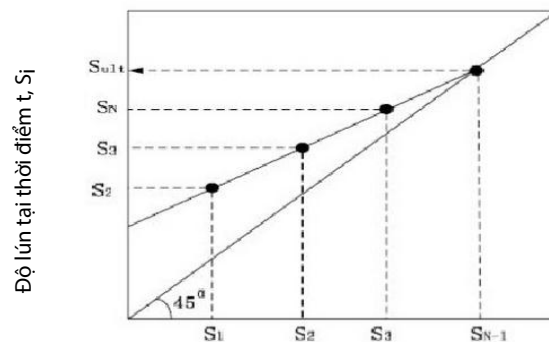
4. ASSESS DEGREE OF CONSOLIDATION AFTER GROUND IMPROVEMENT:

Assess Degree of Consolidation after ground improvement using some methods as below as:

4.1. Assess Degree of Consolidation on ground surface settlement data

4.1.1. Asaoka Method

- Based on the monitoring data, the final settlement estimate was calculated using the Asaoka method. The nature of this method is as follows:
 - Asaoka demonstrated that if monitoring curve was divided into many S_i points with equal time intervals, when the axis of the graph with the horizontal axis is S_{i-1} and the vertical axis is S_i , the points are straight lines. This is only true when the working load is constant, which can be as follows:



Settlement at t-1, S_{i-1}

Figure 9: Modeling diagrams by Asaoka method

- The final settlement is the intersection between the points and the line connecting the 45 degree angle.

No./ STT	S. plate/ Tên bàn lún	Asaoka method/ Tính toán bằng pp Asaoka				
		S (m)	S_r (m)	S_f (m)	U (%)	U_{ave} %
1	S18	0.369	0.394	0.025	93.73%	92.75 %
2	S10A	0.435	0.468	0.033	92.96%	
3	S13	0.387	0.423	0.036	91.56%	

4.1.2. Hyperbolic Method

Hyperbolic Method for Predicting Final Settlement

Tan et al. (1991) proposed a hyperbolic relationship between monitored settlement (s) and consolidation time (t), which includes two linear segments

$$s = \frac{t}{\alpha + \beta t} \quad \text{or} \quad \frac{t}{s} = \alpha + \beta t \quad (2)$$

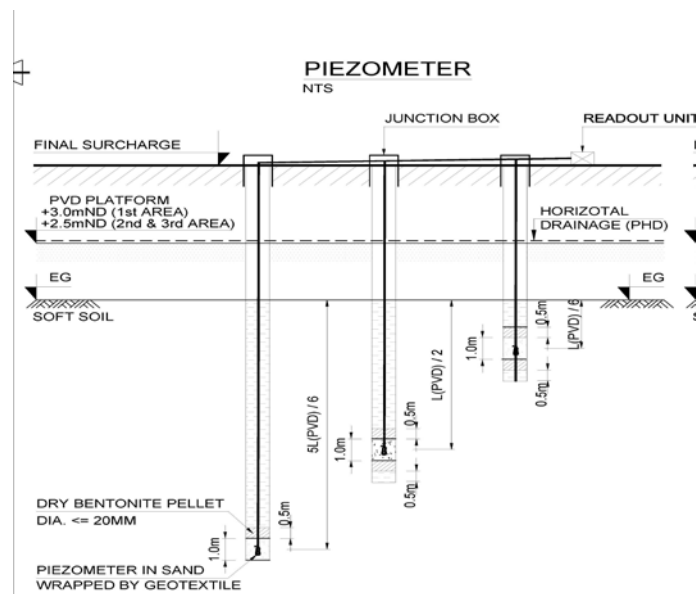
Hence the ultimate (or final) settlement s_f was defined as

$$\lim_{t \rightarrow \infty} s = \lim_{t \rightarrow \infty} \frac{1}{\frac{\alpha}{t} + \beta} = s_f = \frac{1}{\beta} \quad (3)$$

Where α and β are the intercept and the slope of the initial linear line.

Settlement no S10A	1. Parameter		2. Ultimate (Final) settlement S_F	S_F (mm)	Average degree of consolidation
	α : intercept of a straight line in t/sversust plot;	0.1857	3. Settlements at time t_i	S_{t_i} (mm)	
	β : slope of a straight line int/sversust plot	0.0049	4. Degree of consolidation	U (%)	
Settlement no S13	1. Parameter		2. Ultimate (Final) settlement S_F	S_F (mm)	
	α : intercept of a straight line in t/sversust plot;	0.1039	3. Settlements at time t_i	S_{t_i} (mm)	
	β : slope of a straight line int/sversust plot	0.0037	4. Degree of consolidation	U (%)	
Settlement no S18	1. Parameter		2. Ultimate (Final) settlement S_F	S_F (mm)	
	α : intercept of a straight line in t/sversust plot;	0.0579	3. Settlements at time t_i	S_{t_i} (mm)	
	β : slope of a straight line int/sversust plot	0.0023	4. Degree of consolidation	U	

4.2. Evaluation of cohesion rate based on the results of monitoring of pore water pressure and groundwater level



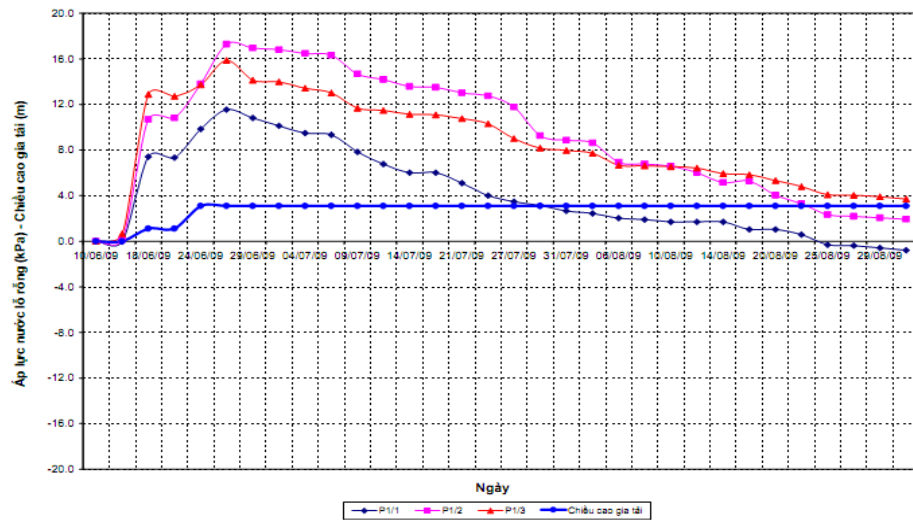


Fig 10. : Install piezometer and Chart of pore pressure(illustration)

Surplused pore water pressure is increased by the Remaining load process and gradually dissipating in the value of "0" when the consolidation reaches 100%.

✓ Cohesion rate as pore pressure $UWP\% = (CS_{max} - EPWP) / CS_{max} * 100\%$

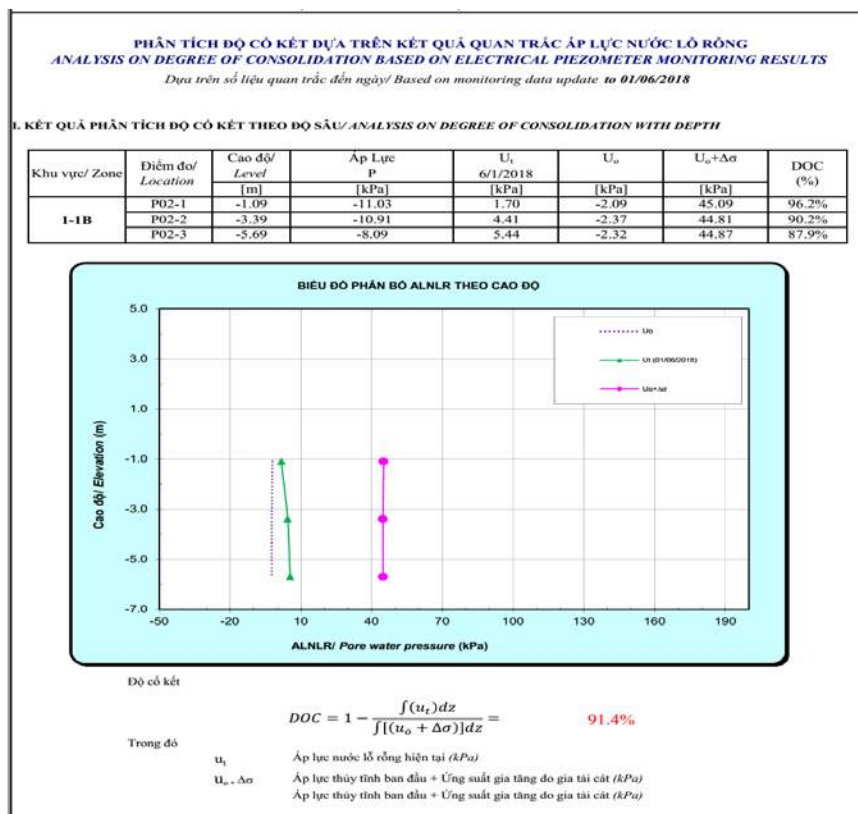
Where: CS_{max} : Max cohesion pressure

EPWP: Surplus pore pressure

EPWP = PWP – SWP.

PWP: Pore pressure

SWP: static pressure

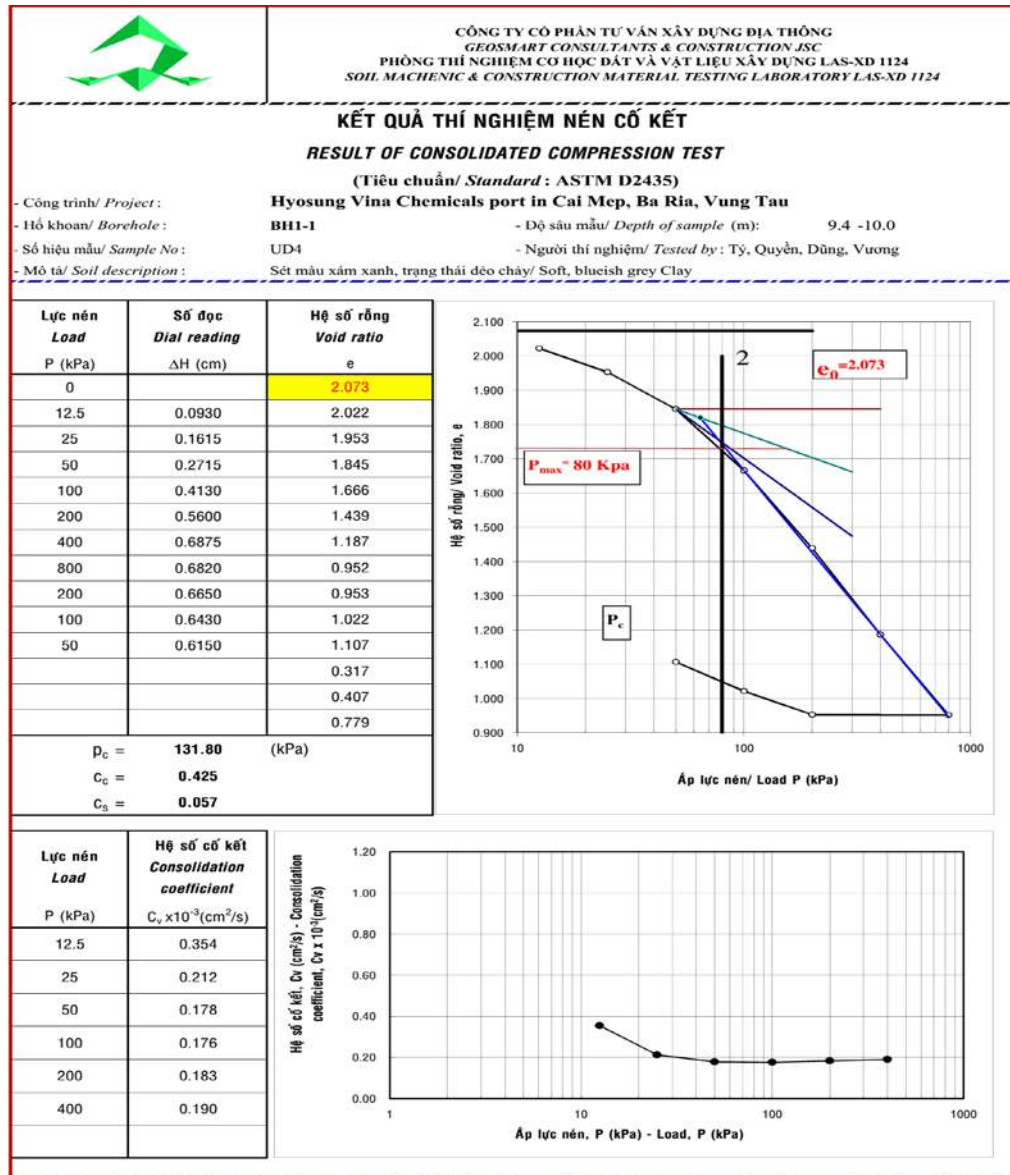


4.3. Assess Degree of Consolidation on ground surface settlement data using in lab test

$$Q = \frac{e_0 - e_t}{e_0 - e_c}$$

$$Q = \frac{2.073 - 1.784}{2.073 - 1.72} = 93.39\%$$

- e_0 : natural pore pressure
- e_t : Natural pore pressure after ground improvement
- e_c : Estimated pore pressure bear completed surcharge load and live load



**Chart of natural pore pressure of soil before ground improvement
And attach surcharge load & live load (Pmax)**

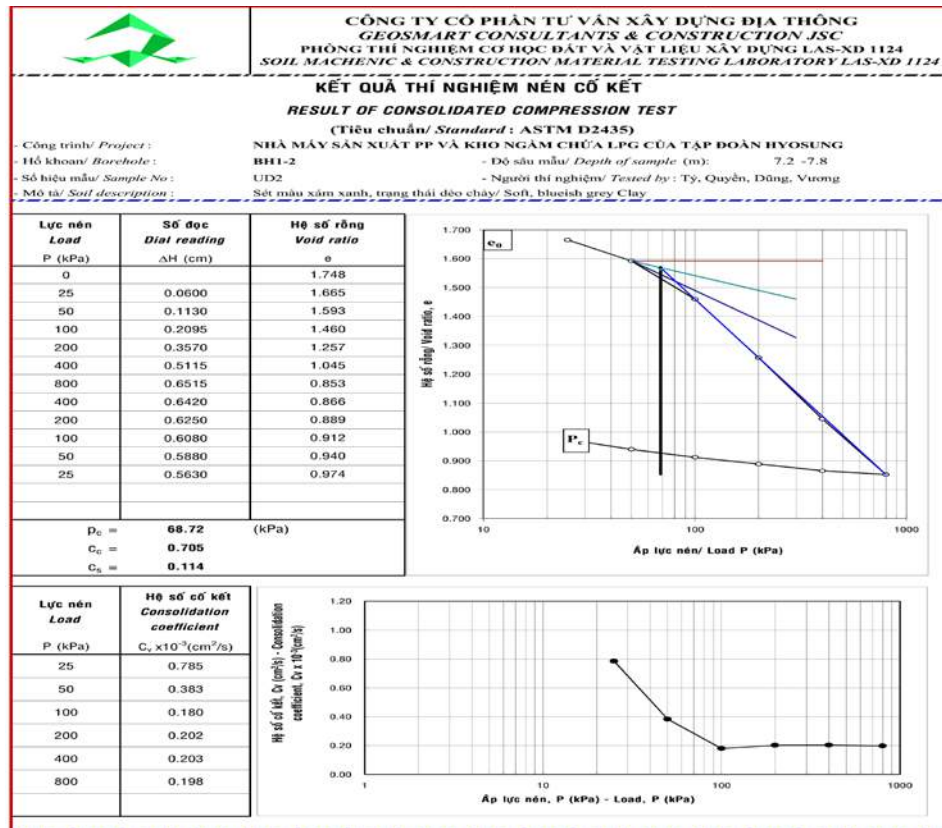


Chart of natural pore pressure of soil after ground improvement

5. OEDOMETETER TEST RESULTS OF SOIL AFTER GROUND IMPROVEMENT TO FIGURE OUT ULTIMATE SERVICE LOAD.

The oedometer tests are not only for the determination of maximum pass pressure, but also used for the comparison with the operation load, in addition, is used for determination of secondary settlement coefficient to check the residual settlement. Detail results are shown on the Appendice



CÔNG TY CỔ PHẦN TƯ VẤN XÂY DỰNG ĐỊA THÔNG/ GEOSMART CONSTRUCTION CONSULTANT JSC
PTN Cơ học đất & Vật Liệu xây dựng Las- XD 1124 / Soil mechanic & Construction material testing laboratory No 1124
ISO 9001:2008
DC/ Add: 26 Đường 711, KP2, P. Phú Hữu, Q.9, TP.HCM
ĐT/ Tel: (+84) 93 212 8081; (+84) 90 887 9089

Công trình: Cảng Hóa chất của tập đoàn Hyosung Vina

Project: Hyosung Vina Chemicals Port

Gói thầu/ Package: Xử lý nền/ Soil improvement

Địa điểm: KCN Cái Mép, Huyện Tân Thành, Tỉnh Bà Rịa - Vũng Tàu

Location: Cai Mep Industrial Zone, Tan Thanh District, Ba Ria - Vung Tau Province

Vị trí/ Point	BH01	BH02	BH03	BH04	BH05	BH06
Cao độ thiết kế/ Designed elevation, z (m)	5.500	5.500	5.500	5.500	5.500	5.500
Cao độ đỉnh lớp xử lý/ Elevation of Top of soil treatment, (zf) (m)	0.109	-0.400	-0.980	-0.330	0.860	0.330
Bề dày đắp/ Fill elevation (z-zf) (m)	5.391	5.900	6.480	5.830	4.640	5.170
Tải trọng đắp/ Fill load (z-zf)*18, (kPa)	97.038	106.200	116.640	104.940	83.520	93.060
Hoạt tải/ live load (kPa)	20.000	20.000	20.000	20.000	20.000	20.000
Tải kết cấu áo bãi bề dày 0.2m /load of road arrangement facilities with thickness: 0.2m, (kPa)	4.500	4.500	4.500	4.500	4.500	4.500
Cao độ mực nước ngầm tĩnh ban đầu / Static Ground water level, (zw) (m)	3.046	3.046	3.046	2.678	2.678	1.633
Đẩy nổi/ Buoyant Density (zw-zf)*9.81, (kPa)	-28.78	-33.77	-39.45	-29.48	-17.82	-12.77
Tải khai thác/ Service load, (kPa)	92.76	96.93	101.69	99.96	90.20	104.79
Tải trọng bên trên đất yếu/ Load above Soft soil	72.76	76.93	81.69	79.96	70.20	84.79
Ứng suất hiện hữu trên mặt/ Effective pressure at surface (kPa)	64.82	70.63	64.95	73.12	77.58	82.63

6. RESIDUAL SETTLEMENT DURING OPERATION

Summary on the residual settlement consisting of primary and secondary settlement are shown in the below table:

Vị trí mẫu/ Location of Sample	Bề dày Thickness	Độ sâu Depth	Dung trọng đáy nổi/ Buoyant Density	Thông số cố kết Consolidation Parameters				Ứng suất hiệu hữu Effective Presssure	Tải gia tăng incremental load	Tải khai thác Service load	Lún cố kết Consolidati on settlement	Lún từ biển Secondary settlement
				CR	RR	Pc	Cae					
	(m)	(m)	(KN/m ³)			(kPa)		(kPa)	(kPa)	(kPa)	(m)	(m)
	4.00	2.00	6.08	0.255	0.047	118.5	0.001645	76.98	22.94	99.92	0.0213	0.0106
BH01-1-UD3	4.00	6.00	6.08	0.255	0.047	118.5	0.008925	101.30	22.94	124.24	0.0167	0.0573
	5.20	10.60	6.08	0.255	0.047	118.5	0.008925	129.27	22.94	152.20	0.0941	0.0735
TỔNG ĐỘ LÚN DƯ (20 NĂM), cm Residual Settlement (20 Years)	27.34										0.1320	0.1414

Vị trí mẫu/ Location of Sample	Bề dày Thickness	Độ sâu Depth	Dung trọng đáy nổi/ Buoyant Density	Thông số cố kết Consolidation Parameters				Ứng suất hiệu hữu Effective Presssure	Tải gia tăng incremental load	Tải khai thác Service load	Lún cố kết Consolidati on settlement	Lún từ biển Secondary settlement
				CR	RR	Pc	Cae					
	(m)	(m)	(KN/m ³)			(kPa)		(kPa)	(kPa)	(kPa)	(m)	(m)
BH02-2-UD3	6.90	3.45	6.04	0.376	0.038	184.1	0.01316	91.47	21.30	112.77	0.0238	0.1459
	2.20	8.00	8.00			184.1	0	123.41	21.30	144.71		0.0000
	1.00	9.60	6.04	0.376	0.038	184.1	0.00133	134.64	21.30	155.94	0.0024	0.0021
TỔNG ĐỘ LÚN DƯ (20 NĂM), cm Residual Settlement (20 Years)	17.43										0.0263	0.1481

Vị trí mẫu/ Location of Sample	Bề dày Thickness	Độ sâu Depth	Dung trọng đáy nổi/ Buoyant Density	Thông số cố kết Consolidation Parameters				Ứng suất hiệu hữu Effective Presssure	Tải gia tăng incremental load	Tải khai thác Service load	Lún cố kết Consolidati on settlement	Lún từ biển Secondary settlement
				CR	RR	Pc	Cae					
	(m)	(m)	(KN/m ³)			(kPa)		(kPa)	(kPa)	(kPa)	(m)	(m)
	3.00	1.50	6.35	0.425	0.057	131.8	0.01275	74.47	6.84	81.31	0.0065	0.0616
BH03-3-UD3	3.00	4.50	6.35	0.425	0.057	131.8	0.01275	93.52	6.84	100.36	0.0052	0.0616
	2.60	7.30	6.35	0.425	0.057	131.8	0.001995	111.30	6.84	118.14	0.0038	0.0084
TỔNG ĐỘ LÚN DƯ (20 NĂM), cm Residual Settlement (20 Years)	14.71										0.0156	0.1315

Page 2

RESIDUAL SETTLEMENT FOR ZONE A2- HYOSUNG PORT

Vị trí mẫu/ Location of Sample	Bề dày Thickness	Độ sâu Depth	Dung trọng đáy nổi/ Buoyant Density	Thông số cố kết Consolidation Parameters				Ứng suất hiệu hữu Effective Presssure	Tải gia tăng incremental load	Tải khai thác Service load	Lún cố kết Consolidati on settlement	Lún từ biển Secondary settlement
				CR	RR	Pc	Cae					
	(m)	(m)	(KN/m ³)			(kPa)		(kPa)	(kPa)	(kPa)	(m)	(m)
	4.00	2.00	6.04	0.374	0.023	226.4	0.000805	85.20	21.84	107.04	0.0091	0.0052
BH04-4-UD4	4.00	6.00	6.04	0.374	0.023	226.4	0.000805	109.36	21.84	131.20	0.0073	0.0052
	3.30	9.65	6.04	0.374	0.023	226.4	0.000805	131.41	21.84	153.25	0.0051	0.0043
TỔNG ĐỘ LÚN DƯ (20 NĂM), cm Residual Settlement (20 Years)	3.61										0.0215	0.0146

Vị trí mẫu/ Location of Sample	Bề dày Thickness	Độ sâu Depth	Dung trọng đáy nổi/ Buoyant Density	Thông số cố kết Consolidation Parameters				Ứng suất hiệu hữu Effective Presssure	Tải gia tăng incremental load	Tải khai thác Service load	Lún cố kết Consolidati on settlement	Lún từ biển Secondary settlement
				CR	RR	Pc	Cae					
	(m)	(m)	(KN/m ³)			(kPa)		(kPa)	(kPa)	(kPa)	(m)	(m)
	4.00	2.00	6.02	0.29	0.028	104.1	0.00098	89.62	7.62	97.24	0.0040	0.0063
BH05-5-UD3	3.00	5.50	6.02	0.29	0.028	104.1	0.01015	110.69	7.62	118.31	0.0252	0.0487
	3.30	8.65	6.02	0.29	0.028	104.1	0.01015	129.66	7.62	137.28	0.0237	0.0536
TỔNG ĐỘ LÚN DƯ (20 NĂM), cm Residual Settlement (20 Years)	16.15										0.0529	0.1086

Vị trí mẫu/ Location of Sample	Bề dày Thickness	Độ sâu Depth	Dung trọng đáy nổi/ Buoyant Density	Thông số cố kết Consolidation Parameters				Ứng suất hiệu hữu Effective Presssure	Tải gia tăng incremental load	Tải khai thác Service load	Lún cố kết Consolidati on settlement	Lún từ biển Secondary settlement
				CR	RR	Pc	Cae					
	(m)	(m)	(KN/m ³)			(kPa)		(kPa)	(kPa)	(kPa)	(m)	(m)
	3.00	1.50	6.02	0.277	0.062	107.7	0.00217	91.66	17.16	108.82	0.014	0.010
BH06-6-UD3	3.00	4.50	6.02	0.277	0.062	107.7	0.009695	109.72	17.16	126.88	0.052	0.046
	2.50	7.25	6.02	0.277	0.062	107.7	0.009695	126.28	17.16	143.44	0.038	0.038
TỔNG ĐỘ LÚN DƯ (20 NĂM), cm Residual Settlement (20 Years)	19.97										0.105	0.095

Page 3

RESIDUAL SETTLEMENT FOR ZONE A2- HYOSUNG PORT

The residual settlement after 20 years with both the primary and secondary settlement at the inspection area Zone A2 are: 27.34 cm; 17.43cm; 14.71cm; 3.61cm;16.15cm and 19.97 cm lesser than the allowable residual settlements in 20 years: ≤ 30cm

BACK ANALYSIS OF SOME CHARACTERISTICS OF SOIL AFTER GROUND IMPROVEMENT

When and after ground improvement, some characteristics of soil will be improved/increased usefully as: Shear strength, density, Pre-consolidation pressure (Pc), Effective pressure at surface (kPa), service load of ground, degree of consolidation; Some characteristics of soil will be lower/decreased in useful trend as: water content, void ratio/ pore pressure; liquid limited and plastic limit, Compression index...

6.1. Reduction of water content, liquid limit (%), Plastic limit (%)

Changes in water content can be estimated based on field settlement data (Stamatopoulos and Kotzias, 1985) as follows:

$$\Delta w_n = - \left(w_n + \frac{1}{G} \right) \frac{\delta}{h}$$

where w_n , Δw_n are the original and change of natural water content; G is the special gravity of soil grains, δ is the settlement under preloading, and h is the thickness of compressible soils.

Fig. 11 Illustrated the reduction of water content with depth for test embankment after 160 days of preloading compared with the mean values of the initial water contents. The back calculated values of water content from settlements after treatment are also plotted in Fig. 11 for test embankment and are good agreement with the measured water content data.

Moisture content (%)	
LBH03 VS BH1-1	
Before SI	After SI
20.80	27.80
79.70	75.40
77.90	68.80
77.10	67.50
86.10	
24.90	28.70
LBH02 VS BH1-2	
Before SI	After SI
20.80	17.60
69.70	64.50
77.30	58.40
69.40	57.60
68.30	
20.90	18.50

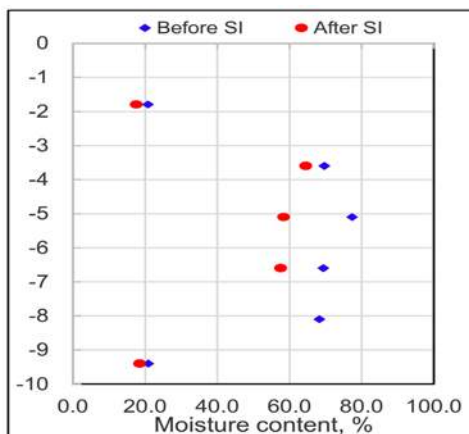
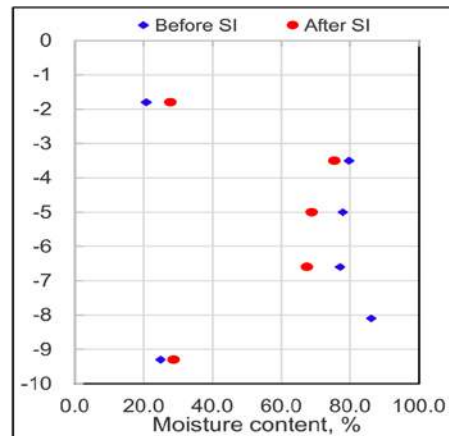
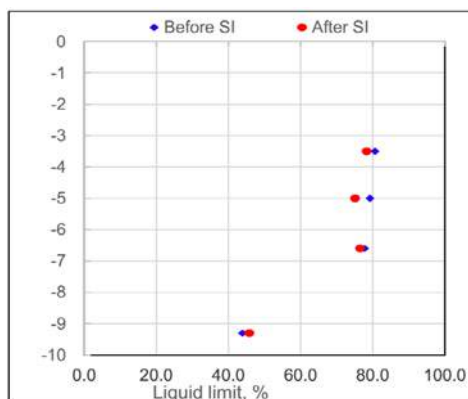
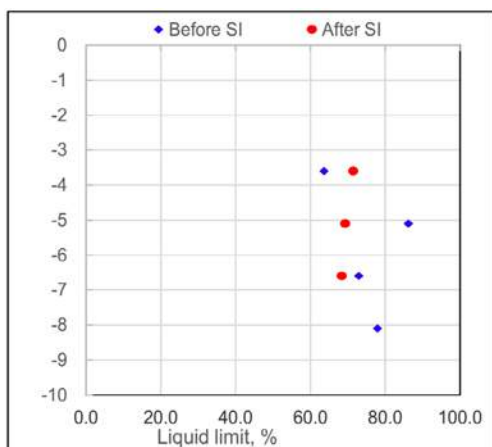
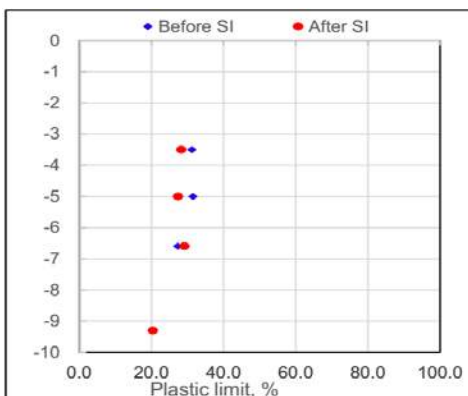


Fig. 6-6 Back-calculated water content from settlements

ZONE 1-1 LBH03 VS BH1-1		
Liquid limit (%)		% Difference
Before SI	After SI	
80.60	78.34	3%
79.20	75.14	5%
77.70	76.49	2%
43.90	45.80	-4%

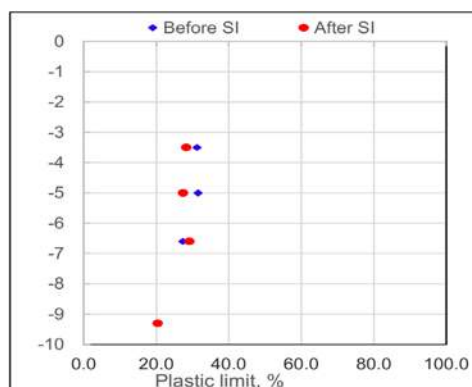


Plastic limit (%)		% Difference
ZONE 1-1		
Before SI	After SI	
31.20	28.30	9%
31.50	27.40	13%
27.30	29.19	-7%
20.50	20.40	0%



ZONE 1-2, LBH02 vs BH1-2		
Liquid limit (%)		
Before SI	After SI	% Difference
63.60	71.43	-12%
86.20	69.30	20%
72.90	68.40	6%
77.90		

ZONE 1-2, LBH02 vs BH1-2		
Plastic limit (%)		
Before SI	After SI	% Difference
27.10	25.23	7%
33.60	23.10	31%
27.90	20.80	25%
27.60		



6.2. Reduction of pore pressure (void ratio)

Void ratio, ZONE 1-1 LBH03 VS BH1-1		
Before SI	After SI	% Difference
2.073	1.748	-19%
2.136	1.965	-9%
2.096	1.880	-11%
2.077	1.825	-14%
0.680	0.776	12%

6.3. Increase in undrained shear strength

The increase in undrained shear strength, S_u , was predicted by the SHANSEP technique (Ladd 1991) as follows:

$$\left(\frac{S_u}{\sigma'_{vo}} \right)_{OC} = \left(\frac{S_u}{\sigma'_{vo}} \right)_{NC} OCR^m$$

where OCR is the over consolidation ratio; σ'_{vo} is the effective overburden pressure; and NC and OC denote normally consolidated and over-consolidated, respectively. Changes in un-drained shear strength can also be estimated from the following equations based on field settlement data (Stamatopoulos and Kotzias, 1985):

$$\Delta S_u = \left(\frac{1 + w_n G}{0.434 C_c} \right) S_u \frac{\delta}{h}$$

where S_u , ΔS_u are the original and change of un-drained shear strength; w_n , Δw_n are the original and change of natural water content; G is the special gravity of soil grains, C_c is the coefficient of compressibility, δ is the settlement under preloading, and h is the thickness of compressible soils.

The increase in un-drained shear strength, S_u , was also obtained from piezocone penetration tests as follows:

$$S_u = \frac{q_t - \sigma_{vo}}{N_{kt}}$$

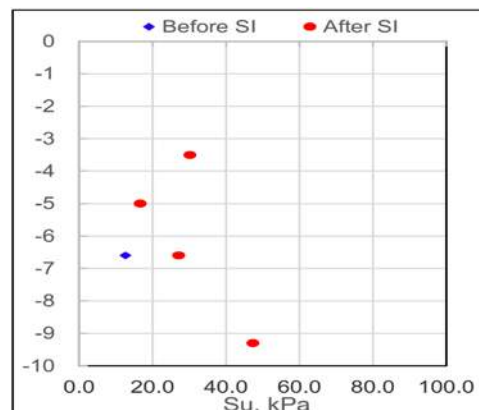
where q_t is the corrected cone resistance; σ_{vo} is the total overburden stress, N_{kt} is the cone factor

($N_{kt} = 12$ for soft clay in this area). The increase of shear strength can be estimated from the SHANSEP technique (Eq. *). In this project, the SHANSEP equation can be obtained from field vane shear test, oedometer test and constant rate of strain (CRS) test as follows:

$$\frac{S_u}{\sigma'_{vo}} = 0.215 * OCR^{0.805}$$

LBH03 VS BH1-1

Su (kPa)	
Before SI	After SI
	30.16
	16.62
12.60	27.08
	47.32



LBH02 VS BH1-2

Su (kPa)	
Before SI	After SI
	57.46
	19.20
13.70	16.64
	42.30
	25.60

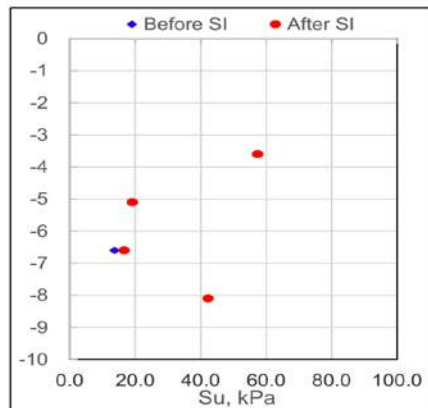
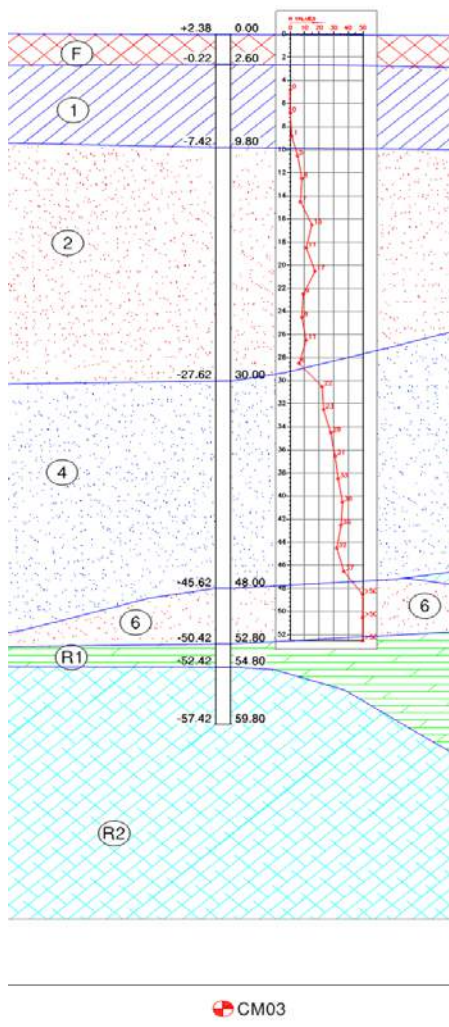


Fig. 6-7 un-drained shear strength

6.4. SPT Numbers prior and after ground improvement

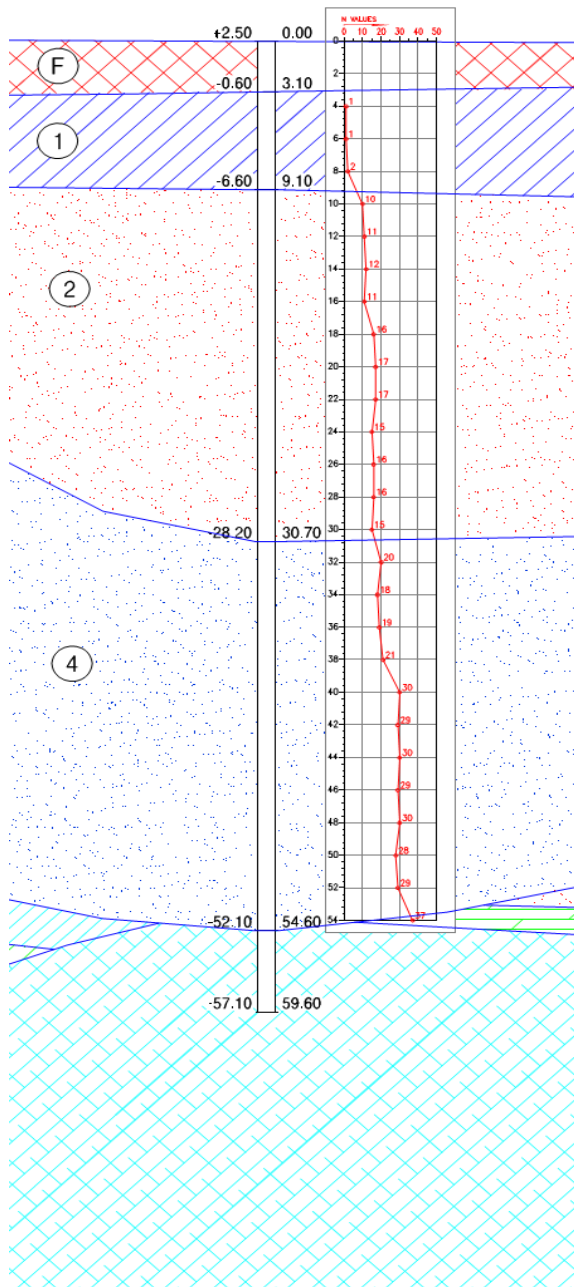
6.4.1. Based on N_{SPT} values before and after ground improvement

LBH03 VS BH1-1



HÌNH TRỤ HỒ KHOAN BOREHOLE LOG									
CÔNG TRÌNH (Project): PP PRODUCTION PLANT AND LPG FACTORY OF HYOSUNG CORPORATION									
GỢI THẦU (Package): SOIL IMPROVEMENT									
ĐỊA ĐIỂM (Location): KCN Cái Mep, Tỉnh Bà Rịa - Vũng Tàu					ĐỘ SÂU MỨC NƯỚC NGẦM (Depth of ground water):				
HỒ KHOAN SỐ (Borehole No): BH1-1					NGÀY KHOAN (Date): 11-05-2018				
CHIỀU SÂU HỒ KHOAN (Total depth of hole): 14.00m					TỌA ĐỘ (Co-ordinates): X: 1165245.809				
CAO ĐỘ (Elevation): 5.412m					Y: 421887.187				
ĐỘ SÂU DEPTH (m)	ELEVATION CAO ĐỘ (m)	ĐỘ SÂU THICKNESS (m)	MẬT ĐỘ SOIL GRAPH 1:100	SỐ HIỆU MẪU SAMPLE NUMBER	MÔ TẢ ĐẤT SOIL DESCRIPTION	THÍ NGHIỆM XUYẾN TIÊU CHUẨN: STANDARD PENETRATION TEST (SPT)			
						15 cm	15 cm	15 cm	BIỂU ĐỒ GRAPH
0	5.412								
1									
2									
3									
4									
5									
6									
7									
8									
9									
10									
11									
12									
13									
14									
15									
16									
17									
18									

LBH02 VS BH1-2



CM02

HÌNH TRỤ HỒ KHOAN BOREHOLE LOG									
CÔNG TRÌNH (Project): PP PRODUCTION PLANT AND LPG FACTORY OF HYOSUNG CORPORATION									
GÓI THẦU (Package): SOIL IMPROVEMENT									
ĐỊA ĐIỂM (Location): KCN Cui Mep, Tinh Ba Ria - Vung Tau					ĐỘ SÂU MỨC NƯỚC NGẦM (Depth of ground water):				
HỒ KHOAN SỐ (Borehole No): BH1-2					NGÀY KHOAN (Date): 11-05-2018				
CHIỀU SÂU HỒ KHOAN (Total depth of hole): 12.00m					TỌA ĐỘ (Co-ordinates): X: 1185432.923				
CAO ĐỘ (Elevation): 5.539m					Y: 421887.437				
ĐỘ SÂU DEPTH (m)	ELEVATION CAO ĐỘ (m)	ĐỘ DÀY THICKNESS SỐ CẤP ĐỘ ĐÀT SOIL GRADE 1/100	SỐ HIỆP AN SAMPLE NUMBER	ĐỘ SÂU LẤY MẪU & THÍ NGHIỆM SPT DEPTH OF SAMPLE & SPT TEST	MÔ TẢ ĐẤT SOIL DESCRIPTION	THÍ NGHIỆM XUYẾN TIÊU CHUẨN STANDARD PENETRATION TEST (SPT)			
						15 cm	15 cm	15 cm	BIỂU ĐỒ GRAPH
0	0.00								
1	5.539								
2	3.50				Cát san lấp, màu nâu vàng Yellowish brown filling sand				
3	2.039								
4	1.30				Sét màu xám xanh, trạng thái dẻo cứng Stiff, bluish grey Clay				
5	0.739				Cát hạt thô màu nâu vàng, kết cấu rời rạc Loose, yellowish brown Coarse sand				
6	-0.561								
7									
8	4.60				Sét màu xám xanh, trạng thái dẻo cứng Stiff, bluish grey Clay				
9									
10									
11	-5.161				Sét xám trắng, nâu đỏ, dẻo cứng Clay				
12	-5.761				Cát pha xám trắng, nâu đỏ, cứng Hard, whitish grey, reddish brown Clayey sand				
13	-6.461				Kết thúc hố khoan tại độ sâu 12.0m Finished borehole at the depth of 12.0m				
14									
15									
16									
17									
18									

6.4.2. Based on natural water values before and after ground improvement

KẾT QUẢ QUAN TRẮC MỰC NƯỚC NGẦM MONITORING RESULT FOR GROUND WATER LEVEL							
Dự án: Nhà máy sản xuất PP và kho ngầm chứa LPG của tập đoàn Hyosung							
Project: PP Production Plant and LPG Cavern Project of Hyosung Corporation							
Địa điểm: Khu công nghiệp Cái Mép, Huyện Tân Thành, Tỉnh Bà Rịa - Vũng Tàu							
Location: Cai Mep Industrial zone, Tan Thanh District, Ba Ria - Vung Tau Province							
Giếng số/ Well No.	W02 vs BH1-1		Vị trí/ Location:		X (m)	1165235.826	
Ngày lắp đặt/ Installed date	12/30/2017				Y (m)	421789.177	
STT/ No.	Ngày/ Date	Thời gian/ Time	Số đọc/ Reading (m)	Cao độ đỉnh ống/ Tube Elevation (m)	Cao độ mực nước Ele. of g. water level (m)	Cao độ nền Fill Elv. (m)	Ghi chú/ Remark
1	03/01/2018	11:00	1.13	4.358	3.23	3.228	
2	04/01/2018	10:00	1.10	4.358	3.26	3.258	
3	05/01/2018	15:00	1.13	4.355	3.23	3.225	
4	06/01/2018	14:00	1.70	5.375	3.68	3.680	
5	07/01/2018	16:00	1.70	5.370	3.67	3.672	
6	08/01/2018	10:00	1.70	5.375	3.68	3.675	
7	09/01/2018	15:00	1.70	5.352	3.65	3.650	
8	10/01/2018	9:00	1.05	5.352	4.30	4.302	
9	11/01/2018	10:00	1.07	5.373	4.30	4.303	
10	12/01/2018	14:00	2.02	6.250	4.23	4.230	
11	13/01/2018	16:00	1.80	6.255	4.46	4.455	
12	14/01/2018	10:00	1.34	6.255	4.92	4.915	
13	15/01/2018	9:30	1.34	6.256	4.92	4.916	
14	16/01/2018	14:00	1.26	6.239	4.98	4.979	
15	17/01/2018	10:00	1.24	6.245	5.01	5.005	
16	18/01/2018	14:00	0.93	6.236	5.31	5.306	
17	19/01/2018	15:00	1.89	7.250	5.36	5.360	
18	20/01/2018	15:00	1.97	7.262	5.29	5.292	
19	21/01/2018	15:00	2.08	7.252	5.17	5.172	
20	22/01/2018	15:00	2.17	7.147	4.98	4.977	
21	23/01/2018	15:00	1.65	7.145	5.50	5.495	
22	24/01/2018	10:00	2.49	7.236	4.75	5.950	
23	25/01/2018	9:30	2.65	7.235	4.59	5.940	
24	26/01/2018	10:00	2.74	7.022	4.28	5.949	
25	27/01/2018	9:30	2.73	7.225	4.50	5.925	
26	28/01/2018	11:25	2.79	7.223	4.43	5.933	
27	29/01/2018	9:00	2.77	7.126	4.36	5.936	

KẾT QUẢ QUAN TRẮC MỰC NƯỚC NGẦM MONITORING RESULT FOR GROUND WATER LEVEL							
Dự án: Nhà máy sản xuất PP và kho ngầm chứa LPG của tập đoàn Hyosung							
Project: PP Production Plant and LPG Cavern Project of Hyosung Corporation							
Địa điểm: Khu công nghiệp Cái Mép, Huyện Tân Thành, Tỉnh Bà Rịa - Vũng Tàu							
Location: Cai Mep Industrial zone, Tan Thanh District, Ba Ria - Vung Tau Province							
Giếng số/ Well No.	W02 vs BH1-1		Vị trí/ Location:		X (m)	1165235.826	
Ngày lắp đặt/ Installed date	12/30/2017				Y (m)	421789.177	
STT/ No.	Ngày/ Date	Thời gian/ Time	Số đọc/ Reading (m)	Cao độ đỉnh ống/ Tube Elevation (m)	Cao độ mực nước Ele. of g. water level (m)	Cao độ nền Fill Elv. (m)	Ghi chú/ Remark
28	30/01/2018	15:00	2.91	7.130	4.22	5.930	
29	31/01/2018	10:00	2.88	7.220	4.34	5.924	
30	01/02/2018	11:25	2.90	7.225	4.33	5.930	
31	02/02/2018	9:30	2.80	7.216	4.42	5.911	
32	04/02/2018	15:30	3.16	7.205	4.05	5.894	
33	05/02/2018	9:30	3.11	7.208	4.10	5.989	
34	06/02/2018	9:00	3.15	7.208	4.06	5.989	
35	07/02/2018	15:00	3.10	7.200	4.10	5.890	
36	09/02/2018	15:30	3.28	7.198	3.92	5.890	
37	10/02/2018	9:00	3.36	7.195	3.84	5.623	
38	11/02/2018	9:30	3.43	7.195	3.77	5.856	
39	13/02/2018	15:00	3.52	7.189	3.67	5.853	
40	15/02/2018	9:00	3.58	7.185	3.61	5.842	
41	17/02/2018	9:30	3.61	7.184	3.57	5.831	
42	19/02/2018	15:00	3.62	7.182	3.56	5.847	
43	21/02/2018	15:00	3.64	7.179	3.54	5.831	
44	23/02/2018	9:00	3.65	7.175	3.53	5.805	
45	25/02/2018	9:00	3.66	7.166	3.51	5.817	
46	04/03/2018	10:00	3.82	7.159	3.34	5.760	
47	12/03/2018	9:00	3.85	7.155	3.31	5.743	
48	17/03/2018	9:00	3.87	7.153	3.28	5.736	
49	23/03/2018	10:00	4.23	7.152	2.92	5.757	
50	26/03/2018	11:00	4.08	7.151	3.07	5.671	
51	30/03/2018	9:00	4.10	7.156	3.06	5.699	
52	06/04/2018	9:30	4.15	7.133	2.98	5.629	
53	13/04/2018	9:00	4.20	7.130	2.93	5.721	
54	20/04/2018	10:00	4.25	7.126	2.88	5.675	
55	27/04/2018	9:30	4.28	7.123	2.84	5.637	

KẾT QUẢ QUAN TRẮC MỰC NƯỚC NGẦM MONITORING RESULT FOR GROUND WATER LEVEL							
Dự án: Nhà máy sản xuất PP và kho ngầm chứa LPG của tập đoàn Hyosung							
Project: PP Production Plant and LPG Cavern Project of Hyosung Corporation							
Địa điểm: Khu công nghiệp Cái Mép, Huyện Tân Thành, Tỉnh Bà Rịa - Vũng Tàu							
Location: Cai Mep Industrial zone, Tan Thanh District, Ba Ria - Vung Tau Province							
Giếng số/ Well No.	W02 vs BH1-1		Vị trí/ Location:		X (m)	1165235.826	
Ngày lắp đặt/ Installed date	12/30/2017				Y (m)	421789.177	
STT/ No.	Ngày/ Date	Thời gian/ Time	Số đọc/ Reading (m)	Cao độ đỉnh ống/ Tube Elevation (m)	Cao độ mực nước Ele. of g. water level (m)	Cao độ nền Fill Elv. (m)	Ghi chú/ Remark
56	04/05/2018	8:30	4.29	7.120	2.83	5.613	
57	11/05/2018	8:00	4.30	7.118	2.82	5.587	
58	18/05/2018	8:30	4.32	7.115	2.80	5.532	
59	25/05/2018	9:30	4.40	7.110	2.72	5.502	
60	01/06/2018	8:00	4.42	7.108	2.69	5.464	

KẾT QUẢ QUAN TRẮC MỰC NƯỚC NGẦM MONITORING RESULT FOR GROUND WATER LEVEL							
Dự án: Nhà máy sản xuất PP và kho ngầm chứa LPG của tập đoàn Hyosung							
Project: PP Production Plant and LPG Cavern Project of Hyosung Corporation							
Địa điểm: Khu công nghiệp Cái Mép, Huyện Tân Thành, Tỉnh Bà Rịa - Vũng Tàu							
Location: Cai Mep Industrial zone, Tan Thanh District, Ba Ria - Vung Tau Province							
Giếng số/ Well No.	W05 vs BH1-2		Vị trí/ Location:		X (m)	1165343.309	
Ngày lắp đặt/ Installed date	1/5/2018				Y (m)	421894.912	
STT/ No.	Ngày/ Date	Thời gian/ Time	Số đọc/ Reading (m)	Cao độ đỉnh ống/ Tube Elevation (m)	Cao độ mực nước Ele. of g. water level (m)	Cao độ nền Fill Elv. (m)	Ghi chú/ Remark
1	15/01/2018	11:00	0.51	3.580	3.070	3.070	
2	22/01/2018	10:00	1.51	4.683	3.173	3.173	
3	23/01/2018	15:00	1.45	4.689	3.239	3.328	
4	24/01/2018	10:00	1.10	4.779	3.679	3.433	
5	25/01/2018	9:30	1.08	4.778	3.698	3.683	
6	26/01/2018	10:00	0.84	4.779	3.939	3.684	
7	27/01/2018	9:30	1.39	5.866	4.476	4.005	
8	28/01/2018	11:25	1.41	5.377	3.967	3.985	
9	29/01/2018	9:00	0.84	5.348	4.508	4.709	
10	30/01/2018	15:00	1.62	6.158	4.538	4.668	
11	31/01/2018	15:00	1.35	6.150	4.801	5.151	

KẾT QUẢ QUAN TRẮC MỨC NƯỚC NGẦM MONITORING RESULT FOR GROUND WATER LEVEL							
Dự án: Nhà máy sản xuất PP và kho ngầm chứa LPG của tập đoàn Hyosung							
Project: PP Production Plant and LPG Cavern Project of Hyosung Corporation							
Địa điểm: Khu công nghiệp Cái Mép, Huyện Tân Thành, Tỉnh Bà Rịa - Vũng Tàu							
Location: Cai Mep Industrial zone, Tan Thanh District, Ba Ria - Vung Tau Province							
Giếng số/ Well No.		W05 vs BH1-2		Vị trí/ Location:	X (m)	1165343.309	
Ngày lắp đặt/ Installed date		1/5/2018			Y (m)	421894.912	
STT/ No.	Ngày/ Date	Thời gian/ Time	Số đọc/ Reading (m)	Cao độ đỉnh ống/ Tube Elevation (m)	Cao độ mực nước Ele. of g. water level (m)	Cao độ nền Fill Elev. (m)	Ghi chú/ Remark
12	01/02/2018	9:30	1.61	6.143	4.538	5.107	
13	02/02/2018	9:30	2.40	7.029	4.629	5.898	
14	03/02/2018	9:00	2.43	7.012	4.582	5.843	
15	04/02/2018	15:30	1.18	6.990	5.810	5.880	
16	05/02/2018	9:30	1.24	6.993	5.758	5.843	
17	06/02/2018	9:00	1.29	6.896	5.608	5.837	
18	07/02/2018	15:00	1.34	6.979	5.639	5.827	
19	08/02/2018	14:00	1.39	6.978	5.588	5.857	
20	09/02/2018	14:00	1.35	6.970	5.620	6.035	
21	10/02/2018	14:00	1.36	6.961	5.601	5.787	
22	11/02/2018	9:30	1.36	6.952	5.592	5.849	
23	12/02/2018	9:00	1.38	6.950	5.570	5.832	
24	13/02/2018	14:00	1.39	6.947	5.557	5.826	
25	14/02/2018	15:00	1.42	6.945	5.525	5.842	
26	15/02/2018	9:30	1.45	6.943	5.493	5.849	
27	16/02/2018	9:00	1.46	6.943	5.483	5.833	
28	17/02/2018	9:30	1.48	6.942	5.462	5.821	
29	18/02/2018	9:00	1.52	6.940	5.420	5.840	
30	19/02/2018	9:30	1.53	6.939	5.409	5.831	
31	20/02/2018	9:00	1.55	6.935	5.385	5.823	
32	21/02/2018	9:00	1.57	6.932	5.362	5.811	
33	23/02/2018	9:00	1.45	6.928	5.478	5.783	
34	25/02/2018	9:00	1.47	6.925	5.455	5.701	
35	27/02/2018	10:00	1.47	6.925	5.455	5.701	
36	01/03/2018	9:00	1.38	6.924	5.544	5.755	
37	03/03/2018	10:00	1.51	6.920	5.410	5.740	
38	05/03/2018	9:00	1.51	6.911	5.401	5.683	

KẾT QUẢ QUAN TRẮC MỨC NƯỚC NGẦM MONITORING RESULT FOR GROUND WATER LEVEL							
Dự án: Nhà máy sản xuất PP và kho ngầm chứa LPG của tập đoàn Hyosung							
Project: PP Production Plant and LPG Cavern Project of Hyosung Corporation							
Địa điểm: Khu công nghiệp Cái Mép, Huyện Tân Thành, Tỉnh Bà Rịa - Vũng Tàu							
Location: Cai Mep Industrial zone, Tan Thanh District, Ba Ria - Vung Tau Province							
Giếng số/ Well No.	W05 vs BH1-2			Vị trí/ Location:	X (m)	1165343.309	
Ngày lắp đặt/ Installed date	1/5/2018				Y (m)	421894.912	
STT/ No.	Ngày/ Date	Thời gian/ Time	Số đọc/ Reading (m)	Cao độ đỉnh ống/ Tube Elevation (m)	Cao độ mực nước Ele. of g. water level (m)	Cao độ nền Fill Elev. (m)	Ghi chú/ Remark
39	07/03/2018	9:00	1.50	6.905	5.405	5.658	
40	09/03/2018	10:00	1.42	6.912	5.492	5.675	
41	11/03/2018	11:00	1.48	6.908	5.428	5.661	
42	13/03/2018	9:00	1.50	6.905	5.405	5.661	
43	17/03/2018	9:00	1.53	6.901	5.371	5.604	
44	23/03/2018	10:00	1.96	6.883	4.923	5.630	
45	26/03/2018	11:00	2.06	6.873	4.813	5.551	
46	30/03/2018	9:00	2.10	6.866	4.766	5.564	
47	06/04/2018	9:30	2.27	6.841	4.571	5.571	
48	13/04/2018	9:00	2.38	6.836	4.456	5.571	
49	20/04/2018	10:00	2.42	6.834	4.414	5.574	
50	27/04/2018	9:30	2.57	6.830	4.260	5.551	
56	04/05/2018	8:30	2.65	6.827	4.177	5.524	
57	11/05/2018	8:00	2.75	6.823	4.073	5.476	
58	18/05/2018	8:30	2.82	6.820	4.000	5.411	
59	25/05/2018	9:30	2.98	6.815	3.835	5.403	

With ground improvement by PVD plus surcharge which surcharge load was backfilled to increase compression load to strengthen velocity of underground seepage flow and excess pore pressure in the soft soil is designed to be dissipated through the horizontal drainage system on the top of PVDs that can be either the sand blanket or prefabricated band drains (PBD).

Those effective parameters **increased** after ground improvement as the above mentioned as: Degree of Consolidation, settlement rate, effective pressure, soil shear strength.... Actually this is increasing of soil properties.

And effective parameters **decreased with better trend** after ground improvement as also the above mentioned as pore pressure, (water level), water content,...

However there was **not or lightly increasing** of N_{SPT} value blow counts parameter because of some conditions as:

+ Ground after improvement is still in saturation state in spite of **decreasing of** pore pressure or/and water level: void ratio of soil sizes (volume) reduced but soil still hydrated underground water (see **Fig. 6-6 Back-calculated water content from settlements**) and can see at average N_{SPT} in depth, prior and after soil improvement versus water level table **6.4.3.1. Based on natural water values before and after ground improvement.**

- + Soft soil before improvement is very soft marine clay and surcharged by pumping on yard area this is so-called static surcharge method (not really disturbed much to soil structure unlike vibro sand/ stone columns methods)
- + Energy of SPT hammer is too high (63.6 Kg) with very soft sensitive clay thus it is so difficult to measure for.

7. RESULTS DISCUSSIONS

- ✓ Comparison of degree of consolidation from settlement, pore pressure data and Vane shear test test from soil investigation after treatment

By field measurements			Combine In situ Field Soil investigation& In lab test before & after treatment
Settlement data		Pore pressure data	
Asaoka's Method	Hyperbolic's Method	Barron's Method	$Q = \frac{e_0 - e_t}{e_0 - e_c}$
92.75%	89.2	91.4%	93.39%

- ✓ The average Degree of consolidation (DOS) was assessed based on both settlement (ground surface settlement plate) and pore pressure data which indicated that DOS estimated from settlement data was higher than that estimated from pore water pressure data due to maintenance at higher levels of the excess pore pressures during the progress of consolidation
- ✓ The average Degree of consolidation (DOS) predicted using Asaoka's Method (Asaoka, 1978) higher than Hyperbolic's Method (Tan, 1996)
- ✓ There is good match results in Assessment of DOC between Field measurements and Combine In situ Field Soil investigation& In lab test before & after treatment method for are good match assessment at Hyosung Vina Chemicals Project. However The average Degree of consolidation (DOS) figured out from combining In situ Field Soil investigation& In lab test before & after treatment higher than by field measurements (Included Asaoka, Hyperbolic, Pore pressure and Combine In situ Field Soil investigation& In lab test before & after ground treatment method)
- ✓ Because of good agreement between assessment method and results of DOC was mostly match with estimation of DOC and also settlement as well as time to achieve or/and for surcharge removal that indicated there was good design calculation and matched to all predicted DOC based Monitored Data for **Hyosung Vina Chemicals Project at Ba Ria Vung Tau Province, Viet Nam.**

ACKNOWLEDGMENTS

- ✓ The author would like to thank Associate Professor Nguyen Huy Phuong for providing advice on key content of this paper.

REFERENCES

- ❖ Asaoka, A., (1978), *Observational Procedure of Settlement Prediction, Soil and Foundations*, Vol. 18, No. 4, pp. 87–101. Tan, T. S., Inoue, T., and Lee, S.L. (1991), "Hyperbolic Method for Consolidation Analysis", *Journal of Geotechnical Eng'g*, Vol. 117, No. 11, pp. 1723-1737.
- ❖ Study, analysis and assess effectiveness of soft soil improvement based on monitoring results and soil investigation after treatment- P.V. Long D. Eng, General Director of Vina Mekong Engineering Consultants JS Company (VMEC)

LANDSLIDE RISK ASSESSMENT BY SITE INVESTIGATION AND NUMERICAL ANALYSIS IN AN KHE PASS, VIETNAM

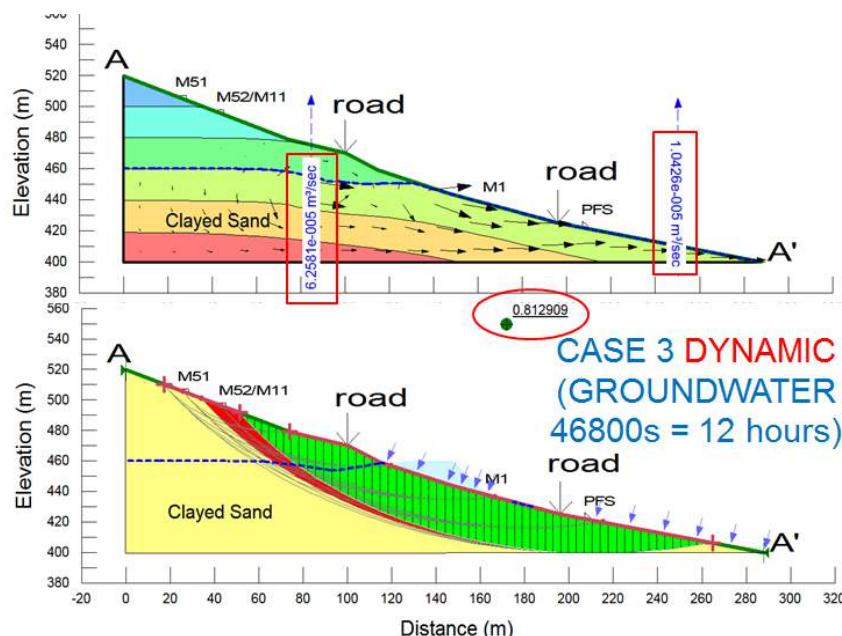
ĐÁNH GIÁ RỦI RO TRƯỢT LỞ BẰNG KHẢO SÁT HIỆN TRƯỜNG VÀ PHÂN TÍCH MÔ HÌNH TẠI ĐỒ AN KHÊ, VIỆT NAM

Nguyen Huynh Thong, Le Thanh Phong, Bui Trong Vinh, Toshihiro Asakura, Naotoshi Yasuda

ABSTRACT

The study considers the potential landslide area at An Khe Pass top and analyzes the causes and factors triggering instability. Site investigation and Limit Equilibrium method (LEM) are two key methods used. Initial results indicate that this area includes many sensitively unstable locations along An Khe Pass, particularly at an elevation from 400 to 550 m. The study also analyzed the mechanical properties of engineering geology, hydrology, geomorphology, weathering, and land use around sensitive areas. Results of model simulations demonstrated that depending on the rainfall intensity in a rainy season, the surface flow eroded material strongly and caused liquefaction quickly leading the loss of balance on slopes, causing critical roads no active and paralysis. Therefore, the factor safety of research get 0.81 and a fundamentalist to evaluate the impacts of geodynamic processes and to propose appropriated solutions for prevention.

KEYWORDS: landslide, laboratory testing, LEM, rainfall intensity, geodynamic processes



Dr. Nguyen Huynh THONG

Department of Earth Resources and Environment, Faculty of Geology and Petroleum Engineering, HCMC University of Technology (HCMUT)

Email: nhthong@hcmut.edu.vn, corresponding author

Tel: 0908782913

MEng. Le Thanh PHONG

Department of Earth Resources and Environment, Faculty of Geology and Petroleum Engineering, HCMC University of Technology (HCMUT)

Dr. Bui Trong VINH

Department of Earth Resources and Environment, Faculty of Geology and Petroleum Engineering, HCMC University of Technology (HCMUT)

Prof. Toshihiro ASAKURA

Department of Civil and Earth Resources, Faculty of Engineering, Kyoto University

Dr. Naotoshi YASUDA

Department of Civil and Earth Resources, Faculty of Engineering, Kyoto University

I. Introduction

An Khe Pass (Figure 1) is the Pass elbow located on 19th highway connecting between Binh Dinh and Gia Lai province as well as is the critical road linking of Tay Nguyen area, Viet Nam to Laos and Cambodia. With the Pass length about 20 km on 19th highway, An Khe is one of the important economic roads of highland area. However, because of the terrain of mountain with elevation changing from 200 to 500 m, thickness weathering layer, especially at the top of An Khe Pass 600 m elevation, elbow shape, 40 degree inclination lead to geological dynamic processes such as landslide, slope failures, debris flow, and so on damaging to the national highway.

Moreover, the climate of An Khe is the same with climate of Binh Dinh province, Tay Nguyen, hence rainy season usually prolongs from October to February in next year, especially being the heavy rainfall in November, increasing the surface runoff on slope, and promoting the slope failures.

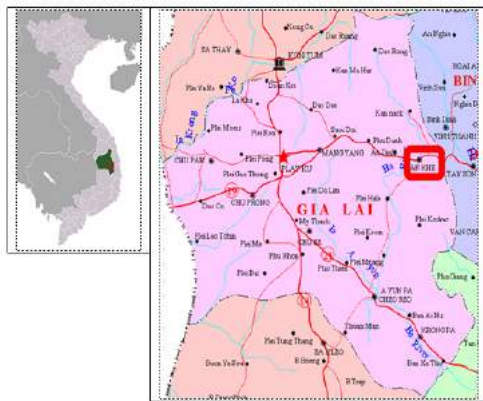


Figure 1: Location of Research Study

II. Data material and Method

II.1 Data material

To prepare for input parameters, the existing data from reports, publication, and papers as well as the primary data from field investigation are referred. Due to the very narrow and complicated terrain at the top of An Khe Pass, field investigation by geological drilling cannot active at the potential slope failures; therefore, the research collected some soil samples by manual method in dry and rainy season to identify the properties of soil.

Furthermore, the existing and new slope failures are also measured and recorded with information such as inclination, height, width as well as description about biogeography

II.2 Method

Limit Equilibrium Method (LEM) is one of the Finite Element Methods (FEM). This method is used to calculate and evaluate each slice of slope. Up to now, the LEM is certified as numerical method to analyze for sliding slice of soil following the Coulomb's law (Carol and et. al, 2014). Hence, the research uses LEM as the analyzed method for calculating and evaluating on slope failures. Accordingly, the essentially geological tool including SeepW and SlopeW is applied.

III. Analysis and Result

From the features of research area and information of input parameters, the collected profiles are analyzed with assumption situations of dry and rainy season, as well as changing of groundwater (GW) table. In the Figure 2, the profile AA', BB', CC' design to cut through the elbow of An Khe Pass with elevation change from 480 – 500 m to 400 m at the end point of modeling.



Figure 2: Cross-section for modeling

The analyzed results show, with none GW case, the factor safety (FS) is around 1.112 to 1.345 (standard FS equal 1.0, the minimum FS for safety evaluation of slope). Nevertheless, in the GW case (by field investigation, recharging to GW table is filled by Gia Lai river above, especially extra volume in rainy season), FS reduces strongly and gets 0.6 to 0.8, leading to easily failure (Figure 3).

In research, analyzing and calculating about FS changing follow the ability of infiltration in rainy season also carried out. By the laboratory testing, almost clayed sand are found and infiltration changing 10% to 15% (considering to terrain feature). According to [landslide report of An Khe Pass top \(2011\)](#), the annually average rainfall gets about 5.5×10^{-8} to 5.8×10^{-8} m/s. Thus, the ability of infiltration of water is calculated with approximately value around 3.6×10^{-9} m/s, using for input parameter of dynamic modeling. Output result of FS varies from 0.6 to 0.7, occurred failure (Figure 3).

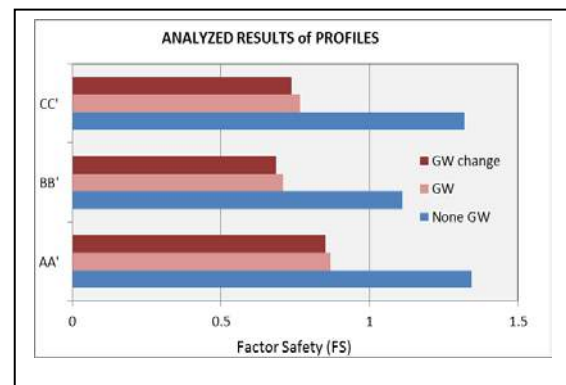


Figure 3: Analyzed results of representative profile at An Khe Pass top

Based on the output results, FS gets smaller than 1.0 need evaluated and checked carefully in the field. In the researching limitation, the FS results of modeling are compared with the old slope failure in the field. Finally, location of slope failures as well as GW is completely the same in site.

IV. Conclusion and Suggestion

An Khe Pass area, especially in Pass top location existed many the potential slope failure such as landslide, rock fall, debris flow, and so on. When hazard occurs, not only happen the economic loss, damage the critical highway, but also lead to human being loss. Therefore, the early warning system and the appreciated technical solution (embankment, drain system, and so on) need executed.

To get more advantages about solution, the research carried out interpolation the FS contour along representative profiles due to suggest the appreciated countermeasures around failure slope. By that way, FS always get value larger than 1.0 and located outside highway (Figure 4), thus, only focusing on the traffic situation in dry season.

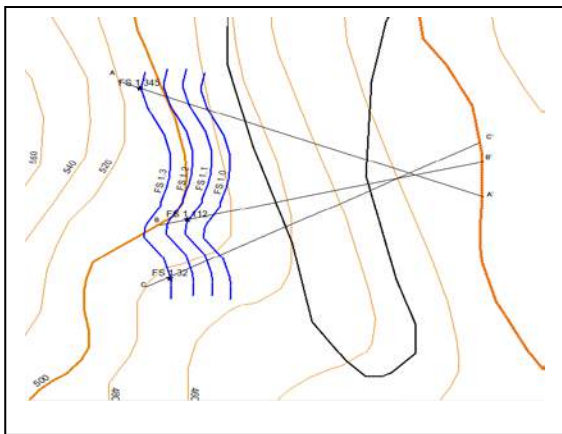


Figure 4: Interpolation of FS contour in dry season

As for rainy season, failure not only occurs at Pass top, but also fails on many positions along 19th highway leading to completely damage road. Strongly suggestion about research project for 19th highway by digital elevation method (DEM) to manage and solute troubles immediately.

Acknowledgment

Authors would like to express special thanks to Ho Chi Minh City University of Technology – VNU-HCM, under grant number T-ĐCDK-2017-53 by funded support. Moreover, a big thank to Japanese Peofessors from Kyoto University, Japan provided advices and consultants to research.

Reference

- [1] Carol M., Zeena F., Arup, Peter H. (2014). "Slope Stability analysis – limit equilibrium or the finite element method". Paper in GE's, Civil Engineer
- [2] Binh Dinh landslides, 2011. VOV news, Viet Nam

[3] Landslide report of An Khe Pass top, 2011. E&R of Binh Dinh Ministry, Viet Nam

THE SLOPE STABILITY ASSESSMENT FOR OPEN PIT MINING EXTRACTION

ĐÁNH GIÁ ỔN ĐỊNH MÁI DỐC TRONG KHAI THÁC MỎ LỘ THIÊN

Tran Le Hoang Tu, Nguyen Huynh Thong

ABSTRACT

In Viet Nam, open pit mining extraction creates many unsafe problems, especially problems of slope instability. The slope was established from excavation peel soil process, due to the purpose of deep mining and threaten to lives of the worker, engineer, resident when landslides occur. Therefore, human need to assessment and research methods excavate slope stability in and after mining extraction, in future will develop new projects at here.

Geology and hydrogeology data were collected from field trips and geological survey. Important positions in entire survey area were assessed and choose to determine the build of a model. Finite Elements Method (FEM) was solved stability and displacement problems. Additionally, the input parameter of main physical properties of soil, rainfall and neighboring buildings was collected for calculation.

The result of paper showed slope excavation do change the structure of soil and led to increased risk of landslides. Value of stable coefficient (K) is 1.25 for assessment level of stability. Method of excavation does not cut slope angle 38 degrees (1:1.25) ensures stability with deep 15m and $K_{38}=1.3824$. Method of excavation does cut slope with height 5m, width 3m and slope angle 63 degrees (1:0.5) ensures stability with deep 15m and $K_{63}=1.2538$.

The result of the paper is a basis for selecting the method of slope excavation to fit natural features of mine. Method of excavation does not cut slope with slope angle 38 degrees ensures stability but it does not fit with the small area of mineral mine, because of doing not open pit mining extraction. Method of excavation does cut slope with height 5m, width 3m and slope angle 63 degrees is suitable for the large and small area of mining but excavating technique is high than the method of excavation does not cut slope.

KEYWORDS: *instability, Finite Elements Method, stable coefficient, displacement*

BEng. Tran Le Hoang TU

Department of Earth Resources and Environment, Faculty of Geology and Petroleum Engineering, HCMC University of Technology (HCMUT)

Dr. Nguyen Huynh THONG

Department of Earth Resources and Environment, Faculty of Geology and Petroleum Engineering, HCMC University of Technology (HCMUT)

Email: nhthong@hcmut.edu.vn, corresponding author

Tel: 0908782913

LANDSLIDE DISASTER AND APPLICATION POSSIBILITY OF LANDSLIDE EARLY WARNING SYSTEM (LEWS) IN LAM DONG PROVINCE, SOUTHERN VIETNAM

Bui Trong Vinh, Pham Thanh Phuc, Le Thanh Phong, Nguyen Huynh Thong,
Tran Anh Tu, Nguyen Viet Ky, Kanno Takami, Kiyono Junji

ABSTRACT

Landslide disasters have occurred and caused many houses cracked, collapsed and lives in many countries. Bao Loc city belongs to Lam Dong Province, southern Vietnam, locates on Di Linh – Bao Loc plateau about 800 – 1000m elevation with complex mountainous terrain. Residents living there have to evacuate to temporary areas supported by local government. In order to reduce damages of assets and costs of lives, mechanism of landslide hazard need to be investigated and assessed. The main cause was soil extraction activities at toe of slope, which lost the counterweight berm, associated with the moisture increase of soil due to heavy rainfall in rainy season. The 1.2-hectare landslide area was investigated with reduced shear strength of slope materials.

The analysis results from GeoStudio software show that the slope is stable in dry season with the minimum factor of safety (FS) is 1.474, in rainy season the slope is unstable with minimum factor of safety (FS) is 0.896 commensurate with groundwater present model.

The analysis results from Band Stability and Toe Erosion also show that the slope is unstable with the minimum factor of safety (FS) is 0.73. The results of the micro tremor observation also show the study area is potentially very high landslide.

The extensometer was also installed to record the extension of the cracks in the hazard zone. The results showed that some cracks have been developed especially in the rainy season. The unmanned aerial vehicle (UAV) was also used to monitor and investigate the small and large landslide areas.

A landslide early warning system (LEWS) for predicting landslide disasters using global navigational satellite system (GNSS) has been also developed. The preliminary results showed that the landslide early warning can be applied in the area but it depended on many installed factors and infrastructure of the local telecommunication system.

KEYWORDS: *landslide disaster, Bao Loc City, Vietnam, LEWS, GNSS, UAV, FS*

Dr. Bui Trong Vinh

Lecturer, Department of Earth Resource and Environment, Faculty of Geology and Petroleum Engineering, HCM City University of Technology

Email: btvinh@hcmut.edu.vn

Mr. Pham Thanh Phuc

HCM City University of Technology

MEng. Le Thanh Phong

HCM City University of Technology

Dr. Tran Anh Tu

HCM City University of Technology

Dr. Nguyen Huynh Thong

HCM City University of Technology

A/Prof. Nguyen Viet Ky

HCM City University of Technology

Dr. Kanno Takami

Kawasaki Geological Engineering Co. Ltd, Hanoi Branch, Japan

Dr. Kiyono Junji

Kyoto University, Japan

RIP CURRENT AND BEACH CIRCULATION HAZARDS IN VUNG TAU BEACH – VIETNAM

CÁC MỐI NGUY VỀ RIP VÀ DÒNG CHẢY Ở BIỂN VŨNG TÀU – VIỆT NAM

Bui Trong Vinh, Huynh Trung Tin, Jung Lyul Lee

ABSTRACT

Vung Tau Beach in Vietnam is well-known place for million tourists to visit and enjoy annually. However, each year, thousands of beach goers have been drown by rip currents and beach circulation. In this paper, the authors have investigated and identified the characteristics of the rip current and beach circulation hazards in Vung Tau Beach using satellite images and numerical model. It is found that, the occurrence of rip currents and beach circulation depends on the change of tidal level, wave attack and bottom topography seasonally. Two main types of rip flow including the “exit flow” and the “circulation flow” have been identified. The effects of the groin structure and remaining hard rock on rip currents have been also investigated.

KEYWORDS: *Vung Tau Beach, Rip Current, Hazards, Exit Flow, Beach Circulation Flow*

TÓM TẮT

Bãi biển Vũng Tàu được biết đến như 1 địa điểm du lịch nổi tiếng, thu hút hàng triệu khách du lịch hàng năm. Tuy nhiên, mỗi năm, Vũng Tàu có hàng ngàn trường hợp đuối nước do dòng rip và các dòng chảy ven biển. Trong nội dung bài báo này, các tác giả đã sử dụng ảnh vệ tinh và mô hình số để phân tích và nhận diện các đặc điểm của dòng rip và các dòng chảy ven

biển Vũng Tàu. Kết quả cho thấy, sự xuất hiện của các dòng rip và dòng chảy ven bờ phụ thuộc vào sự thay đổi của thủy triều, tác động của sóng và sự biến đổi địa hình đáy biển theo mùa. 2 cơ chế chính của dòng rip được nhận diện là các dòng “tách bờ” và dòng “hoàn lưu”. Bên cạnh đó, sự ảnh hưởng của công trình mỏ hàn và các dải đá gốc đến sự phân bố của dòng rip cũng được phân tích và đánh giá.

DR. BUI TRONG VINH

Vice Dean, Faculty of Geology and Petroleum Engineering, HCMC University of Technology (HCMUT).

Email: btvinh@hcmut.edu.vn, **corresponding author**

Tel: 091 3634448

M.S. HUYNH TRUNG TIN

Researcher, Department of Earth Resources and Environment, Faculty of Geology & Petroleum Engineering, HCMC University of Technology (HCMUT).

Email: httinvn@gmail.com.

Tel: 0902 778189

PROF. JUNG LYUL LEE

Graduate School of Water Resources, Sungkyunkwan University, 25-2 Sungkyunkwan-ro, Jongno-gu, Seoul, Korea

Email: jilee6359@hanmail.net

APPLICATION OF S-SHAPE CURVE EQUATION TO DESCRIBE CONSOLIDATION TEST RESULTS USING CURVE FITTING TOOL

ỨNG DỤNG PHƯƠNG TRÌNH ĐƯỜNG CONG S-SHAPE ĐỂ BIỂU DIỄN KẾT QUẢ THÍ NGHIỆM NÉN CỐ KẾT BẰNG CÁCH SỬ DỤNG CÔNG CỤ CURVE FITTING

Dr. Vo Dai Nhat, Tran Van Thanh

ABSTRACT

The objective of this paper is to research on application of S-shape curve equation to describe consolidation test results by using curve fitting tool based on analysis of factors of model including SSE, R-square, Adjusted R-square and RMSE. The consolidation test results are plotted properly and then three S-shape curve equations introduced by Brooks and Corey (1964), van Genuchten (1980) and Fredlund and Xing (1994) are used to fit the tested data. The goodness of fit is shown and finally the capability of application of S-shape curve equations is proposed. By testing with more than 30 samples together with applying curve fitting tool, the results show that Fredlund and Xing model is the most appropriate one to describe consolidation test results.

KEYWORDS: *S-shape curve, consolidation, curve fitting*

TÓM TẮT

Mục tiêu của bài báo là nghiên cứu việc ứng dụng phương trình đường cong S-shape để biểu diễn kết quả thí nghiệm nén cố kết bằng cách sử dụng công cụ Curve Fitting Tool dựa vào sự phân tích các thông số mô hình bao gồm SSE, R^2 , R^2 hiệu chỉnh và RMSE. Kết quả thí nghiệm nén cố kết được vẽ một cách hợp lý và ba phương trình đường cong của các tác giả Brooks and Corey (1964), van Genuchten (1980) and Fredlund and Xing (1994) được dùng để mô tả số liệu kết quả thí nghiệm. Sự phù hợp của mô hình được trình bày và khả năng ứng dụng các phương trình đường cong S-shape cũng được đề xuất. Bằng thực nghiệm với hơn 30 mẫu thí nghiệm cùng với việc ứng dụng công cụ curve fitting, cho thấy mô hình của Fredlund and Xing là phù hợp nhất để mô tả thí nghiệm nén cố kết.

TỪ KHÓA: *đường cong S-shape, cố kết, Curve Fitting*

DR. VO DAI NHAT

Lecturer, Department of Geotechnics, Faculty of Geology and Petroleum Engineering, HCMC University of Technology

Email: nhatvodai@hcmut.edu.vn, **corresponding author**

Tel: 0903013136

TRAN VAN THANH

Department of Geotechnics, Faculty of Geology and Petroleum Engineering, HCMC University of Technology

Email: 1552342@hcmut.edu.vn

Tel: 0967712397

EVALUATION OF EFFECTS OF UNDRAINED AND DRAINED CONDITIONS ON RAFT FOUNDATION WITH DIFFERENT FACTORS OF SAFETY USING THREE DIMENSIONS FINITE ELEMENT ANALYSIS

ĐÁNH GIÁ ẢNH HƯỞNG CỦA ĐIỀU KIỆN KHÔNG THOÁT NƯỚC VÀ THOÁT NƯỚC TRÊN MÓNG BÈ VỚI NHỮNG HỆ SỐ AN TOÀN KHÁC NHAU SỬ DỤNG PHƯƠNG PHÁP PHẦN TÍCH PHẦN TỬ HỮU HẠN BA CHIỀU

Tran Van Tuan, Nguyen Qui Ninh, Truong Quynh Nhu, Luu Duc Cuong

ABSTRACT

This paper presents the results of three dimensions finite element (3D FE) analysis of raft foundations with different factors of safety (FS) in undrained and drained conditions. Three cases including Case 1 (FS = 1), Case 2 (FS = 2) and Case 3 (FS = 3) were considered in this study. For each case, undrained and drained conditions were examined in the analysis in order to evaluate variations of settlements of the foundations as well as ground surface settlement, failure mechanisms and failure zones. Variation of ultimate bearing capacity was determined for undrained and drained conditions before considering three above cases. The results showed that drained condition had considerable effects on the ultimate bearing capacity and settlement of raft foundations as well as failure mechanisms and failure zones. When drained condition was applied to the models, the ultimate bearing capacity of raft foundation increased 503% and the settlements of raft foundations increased about 39% in Case 2 and 45% in Case 3 while decreased 91% in Case 1. Variation of failure mechanisms and failure zones was also figured out and some discussions were given.

KEY WORDS: Raft, settlement, failure mechanism, failure zone, undrained and drained analyses.

TÓM TẮT

Bài nghiên cứu này trình bày kết quả của phương pháp phần tử hữu hạn ba chiều (3D FE) phân tích móng bè với những hệ số an toàn (FS) khác nhau trong điều kiện không thoát nước và thoát nước. Ba trường hợp bao gồm: trường hợp 1 (FS = 1), trường hợp 2 (FS = 2) và trường hợp 3 (FS = 3) đã được xem xét trong nghiên cứu này. Mỗi trường hợp, điều kiện không thoát nước và thoát nước đã được xem xét để đánh giá biến động của độ lún của móng cũng như lún bề mặt, cơ chế phá hoại và vùng phá hoại. Sự thay đổi của sức chịu tải cực hạn đã được xác định trong điều kiện không thoát nước và thoát nước trước khi xem xét ba trường hợp trên. Kết quả đã chỉ ra rằng điều kiện thoát nước có ảnh hưởng đáng kể lên sức chịu tải cực hạn của móng bè cũng như cơ chế phá hoại và vùng phá hoại. Khi điều kiện thoát nước được áp dụng cho mô hình, sức chịu tải cực hạn của móng bè tăng 503% và độ lún của móng bè tăng khoảng 39% ở trường hợp 2 và 45% ở trường hợp 3 trong khi tăng 91% ở trường hợp 1. Việc thay đổi cơ chế phá hoại và vùng phá hoại cũng được vẽ ra và một số bình luận đã được đưa ra.

TỪ KHÓA: Bè, độ lún, cơ chế phá hoại, vùng phá hoại, phân tích không thoát nước và thoát nước.

DR. TRAN VAN TUAN

Department of civil engineering, Can Tho university, Can Tho, Vietnam.

Email: tranvantuan567@gmail.com **corresponding author**

Tel: 0901088944

NGUYEN QUI NINH

Master student, Division of hydraulic, Department of Agriculture, Can Tho, Vietnam

Email: nguyenquinh@gmail.com

Tel: 01667141976

TRUONG QUYNH NHU

Bachelor student, CanTho university, CanTho, Vietnam.

Email: nhunhu2929@gmail.com

Tel: 01644098276

LUU DUC CUONG

Bachelor student, CanTho university, CanTho, Vietnam.

Email: cuongcuong1717@gmail.com

Tel: 0901024097

DETERMINE GROUND WATER IN CENTRAL HIGHLAND IN VIETNAM

XÁC ĐỊNH NƯỚC NGẦM TẠI KHU VỰC TÂY NGUYÊN

Trương Quốc Thanh, Nguyễn Xuân Kha, Nguyễn Thị Nhu Dung, Đỗ Quang Khanh, Trần Văn Xuân

ABSTRACT

In the dry season, the demand using water for agriculture in central Highland in Vietnam extremely increases high. To face this problem, the present study aims to investigate the groundwater accumulations present in the Central Highland in Vietnam by geophysical methods. In this case, resistivity method is useful in the exploration for safe, quick and abundant groundwater. Resistivity data interpretation was carried out using the measurement data to determine the depth to the layer contain groundwater. The results of resistivity interpretation indicated that the depth of the groundwater surface is 30 to 50m. Eight imagines electrical of Wenner array were measured with AB ranging from 200 m to 400 m at the study area. The results of the quantitative interpretation of geoelectrical data indicated that the subsurface section consists of six abnormal resistivity zone; and the bedrock below this zone has high resistivity. The groundwater contains in weather rock having high fractured and porosity. The range resistivity of groundwater potential is 20-100ohm-m

KEYWORDS: Wenner array; resistivity, central highland, groundwater, fractured rock

TÓM TẮT

Vào mùa khô, nhu cầu sử dụng nước cho nông nghiệp ở Tây Nguyên ở Việt Nam cực kỳ cao. Đối mặt với vấn đề này, nghiên cứu này nhằm mục đích tìm kiếm các mạch nước tại khu vực Tây Nguyên bằng phương pháp địa vật lý. Trong trường hợp này, phương pháp điện trở suất được áp dụng là hiệu quả trong quá trình tìm kiếm khảo sát nước ngầm một cách an toàn, hiệu quả và nhanh chóng. Việc minh giải tài liệu điện trở suất giúp xác định độ sâu của lớp đất đá chứa nước bên dưới. Kết quả minh giải điện trở suất cho thấy nước ngầm tại khu vực khảo sát nằm ở độ sâu từ 30 đến 50m. Có 8 mặt cắt điện trở suất sử dụng hệ điện cực Wenner được đo khảo sát trong khu vực với chiều dài mặt cắt từ 200 đến 400m. Kết quả minh giải định lượng tài liệu điện trở trong khu vực đã xác định được 6 đới dị thường điện trở suất và lớp đá móng bên dưới có điện trở suất cao trong khu vực nghiên cứu. Nước ngầm được phát hiện chứa trong lớp đất đá phong hóa có độ rỗng và khe nứt cao. Đới chứa nước ngầm có giá trị điện trở suất dao động trong khoảng từ 20-100ohm-m.

TỪ KHÓA: hệ điện cực Wenner, điện trở suất, Tây Nguyên, nước ngầm, đá nứt nẻ

M.S Trương Quốc Thanh Researcher, Department of Geology Petroleum Engineering, Faculty of Geology and Petroleum Engineering, HCMC University of Technology (HCMUT)

Email: tquocthanh@hcmut.edu.vn

Tel: 0383802022

M.S Nguyễn Xuân Kha Lecturer, Department of Geology Petroleum Engineering, Faculty of Geology and Petroleum Engineering, HCMC University of Technology (HCMUT)

Email: nxkha@hcmut.edu.vn

Tel: 0903351117

M.S Nguyễn Thị Nhu Dung Lecturer, Department of Geology, Faculty of Geology, Environmental University – UNRE-HCMC

Dr Đỗ Quang Khanh Lecturer, Department of Drilling and Production, Faculty of Geology and Petroleum Engineering, HCMC University of Technology (HCMUT)

Email: dqkhanh@hcmut.edu.vn

Tel: 0936397733

Asso.Prof Dr Trần Văn Xuân Lecturer, Department of Geology Petroleum Engineering, Faculty of Geology and Petroleum Engineering, HCMC University of Technology (HCMUT)

Email: tvxuan@hcmut.edu.vn, **corresponding author**

Tel: 0903700770

PREDICTION OF OILFIELD SCALE DEPOSITION ALONG THE WELLBORE: FUNDAMENTALS AND APPLICATIONS

DỰ BÁO SA LẮNG MUỐI TRONG LÒNG GIẾNG: NỀN TẢNG VÀ ỨNG DỤNG

Lan Mai-Cao*, Bao-Tram Bui-Nguyen

ABSTRACT

In recent years, some oil producing wells in Cuu Long basin have had serious problems with oilfield scale deposition. Mineral scales (mainly CaCO_3) appears massively at high concentrations, causing obstruction of the pipe flow and thus leading to the reduction in oil production. Although oilfield scale deposition problems have occurred quite frequently in Vietnam, they have not attracted much attention from researchers.

The main contents presented in this paper include: (i) Calculation of the scaling tendency and the amount of scale deposition when it occurs; (ii) Study of the influences that flow dynamics has on scale deposition along the wellbore; (iii) Prediction of mineral scale deposition in the well X-1.

The study on well X-1 shows that there exists mineral scale deposit (mainly CaCO_3) with the estimated amount of scale deposit greater than 12mg/L. In addition, the comparison between the results from this study with those from ScaleChem software (OLI System) shows that the difference in results between the two approaches is insignificant (less than 1%) and thus prove the reliability of the computational workflow used in this study.

In addition, an important contribution of this study compared to that by H.Long et al. (2016) [1] is that the influence of flow dynamics on the mineral scale deposition was taken into account in predicting the amount of scale deposit along the wellbore of X-1 with the combination of ScaleChem (OLI System) and PIPESIM (Schlumberger).

KEYWORDS: oilfield mineral scale deposition, scaling tendency, saturation index, thermodynamics, flow dynamics.

TÓM TẮT

Trong những năm gần đây, các giếng khai thác dầu khí ở bể Cửu Long, Việt Nam đang gặp vấn đề về sa lắng muối rất nghiêm trọng. Muối vô cơ (chủ yếu là CaCO_3) xuất hiện với hàm lượng lớn, gây cản trở dòng chảy trong hệ thống khai thác và làm sụt giảm sản lượng khai thác. Mặc dù sa lắng muối trong khai thác dầu khí ở Việt Nam xảy ra khá phổ biến, vấn đề này vẫn chưa được các nhà nghiên cứu quan tâm đúng mức.

Các nội dung chính được trình bày trong bài báo này bao gồm: (i) Xác định khả năng sa lắng muối cũng như dự báo lượng sa lắng muối trong ống khai thác; (ii) Khảo sát ảnh hưởng của dòng chảy trong giếng khai thác đến quá trình sa lắng muối; (iii) Kết quả dự báo sa lắng muối trong giếng X-1.

Kết quả nghiên cứu với giếng X-1 cho thấy có hiện tượng sa lắng muối trong quá trình khai thác với hàm lượng sa lắng muối CaCO_3 trong giếng dự đoán là hơn 12 mg/L. Ngoài ra, việc so sánh kết quả tính toán từ nghiên cứu này với kết quả tính toán từ phần mềm thương mại ScaleChem (OLI System) cho thấy sai lệch giữa hai kết quả là rất nhỏ (dưới 1%) qua đó khẳng định mức độ tin cậy trong tính toán nhiệt động lực học của nghiên cứu này.

Ngoài ra, một đóng góp quan trọng của nghiên cứu này so với công trình của H.Long et al. (2016) [1] là đưa vào xem xét ảnh hưởng của dòng chảy dầu khí trong giếng đến lượng muối sa lắng dọc theo đường ống khai thác của giếng X-1 qua việc kết hợp hai phần mềm ScaleChem (OLI System) và PIPESIM (Schlumberger).

TỪ KHÓA: sa lắng muối vô cơ, xu hướng đóng cặn, chỉ số bão hòa, nhiệt động lực học, động lực học về dòng chảy.

Lan Mai-Cao, Ph.D. (USQ, Australia)

Corresponding Author,

Faculty of Geology and Petroleum Engineering, Ho Chi Minh City University of Technology.

Email: maicaolan@hcmut.edu.vn

Bao-Tram Bui-Nguyen

Faculty of Geology and Petroleum Engineering, Ho Chi Minh City University of Technology.

Email: 1450307@hcmut.edu.vn

SAND PRODUCTION POTENTIALS IN PETROLEUM WELLS AT VIETNAM

KHẢ NĂNG SINH CÁT TRONG CÁC GIẾNG DẦU KHÍ TẠI VIỆT NAM

Do Quang Khanh, Nguyen Tuan, Kieu Phuc

ABSTRACT

Sand production is usually related to petroleum wells in unconsolidated and weakly consolidated formations. The sand produced during exploration and exploitation operations will seriously affect the reservoir quality, reduce the recovery factor, cause rapid erosion of the equipment, etc. resulting in significant damages to the investors.

This study aims to predict the potentials of sand production in petroleum wells at Nam Con Son basin, offshore Vietnam. The predictive model of sand production is established from reservoir geomechanical model using the shear failure criterion. It could calculate critical pressures along the well depths such as critical bottom-hole pressures (CBHFP), critical drawdown pressures (CDP), critical reservoir pressures (CRP). A calculating program written by MATLAB programming language is also developed to describe the critical pressure charts along the well depths and allow to evaluate the impacts of parameters such as the depleted reservoir pressures, rock strengths, etc.

Based on these obtaining charts and their analyses for the studied petroleum wells at Nam Con Son basin, the sand production potentials are evaluated and predicted. The appropriate production depths of the studied wells will be selected to mitigate the sand appearance, to have appropriate measures for well completion and production as well as to draw up a reasonable reservoir management strategy.

KEYWORDS: Sand production, Critical drawdown, Shear failure, Vietnam.

TÓM TẮT

Sinh cát thường liên quan đến các giếng dầu khí ở những thành hệ cổ kết yếu và không cổ kết. Cát được sinh ra trong quá trình thăm dò và khai thác dầu khí sẽ ảnh hưởng nghiêm trọng đến chất lượng vỉa chứa, làm giảm hệ số thu hồi, nguyên nhân làm ăn mòn nhanh các thiết bị, v.v... dẫn đến thiệt hại đáng kể cho các nhà đầu tư.

Nghiên cứu này nhằm mục đích dự đoán khả năng sinh cát trong các giếng dầu khí tại bồn trũng Nam Côn Sơn, ngoài khơi Việt Nam. Mô hình dự báo về sự sinh cát được thiết lập từ mô hình địa cơ vỉa chứa sử dụng tiêu chuẩn hư hỏng cắt. Nó có thể tính toán các áp suất tới hạn dọc theo các độ sâu thân giếng như áp suất đáy giếng tới hạn, áp suất giảm thiểu tới hạn, áp suất vỉa chứa tới hạn. Một chương trình tính toán được viết bởi ngôn ngữ lập trình MATLAB cũng được phát triển để mô tả các biểu đồ áp suất tới hạn dọc theo độ sâu thân giếng và cho phép đánh giá những tác động của các tham số như áp suất vỉa chứa suy kiệt, độ bền đá, v.v...

Dựa trên các biểu đồ thu thập và phân tích của chúng cho các giếng dầu khí được nghiên cứu tại bồn trũng Nam Côn Sơn, khả năng sinh cát được đánh giá và dự đoán. Độ sâu sinh cát thích hợp của các giếng được nghiên cứu sẽ được lựa chọn để giảm thiểu sự xuất hiện cát, nhằm có biện pháp thích hợp để hoàn thiện giếng và khai thác cũng như xây dựng một chiến lược quản lý vỉa chứa một cách hợp lý.

TỪ KHÓA: Sinh cát, Giảm áp tới hạn, Hư hỏng cắt, Việt Nam.

DR. DO QUANG KHANH

Lecturer, Faculty of Geology and Petroleum Engineering, HCMC University of Technology (HCMUT)

Email: dqkhanh@hcmut.edu.vn, **corresponding author**

Tel: 0936 39 77 33

M.E. NGUYEN TUAN

Lecturer, Faculty of Geology and Petroleum Engineering, HCMC University of Technology (HCMUT)

Email: nguyentuan@hcmut.edu.vn

Tel: 0934 654 654

B.E. KIEU PHUC

Lecturer, Faculty of Geology and Petroleum Engineering, HCMC University of Technology (HCMUT)

Email: kieu-phuc@hcmut.edu.vn

Tel: 0934 058 158

APPLICATION OF CAPACITANCE – RESISTANCE MODELS TO SECONDARY OIL RECOVERY BY WATERFLOODING

Ta Quoc Dung, Pham Son Tung, Huynh Van Thuan

Faculty of Geology and Petroleum Engineering, Ho Chi Minh University of Technology

ABSTRACT

The capacitance – resistance model (CRM) is the result of the equivalence between a reservoir system and a RC circuit. To build the CRM, we need to determine two variables, which are the time constant and the connectivity.

This study focused on three different control volumes for CRMs: 1) the volume of the entire field - CRMT, 2) the drainage volume of each producer - CRMP, 3) the drainage volume between each injector/producer pair - CRMIP.

The CRM allows for quick estimation of the total rate. So that, to estimate the oil production rate needs to combine with empirical oil fractional – flow models. This paper chose the Gentil model to use in conjunction with a CRM model and proposing the forecasting of oil production rate.

This study evaluates the level of efficiency as well as the reliability of the CRM through two particular reservoirs. The first reservoir is assumed as an entire reservoir, which has an injector and a producer. The CRMT was applied to the reservoir and giving the estimated data quite close to actual data. The second reservoir, the 5 spot model was built in Computer modelling group software (CMG), which provided injection/production data. The estimated forecast result, which was obtained after applying CRMIP for this reservoir, was close to the result given by CMG. However, the oil rate had a relatively large deviation in the forecast compared with CMG data, so the empirical parameters of the Gentil model need to be updated after a period of time.

KEY WORDS: *capacitance – resistance model, production forecast, oil secondary recovery, waterflooding.*

THE GROUNDWATER RESOURCES SUSTAINABILITY OF THE UPPER – MIDDLE PLEISTOCENE AQUIFER IN CA MAU PENINSULA UNDER IMPACT OF CLIMATE CHANGE AND SOME OF ADAPTIVE SOLUTIONS

**TÍNH BỀN VỮNG TÀI NGUYÊN NƯỚC DƯỚI ĐẤT TẦNG CHỨA NƯỚC PLEISTOCENE GIỮA
TRÊN VÙNG BẮN ĐẢO CÀ MAU DƯỚI TÁC ĐỘNG CỦA BIẾN ĐỔI KHÍ HẬU
VÀ CÁC GIẢI PHÁP ỨNG PHÓ**

Dao Hong Hai, Nguyen Viet Ky, Bui Tran Vuong

ABSTRACT

Ca Mau peninsula covers an area of 16,940 km², including Ca Mau, Bac Lieu, Soc Trang, Hau Giang, Can Tho, and a part of Kien Giang provinces, which have agriculture is the mainly activities of the people. Groundwater resource was extracted with large quantities and have not yet controlled, combine with climate change in Ca Mau peninsula reduced groundwater levels and saltwater intrusion in the aquifers. Therefore, to predict groundwater sustainability under climate change impacts, this research used the results of the groundwater flow model, the salinity transportation model, and the recharging model to calculate the Total groundwater abstraction/Groundwater recharge Indicator (Indicator 1); Groundwater depletion Indicator (Indicator 2); Groundwater salinity indicator (Indicator 3). Calculated results show that the increase of Indicator 1: in 2015 there are 13/43 sustainable districts, 1/43 relatively sustainable districts, and 29/43 unsustainable districts. To the 2090 this index has changed 33/43 unsustainable districts, 1/43 relatively sustainable districts, and 9/43 sustainable districts. Indicator 2 in the 2015 there are 21/43 sustainable districts, 10/43 relatively sustainable districts, and 12/43 unsustainable districts. To the 2090 there are 7/43 sustainable districts, 12/43 relatively sustainable districts, 24/43 unsustainable districts. Indicator 3: in the 2015 there are 11/43 low salinity districts, 10/43 medium salinity districts, and 22/43 high salinity districts. To the 2090 there are 7/43 low salinity districts, 11/43 medium salinity districts, and 25/43 high salinity districts. Study results show that the climate change has impacted to all aquifers in Ca Mau peninsula, which increase the areas of unsustainable districts for the period from 2015 to

2090. This study contributes to support the groundwater managers in activities of planning, management and exploitation of groundwater resources more reasonable in Ca Mau peninsula.

KEYWORDS: sustainability indicator; groundwater in Ca Mau peninsula; groundwater sustainability; climate change.

TÓM TẮT

Bán đảo Cà Mau có diện tích 16.940 Km², bao gồm các tỉnh Cà Mau, Bạc Liêu, Sóc Trăng, Hậu Giang, Cần Thơ, và một phần tỉnh Kiên Giang. Khu vực này người dân sống chủ yếu là sản xuất nông nghiệp. Nguồn tài nguyên nước dưới đất tại đây đang được khai thác với trữ lượng lớn, và chưa có chính sách qui hoạch và kiểm soát hợp lý, thêm vào đó hiện tượng biến đổi khí hậu gây ra các hiện tượng xâm nhập mặn và hạ thấp mực nước trong các tầng chứa nước trong khu vực. Vì vậy việc dự báo tính bền vững nguồn tài nguyên nước dưới đất dưới tác động của BĐKH dựa vào kết quả của mô hình dòng chảy nước dưới đất, mô hình dịch chuyển biên mặn, và kết quả của mô hình bổ cập để tính toán các chỉ số Tổng lượng nước khai thác/ lượng bổ cập nước dưới đất (chỉ số 1); Chỉ số suy giảm nước dưới đất (chỉ số 2); Chỉ số xâm nhập mặn nước dưới đất (chỉ số 3). Kết quả tính toán cho thấy có sự gia tăng của chỉ số 1 năm 2015 có 13/43 huyện bền vững, 14/43 huyện tương đối bền vững và 29/43 huyện không bền vững. đến năm 2090 chỉ số này đã thay đổi, có 33/43 huyện không bền vững, 1/43 huyện tương đối bền vững và 9/43 huyện bền vững. Chỉ số 2 cho thấy năm 2015 có 21/43 huyện bền vững, 10/43 huyện tương đối bền vững, và 12/43 huyện không bền vững. đến năm 2090 chỉ số này đã thay đổi có 7/43 huyện bền vững, 12/43 huyện tương đối bền vững, và 24/43 huyện không bền vững. Chỉ số 3 năm 2015 có 11/43 huyện có mức độ xâm nhập mặn thấp, 10/43 huyện có mức độ xâm nhập mặn trung bình và 22/43 huyện có mức độ xâm nhập mặn cao. Đến năm 2090 có sự thay đổi có 7/43 huyện có mức độ xâm nhập mặn thấp, 11/43 huyện có mức độ xâm nhập mặn trung bình và 25/43 huyện có mức độ xâm nhập mặn cao. Những kết quả nghiên cứu cho thấy tác động của biến đổi khí hậu đã tác động đến tất cả các tầng chứa nước trong khu vực bán đảo Cà Mau, cụ thể nó đã làm gia tăng các huyện có các chỉ số không bền vững từ năm 2015 đến 2090. Và nghiên cứu này Cung cấp công cụ hỗ trợ cho các nhà quản lý trong các hoạt động quy hoạch, quản lý và khai thác nước dưới đất ở bán đảo Cà Mau hợp lý hơn.

TỪ KHÓA: chỉ số bền vững, nước dưới đất bán đảo Cà Mau, tính bền vững nước dưới đất, biến đổi khí hậu

DR. DAO HONG HAI

ASSOC. PRO. DR. NGUYEN VIET KY

Department of Geotechnics, Faculty of Geology and Petroleum engineering, Ho Chi Minh city university of technology (HCMUT)

E-mail: dhhai@hcmut.edu.vn, **corresponding author**

Tel: 0902040478

DR. BUI TRAN VUONG

Division of Water Resources Planning and Investigation for the South of Vietnam.

DETERMINE THE COMPONENTS OF LITHOLOGY - RATIO OF MINERALS AND CHARACTERISTICS OF POROSITY AND PERMEABILITY IN FRACTURED BASEMENT

Nguyen Xuan Kha¹, Pham Xuan Son², Nguyen Lam Anh², Hoang Van Quy²,
Truong Quoc Thanh¹, Nguyen Thi Y Nhi¹ Tran Van Xuan^{1*}

¹ Ho Chi Minh City University of Technology

² VSP Research & Engineering Institute

Corresponding author: Tran Van Xuan (tvxuan@hcmut.edu.vn)

ABSTRACT

The discovery of the oil in the basement of Bach Ho oil field in the Cuu Long basin of Vietnamese continental shelf since 1987, the oil in the fractured basement is more interested in the world. Especially for the fractured basement, the lithological physics of the basement has not only played an important role in assessing the reserve but also directed the expansion of exploration and exploitation at Bach Ho field. The fractured basement is characterized by complex geological structure, heterogeneity, especially in lithological composition and porous system. This project involves collecting, correlation and analyzing the data and performance methods of explaining well logging data in fractured basement at the specific well with the support of FRP software-Well Insight. The results of calculating the total porosity and the proportion of highly reliable minerals were verified by the high correlation coefficient between the theoretical and practical curves (GR: 98.69%, RHOB: 94.87%, DT: 86.81% NPHI: 96.35%), at last checked with sample data for reliable assessment.

KEYWORDS: Cuu Long Basin, fractured basement reservoir, FRP, well logging, porosity rock